The role of large-scale eddies in the nonlinear equilibration of a multi-level model of the mid-latitude troposphere.

by

Amy Beth Solomon

Submitted to the Department of Earth, Atmospheric and
Planetary Science
in partial fulfillment of the requirements for the degree of

Doctor of Philosophy

at the

MASSACHUSETTS INSTITUTE OF TECHNOLOGY

September 1997
[February 1998]

Author ⌣ ....
Department of Earth, Atmospheric and Planetary Science
September 19, 1997

Certified by..
Peter H. Stone
Professor of Meteorology
Thesis Supervisor

Accepted by ....
Thomas H. Jordan
Chairman, Department of Earth, Atmospheric and Planetary
Science

The role of large-scale eddies in the nonlinear equilibration of a multi-level model of the mid-latitude troposphere.

by

Amy Beth Solomon

Abstract

The role of waves in maintaining the mid-latitude tropospheric climate is investigated in a dry high resolution quasi-geostrophic β-plane channel model which is coupled to an equation for the horizontally averaged static stability tendency. This coupling allows for the feedback between vertical eddy heat fluxes and the vertical temperature structure, which is typically neglected in quasi-geostrophic models. It is important to include this process in order to understand the dynamical balance in the boundary layer. The model includes simple parameterizations of heating. surface friction and fluxes by turbulent eddies.

Studies of the impact of vertical resolution on the model's equilibrated climate and fluxes show that, given the standard set-up of the model, decreasing the resolution stabilizes the eddies. Coupling the model to an equation for the surface air temperature tendency eliminated this dependence on the vertical resolution.

The model's climate is found to be separated into two dynamical regimes, one within the boundary layer and the other within the free troposphere. In the free troposphere the potential vorticity gradients are relatively independent of the parameters and parameterizations used to define the boundary layer, although the equilibrated static stability and meridional temperature gradients are not. The potential vorticity gradients are essentially eliminated in the mid troposphere, in agreement with observations. The complete homogenization of pv occurs in the region where the baroclinic waves have a critical layer.

The dynamics in the boundary layer are determined by the tropopause potential vorticity structure and the parameterization of the turbulent fluxes of heat and momentum in the atmospheric boundary layer. Thermal diffusion in the boundary layer prevents the modification of the mean temperature structure by damping temperature fluctuations. This result is consistent with the recent observational study by Swanson and Pierrehumbert (1997).

A three dimensional time dependent linear stability analysis is used to demonstrate that the equilibrated climate is stable to linear perturbations. These results are contrasted with the results of a one dimensional stability analysis to show the sensitivity of these results to the treatment of the meridional structure of the eddies.

The feedbacks which maintain the static stability are shown to play a significant role in the homogenization of the potential vorticity above the atmospheric boundary layer (ABL). These feedbacks are also shown to couple the dynamics within the ABL with the upper troposphere in a study of the sensitivity of the vertical structure of the large scale eddies to changes in the radiative equilibrium temperature gradients.

Thesis Supervisor: Peter H. Stone
Title: Professor of Meteorology

Acknowledgments

This thesis is dedicated to my mother and father, Joan and Herschel Solomon. Your love of life and openmindedness is a gift to all who have the pleasure of knowing you.

I would like to thank my two remarkable sisters, Dore Bowen and Rachel Kardos. We have all chosen very different paths in life but we have never forgotten to turn around and wave and blow kisses periodically.

Thank you to my advisor, Dr. Peter Stone, for without his guidance and patience, I would not be embarking upon this rewarding career. I would like to thank Drs. Richard Lindzen, Reginald Newell, and John Marshall for their insightful suggestions which helped to clarify many of the ideas in this thesis. Thank you to Dr. Kevin Trenberth at the National Center for Atmospheric Research. Your unwavering support and encouragement has been a source of inspiration.

And to all of my wonderful friends at MIT. Life would not have been the same without zenning with Natalie Mahowald, guffawing with Adam Sobel, spontaneously reciting poetry with Danny Davidoff and John Olson, and of course, slipping away to matinees with Gunter Siddiqi. Thank you to Gerard Roe and Bonnie Souter for the fantastic bike adventures. I would never have been so crazy as to dream up these challenges, but am very glad that you did. And to Nili Harnik, Boaz Nemet, Constantine Giannitsis, Christophe Herbaut, and Rebecca Morss who I will always remember as listening and dancing to Latin music on a hot summer night. And of course, to my dear friends, Gidon Eshel, David Keith, and Susan Poole, who like myself have a taste for the out-of-doors and who helped me to keep life as a graduate student in perspective.

Thank you to the National Center for Atmospheric Research, which is sponsored by the National Science Foundation, for the use of the NCEP and ECMWF observational analyses.

Contents

List of Tables

8

List of Figures

Chapter 1

Introduction

This thesis work is an investigation of the interaction between large scale eddies and the mean climate in a multi-level quasi-geostrophic β-plane channel model. This study focuses on two aspects of this interaction. These aspects are the maintenance of the temperature structure near the lower boundary and the homogenization of potential vorticity in the mid troposphere.

1.1   Motivation

1.1.1   Dynamics at the lower boundary

The first question that is addressed in this process model study is what are the processes and feedbacks that are responsible for the observed temperature structure and eddy fluxes near the lower boundary? This question is motivated by the observation that heat fluxes in GCM's tend to be larger than observed heat fluxes even though the modeled temperature gradients are close to observations (Stone and Risbey 1990; Gleckler et $al.$ 1995). It has been proposed that this is due to inadequate representations of the processes and feedbacks that are responsible for the maintenance of the vertical temperature structure near the lower boundary (Stone and Nemet 1996). Three main studies are highlighted in this investigation of the maintenance of the temperature structure near the lower boundary. They are the impact of vertical resolution in the boundary layer, the importance of the feedback between vertical eddy heat fluxes and the static stability and thirdly, the sensitivity of the temperature structure to changes in the surface drag and eddy diffusion coefficients that define the boundary layer.

Two-level quasi-geostrophic and primitive equation models have been used to investigate the nonlinear equilibration of a baroclinically unstable basic state in a host of studies (Held and Suarez 1978; Stone and Branscome 1991; Zhou and

Stone 1992a; Zhou and Stone 1992b; Cehelsky and Tung 1991). These models of baroclinic instability generally assume that large scale waves, which are resolved by the two-level geometry, are primarily responsible for the modification of the mean temperature structure. This conclusion has typically been based on the scaling analysis of Held (1978a) which shows that the shallow waves are relatively inefficient in transporting heat.

Can two-level models, some of which are mentioned above, simulate the eddy-mean flow interaction in the troposphere? Observed annual mean midlatitude sensible heat fluxes in both hemispheres peak at 850 mb, become small in the mid troposphere and have a secondary maximum in the upper troposphere (Trenberth 1992). Therefore, modification of climate forcing in limited regions of the troposphere may have different eddy responses. This problem has been investigated in the context of greenhouse warming, where an increased concentration of greenhouse gases leads to smaller lower tropospheric temperature gradients but larger tropospheric gradients than does the present climate (Manabe and Wetherald 1975), by studies which used multi-level quasi-geostrophic models, such as Held and O'Brien (1992) and Pavan (1996). These studies found that the dynamics in a multi-level quasi-geostrophic model are more sensitive to changes in the lower tropospheric temperature gradients than to changes in the upper tropospheric gradients. It is hypothesized that this is due to the importance of shallow eddies which are more sensitive to changes in the vertical profile of the temperature structure than the deeper eddies which are only sensitive to mean tropospheric fields. These studies support the claim that two-level model studies can simulate eddy-mean flow interaction in a vertically averaged sense, but they also suggest that any simulation of the observed troposphere must be able to resolve the shallow waves that modify the vertical distribution of the eddy and mean fields. Therefore, it may be necessary to resolve these shallow eddies in order to simulate the eddy response to more realistic changes in climate forcing.

The concentration of sensible poleward heat fluxes above the planetary boundary layer in observations suggests that processes near the Earth's surface inhibit eddy heat transport in the regions where the source of available potential energy for the growth of the wave is a maximum. The dominant process that is responsible for the reduction in the eddy heat transports at the surface is surface friction. The role of surface friction in modifying the characteristics of the baroclinic waves has been studied by Valdes and Hoskins (1988) and Lin and Pierrehumbert (1988). These studies used linearized quasi-geostrophic and primitive equation models to demonstrate that Ekman pumping damps out the shallow waves at the top of the boundary layer, leaving the large scale waves to modify the baroclinically unstable basic state. This result has been disputed by Farrell (1985) who argues that, using realistic values of the eddy diffusion coefficient, Ekman damping damps out all normal mode baroclinic waves. Farrell argues that it is non normal modes that are responsible for the eddy heat transport that is observed in the midlatitude lower troposphere. Whether or not Ekman pumping completely stabilizes the normal mode baroclinic waves in the troposphere, it is

clear that the results are very sensitive to the parameters that are used to define the boundary layer.

Gutowski *et al.* (1989) studied the role of surface friction and surface heat fluxes in modifying the eddy-mean flow interaction. Their study showed that there was an important negative feedback between the surface heat fluxes and the vertical eddy heat fluxes. When the surface heat fluxes were removed, the vertical eddy heat fluxes caused large increases in the static stability at the lower boundary. Surface heat fluxes counteract this large increase in the static stability by downgradient mixing of potential temperature. The reduction of the static stability in the boundary layer causes the boundary layer to be more baroclinically unstable which causes the large scale eddies to transport more heat poleward, reducing the meridional temperature gradients. In order to understand the dynamics that are responsible for the observed distribution of heat fluxes and mean temperatures, it is necessary to study the feedbacks between these processes and the equilibrated state that is determined by them.

These feedbacks, which are neglected in classic quasi-geostrophic models, are also important in the sensitivity of the temperature structure to changes in climate forcing. Studies of baroclinic adjustment which include variable static stability have demonstrated that the negative feedback between the vertical eddy heat flux and the static stability plays a significant role in reducing the sensitivity of the model's climate to changes in external forcing. In models with fixed static stability, the equilibrium shear is found to be linearly proportional to the static stability and relatively insensitive to the changes in external forcing (Stone and Branscome 1991: Zhou and Stone 1992a). In two-level models that include a variable static stability, the sensitivity of the climate to changes in external forcing was reduced (Held and Suarez 1978; Held 1978a; Zhou and Stone 1992b). demonstrating the significance of the feedbacks between the dynamical heat fluxes in stabilizing the climate, as suggested by Stone (1972).

Increasing vertical resolution may modify the characteristics of the baroclinic waves by resolving the potential vorticity gradients more accurately. Previous studies of the barotropic point jet, which is mathematically homomorphic to the linearized Boussinesq Charney problem (Lindzen *et al.* 1983) , have shown that the stability characteristics of a baroclinically unstable flow are a function of the vertical resolution. An increase in the vertical resolution resolves the delta function jump in the potential vorticity at the lower boundary of the model, making the model more baroclinically unstable. A decrease in the vertical resolution decreases the magnitude of the jump in the potential vorticity at the lower boundary, stabilizing the model. It is not clear how this result translates to the full three-dimensional quasi-geostrophic model, but it suggests that two-level models may not be simulating the degree of the instability in the troposphere accurately. Therefore, an increase in the vertical resolution may have a significant impact on the stability characteristics of the baroclinic waves.

1.1.2 Homogenization of potential vorticity

The second question that is addressed in this study is what is the extent of the pv homogenization in a multi-level quasi-geostrophic beta plane channel model and how does this relate to current theories about the nonlinear equilibration of the observed mid-latitude troposphere? This question is motivated by the study of Lindzen (1993) which hypothesized that a possible simplistic equilibrated state which describes the observed mid-latitude troposphere is a state where the pv gradients in the mid troposphere have been homogenized such that waves propagating along the tropopause and the surface of the earth can no longer interact.

Adiabatic and inviscid process model studies have demonstrated that linear adjustment theory predicts the equilibrated state of an initially unstable flow, but these model studies have had little success in simulating the observed climate. Model studies that include simple representations of diabatic heating and surface friction have been relatively successful in simulating the observed large scale dynamics (Held and Suarez 1978; Stone and Branscome 1991). These two-level model studies attempt to relate the climate of a forced/dissipated model to the climate predicted by linear/inviscid/adiabatic criteria. It is not clear that this is justified.

The Charney-Stern criterion for instability is a necessary condition for instability but it is not sufficient. A basic state which has a change of sign in the meridional gradient of potential vorticity may be stable. A linear stability analysis of the equilibrated state proposed by Lindzen (1993) would show that the baroclinic normal modes have been stabilized but this state would still satisfy the Charney-Stern criteria necessary condition for instability.

The equilibrated state proposed by Lindzen (1993) is consistent with the observational studies of Sun and Lindzen (1994), Morgan (1994), and Fullmer (1982b) which have shown that the potential vorticity gradients in the extratropics are significantly less than β, the meridional gradient of planetary vorticity, in the mid troposphere but large in the planetary boundary layer and a maximum at the tropopause. These studies make it clear that the observed extratropical temperature structure is determined, in part, by the mixing of potential vorticity along isentropic surfaces.

In order to resolve this state it is necessary to be able to decouple the dynamics between the surface, the mid troposphere and the tropopause. A two-level model couples the dynamics in the lower troposphere with the upper troposphere. This causes the dynamics at the jet and the dynamics in the boundary layer to interact in a very artificial way. If this equilibrated state approximates the dynamics in the atmosphere then the equilibrated state of the two-level model will have very little to do with the observed climate. If the dynamics in the observed climate are roughly approximated by the state hypothesized by Lindzen (1993), a model with more than two levels would be necessary to resolve it.

There have been many studies done concerning the homogenization of pv in subtropical ocean gyres. Fundamental studies by Rhines and Young, RY from here on, (Rhines and Young 1982a,b; Young and Rhines 1982) have demonstrated that there is very efficient homogenization of pv in layers that are not directly in contact with the wind-driven Ekman pumping at the ocean's surface. These studies were done using simple quasi-geostrophic layer models which neglected cross interface motion. Neglecting cross interface motion means that diabatic processes, that change the density in a layer, are neglected. In models of the atmosphere, neglecting these processes result in a climate which bears very little resemblance to observations (Gutowski *et al.* 1989). Therefore, model's which neglect these processes may not be very useful in understanding the wave-mean flow interaction in the atmosphere.

In subtropical ocean gyres, geostrophic streamfunctions which emanate from the eastern boundary have streamfunctions which are equal to zero, due to the Sverdrup streamfunction which vanishes at the easten boundary. Therefore. in order for there to be any circulation along a geostrophic contour, the contour must be disconnected from the eastern boundary. Rhines and Young chose an Ekman pumping velocity such that this condition is satisfied. The Ekman pumping velocity needed to close the geostophic contours is equivalent to the condition that the progress of a westward propagating baroclinic Rossby wave, with a characteristic horizontal velocity which exceeds βL_d^2, has been arrested (Pedlosky 1996). where L_d is Rossby deformation radius. In the RY studies, pv which is enclosed by a closed geostrophic contour, in layers below the directly forced upper layer, become well-mixed as long as the dissipation is sufficiently small. After the pv becomes homogenized, the fluxes which were reponsible for the mixing, decay away.

This scenario of mixing in a subtropical ocean gyre is significantly different from mixing in the atmosphere. In the atmosphere, closed geostrophic contours are a product of wave-mean flow interaction and are not directly forced independent of the eddies. Also, heating and friction in the atmosphere are continually acting to destabilize the eddies. Therefore, the efficient mixing of pv. that was found in subtropical ocean gyres, would not be expected in the atmosphere. In the atmosphere, wave-mean flow interaction would be expected to occur in regions of strong damping (McIntyre and Norton 1990) and near the critical level (Stewartson 1978, Warn and Warn 1978, Killworth and McIntyre 1985). In the equilibrated state, eddy forcings would be expected to continually act against the forcings of external heating and dissipation in life cycles of 'saturation-propagation-saturation' (Edmon *et al.* 1980, Hoskins 1983, Hoskins *et al.* 1985, Held and Hoskins 1985, Randel and Held 1991).

1.1.3   Strategy for investigating these questions

The first objective of this thesis work is to develop a quasi-geostrophic β-plane channel model with variable vertical resolution which is coupled to an equation

for the static stability tendency. The second objective is to study the maintenance of the temperature structure at the lower boundary as a function of the processes and feedbacks that are simulated in this simple representation of the midlatitude troposphere. The third objective is to investigate the modification of the model's nonlinear equilibration as resolution and internal parameters are varied.

Initial runs with the model have shown that the equilibrated state, without a representation of a stratosphere/tropopause, can be separated into these two studies. That is, the equilibrated state is roughly characterized by a mid troposphere with homogenized potential vorticity and a boundary layer whose potential vorticity gradients are a function of the parameters that define the boundary layer. When a stratosphere/tropopause is included in the model, potential vorticity mixing in the mid troposphere is enhanced and the potential vorticity gradients in the boundary layer are significantly reduced.

1.2   Summary of previous work

1.2.1   Criterion for stability

Charney and Stern (1962) derived a necessary criterion for the existence of an unstable wave in a quasi-geostrophic continuous atmosphere. Friction and heating were neglected in the derivation and the perturbations were assumed to be normal modes. In order for the growth rate of the wave to be nonzero, the necessary criterion is that:

$$\int_0^L dy \left(\int_{z_b}^{z_t} dz \frac{\rho \overline{q}_y |\phi|^2}{|\overline{u} - c|^2} \right) + \frac{f_0^2}{N^2} \left(\frac{\rho \overline{u}_z |\phi|^2}{|\overline{u} - c|^2} \right) \Big|_{z_b}^{z_t} = 0$$

Where, from here on, y and z are latitude and height, respectively, and ρ is equal to the basic state density, $\overline{q}_y$ is the meridional gradient of the pseudo-potential vorticity (from here on referred to as potential vorticity), $\overline{u}$ is the basic state zonal wind, $\overline{u}_z$ is the basic state zonal wind shear, c is the phase speed of the wave, ϕ is equal to the geopotential, f_0 is the Coriolis parameter at 45N, and N is the Brunt-Vaisala frequency. Where the equation is integrated in the vertical between z_b and z_t and in the latitudinal direction between 0 and L. In an atmosphere that has upper and lower boundaries and no meridional temperature gradients at these boundaries, the necessary condition for the existence of an unstable wave is that the meridional gradient of the potential vorticity, $\overline{q}_y$, does not change sign in the domain. In a quasi-geostrophic atmosphere, $\overline{q}_y$ is given by:

$$\overline{q}_y = \beta - \overline{u}_{yy} - \frac{f_0^2}{\rho} \frac{\partial}{\partial z} \frac{\rho}{N^2} \frac{\partial \overline{u}}{\partial z}$$

Where β is the planetary potential vorticity gradient, $\bar{u}_{yy}$ is the barotropic component of the potential vorticity gradient, and the last term in the equation is the baroclinic component of the potential vorticity gradient. Since $\bar{q}_y$ tends to be greater than zero, due to the dominance of the β term, an atmosphere with regions of negative $\bar{q}_y$ is considered to be potentially unstable. A sufficient condition for stability, by this criterion, is that the potential vorticity gradient does not change sign in the domain.

Bretherton (1966) derived a modified form of $\bar{q}_y$, for a purely baroclinic flow, which expressed meridional temperature gradients at the upper and lower boundaries as delta functions of potential vorticity. The modified potential vorticity gradient is

$$\tilde{\bar{q}}_y = \bar{q}_y - \frac{f_0^2}{N^2}\frac{\partial \bar{u}}{\partial z}\Big\{\delta(z - z_b) - \delta(z - z_t)\Big\}.$$

This modified expression for the potential vorticity gradient incorporates the surface temperature gradients into the definition of the potential vorticity which reduces the Charney-Stern criterion for instability to

$$\int_0^L dy \int_{z_b}^{z_t} dz \frac{\rho \tilde{\bar{q}}_y |\phi|^2}{|\bar{u} - c|^2} = 0.$$

Where the limits of integration are as defined previously. With this form of the potential vorticity gradient and the instability criterion, the necessary condition for instability is a change of sign in the potential vorticity gradient in the domain, regardless of the temperature gradients at the boundaries. The Charney-Stern criterion for instability is used in most process models to determine whether a flow has been stabilized to growing waves.

In the two-level model, the upper layer has $\bar{q}_y > 0$ and the lower layer $\bar{q}_y < 0$ due to the constant shear in the interior that goes to zero at the boundaries. By the Charney-Stern theorem, this basic state is potentially unstable to growing waves. The modification of the basic state necessary to stabilize the growing waves, is the increase of the potential vorticity gradient in the lower layer such that $\bar{q}_y = 0$. Then the basic state $\bar{q}_y$ of the two-level model will be non-negative and the flow will satisfy the sufficient condition for stability. The shear that satisfies this condition for stability, neglecting $\frac{\partial^2 \bar{u}}{\partial y^2}$, is given as follows:

$$\bar{q}_y = \beta - \frac{2f^2}{N^2 H}\frac{\partial \bar{u}}{\partial z} = 0$$

$$\frac{\partial \bar{u}}{\partial z}\Big|_c = \frac{\beta H N^2}{2f^2},$$

where H is the vertical scale height and f is the Coriolis parameter. This is the critical shear derived from the Charney-Stern criterion for instability. It is linearly proportional to the static stability. The two-level model calculates the shear at

only one level. This shear is not constant with height since the shear goes to zero at the upper and lower boundaries.

In a two-level model that allows the static stability to be variable, this criterion for stability is expressed as a critical slope of the isentropes. The static stability is defined to be

$$N^2 = \frac{g}{\rho} d\theta/dz,$$

where g is the acceleration of gravity and θ is potential temperature. Using the thermal wind relation:

$$du/dz = -\frac{g}{f\rho} d\theta/dy$$

the critical slope of the isentropes is given by

$$S = -\frac{f}{N^2} \frac{\partial \overline{u}}{\partial z} |_c.$$

Which is equal to a constant in the two-level model. This is the isentropic slope sufficient to stabilize the baroclinic waves in a two-level model. If the basic state of the flow is adjusted such that the growth of the baroclinic eddies is just zero, this basic state is referred to as the neutral state.

1.2.2   Quasi-geostrophic two-level models

Stone and Branscome (1991) studied large scale eddies in a two-level quasi-geostrophic midlatitude β-plane model. The flow in the model was forced by Newtonian cooling. Friction was represented by a linear surface drag at the lowest level. The initial state of the model was a temperature structure in radiative equilibrium and a zonal wind in thermal wind balance. A random perturbation was added to the initial state and the model was run until it reached a steady state. In this model the static stability was set equal to a constant , so the change in the temperature structure due to baroclinic adjustment was characterized by the steady state meridional temperature gradient. The results of the study showed that the shear of the steady state was proportional, and supercritical, to the critical shear of the two-level model. The critical shear of the two-level model is the shear that is required to stabilize all of the baroclinic eddies. Stone (1978) proposed that the baroclinic eddies will act to adjust the initial shear to this critical shear, thereby stabilizing the eddies. This is called the baroclinic adjustment hypothesis. The result of the Stone and Branscome study imply that a weaker form of the baroclinic adjustment hypothesis has a strong influence in determining the equilibrium temperature structure. A further result of this study was that the meridional temperature gradient was independent of the magnitude of the diabatic forcing and linearly proportional to the static stability. The equilibrium shear in this study was found to be relatively independent to changes in

the diabatic heating. The equilibrium shear is also linearly proportional to the static stability. These results are also consistent with the baroclinic adjustment hypothesis and with the neutral state predicted by the Charney-Stern criterion for stability. The main difference between the results of this study and the predicted neutral state is that the equilibrium shear is still unstable by the Charney-Stern theorem, even though the growth of the baroclinic eddies has been suppressed in the model. The extreme vertical truncation in the two-level model makes it unclear how these processes would be manifest in the atmosphere, or even in a model with continuous vertical structure.

1.2.3   Baroclinic adjustment in continuous models

In a study of the mean flow adjustment by a growing baroclinic wave, Gutowski *et al.* (1989) derived the mean state that was stable to the growing eddies. This study demonstrated that the minimal adjustment necessary to stabilize an initially unstable flow to baroclinic eddies satisfied the equation,

$$\overline{q}_y = 0. \qquad (1)$$

This derivation assumes that the slope of the isentropes goes to zero at the lower boundary:
$$S(z = 0) = 0 \qquad (2).$$

The upper part of the atmosphere is assumed to be unchanged by the baroclinic adjustment process. The adjusted isentropic slope is assumed to be equal to the initial isentropic slope at the top of the adjusted region

$$S_A(z_A) = S_0(z_A) \qquad (3)$$

where z_a is the adjustment height, $S_A(z)$ is the adjusted slope of the isentropes and $S_0(z)$ is the initial isentropic slope. If the basic state zonal wind is assumed to be constant in the meridional direction then.

$$\overline{q}_y = \beta + f \frac{\partial \rho S(z)}{\rho \partial z}. \qquad (4)$$

where $\rho = \rho_0 e^{-z/H}$ is the basic state density and H is the density scale height.

From (1), (2), and (4) the adjusted slope of the isentropes is derived to be

$$S_A(z) = \frac{\beta H}{f}(1 - e^{z/H}).$$

From (3), the height where the adjusted isentropes match to the initial isentropes is derived to be
$$z_A = H ln(1 - f S_0(z_a)/\beta H).$$

This is the adjustment height that was derived by Lindzen and Farrell (1980), in a study of baroclinic adjustment in a continuous atmosphere.

In the two-level model the density is constant and the adjustment height is fixed, due the vertical discretization of the model, to $H/2$. The adjusted slope of the isentropes reduces to

$$S_A(H/2) = -\frac{\beta H}{2f}.$$

Using the definition of the isentropic slope and the thermal wind relation,

$$S = \frac{\partial\theta/\partial y}{\partial\theta/\partial z} = \frac{-f\partial u/\partial z}{N^2}.$$

Now, setting these two expressions for the adjusted isentropic slope to be equal:

$$\frac{\beta H}{2f} = \frac{f\partial u/\partial z}{N^2}$$

In a two-level model, the static stability is held constant and this equation reduces to the Phillips' critical shear for stability,

$$\frac{\partial u}{\partial z} = \frac{\beta N^2 H}{2f^2}.$$

There are two limiting cases for the baroclinic adjustment in this derivation. The first case allows the static stability to vary while the shear is held constant. The second case allows the shear to vary and the static stability is held constant. The first limiting case, where the shear is held constant, was investigated by Gutowski (1985b). The adjusted static stability goes to infinity at the lower boundary. The equilibrium state was calculated to be the neutral state predicted by the linear adjustment theory. The study found this adjusted state matches the observations better than the moist adiabat in winter but not in summer. The observations show that the static stability does not asymptote to infinity at the ground. Lindzen and Farrell (1980) investigated the second limiting case, where the static stability is held fixed. The zonal wind shear in this adjustment goes to zero at the ground. By the thermal wind relation, this is equivalent to removing the temperature gradients at the lower boundary. Both of these limiting cases result in a neutral state that is quite different from what is observed in the atmosphere. This is due partly to the boundary condition that is imposed on the adjusted isentropic slope at the lower boundary. The critical slope of the isentropes is assumed to go to zero at the lower boundary. Observations show that the slope of the isentropes does not go to zero at the Earth's surface, due to the production of potential vorticity by sources, such as diabatic heating. This is imposing an unphysical boundary condition on the adjusted state, so it is not surprising that the resulting neutral state is different from the observed climate.

Gutowski (1989) investigated the modification of the baroclinic adjustment process over the life cycle of a baroclinic wave when both the static stability and the zonal wind shear are allowed to vary. This study demonstrated that, without forcing, the neutral state of the model is predicted by the linear adjustment theory. In the absence of forcing, the adjustments in the static stability and the zonal wind shear were found to have almost equal contributions. When surface friction was included, zonal wind shear adjustment was inhibited. When surface heat flux was included, the adjustment of the static stability was inhibited. When both of these processes were included in the model, the vertical profiles of the static stability and the zonal wind shear were found to simulate the observed profiles well. This study suggests that surface friction and surface heat flux are needed in a model to simulate the observed structure of the atmosphere. It also indicates the necessity of adequate vertical resolution and dynamical feedbacks. A further result is that this very simplified model can simulate observed static stability and zonal wind shear profiles reasonably well, even though moist convection and latent heating have been excluded.

Chapter 2

The Model

2.1 Introduction

The model used in this study integrates the quasi-geostrophic equations coupled to an equation for the horizontally averaged potential temperature on a mid latitude β-plane. The model has variable vertical and horizontal resolution. The zonal, meridional and vertical coordinates are evaluated in gridpoint space. Gridpoints in the vertical are equally spaced as a function of pressure. There is a rigid lid at the top and bottom of the model. Therefore, there is no vertical motion at the surface of the model and at zero pressure. There is no flow through the channel walls. Line integrating the zonal mean wind tendency equation at the channel walls gives a further boundary condition that the momentum convergence at the channel walls is equal to zero. Periodic boundary conditions are applied to all fields in the zonal direction.

The variables are arranged in the vertical using the Charney-Phillips grid. This grid places the vertical velocity and the potential temperature at the same levels. Arakawa and Moorthi (1988) compared the two classic vertically discrete systems, the Lorenz grid and the Charney-Phillips grid. This study found that the Lorenz grid has a computational mode that leads to spurious amplification of shortwaves. The problem with the grid was interpreted as a consequence of the spurious mode falsely satisfying the necessary condition for baroclinic instability at the boundaries. The Charney-Phillips grid can not calculate the static stability when it is used in a two-level model. For this reason the Lorenz grid has been used in all two-level model studies that include a variable static stability. The spurious mode is effectively filtered out in the two-level model, but this computational mode causes serious problems in a model with more than two levels.

The model uses the Arakawa Jacobian scheme which conserves mean enstrophy, mean energy, and the average wavenumber. The potential vorticity at time step $t + 1$ is calculated using the centered difference leap frog scheme,

$$q_{t+1} = q_{t-1} + 2\Delta t \frac{\partial q_t}{\partial t}.$$

This time scheme has a computational mode, but it is used due to the computational efficiency of the scheme. The computational mode is removed by averaging the odd and even solutions,

$$q_{t+1} = \frac{1}{2}(q_t + q_{t+1}),$$

after every ten time steps. The Courant-Friedrich condition is used to determine the size of the time step. The routine is set up for fifteen minute time steps. The streamfunction at time step $t + 1$ is calculated by inverting the potential vorticity,

$$\psi_{t+1} = \nabla^{-2}(q_{t+1} - \beta y)$$

The potential vorticity is inverted using the fft solver from the quasi-geostrophic ocean model written by the Space and Atmospheric Physics Group at Imperial College.

All runs are initially in radiative convective equilibrium (RCE). The model is run for 20 days without a perturbation to allow the dynamics in the planetary boundary layer to come into a symmetric equilibrium. Then the model is perturbed with small amplitude waves 1-9. The amplitude of the pressure perturbation at the surface is 10 Pascals in each of the nine waves. The model is run for 1000 days with the statistics being calculated for the last 400 days. This is a sufficiently long run to establish a statistically steady state.

This model has been used to investigate;

- The feedbacks between vertical eddy heat fluxes and static stability and thermal diffusion.
- The robustness of the critical shear, potential vorticity gradients and isentropic slopes.
- The homogenization of potential vorticity.
- The modification of vertical and horizontal eddy fluxes.
- The division of adjustment between the static stability and $\frac{dT}{dy}$.
- The importance of resolving the boundary layer for vertical structure and vertically averaged eddy fluxes and mean temperatures.
- The modification of the results when a tropopause is included in the model.

2.2   Horizontal and vertical dimensions and resolution

The standard control run has a channel width of 10,000 km and a channel length of 5,260 km. The channel width is approximately 90 degrees in latitude and was chosen in order to prevent the dynamics at the channel walls from modifying the dynamics at the center of the channel.

The channel length of the standard control run is equal to the wavelength of the most unstable wave of the symmetric state of the control run, calculated from a 1-D linear stability analysis.

The horizontal resolution of the standard control run is 329 km. This resolution was determined to be the minimum resolution needed to get a convergent equilibrium climate and eddy fluxes with the free parameters of the control run. The resolution in the meridional direction is always set to approximate the resolution in the zonal direction.

The sensitivity of the model's climate to changes in horizontal resolution is discussed in Chapter 4.

2.3   The equations

2.3.1   The quasi-geostrophic equations

This model integrates the quasi-geostrophic (qg) potential vorticity equation in pressure coordinates:

$$\frac{\partial q}{\partial t} = -J(\psi, q) - f_0 \frac{\partial}{\partial p} \frac{\dot{Q}R}{spC_p} + \hat{k} \bullet \nabla \times \overrightarrow{F},$$

where R is the ideal gas constant, and C_p is the specific heat at constant pressure. s is the static stability parameter and is written as:

$$s = -\frac{1}{\pi} \frac{\partial [\theta]}{\partial p}$$

where [   ] indicates an areal mean and

$$\pi = \frac{p}{R} \left(\frac{p_0}{p}\right)^{R/C_p}$$

, p_0 is the pressure at the lower boundary.

$$q = \nabla^2 \psi + \beta y + f_0^2 \frac{\partial}{\partial p} \frac{1}{s} \frac{\partial \psi}{\partial p},$$

where ψ is the streamfunction and

$$\beta = \frac{1}{a} \frac{\partial f}{\partial \phi} |_{45\circ},$$

where a is the radius of the earth and ϕ is latitude in meters.

The qg potential vorticity equation is derived from the qg vorticity, qg potential temperature, hydrostatic, and ideal gas equations:

$$D_g(\nabla^2 \psi + \beta y) = f_0 \frac{\partial \omega}{\partial p} + \hat{k} \bullet \nabla \times \vec{F},$$

where *omega* is the vertical velocity in pressure coordinates.

$$D_g \theta^* = -\omega \frac{\partial[\theta]}{\partial p} + \frac{\theta}{c_p T} \dot{Q},$$

where T is temperature.

$$\theta^* = -\pi f_0 \frac{\partial \psi}{\partial p}$$

Where D_g is the total geostrophic derivative :

$$D_g = \frac{\partial}{\partial t} + \vec{v}_g \bullet \nabla$$

and

$$\theta = [\theta](p) + \theta^*(x, y. p, t)$$

Where $*$ indicates the deviation from the areal mean and it is assumed that

$$\frac{\partial \theta^*}{\partial p} \ll \frac{\partial[\theta]}{\partial p}$$

F is friction and $\dot{Q}$ is diabatic heating.

The qg equations make the following approximations:

- The Coriolis parameter can be approximated by the first order Taylor expansion, $f_o + \beta y$, because the latitudinal scales of the perturbations are assumed to be small relative to the radius of the earth.

- The Rossby number, $R_o = U/f_0 L$, is small. Where L is the horizontal spatial scale of variation of the flow.
- The advection due to the ageostrophic wind is negligible relative to the advection due to the geostrophic wind.
- The vertical advection terms are assumed to be small.
- The relative vorticity is assumed to be negligible relative to the Coriolis parameter in the divergence term.

2.3.2   The static stability tendency equation

The qg equations are coupled to an equation for the static stability tendency. This equation is derived from the horizontally averaged thermodynamic equation. The vertical mean potential temperature fluxes are assumed to be insignificant relative to the eddy fluxes. This assumption can be justified by scaling analysis (Gutowski 1983), and is consistent with two-level model results (Zhou and Stone 1993b).

The horizontally averaged potential temperature tendency at time step vt is given by:

$$\frac{\partial}{\partial t}[\theta_t] = -\frac{\partial}{\partial p}[\omega_t^\star \theta_t^\star] + \left[\frac{\dot{Q}_t}{C_p}\right]\left(\frac{p_0}{p}\right)^{R/C_p},$$

where *'s are used to designate deviations from the zonal mean and [ ] again indicates an areal mean.

The static stability parameter is calculated from the updated mean potential temperature.

2.4   Parameterizations used in the model

There are six free parameters in the model. They are:

- ν_T = eddy thermal diffusion coefficient
- ν_m = eddy momentum diffusion coefficient
- c_d = surface drag coefficient
- $\frac{dT_e}{dy}$ = radiative convective equilibrium temperature gradients
- $\frac{dT_e}{dz}$ = radiative convective equilibrium lapse rate
- τ_d = diabatic heating timescale

2.4.1   Winds and temperature in the ABL

a. Fixed sea temperature

This model was not designed to study the evolution of a climate which starts from a state without dynamical transports to a state which approximates the observed climate. In order to accomplish this it would be necessary to include an ocean model and a radiative forcing that changes as a function of the sea surface temperatures. This model is designed to model the response of large scale eddies to a radiative forcing due to realistic ocean temperatures.

Zonal mean sea surface temperatures change by up to 1K/month in the mid latitude oceans (Peixoto and Oort 1992; Shea *et al.* 1990). This is not a negligible temperature tendency and it would be interesting to look at the large scale eddy response to a more realistic time dependent radiative forcing and atmosphere-ocean fluxes. In a process model, it is necessary to limit and isolate processes in order to understand the mechanisms that are responsible for the observed mean fluxes and climate. Therefore, the air-sea interactions in this model are represented by a thermal damping of the surface air back to the underlying ocean and a vertical diffusion of heat throughout the ABL.

A recent observational study by Swanson and Pierrehumbert (1997) investigated whether the observed meridional temperature gradients in the lower troposphere are a result of dynamical eddy diffusivities or are a result of the strong thermal interaction between the lower troposphere and the ocean. This study found that the lower troposphere heat transport is characterized by a thermal damping of temperature fluctuations back to the underlying ocean with a timescale of approximately 1 day. This strong thermal damping was found to reduce the heat flux in the lower troposphere by as much as a factor of two over what it would have been with temperature mixing alone. This thermal damping was determined to be due to the air-sea fluxes of sensible heat. This conclusion was based on the observed symmetry between the cold and warm temperature fluctuations, an asymmetry would be expected from the release of latent heat.

It is very significant to first of all understand the response of the large scale eddies to this strong thermal damping in the lower troposphere. Therefore, the sea surface temperatures (SST's) are held fixed in all of the model runs that are discussed in this thesis. This is the same approach that has been taken in control runs with atmospheric GCM's.

b. Control run

In the control run, there is assumed to be a well-mixed layer between the surface and the first model level. Therefore, the potential temperature of the air above the surface is set equal to the potential temperature at the first model level. This parameterization of the surface air potential temperature causes there to be a deeper mixed region as the vertical resolution is decreased. The standard 17 level run has a mixed region that is 63 mb deep, while the 3 level run has a very unrealistic mixed layer depth of 500 mb.

The surface winds are calculated by linear extrapolation from the first two model levels, following previous model studies such as Stone and Branscome (1991).

c. Interactive surface air temperature

A series of runs was done including an interactive surface air temperature. An interactive surface air temperature is not included in the control run. These runs were done to determine if the model's sensitivity to changes in the vertical resolution is due to inadequate resolution in the ABL. The results of these runs are discussed in Section 6.3.1. The interactive surface air formulation integrates an equation for the surface air temperature along with the quasi-geostrophic equations. The pressure level at which the surface air temperature is calculated is equal to $P_0 + \Delta P/4$. Therefore, the surface air temperature is calculated at a pressure which decreases with a decrease in the vertical resolution. In this formulation the surface winds are calculated assuming that the temperature at $P = P_s$ is in thermal wind balance with the winds at $P = P_1$ and $P = P_0$. The equations that are used to calculate the surface winds are

$$U_0 = U_1 - \frac{R\Delta P}{2P_s f_0} \frac{\partial T_s}{\partial y}$$

$$V_0 = V_1 + \frac{R\Delta P}{2P_s f_0} \frac{\partial T_s}{\partial x}$$

Where U_1 and V_1 are the geostrophic velocities at $P = P_1$ and x and y are the zonal and meridional coordinates. respectively, in units of meters.

An equation for the surface temperature tendency is integrated assuming that the fluxes of heat out of the sea are convergent into the air just at the surface. The vertical wind is assumed to be equal to zero. The sea temperature is held fixed. The turbulent fluxes from the surface air into the first model level are calculated using a flux diffusion approximation. The equation for the surface air temperature tendency is

$$\frac{\partial T_s}{\partial t} = -J(\psi_s, T_s) + \dot{Q}_1 + \dot{Q}_2$$

Where $J(\psi_s, T_s)$ is calculated using the streamfunction $\psi_s = (\psi_0 + \psi_1)/2$, $\dot{Q}_1$ is the thermal diffusion, $\dot{Q}_2$ is the radiative cooling, and $H = 8.5$ km.

Using irregularly spaced pressure levels in the ABL may cause there to be first order errors in the calculation of $\dot{Q}_2$. Kalnay De Rivas (1972) outlined the use of stretched coordinates to eliminate the first order truncation errors that result when centered differences are used to calculate derivatives on irregularly spaced grids. Defining stretched coordinates following Kalnay De Rivas (1972), it is found that using a centered difference formulation to calculate the thermal diffusion results in first order errors of 1% at $P = P_s$ and first order errors of 5%

at $P = P_1$. These errors were determined to be sufficiently small to justify the use of centered difference derivatives in the calculation of the thermal diffusion.

d. Ekman momentum approximation

The parameterization used to represent the vertical diffusion of momentum within the ABL in the control run neglects the dynamics which are needed to resolve an Ekman spiral. In order to get a sense of how including these dynamics modify the model's equilibrated climate and mean fluxes, a few runs were done including both the geostrophic and ageostrophic winds in the turbulent momentum fluxes in the ABL. The results of these runs are discussed in Section 6.3.1 In this formulation the surface air potential temperature is set equal to the potential temperature at the first model level, as was done in the control run.

Bannon and Salem (1995) used a multiple-scale analysis of the baroclinic Ekman layer to show that the momentum equations used in this Section are accurate to O(E). Where E is equal to the ekman number and is equal to $2\nu/(fD^2)$, where D is equal to the vertical scale of the flow. These equations will be referred to as the Ekman momentum approximation.

The formulation used in the control run to parameterize the turbulent flux of momentum within the ABL gives an approximate vertical velocity at $P = P_1$ equal to

$$\omega_1 = -\frac{g}{f_0}(\nu_1\rho_1^2 g \frac{(\zeta_{3/2} - \zeta_{1/2})}{(P_{3/2} - P_{1/2})} + c_d\rho_s|\vec{v}_g|\zeta_g).$$

where ζ is the relative vorticity. Levels 1/2, 1, and 3/2 are located at 968.8 mb, 937.5 mb and 906.3 mb, respectively.

This formulation reduces to the standard parameterization of Ekman pumping at the top of the ABL when the eddy diffusion coefficient is equal to zero, with the top of the boundary layer defined above the lower boundary. The boundary condition used at the lower boundary is $\omega = 0$. When the eddy diffusion coefficient is not equal to zero the height if the boundary later is dependent upon the strength of the vertical diffusion.

This parameterization neglects the contribution of the ageostrophic winds to the turbulent fluxes of momentum within the ABL. This is not justified since the ageostrophic winds are of the order of the geostrophic winds within ABL.

In order to get a sense of the role of the ageostrophic winds in the ABL, the control run has been modified to include the contribution of the ageostrophic winds to the turbulent fluxes of momentum within the ABL and at the surface. The ageostrophic winds are calculated from the surface shear stress,

$$\nu_M\rho^2 g\frac{\partial(\vec{v}_g + \vec{v}_a)}{\partial p} = -c_d\rho_s|\vec{v}_g|(\vec{v}_g + \vec{v}_a)$$

, and by assuming that the first-order balance in the momentum equation is between the coriolis force and the vertical diffusion of momentum. The surface

ageostrophic winds are calculated differently from the surface geostrophic winds because the ageostrophic winds vary on a much shorter vertical scale and the extrapolation from the two lowest model levels did not seem to be justified.

2.4.2   Diabatic heating

Diabatic heating is parameterized in this model by a relaxation back to a radiative convective equilibrium state with a constant diabatic heating timescale. The diabatic heating timescale in the standard model is set equal to 10 days. A constant diabatic heating timescale assumes that the time it takes for a thermal perturbations to dissipate is independent of where it is located. This simplistic assumption does not allow for different timescales in the boundary layer and in the free troposphere.

The radiative convective equilibrium state is represented by a horizontally averaged mean lapse rate, $\frac{dT_e}{dz}$, plus horizontal temperature gradients. $\frac{dT_e}{dy}$. The lapse rate in radiative convective equilibrium is chosen to be a constant -7.0 deg/km. The radiative equilibrium lapse rate would be much larger, closer to -15 deg/km in the troposphere. Since all moist processes have been neglected in this model, the modification of the radiative equilibrium profile by moist convection is taken into account implicitly by assuming that moisture brings the lapse rate close to a moist adiabat.

The horizontal temperature gradients in radiative convective equilibrium are estimated from Manabe and Moller (1961). The latitudinal temperature distribution is chosen to be

$$\theta(y,p) = -21.5 sin(\pi(y - L/2)/(L/2))$$

, for $L/4 \leq y \leq 3L/4$. Where L is the total channel width, which is set equal to 10,000 km in the control run. This gives $\frac{d\theta_e}{dy} = 30$ degrees over the center 2500 km of the channel. A region with zero temperature gradients is extended 2500 km to the north and south of the sine function to insure that the channel walls do not modify the dynamics.

An isothermal stratosphere above 200 mb is included in the control run. Model runs which test the sensitivity of the model's climate to the inclusion of a stratosphere are discussed in Chapter 4.

This crude representation of diabatic heating is consistent with the radiative convective states in cumulus models (Lindzen *et al.* 1982) but cannot represent the boundary layer processes that are responsible for the mixing of potential temperature near the ground. These processes are parameterized by including a linearized parameterization of the vertical diffusion of heat.

The lower boundary is assumed to be a sea surface with fixed temperature, θ_{sea}. A linearized bulk aerodynamic drag formula is used to calculate the surface

heat flux,

$$F_{SH} = -c_d c_p \rho_s |\vec{v}_g|(\theta_{air} - \theta_{sea}),$$

where ρ_s is the surface density. The surface air temperature θ_{air} is assumed to be equal to the potential temperature at the first level, which in the standard 17 level model is 31 mb over the surface. The drag coefficient, $c_d|\vec{v}_g|$, is chosen to be equal to 6×10^{-2}, although in general, the drag coefficient is a function of the stability. This is a large estimate of drag over an ocean surface, it is closer to estimates of drag over land, but it was chosen because the resultant mean state and fluxes closely approximated observations.

Above the surface, the turbulent heat fluxes in the boundary layer are assumed to be diffusive in nature and are parameterized as:

$$F_{SH} = \nu_T(P)\rho^2 g c_p \frac{\partial \theta}{\partial p}$$

$$\nu_T(P) = 10(\frac{P}{P_0})^3 \ m^2/s$$

, where P_0 is the pressure at the lower boundary. The vertical diffusion of heat by the turbulent eddies is then calculated from the fluxes as

$$\frac{\partial \theta}{\partial t} = \frac{g}{c_p}\frac{\partial F_{SH}}{\partial p}$$

A dry convective adjustment is applied to the horizontally averaged potential temperature if the temperature profile is calculated to be statically unstable. This adjustment is only necessary within the boundary layer where the mixing by the turbulent fluxes can cause the flow to become statically unstable.

Without the inclusion of these processes in the boundary layer the static stability at the lowest level becomes very large in the equilibrated state because the eddies transport heat vertically, causing the lowest levels to be cold relative to observations. This stabilization by the baroclinic eddies is predicted by the inviscid, adiabatic neutralization theories but it is not consistent with observations. In order to make the model more realistic it is necessary to include the vertical diffusion of heat from the lower levels. Thermal diffusion in the qg thermodynamic equation damps out the temperature waves. Without this term in the qg thermodynamic equation the meridional heat fluxes peak at the lowest level. When the thermal diffusion is included the meridional heat flux peaks higher up at 800 mb. Since the standard run is chosen to approximate observations, it is important to include thermal diffusion since heat fluxes are observed to decrease below 850 mb.

2.4.3   Friction in the ABL

Friction is parameterized by a linearized bulk aerodynamic drag at the surface and diffusion mixing above the surface, in the same way as was outlined in the previous Section.

The linearized bulk aerodynamic drag formula is used to calculate the wind stress at the surface,

$$\vec{\tau}_s = -c_d \rho_s |\vec{v}_g| \vec{v}_g$$

Where $\vec{v}_g$ is surface wind which has been extrapolated from the two levels above the surface. The surface drag times the ambient wind, $c_d|\vec{v}_g|$, in the standard run is again set equal to 6×10^{-2}.

Above the surface, the turbulent shear stress is calculated using a flux-gradient formulation,

$$\vec{\tau}_M = \rho[\vec{v}^* \omega^*]$$

$$= \nu_M(P)\rho^2 g \frac{\partial \vec{v}_g}{\partial P}$$

where

$$\nu_M(P) = 10(\frac{P}{P_0})^3 \; m^2/s$$

The vertical diffusion of momentum by the turbulent eddies is then calculated from the shear stress as $\vec{F} = g\frac{\partial \vec{\tau}_M}{\partial p}$.

2.5   Description of the control run

This Section briefly summarizes the standard control run.

The free parameters used in the standard control run are:

- $\nu_T(P) = 10(\frac{P}{P_0})^3 m^2/s$
- $\nu_m(P) = 10(\frac{P}{P_0})^3 m^2/s$
- $c_d|\vec{v}_g| = 0.06$
- $\frac{d\theta_e}{dy}$ = -30 K / 2500 km
- $\frac{dT_e}{dz}$ = -7 K/km
- $\tau_d = 10$ days

The standard control run has an isothermal stratosphere above 200 mb.

There are 17 equally spaced pressure levels with a resolution of 62.5 mb. The channel width is 10,000 km with a resolution of 312.5 km. The channel length is 5,260 km with a resolution of 328.8 km.

Chapter 3

Analysis of the control run

3.1 PV gradients in the RCE state of the control run

Figures 3-1 displays the pv gradients, divided by β, for the initial state of the control run. This is the RCE state that the model is being forced towards. The large negative pv gradients at the lowest model level are due to the surface temperature gradients. The large positive pv gradients at the tropopause are due to the jump in the static stability in the lower stratosphere. The negative pv gradients at the sides of the jet are due to the curvature of the jet.

3.2 Time evolution to the equilibrated state

This Section looks at the evolution of the model's climate from the RCE state to the equilibrated state.

Figure 3-2 shows the time evolution of the zonal mean pv gradients at the center of the channel for the first 200 days of the control run integration. The symmetric state spins up after the first 20 days. After day 120, the eddies fluxes are large enough to perceptibly modify the mean pv gradients. The modification of the mean flow starts in the ABL with an increase in the magnitude of the pv gradients at the surface and a decrease at the top of the ABL, approximately 700 mb. This adjustment is due to the vertical eddy heat transports which cool the surface and heat the upper region of the ABL. The efficient mixing of potential temperature by fluxes at the air-sea interface compensate for this cooling at the lower boundary and actually reduce the static stability. This decrease in the static stability increases the slope of the isentropes and the pv gradients near the lower boundary. In the upper region of the ABL the vertical eddy fluxes of heat reduce

control run

d(PV)/d(beta*y)
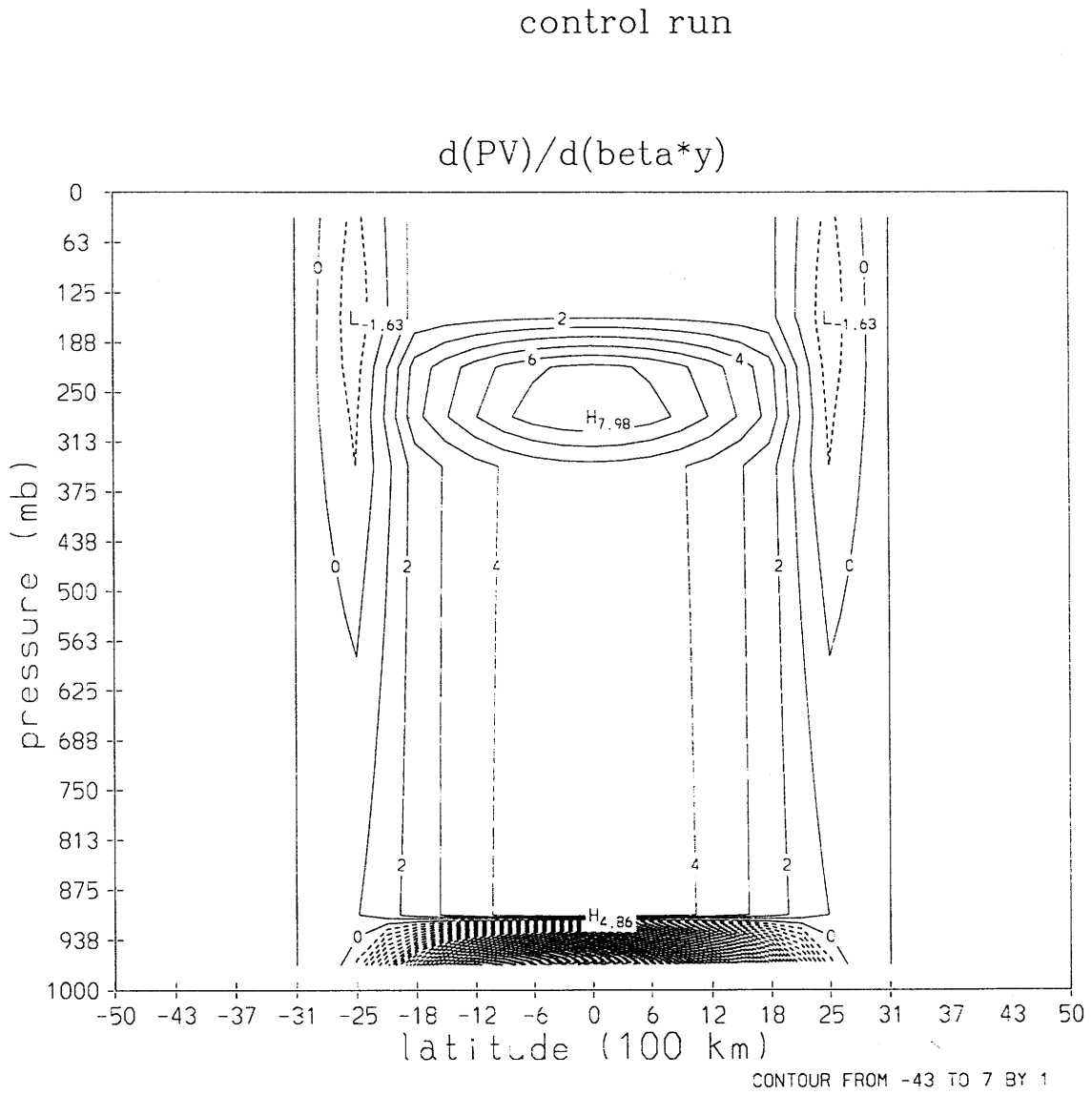
Figure 3-1: PV gradients, divided by β, of the RCE state of the control run, in units of β

the slope of the isentropes and decrease the pv gradients. PV gradients at the tropopause begin to change 20 days after the initial adjustment in the ABL. The homogenization of pv above the ABL is maximized after day 160.

Figure 3-3 shows the evolution of the amplitude of the perturbation pv over the same 200 day period as Figure 3-2. The perturbation pv grows linearly, increasing by an order of magnitude every 15 days, until day 120. The amplitude of the perturbation pv becomes equilibrated when the homogenization of the zonal mean pv above the ABL is maximized, near day 160. The equilibrated perturbation pv has a primary peak at the surface and a secondary peak at the tropopause. There is a minimum in the mid-troposphere where the pv gradients have been homogenized.

Figure 3-4 shows a latitude pressure cross-section of the zonal mean pv gradients just before the run equilibrates. at day 140. This figure shows the the pv mixing begins at the sides of the jet between 400-500 mb. Figure 3-5 shows the amplitude of the perturbation pv on the same day as Figure 3-4. The perturbation pv peaks away from the surface and has only one maximum near 925 mb. The amplitude peaks at the center of the channel and is symmetric about the channel center. Figure 3-6 shows the total pv at 656 mb for the same day as the previous two figures. The 656 mb pressure level was chosen because this is the level where the pv gradients above the ABL are minimized in the equilibrated state. The perturbations are confined within 2000 km on either side of the channel center. The amplitude of the eddies is still increasing and the flow has not yet become equilibrated.

Figures 3-7, 3-8, and 3-9 show the zonal mean pv gradients, the amplitude of the perturbation pv, and the pv at 656 mb when the flow has become equilibrated, respectively. Figure 3-7 shows that the equilibrated state is characterized by a minimum in the pv gradients all along the jet. Above this homogenized region the pv gradients are relatively unchanged from the initial RCE state. Figure 3-8 shows that the amplitude of the equilibrated perturbation pv is symmetric about the channel center and has a minimum in the region where the pv gradients have been eliminated. Figure 3-9 Shows that the equilibrated perturbation pv distorts the pv contours beyond 2500 km on either side of the channel center. Plots of the time evolution of the streamfunction on pressure surfaces between 720 mb and 530 mb (figures not shown) have shown that the streamfunction does not have closed contours in the control run. Therefore, the mixing of pv in CNT is significantly different from the studies of RY which discussed the mixing of pv in subtropical ocean gyres. In this model, efficient pv mixing occurs near the critical level but without closed geostrophic contours.

Figure 3-10 shows the zonal mean pv gradients averaged between day 600 and 1000. The equilibrated pv gradients are very large in the lowest two levels relative to the initial pv gradients. These large gradients are a product of the small static stability which increases the slope of the insentropes. The pv gradients are negative at the first level and positive above. Therefore, the equilibrated state of the model is very unstable by inviscid, adiabatic theories of baroclinic

adjustment. Section 3.3 looks at the linear stability characteristic of the control run. Section 3.4 shows that the mixing in CNT is essentially quasi-linear, although the nonlinearities play a significant role in modifying the phase speed of the eddies. Section 3.5 will show that the dynamical balance in the ABL is quasi-linear and that the large downgradient transport of pv in the ABL is balanced by the vertical diffusion of heat. Section 3.6 looks at the vertical structure of the eddies that are responsible for the maintenance of the equilibrated state.

3.3   Linear three-dimensional time dependent stability analysis

In order to get a sense of whether or not the nonlinear wave-wave interactions play a significant role in the maintenance of the equilibrated state, a linear stability analysis was done. A one-dimensional stability analysis can provide an estimate of the stability of the three-dimensional basic state, but this stability is dependent upon an accurate estimate of the meridional wavelength of the eddies (Ioannou and Lindzen 1986, Lin and Pierrehumbert 1988). This estimate determines whether or not the eddies are linearly stable. In order to get a more accurate estimate of the linear stability of perturbations to the symmetric equilibrium and equilibrated mean states of the nonlinear time dependent model, the nonlinear model was linearized about these basic states. In order to understand the evolution of the wave-mean flow interaction to the equilibrated state, a study of the evolution of the growth rate of waves 1 and 2 from the symmetric state to the equilibrated state was done. All of the forcings used in the nonlinear run are also used in the linearized run. The symmetric state is the state without eddies. where the forcings are allowed to come into equilibrium. The mean states used in these studies were instantaneous in time but zonally averaged. Therefore, the mean state of the three dimensional model is approximated by a two dimensional basic state. The stability of a perturbation on this basic state will be different from the stability of a perturbation on a wavy basic state.

The perturbations on these basic states are assumed to be of the form

$$\psi = \psi_0 \exp[ik(x - ct)],$$

where ψ_0 is the amplitude function, k is the zonal wave number, and c is the phase speed which can be written in terms of its real and imaginary parts: $c = c_r + ic_i$.

The growth rate and real phase speeds of these perturbations are calculated following Gall (1976). The growth rate is calculated from the kinetic energy

$$kc_i = \frac{1}{2K_e}\frac{dK_e}{dt}$$

where K_e is the total eddy kinetic energy of the wave. The real part of the phase speed is calculated as

$$c_r = [k(\psi_s^2 + \psi_c^2)]^{-1}(\psi_c\frac{\partial \psi_s}{\partial t} - \psi_s\frac{\partial \psi_c}{\partial t})$$

where ψ_s and ψ_c are the Fourier coefficients of the perturbation streamfunction,ψ.

The 3D analysis was done using the two-dimensional zonal mean symmetric equilibrium and equilibrated states of the control run. (Figures 3-20).

Figure 3-11 shows the time evolution of the wave 1 streamfunction at the center of the channel using the 2D symmetric state of CNT, this state will be referred to as 2D-CNT-SYM. The growth rate of wave 1 is equal to 0.12/day and the real phase speed is equal to 11.1 m/s. This is consistent with the results of the previous section that showed that the region of pv mixing occurred in areas where the zonal mean wind was approximately 12 m/s. Figure 3-12 shows the vertical and meridional structure of the wave 1 streamfunction. A meridional wavelength can be estimated from this distribution by calculating the distance to the half maximum. Assuming that this is equivalent to 60 degrees of the wavelength, the meridional wavelength would be 6 times this distance. The meridional structure of the wave is seen to be approximately defined by the structure of the jet (the jet goes to zero at the edges of the figure). The width of the streamfunction at the tropopause at half maximum is approximately 3.800 km. This yields an estimate of the meridional wavelength of 11,4000 km or 2.2 times the zonal wavelength. This means that the meridional scale of the eddies is approximately defined by the width of the jet, which is 5,000 km.

Figure 3-13 shows the time evolution of the wave 2 streamfunction at the center of the channel on the 2D-CNT-SYM. The growth rate of wave 2 is equal to 0.12/day and the real phase speed is estimated to be 10.4 m/s. Figure 3-14 shows the vertical and meridional structure of the wave 2 streamfunction. The width of the streamfunction at 600 mb at half maximum is approximately 1,900 km, which gives an estimate of a meridional wavelength that is 2.2 times the zonal wavelength. Therefore, the meridional wavelength of wave 2 is half that estimated for the wave 1 streamfunction.

Figure 3-15 shows the evolution of the growth rate of wave 1 from the symmetric state to the equilibrated state. Only days 110 to 210 are displayed. The growth rate is calculated at 10 day intervals up to day 120 and after day 170. The growth rate is calculated at 2.5 day intervals between day 130 and day 160. The stars on the bottom axis of the figure mark the days where the growth rates were calculated. Each growth rate was calculated by linearizing the nonlinear time-dependent model about the zonally averaged mean state at that day. The growth rates are calculated for each of the 16 pressure levels at which the perturbation streamfunction is defined.

For day 110 to 125, the growth rate is relatively constant from the surface to the 200 mb pressure level, where the amplitude of the perturbation streamfunction

has a maximum. The growth rate decreases sharply above 200 mb, where the amplitude of the perturbation streamfunction also decreases sharply (Figure 3-11).

At day 130, which is coincident with a temporary decrease in the pv gradients above the ABL (Figure 3-2), the growth rates temporarily decrease. At day 140 the growth rates are essentially the same as for the symmetric state. Between day 145 and 150 the growth rates change from those characteristic of the symmetric state to those characteristic of the equilibrated state. All growth rates below 200 mb are negative after day 145. The decrease in the growth rate over a short period is very significant because this means that when the basic state deviates from the equilibrated state, the eddies will be very efficient at adjusting the basic state back to the equilibrated state.

Figure 3-15 shows that wave 1 is linearly damped in the equilibrated state with a damping rate of -0.1/day. This result is most likely due to the use of a zonally averaged basic state in the linear stability analysis. Removing the waves from the basic state, removes the eddy available potential energy. If a wavy basic state had been used in the stability analysis, there would have an additional source of energy to be converted into eddy kinetic energy. This additional source of energy may cause the waves to be neutral to the basic state instead of damped. This is consistent with the balance of terms in perturbation pe equation for the control run (Figure 3-26). This figure shows that the nonlinear wave-wave interaction term in the equation (*'s) is a positive tendency in the mid troposphere.

Figure 3-16 shows the evolution of the growth rate of wave 2 from the symmetric state to the equilibrated state. The stars on the bottom axis of the figure mark the days where the growth rates were calculated. Wave 2 does not have as sharp a transition between growth and decay as wave 1 Figure 3-15). The growth of wave 2 begins to slow after day 120 and becomes neutral at day 140. After day 140 wave 2 is damped. Wave 2 becomes neutral 5 days before wave 1. Therefore, wave 2 may play a role in the equilibration of the mean flow through wave-wave interaction but not through wave-mean flow interaction because wave 2 begins to decay before the basic state has become equilibrated.

CNT zonal mean pv gradients
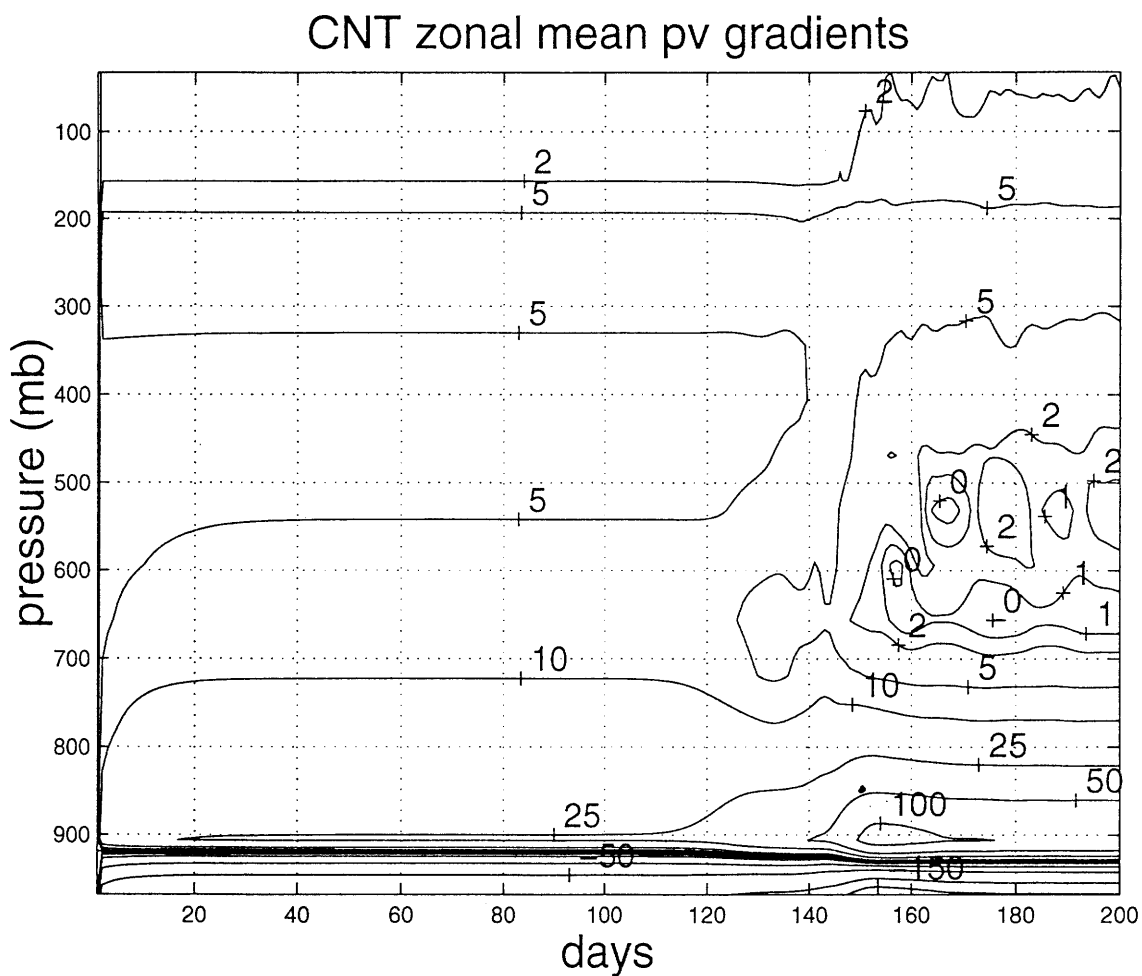
Figure 3-2: Time evolution of the zonal mean pv gradients at the center of the channel from the RCE state to the equilibrated state from the control run, in units of β.
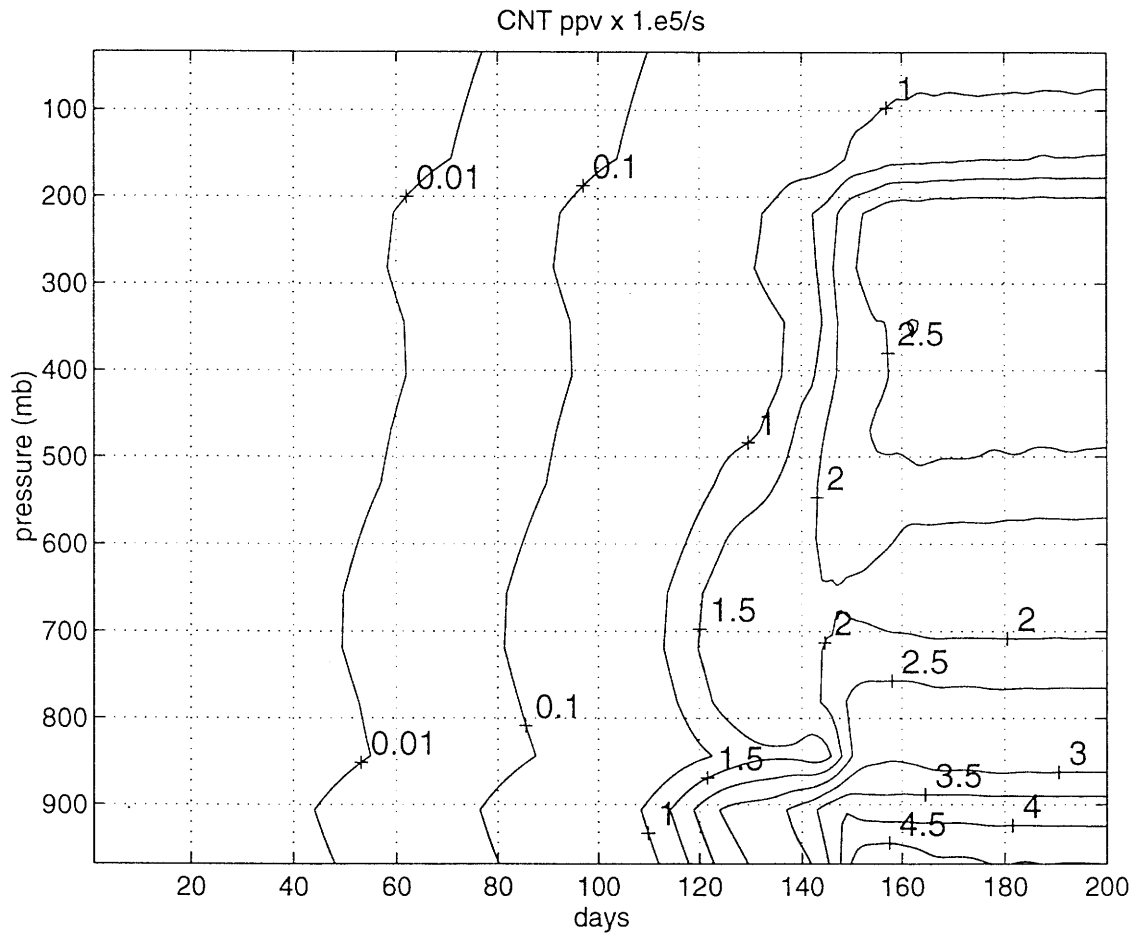
Figure 3-3: Time evolution of the amplitude of the perturbation pv at the center of the channel from the RCE state to the equilibrated state from the control run, in units of $10^{-5}/s$.

CNT zonal mean pv gradients at day 140
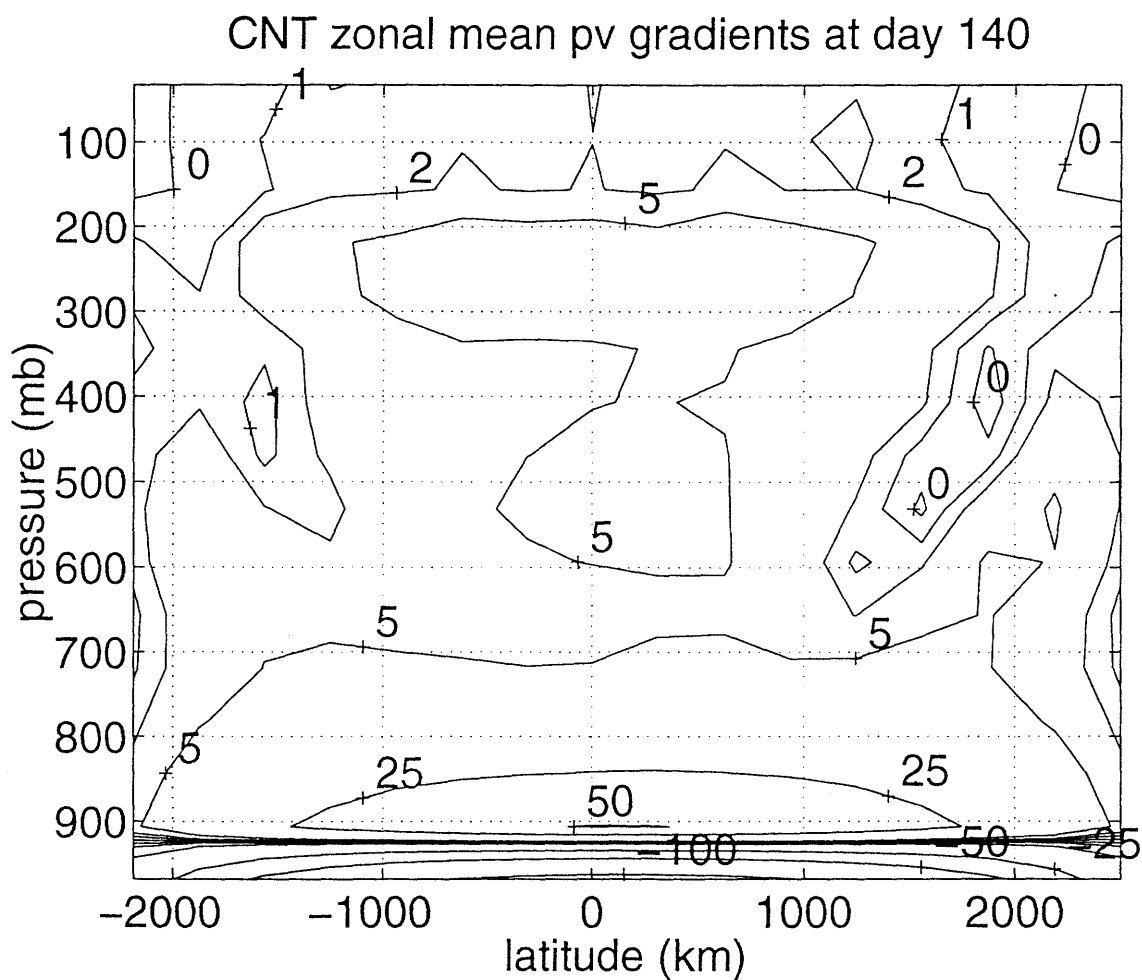
Figure 3-4: Latitude pressure cross-section of the zonal mean
pv gradients at day 140 from the control run, in units of β.

CNT amp. of the ppv at day 140
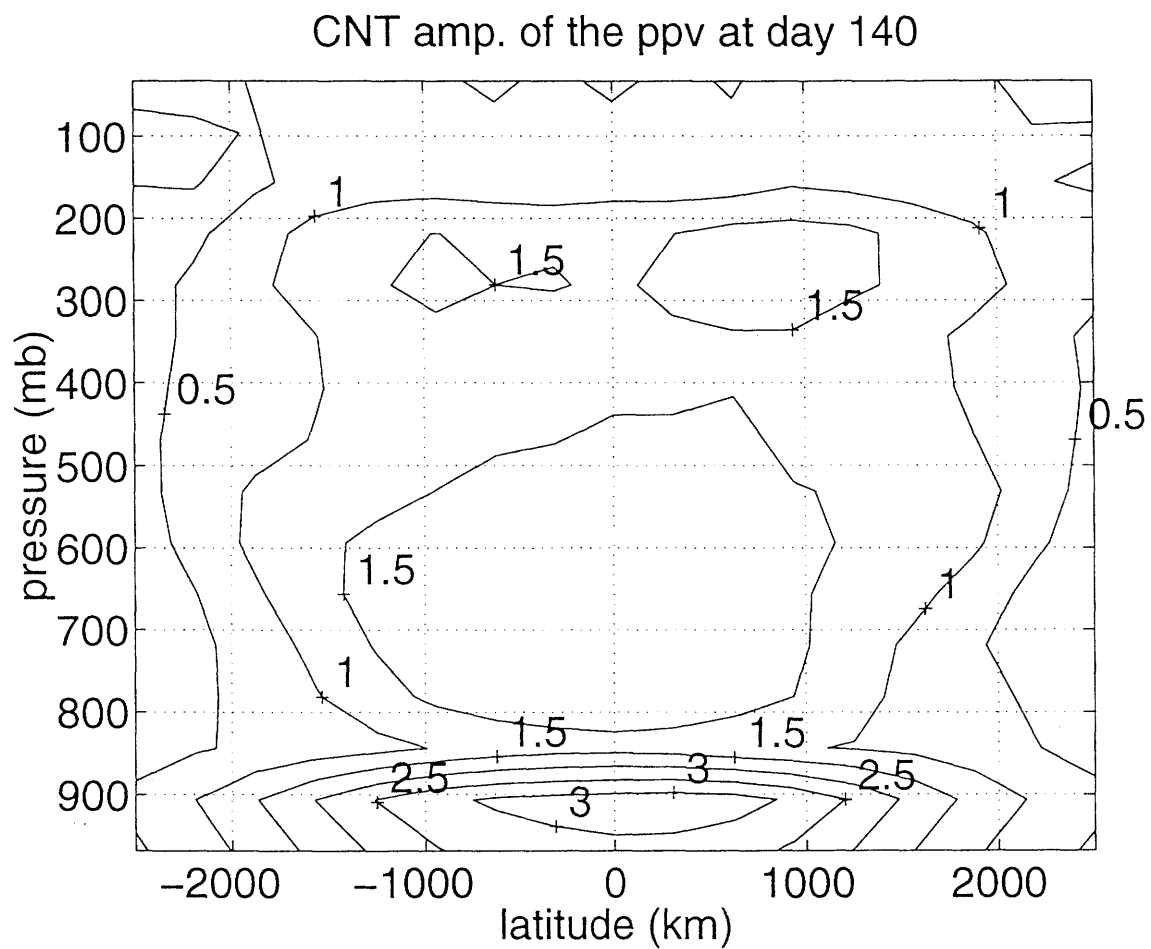
Figure 3-5: Latitude pressure cross-section of the zonal mean amplitude of the perturbation pv at day 140 from the control run, in units of $10^{-5}/s$.
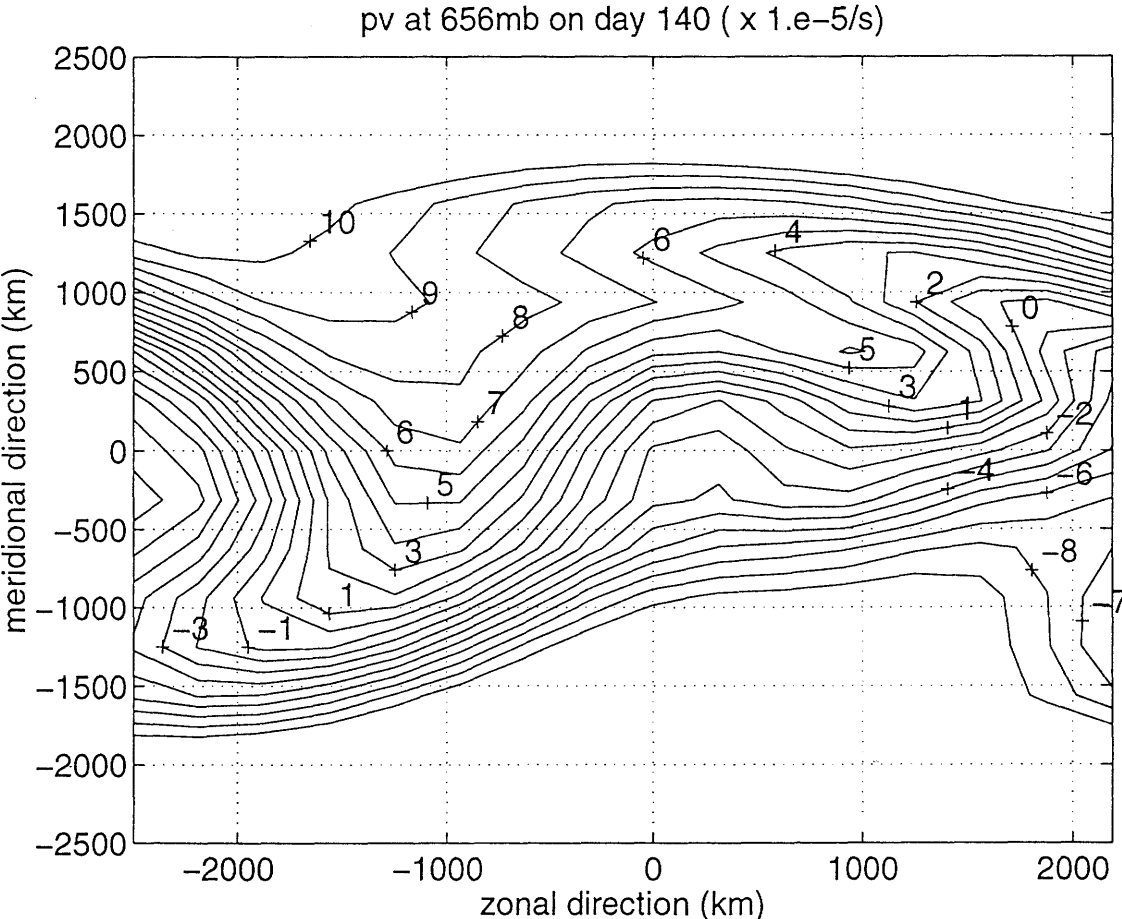
Figure 3-6: PV on the 656 mb pressure surface at day 140 from the control run, in units of $10^{-5}/s$.

CNT zonal mean pv gradients at day 160
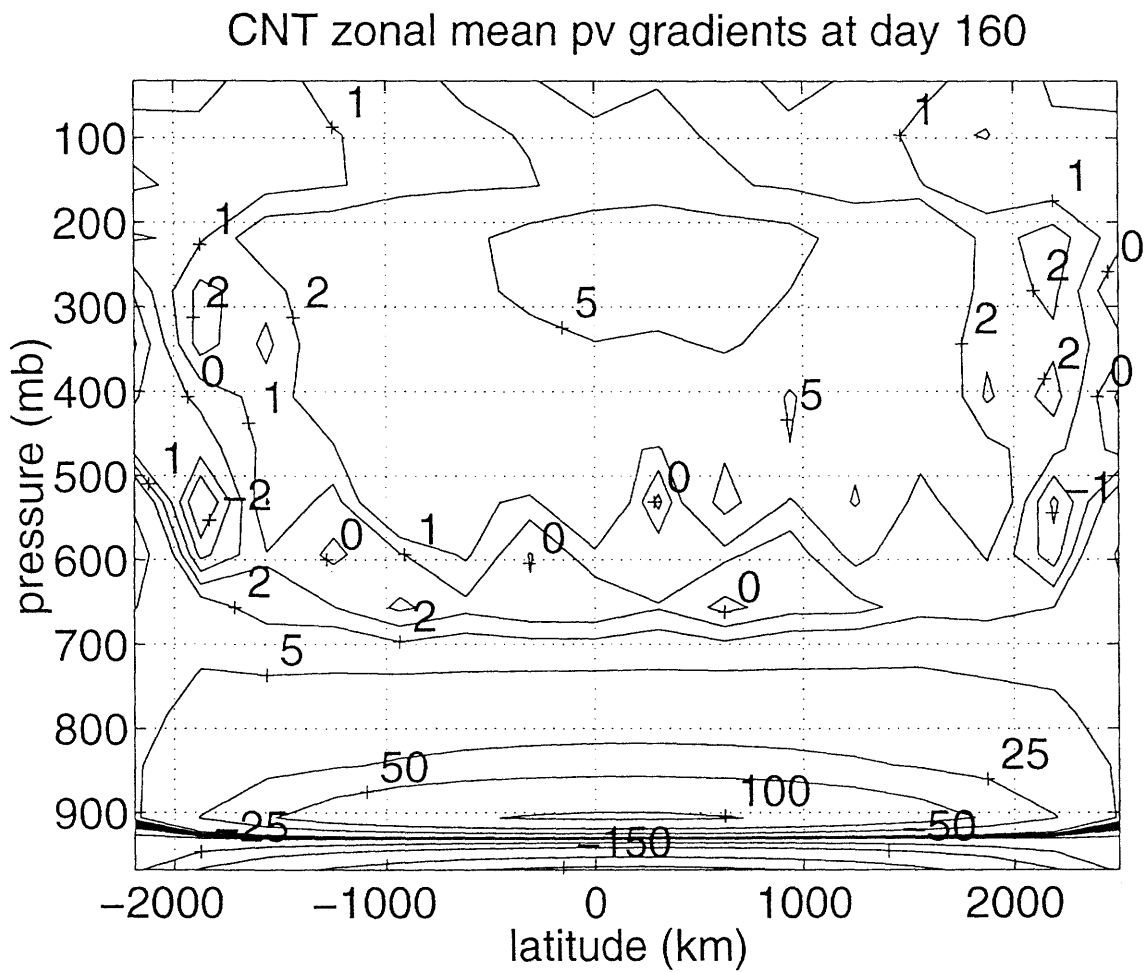
Figure 3-7: Latitude pressure cross-section of the zonal mean
pv gradients at day 160 from the control run, in units of β.

CNT amp. of the ppv at day 160
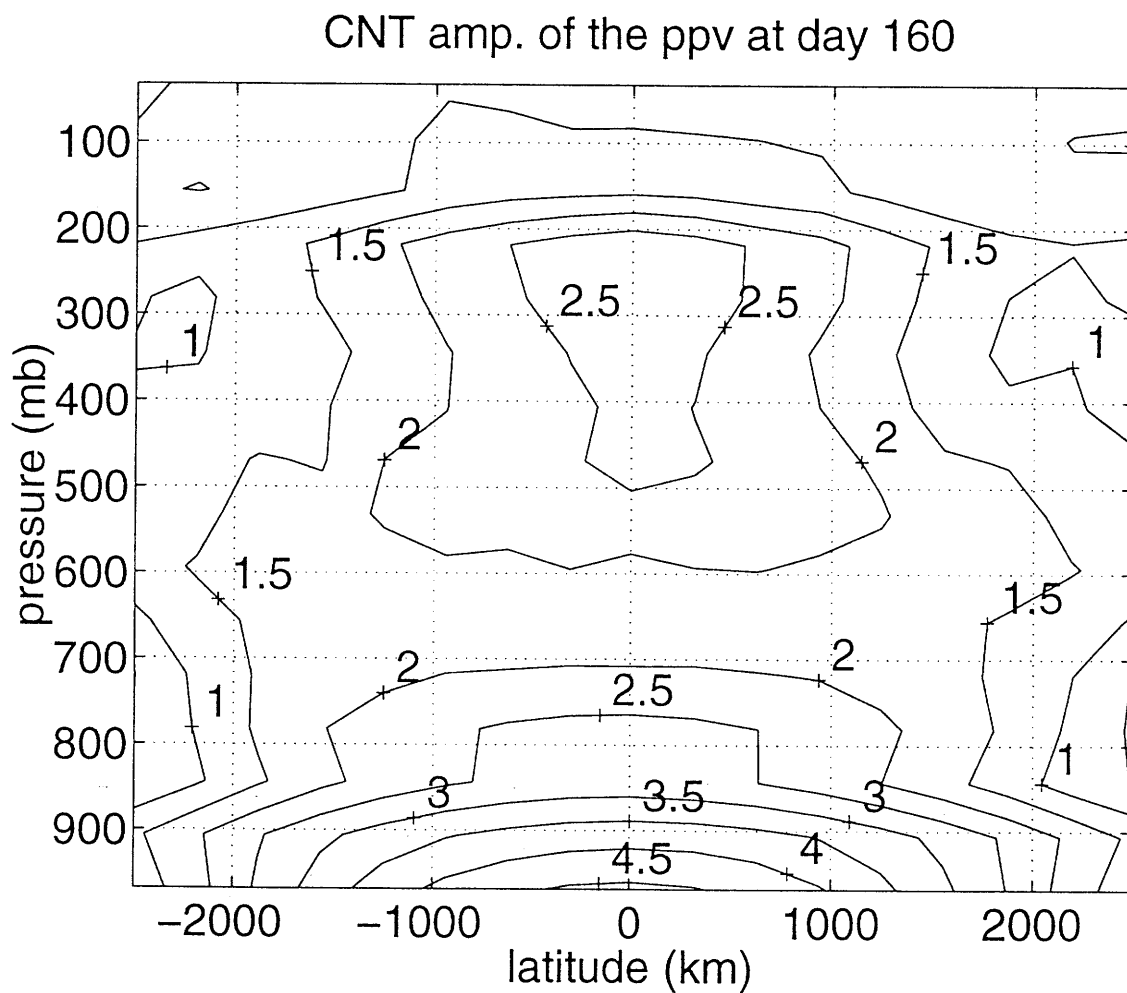
Figure 3-8: Latitude pressure cross-section of the zonal mean amplitude of the perturbation pv at day 160 from the control run, in units of $10^{-5}/s$.

pv at 656mb on day 160 (x 1.e–5/s)
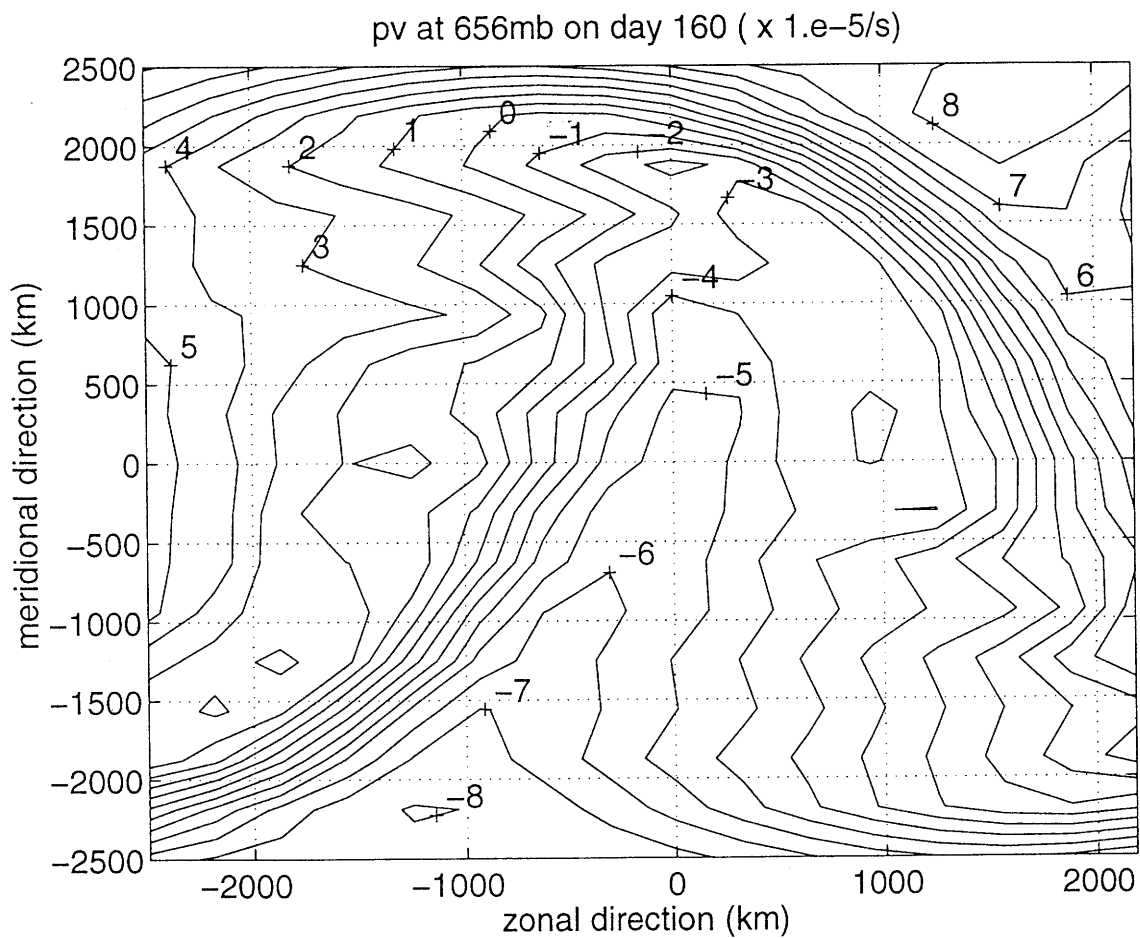
Figure 3-9: PV on the 656 mb pressure surface at day 160 from the control run, in units of $10^{-5}/s$.

control run

d(PV)/d(beta*y)

CONTOUR FROM -152 TO 97 BY 1
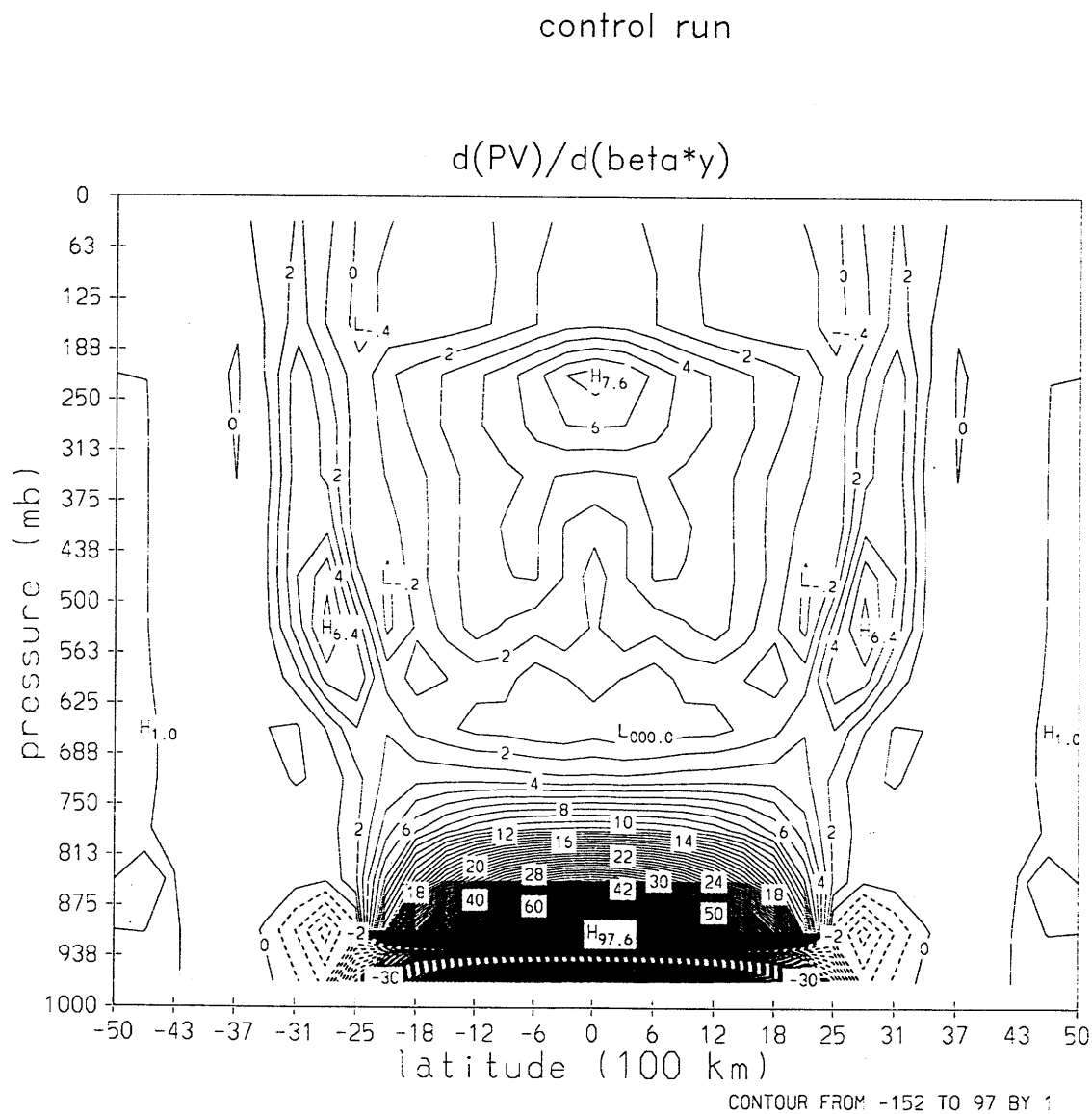
Figure 3-10: PV gradients of the equilibrated state of the control run averaged between day 600-1000, in units of β.

Amp of Z1 on 2D CNT SYM (meters)
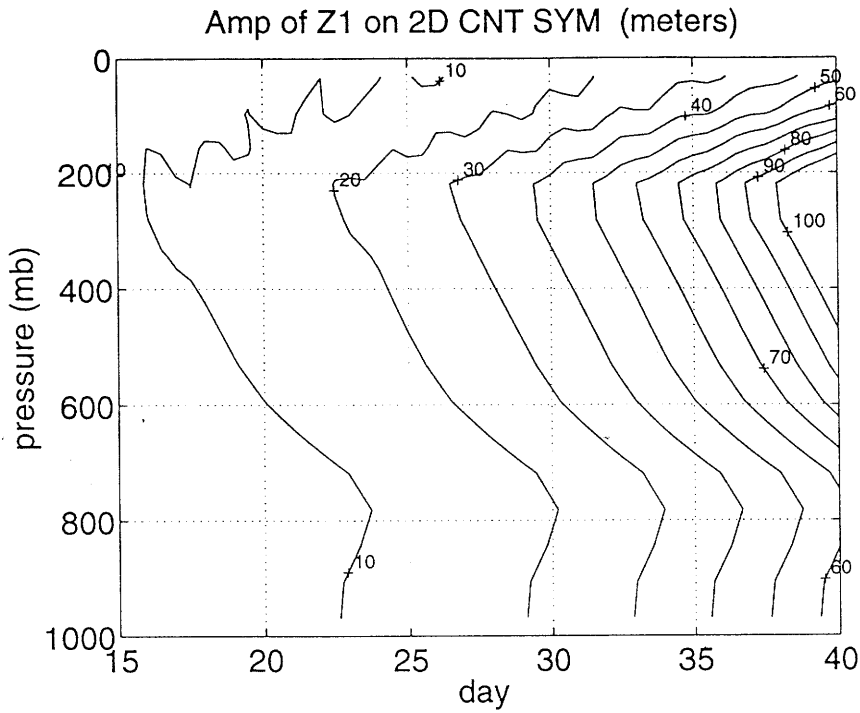
Figure 3-11: Time evolution of the amplitude of wave 1 at the center of the channel on 2D-CNT-SYM.

Amp of Z1 on 2D CNT SYM (meters)
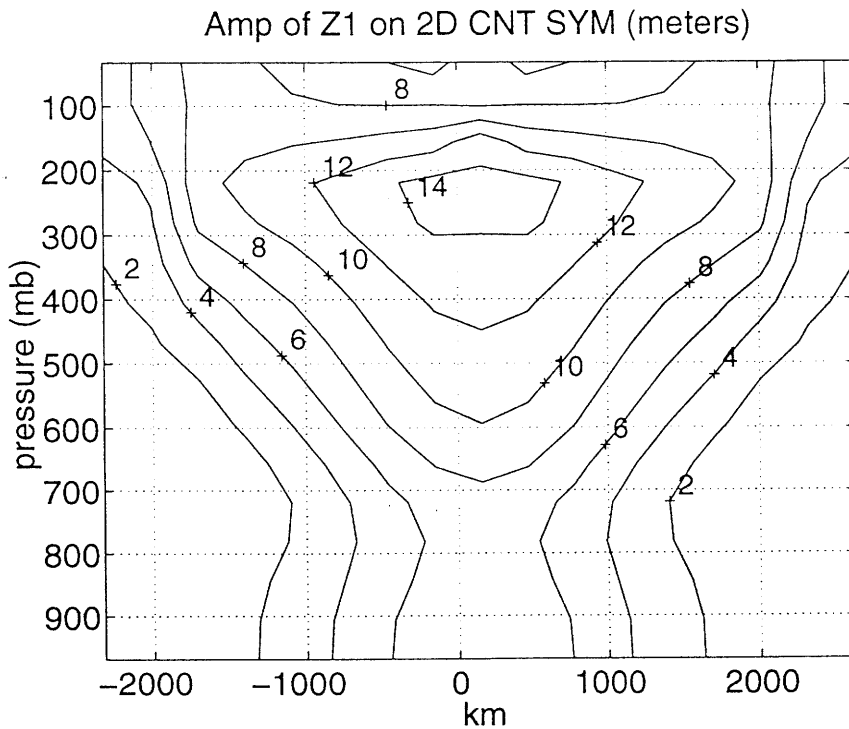
Figure 3-12: Latitudinal pressure distribution of the amplitude of wave 1 on 2D-CNT-SYM.

Amp of Z2 on 2D CNT SYM (meters)
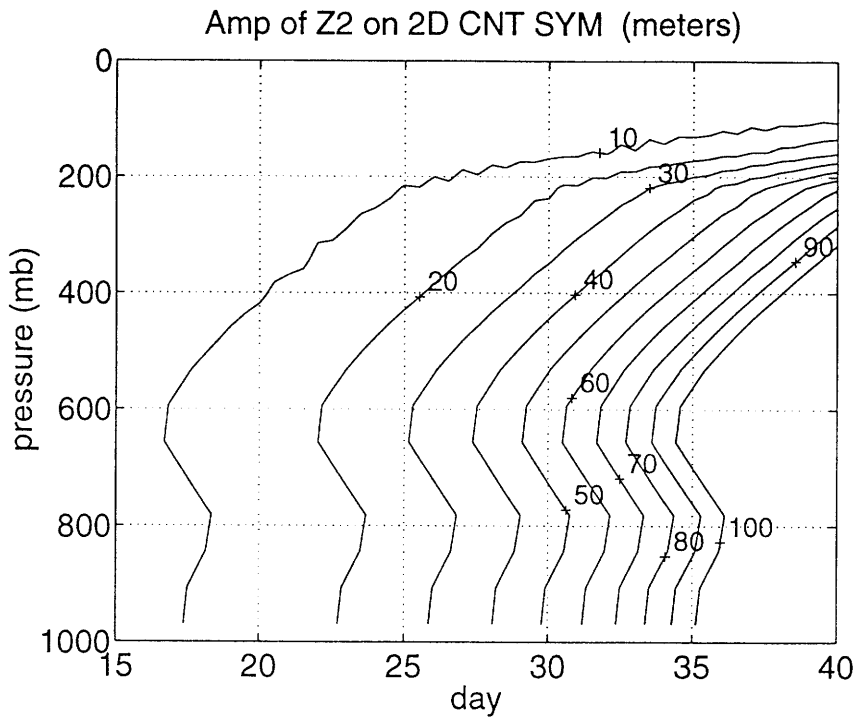
Figure 3-13: Time evolution of the amplitude of wave 2 at the center of the channel on 2D-CNT-SYM.

Amp of Z2 on 2D CNT SYM (meters)
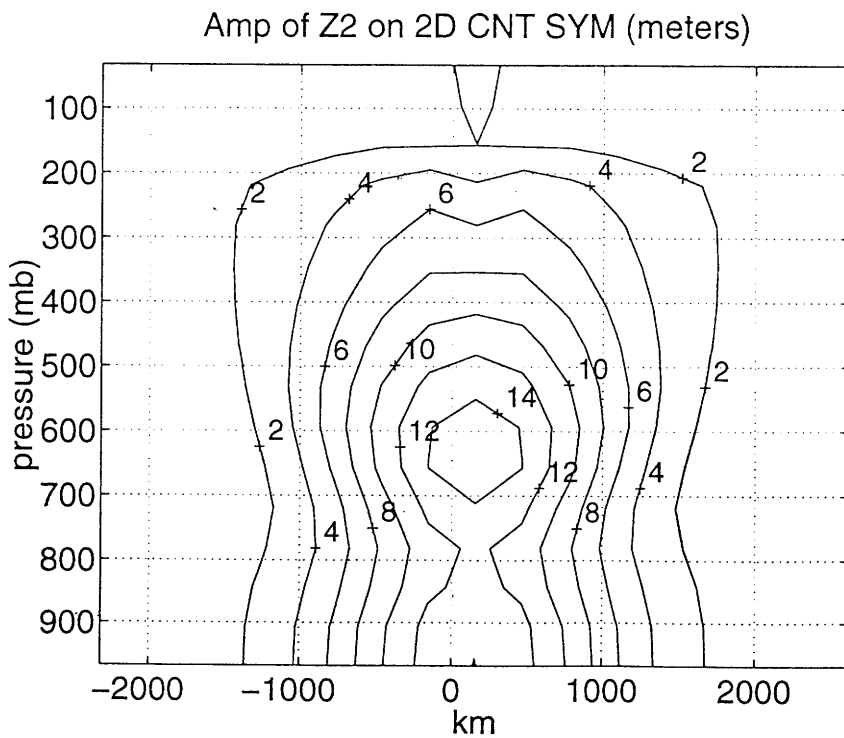
Figure 3-14: Latitudinal pressure distribution of the amplitude of wave 2 on 2D-CNT-SYM.
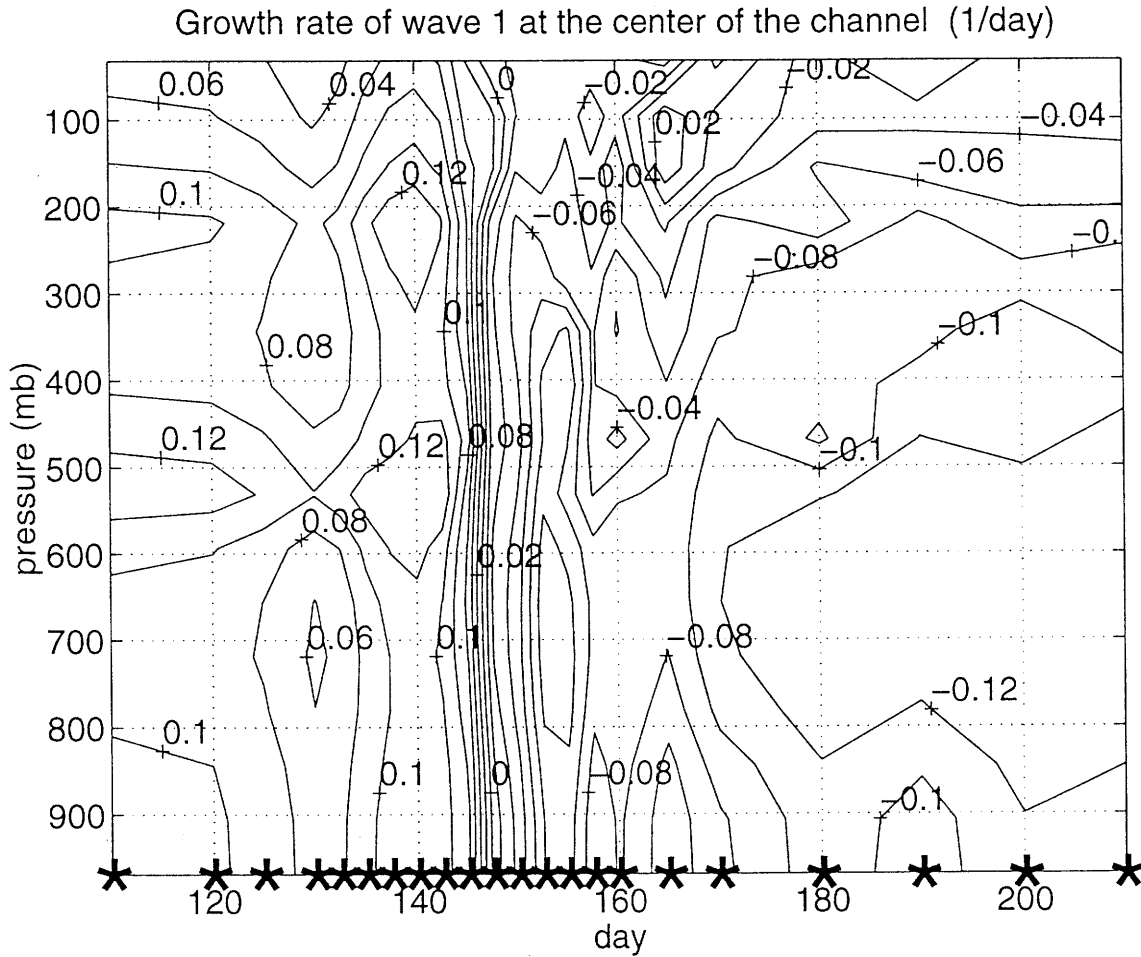
Figure 3-15: Time evolution of the growth rate of wave 1 at the center of the channel from the RCE state to the equilibrated state from the control run, in units of 1/day. The contour interval is 0.02/day. The stars on the bottom axis of the figure show the days at which the growth rates were calculated.
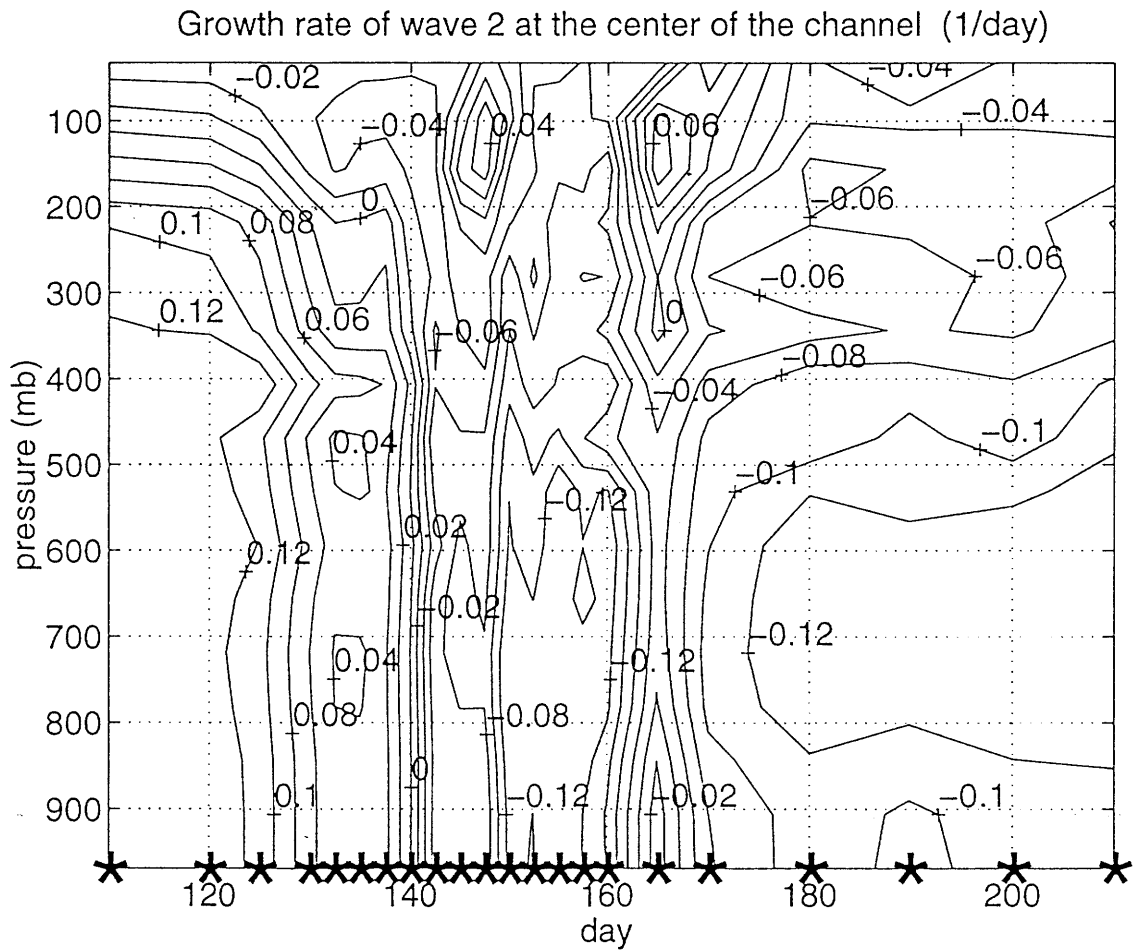
Figure 3-16: Time evolution of the growth rate of wave 2 at
the center of the channel from the RCE state to the equi-
librated state from the control run, in units of 1/day. The
contour interval is 0.02/day. The stars on the bottom axis
of the figure show the days at which the growth rates were
calculated.

3.4 Nonlinear versus quasi-linear equilibrations

In order to understand the role of the nonlinear wave-wave interactions in determining the equilibrated mean state and eddy fluxes, a run with the same parameters as the control run but with the wave-wave interactions suppressed was run. This run will be referred to as WMF. Figure 3-17 shows the equilibrated pv gradients of the WMF run. Comparing this figure to Figure 3-10, equilibrated pv gradients in the control run, it is seen that the pv gradients below 700 mb are very similar but above 700 mb the fields are different. At 656 mb. both CNT and WMF have a minimum in the pv gradients but, while the CNT gradients are almost equal to zero, the WMF gradients are approximately 2β. Above 656 mb, the magnitude of the pv gradients at the center of the channel begin to differ significantly. It is seen that the pv gradients of WMF are less homogenized and are actually larger than the RCE gradients above the ABL.

Another important difference between these two equilibrated pv gradients is the meridional extent of the pv gradients. The pv gradients of WMF are confined to a much smaller meridional region than the CNT gradients. The width of the CNT gradients is relatively unchanged from the RCE gradients.

Figures 3-18 and 3-19 show the static stability and meridional temperature gradients at the center of the channel, respectively, for CNT, WMF and a quasi-linear run where only the fundamental wave is allowed to interact with the mean flow. This run will be referred to as WV1. It is first of all interesting to note that WV1 and WMF are essentially the same. This means that the interaction between the fundamental wave and the mean flow is the dominant quasi-linear process.

In the ABL, below 750 mb. all three runs have essentially the same meridional temperature gradients (Figure 3-19). This means that the shear at the surface is essentially the same for all three runs. Figures 3-20 and 3-21 display the latitude pressure cross-sections of the zonal mean wind for the equilibrated states of WMF and CNT, respectively. The regions where the equilibrated pv gradients are between +/- 0.5β have been shaded in. Since the mixing of pv would be expected to occur near the critical level, the value of the zonal mean wind in the region of mixing is an indication of the phase speed of the waves that are responsible for the mixing. These figures show that the shear in the ABL is the same for WMF and CNT but the magnitude of the zonal mean wind of WMF at the surface is twice that of CNT. The homogenization of the pv in WMF (Figure 3-20) is seen to occur all along the region where the zonal mean wind is approximately 12 m/s, except in the ABL where this region is in an area with strong damping. Since the mixing would be expected to occur in the region near the critical level, the real phase speed of the eddies that are responsible for the mixing would be approximately 12 m/s. A comparison of the shaded regions in Figure 3-21 with the values of the zonal mean wind shows that the

relationship between the zonal mean wind and the homogenization of pv is not as simple in the fully nonlinear run. In the fully nonlinear run, the control run, the homogenization of pv on the sides of the jet occurs in regions where the zonal mean wind is approximately 7.5 m/s, while at 625 mb the mixing occurs in the region where the zonal mean wind is close to 13 m/s. Therefore, the nonlinearities are responsible for causing the relationship between the phase speed of the wave and the area of mixing to be more complicated than in the quasi-linear run. This may be due to the phase speed of the wave being a function of latitude or more than one wave being responsible for the mixing.

Above the ABL, Figure 3-19 shows that the meridional temperature gradients of the quasi-linear (WMF,WV1) runs begin to show large differences from the nonlinear (CNT) runs. The large reduction in the meridional temperature gradients, that extends from 750 mb to 500 mb, in CNT is absent in WMF. Figures 3-20 and 3-21 show that the magnitude of the zonal mean wind at the jet in the equilibrated state of WMF is essentially unchanged from radiative equilibrium while the magnitude of the wind at the jet in the equilibrated state of CNT is reduced by a factor of 13%. The barotropic shear is larger, and the jet width is more meridionally confined, at the tropopause level in the equilibrated state of WMF, relative to the equilibrated state of CNT. This suggests that the eddies are also more meridionally confined in the equilibrated state of WMF, compared to CNT (Ioannou and Lindzen 1986).

The degree of homogenization above the ABL, above 656 mb, is determined by the increase in the static stability and the decrease in the meridional temperature gradients, both of which are less adjusted in the WMF run. Therefore, the equilibrated state of the run which suppresses the wave-wave interactions is fundamentally different from the run which is fully nonlinear.

The latitudinal distribution of the vertical eddy heat fluxes gives a clue as to why there is such a large difference between the equilibrated states of CNT and WMF. Figures 3-22 and 3-23 show the latitudinal pressure distributions of the zonally averaged vertical eddy heat fluxes for CNT and WMF, respectively. These figures show that the nonlinear wave-wave interactions cause the latitudinal extent of the eddies fluxes to increase and the magnitude of the fluxes at the center of the channel to decrease. An average over the region where the eddy fluxes are smaller than -0.01 K Pa/s is the same for both runs. Therefore, the difference in the static stability is primarily due to the way in which the eddy fluxes in the static stability equation were evaluated since an areal average across the whole domain causes the WMF fluxes to be much smaller than the CNT fluxes.

The nonlinear cascade of enstrophy to smaller scales allows shorter waves to influence the dynamics. The most significant wave being wave 2 which has a zonal wind contribution which is symmetric about the channel center and causes the zonal mean winds to decrease at the center of the channel and increase on either side of the channel center. This results in a horizontally broader zonal mean wind, with smaller surface winds at the center of the channel. The lack of homogenization at the center of the channel in the WMF run may be due to the

steering level being in a region of strong damping. A reduction in the zonal mean surface winds, while holding the temperature in the ABL relatively fixed because of strong thermal damping, causes the steering level to move upwards. In the CNT run, the steering level has been raised above the region of strong damping so that the eddy pv fluxes can eliminate the pv gradients more effectively.

These results demonstrate that the large differences between the CNT run and the WMF run are partly due to the way in which the model evaluates the static stability. It would be of interest to see if calculating the static stability locally, instead of averaged over the horizontal domain, would cause the fully nonlinear and the wave-mean flow runs to be more similar. The large differences in the two runs is also due to the nonlinear cascade which broadens the jet and raises the steering level above the region of strong thermal damping.

In order to isolate the importance of resolving the nonlinear cascade, a run was done holding the static stability fixed at the equilibrated static stability of the control run, referred to from here on as WV1FS. Therefore, the difference between this run and the control run is that all wave-wave interactions and all wave-mean flow interactions, except for those due to wave 1, have been neglected in the quasi-geostrophic tendency equation. Figure 3-24 shows the equilibrated zonal mean pv gradients from this run. It is seen that the homogenization of pv above the boundary layer is resolved without the nonlinear cascade. Figure 3-25 shows a comparison of the pv gradients above the ABL for CNT, WV1, and WV1FS. The dashed line with the +'s designates the initial state of the WV1FS run. Comparing this dashed line to the other two dashed lines it is seen that the adjustment to the pv gradients above the ABL with the fixed static stability already accounts for most of the pv homogenization. Very little adjustment by the meridional heat fluxes is needed to completely eliminate the pv gradients above the ABL. This figure shows that even though the pv gradients of WV1FS are equal to those of CNT below 700 mb, the gradients above 700 mb deviate sharply. WV1FS has essentially no adjustment above 550 mb. Since Figures 3-18 and 3-19 showed that a run with only wave 1 is essentially the same as a wave-mean flow run which allowed all resolved waves, it can be concluded that the adjustment above 550 mb in CNT is due to the nonlinear wave-wave interactions.

3.5   Maintenance of the perturbation pv

This Section looks at the dynamical balances which maintains the perturbation pv in the control run. The balance of terms in the perturbation potential enstrophy (pe) tendency equation clearly show the eddy feedbacks that are maintaining the wave activity. This equation is derived by multiplying the equation for the perturbation pv tendency by the perturbation pv. This equation is:

WMF run

d(PV)/d(beta*y)

CONTOUR FROM -141 TO 83 BY CONTOUR INTERVAL 1 LABELS SCALED BY 1
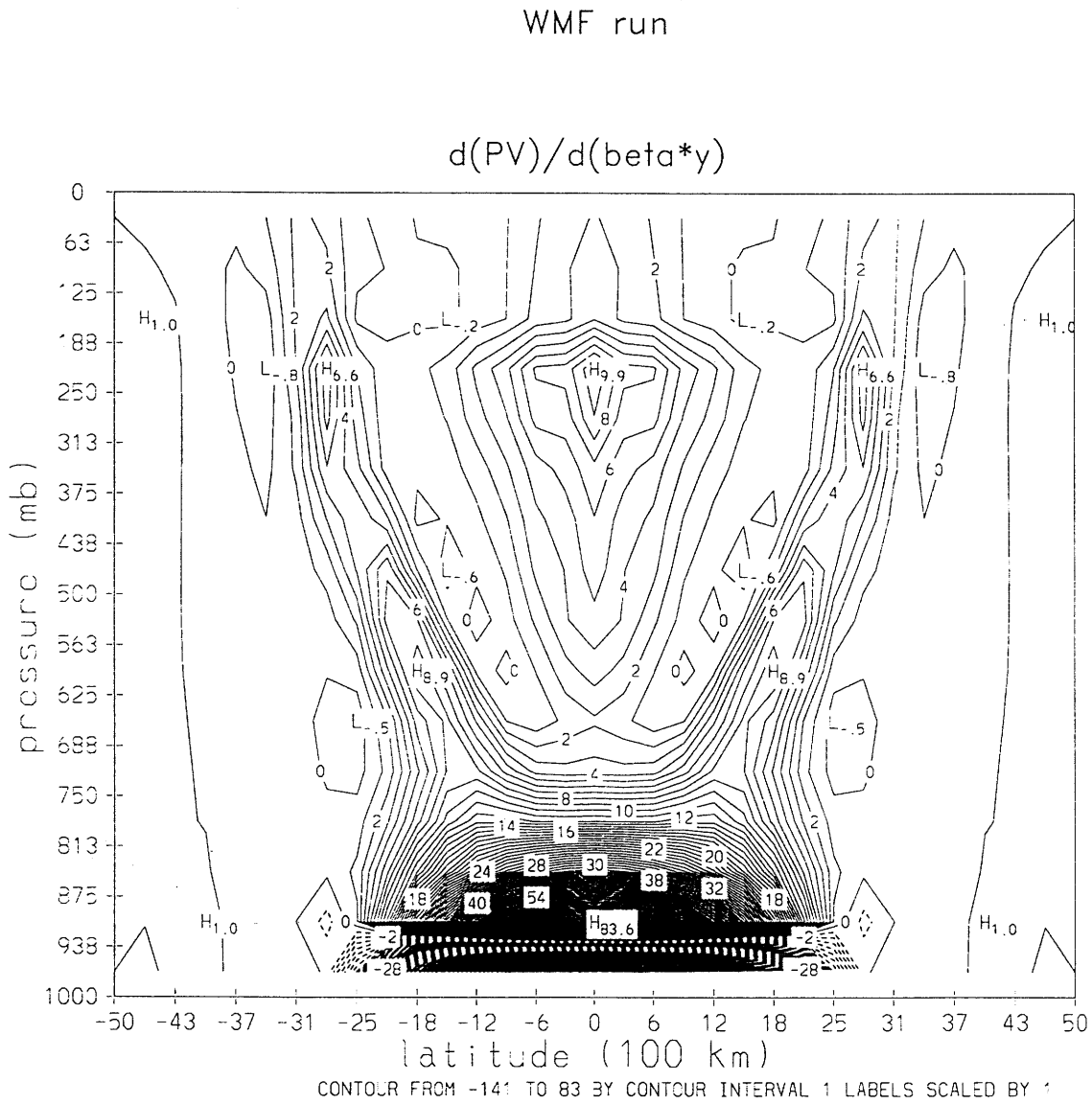
Figure 3-17: Latitude pressure cross-section of the zonally averaged pv gradients in the equilibrated state of WMF, in units of β.
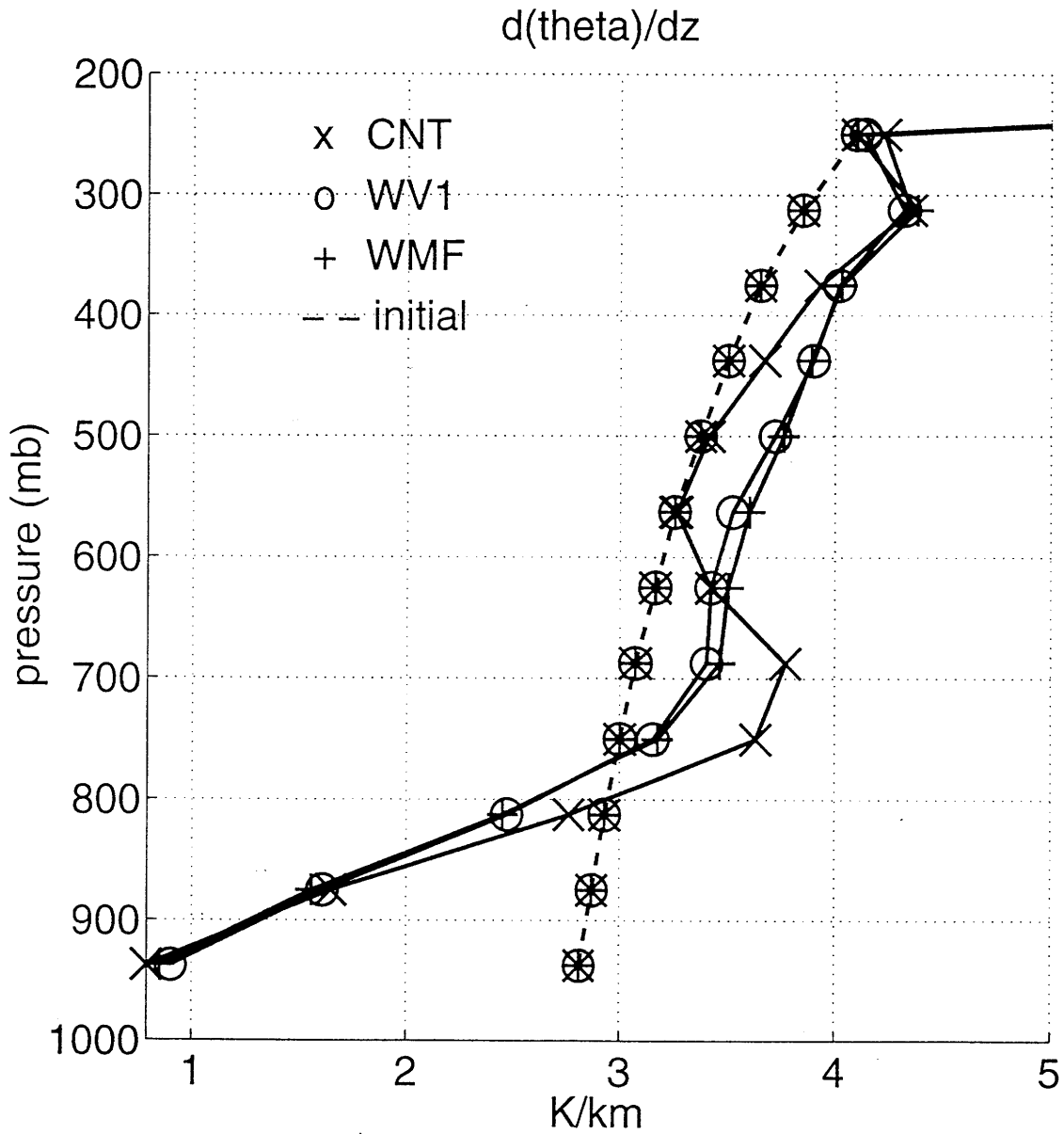
Figure 3-18: Comparison of the static stability at the center of the channel for CNT,WMF and WV1.
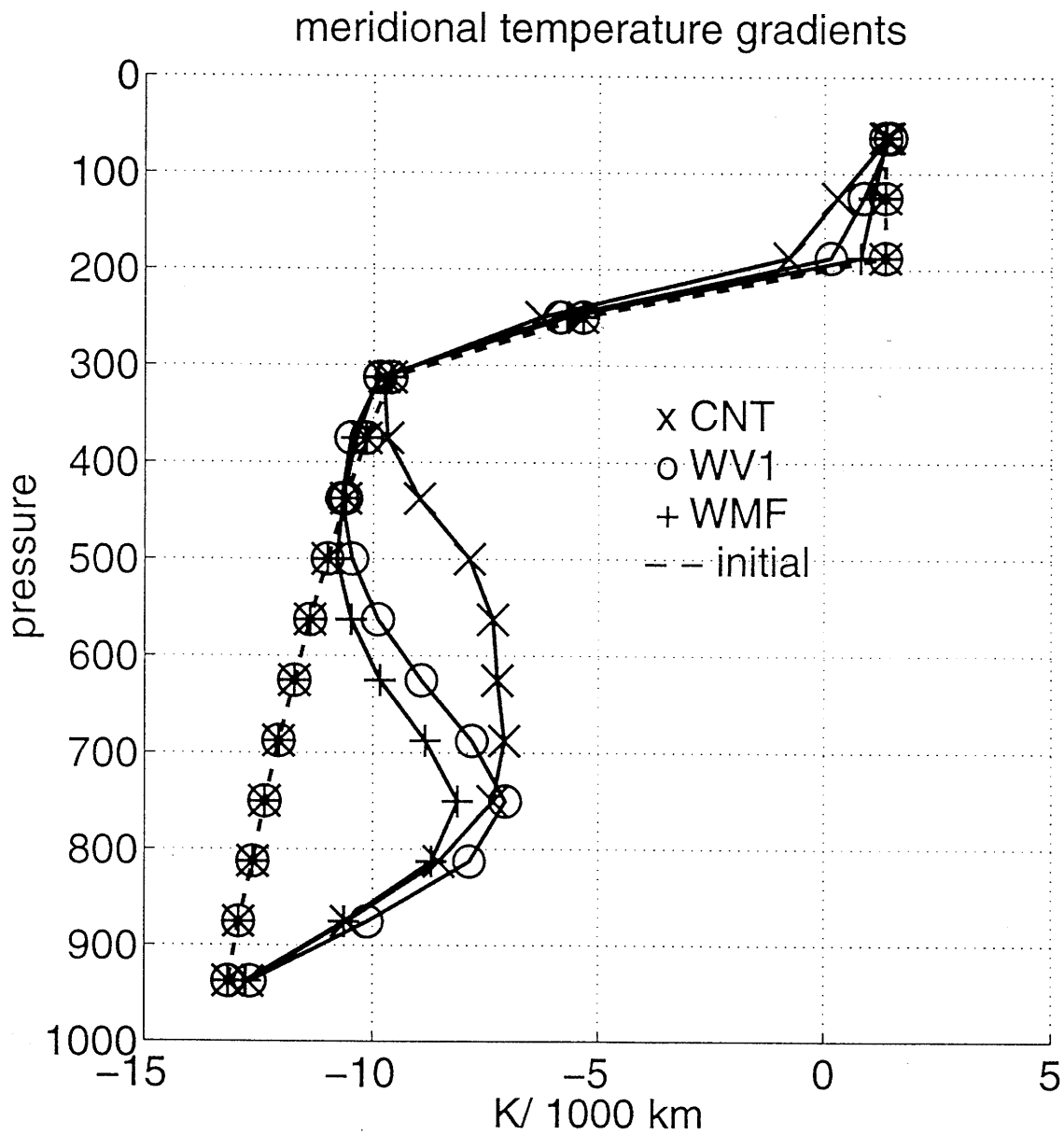
Figure 3-19: Comparison of the meridional temperature gradients at the center of the channel for CNT,WMF and WV1.

wave-mean flow run

Zonal Wind ZM (m/s)

CONTOUR FROM 0 TO 47.5 BY CONTOUR INTERVAL 2.5 LABELS SCALED BY 1
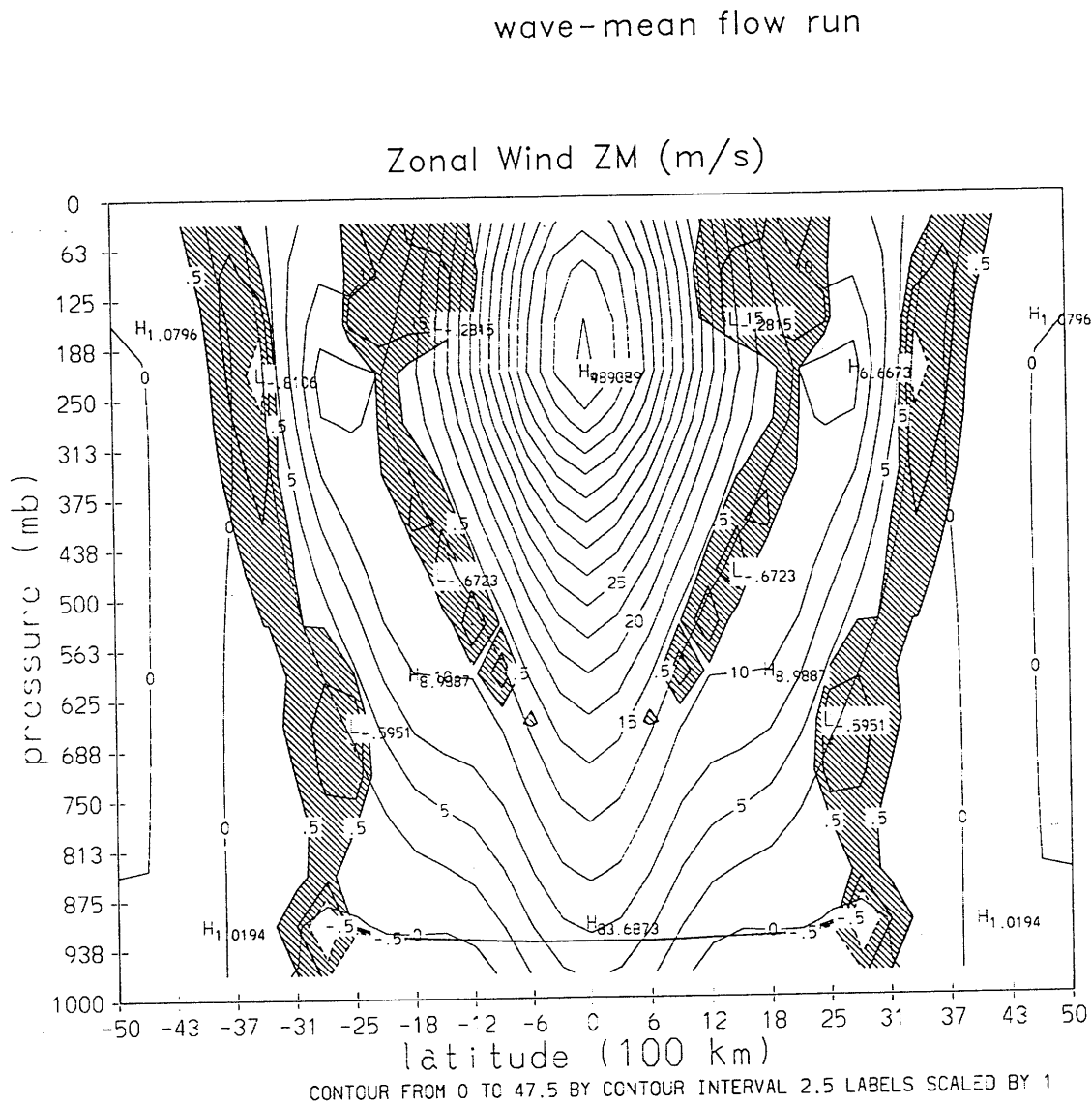
Figure 3-20: Latitude pressure cross-section of the zonal mean wind in the equilibrated state of WMF, with shaded regions for zonal mean pv gradients between +/- 0.5β.

control run

Zonal Wind ZM (m/s)

CONTOUR FROM 0 TO 40 BY CONTOUR INTERVAL 2.5 LABELS SCALED BY 1
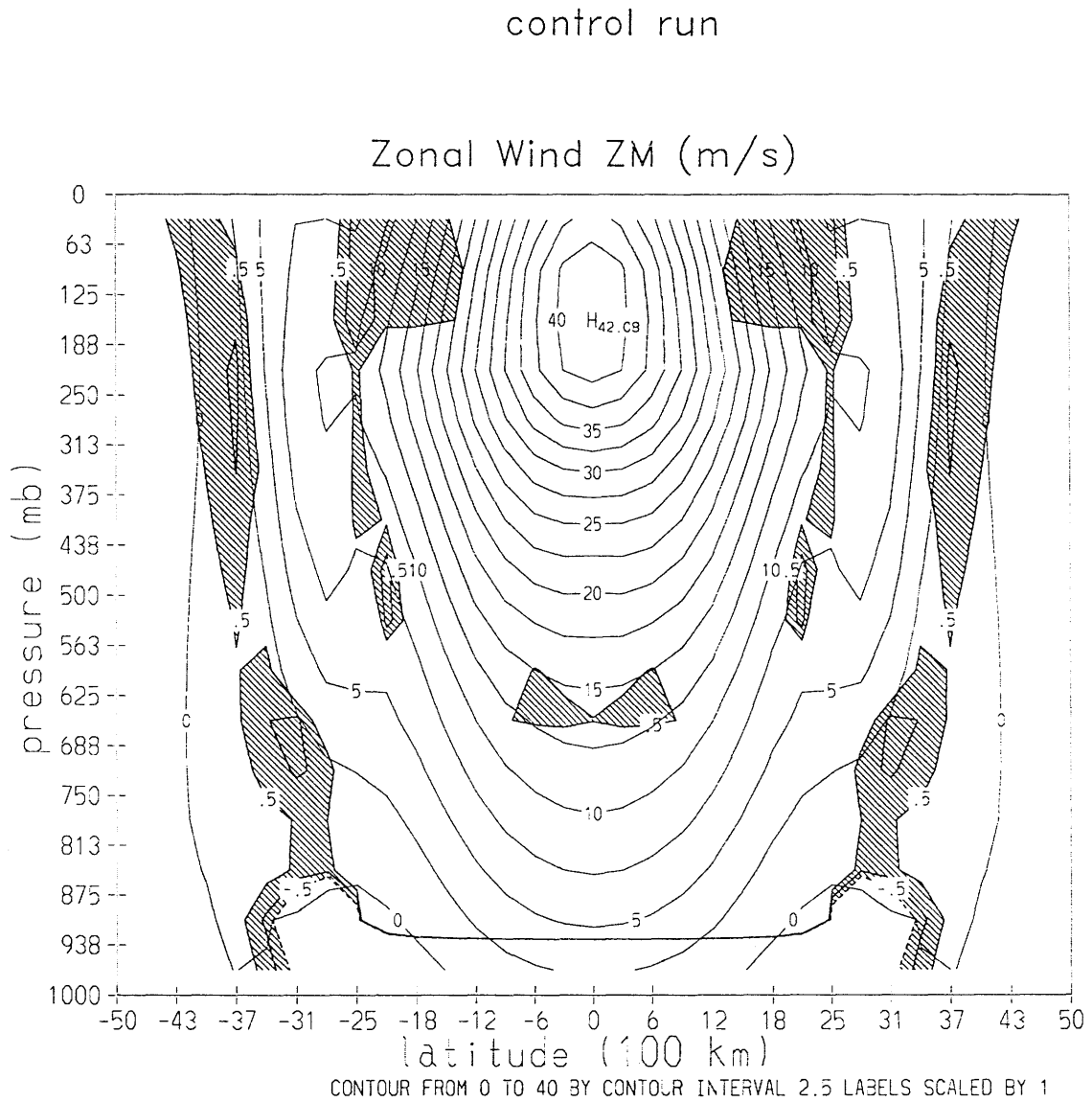
Figure 3-21: Latitude pressure cross-section of the zonal
mean wind in the equilibrated state of CNT, with shaded
regions for zonal mean pv gradients between +/- 0.5β.

CNT
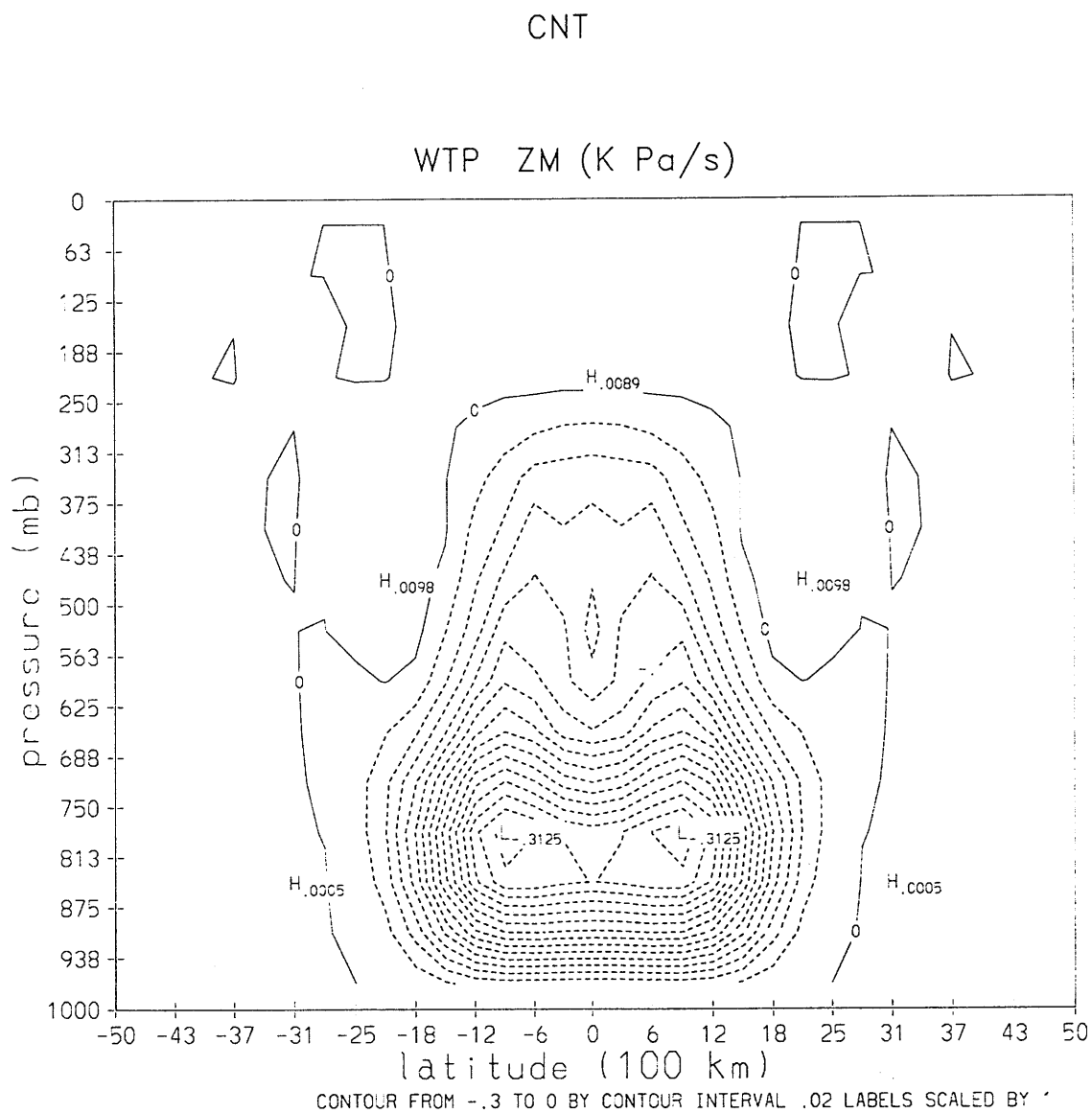
Figure 3-22: Latitude pressure cross-section of the zonal mean vertical eddy heat fluxes in the equilibrated state of CNT.

WMF

WTP   ZM (K Pa/s)

CONTOUR FROM -.425 TO .025 BY CONTOUR INTERVAL .025 LABELS SCALED BY 1
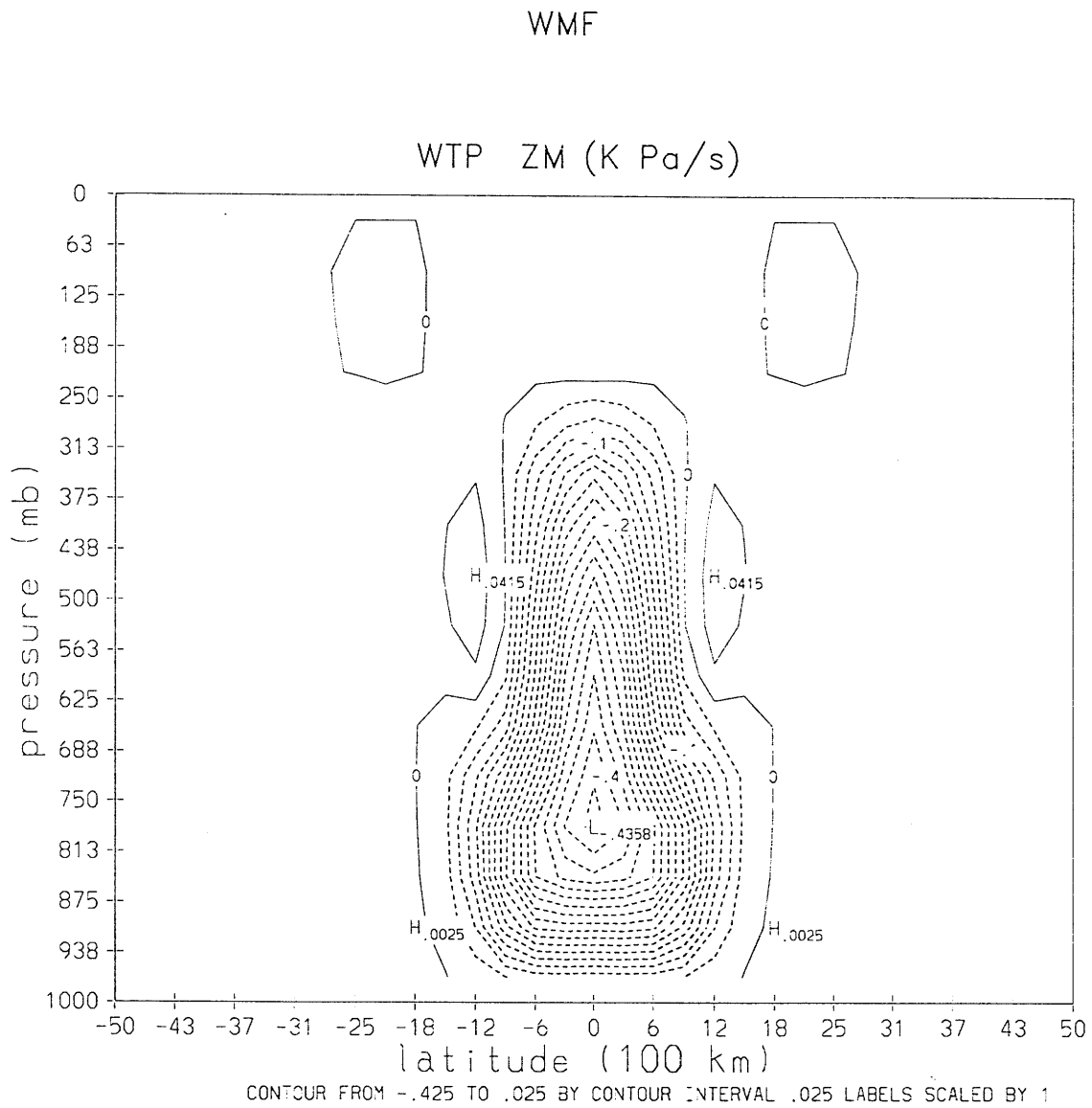
Figure 3-23: Latitude pressure cross-section of the zonal mean vertical eddy heat fluxes in the equilibrated state of WMF.

WMF (fixed CNT ss)

d(PV)/d(beta*y)

CONTOUR FROM -154 TO 94 BY CONTOUR INTERVAL 1 LABELS SCALED BY 1
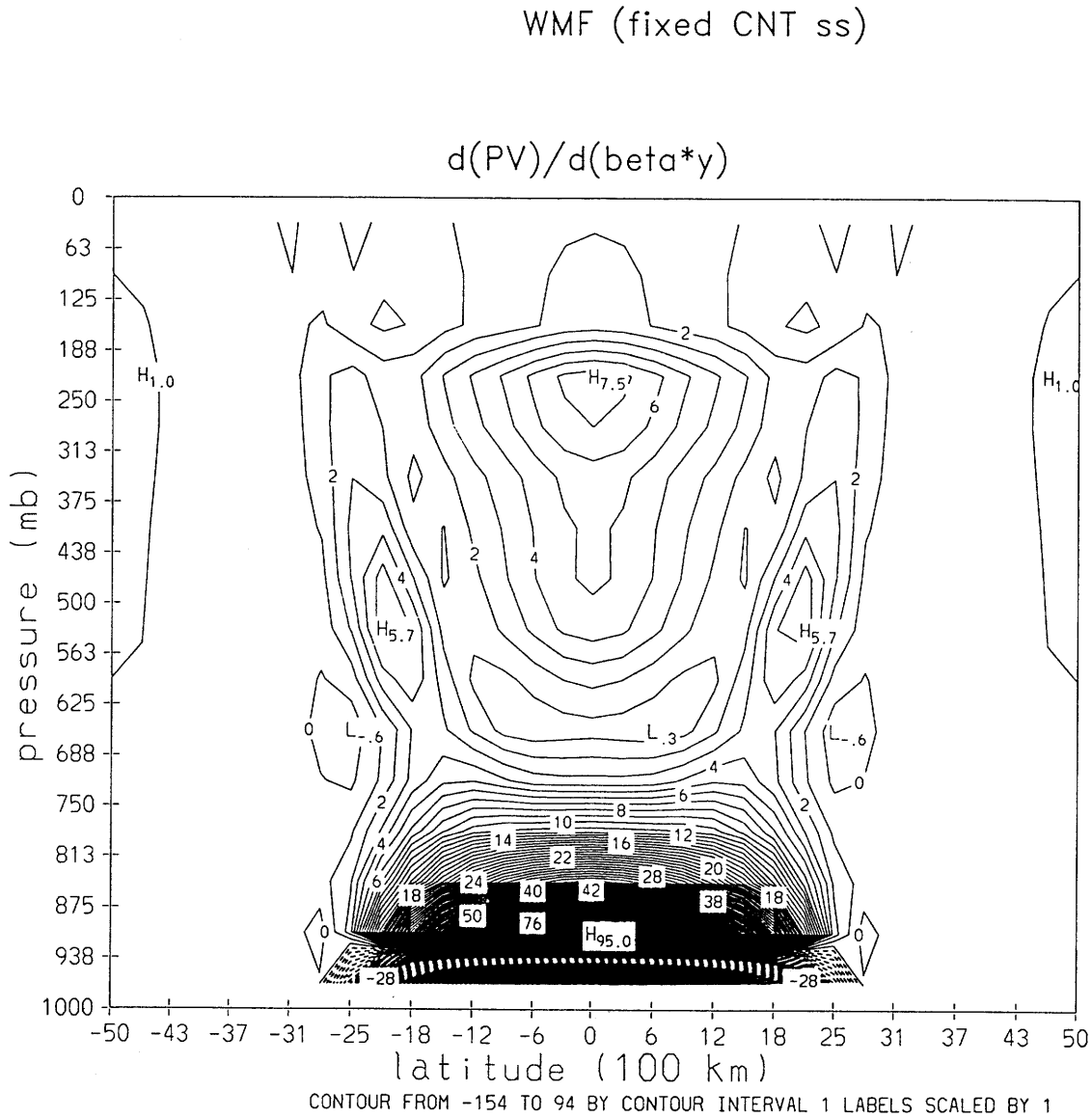
Figure 3-24: Latitude pressure cross-section of the zonally averaged pv gradients in the equilibrated state of WV1FS, when the static stability is held fixed at the static stability from the equilibrated state of the control run, in units of β.

potential vorticity gradients
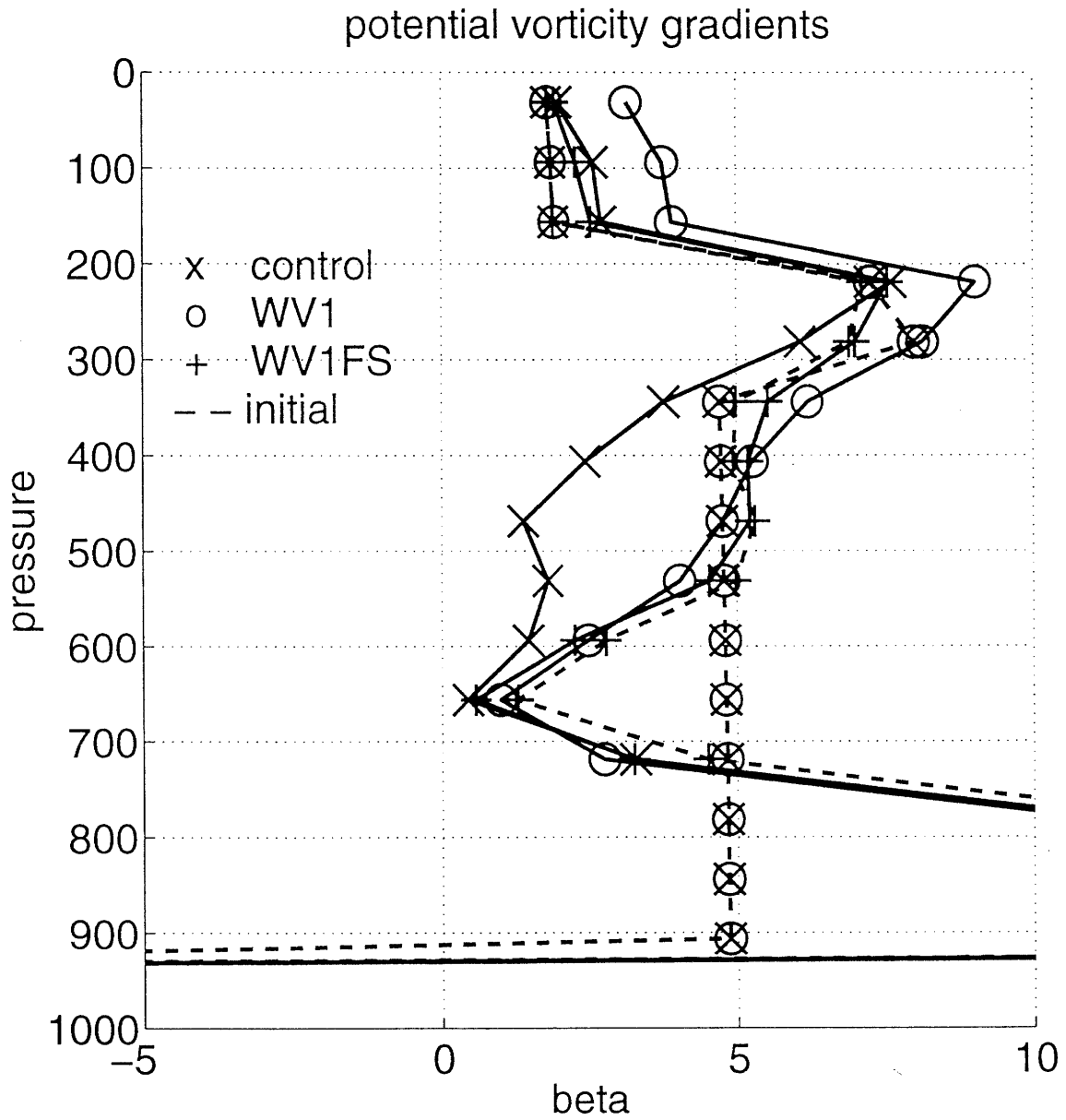
Figure 3-25: Comparison of the zonal mean pv gradients above the ABL at the center of the channel for CNT,WV1 and WV1FS, in units of β.

$$\frac{1}{2}\frac{\partial \overline{q'^2}}{\partial t} = \overline{v'q'}\frac{\partial \overline{q}}{\partial y} - \frac{1}{2}\partial\frac{\overline{v'q'^2}}{\partial y} + \overline{q'(-f_0\frac{\partial}{\partial p}(\frac{g}{\pi}\frac{\partial}{\partial P}\rho\nu_T\frac{\partial \theta}{\partial z} + \frac{\dot{Q}R}{spC_p}) + \hat{k}\bullet\nabla\times\overrightarrow{F})},$$

where v is the meridional wind and primes designate deviations from the zonal mean.

The perturbation pe is equivalent to the magnitude of the potential vorticity anomalies. The terms in the perturbation pe tendency equation indicate which processes are responsible for the maintenance of the anomalies. The first term on the right hand side is the quasi-linear flux of potential vorticity and will be referred to as the downgradient transport of perturbation pv because the correlation between the mean pv flux and the mean pv gradients tends to be negative. Therefore, this term can be thought of as the downgradient transport of perturbation pv which reduces the mean pv gradients and is a source of perturbation pv. The second term on the right hand side is due to the flux of perturbation pv by wave-wave interactions. This flux represents a cascade of perturbation pv to smaller scales and acts as a transfer of perturbation pv from the larger scales to the smaller scales. The last large expression on the right hand side consists of the vertical diffusion of heat, Newtonian cooling, and the vertical diffusion of momentum. respectively. All of these act to damp out the perturbation pv. except for the thermal diffusion at the second model level due to the large decrease in the static stability.

A plot of the terms in the perturbation pe tendency equation for the control run is shown in Figure 3-26. This figure shows that the nonlinear wave-wave interactions become significant above the boundary layer. The balance of terms in the perturbation pe equation show that the nonlinear cascade of perturbation pv is dominant between 400 and 500 mb. Within the ABL the dynamical balance is between the quasi-linear pv transport and the thermal diffusion. The nonlinear wave-wave cascade is insignificant within the ABL and the dynamics are essentially thermally dissipating Rossby waves as discussed by McIntyre and Norton (1990).

3.6   Perturbation pv and pv fluxes in the equilibrated state

This Section outlines the structure of the perturbation pv in the control run that is responsible for the maintenance of the equilibrated state. Figure 3-7 shows the zonal mean latitude pressure cross-section of the amplitude of the perturbation pv in the equilibrated state of the control run. The perturbation pv has two peaks. The primary peak is at the first model level and there is a secondary peak at the tropopause. This perturbation pv has a zonal wavelength corresponding to

the fundamental wavelength of the model (5260 km). Contributions from other wavelengths are negligible.

In order to determine if the perturbation pv at the tropopause is significantly contributing to the pv fluxes within the ABL, the perturbation pv, Figure 3-7, is separated into four regions. These regions are the ABL, the mid troposphere, the tropopause region, and the stratosphere. The tropopause region is defined here as the region between 200 and 350mb. The pv anomalies in each region are then inverted to get the perturbation streamfunction. The zonal mean pv fluxes due to each region are then calculated from the perturbation streamfunction for each region and the perturbation pv of the total field. Therefore the pv fluxes in the ABL that are due to the pv anomalies at the tropopause are a function of the winds in the ABL, which are calculated from the inverted pv anomalies at the tropopause, and the total pv anomalies within the ABL.

It was important to do this study because previous studies of the role of the tropopause in the dynamics within the ABL (Pavan 1996, Robinson 1988), have concluded that the pv anomalies at the tropopause do not significantly contribute to the pv fluxes within the ABL. It is not possible to determine the impact of the pv anomalies at the tropopause on the ABL from the amplitude of the pv anomalies alone, as seen in the results of Robinson (1988). The results of this study are important in understanding whether the equilibrated state is maintained by deep eddies, and Eady-like dynamics, or by shallow waves, and Charney-like dynamics. If the waves that maintain the equilibrated state have deep structure then the dynamics within the ABL will be dependent upon changes in the mean state at the tropopause. Inverting pv anomalies in different vertical layers of the model will be used to illustrate the structure of the perturbation pv and pv fluxes in the equilibrated state. One note of caution is that dividing a pv anomaly, which has deep vertical structure, into vertical regions and inverting these regions to get the pv fluxes may lead to wrong conclusions since the pv flux due to the mode is a sum of all of these fluxes and arbitrary divisions can result in fluxes that have no physical meaning. The division was found to be physically significant in this study because the pv anomalies below the tropopause region were found to make a very small contribution to the pv fluxes within the ABL.

Figure 3-27 shows the latitude pressure cross-section of the zonal mean pv fluxes for the equilibrated state of the control run. Figure 3-28 shows the latitude pressure cross-section of the zonal mean pv fluxes that are calculated from the pv anomalies at the tropopause. Comparing Figure 3-27 to Figure 3-28, it is seen that the pv anomalies at the tropopause are responsible for the majority of the pv fluxes within the ABL, and elsewhere as well. From this is can be concluded that the interactions between the perturbation pv at the tropopause and within the ABL are important in the maintenance of the equilibrated state.
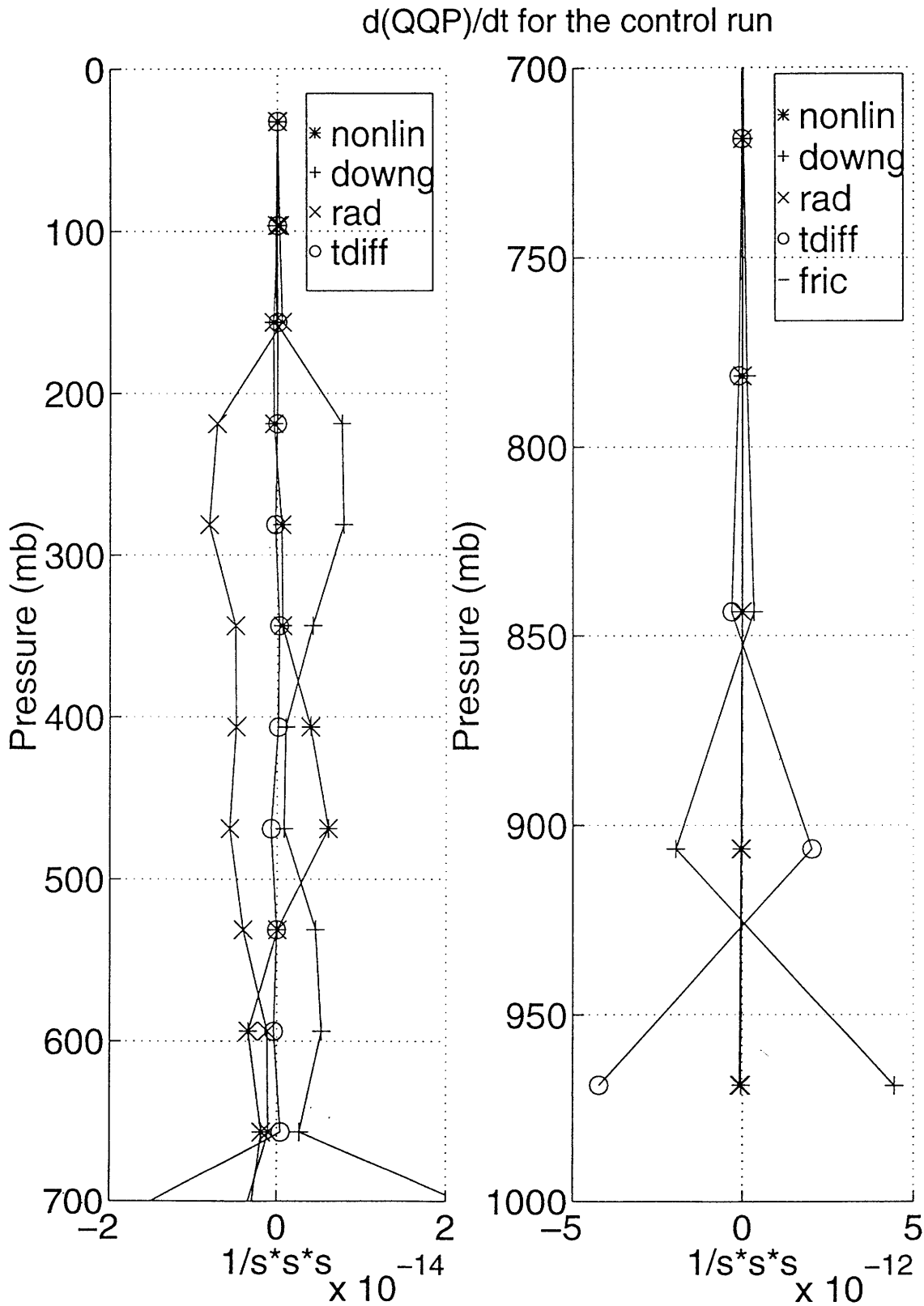
Figure 3-26: Terms in the perturbation pe tendency equation for the control run for a) above the ABL and b) within the ABL.

control run

VQ all levels for 20 day average

CONTOUR FROM -.0006 TC .0015 BY CONTOUR INTERVAL .0001
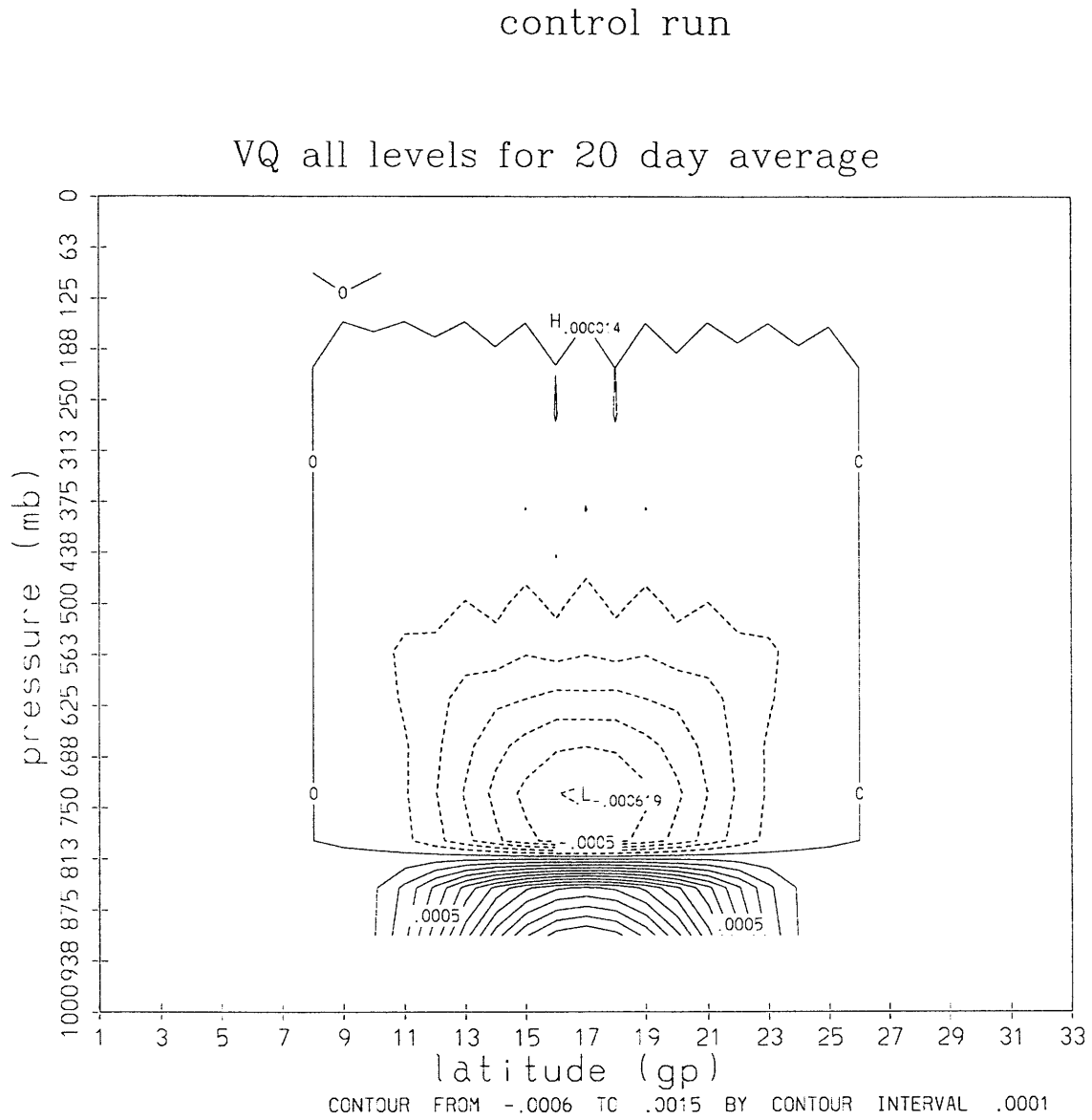
Figure 3-27: Latitude pressure cross-section of the zonal
mean pv fluxes for the equilibrated state of the control run.
Latitudinal axis is in units of gridpoints, where the channel
width (33 gridpoints) is equal to 10,000 km.

control run

VQ levels 9-12 for 20 day average

CONTOUR FROM -.0006 TO .0013 BY CONTOUR INTERVAL .0001
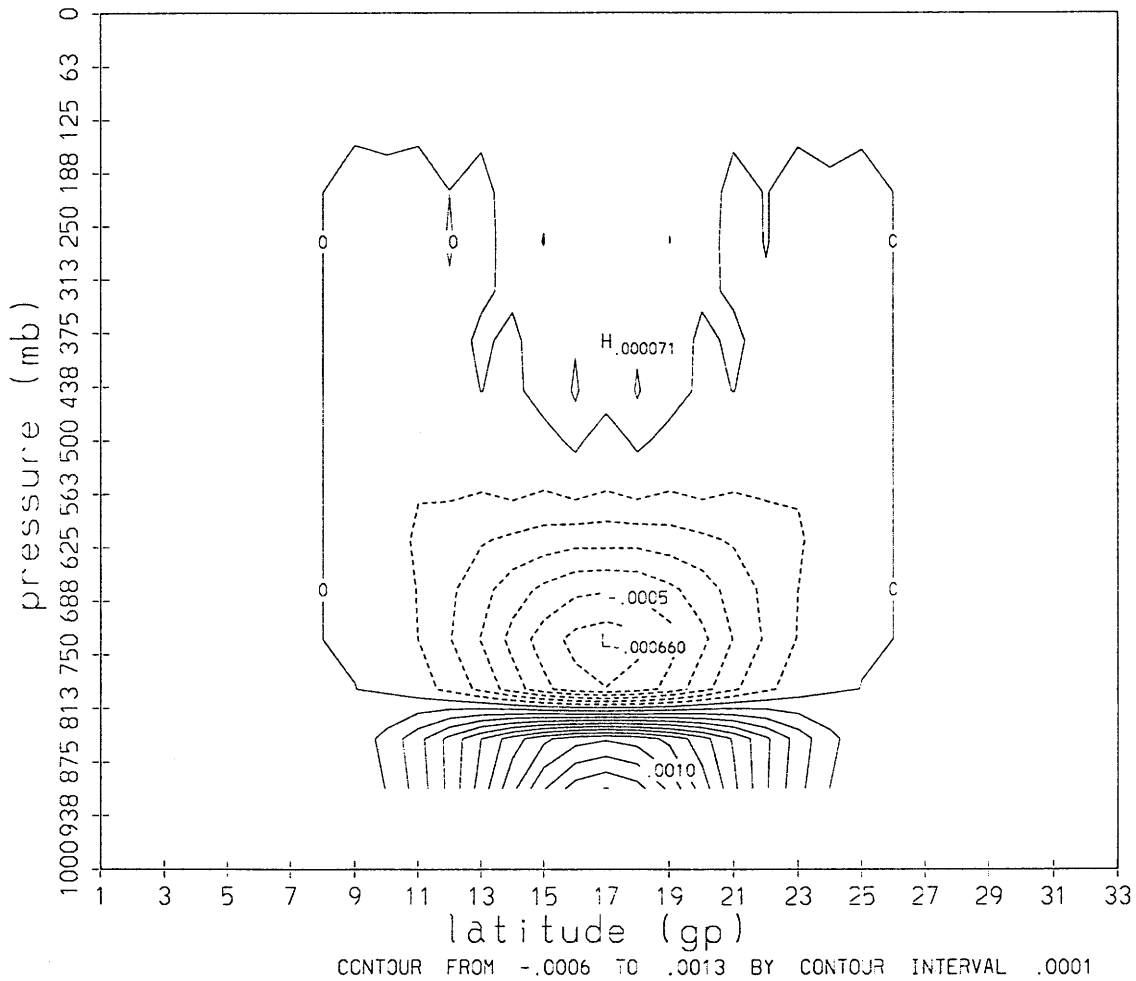
Figure 3-28: Latitude pressure cross-section of the zonal
mean pv fluxes that are calculated from the pv anomalies
at the tropopause. Latitudinal axis is in units of gridpoints,
where the channel width (33 gridpoints) is equal to 10,000
km.

Chapter 4

Standard model run compared to observations

The standard model run has been chosen to approximate observations of the Northern Hemisphere winter climate as closely as possible, given the simple representations of heating and friction and the construction of the ABL in the model.

4.1   Distributions of pseudopotential vorticity

Figure 4-1 displays contours of zonal mean Ertel's potential vorticity and potential temperature for the Northern Hemisphere January 1982-1994 climatology, produced from the NCEP-NCAR reanalysis dataset. Dashed lines in the figure are contours of potential temperature. The lowest contour is 270K and the highest contour is 320K, the contour interval is 10K. The solid lines are contours of potential vorticity (ipv) in units of $m^2 s^{-1} K$ with a contour interval of $5 X 10^{-8} m^2 s^{-1} K$. Figure 4-2 displays the January 1982-1994 zonal mean meridional gradient of Ertel's ipv divided by the contribution from the planetary vorticity, from the same dataset as Figure 4-1. Figures 4-1 and 4-2 show that the ipv in mid latitudes is characterized by large gradients below 800 mb and at the tropopause. Below 800 mb, the meridional temperature gradients are large due to the heating of the atmosphere by the underlying ocean or land. The heating of the air near the surface causes turbulent fluxes of heat and momentum to mix momentum and heat. This heating and mixing results in small values of static stability near the ground. Both the large temperature gradients and the small static stability contribute to the large ipv gradients in the atmospheric boundary layer (ABL). Large ipv gradients are also found at the tropopause where the high ipv stratospheric air interfaces the low ipv tropospheric air.

At the top of the ABL, where thermal capping inversions occur, air from above the ABL is entrained into the boundary layer which can cause ipv gradients

just above the ABL to become negative, as is seen in Figure 4-2. The region of ipv homogenization, which can be seen clearly in Figure 4-1 where the ipv contours are parallel to the isentropes between 40N and 70N, 600 and 700 mb, occurs in the region where the large scale baroclinically unstable Rossby waves have a critical level. Non reversible mixing of ipv along the isentropes reduces the ipv gradients and the slope of the isentropes in this region. The ipv gradients between this region and the tropopause have reduced ipv gradients relative to radiative equilibrium estimates but they are still large relative to β.

In quasi-geostrophic dynamics, pseudopotential vorticity (pv) is conserved following the geostrophic wind, in the absence of friction and diabatic heating. This differs significantly from the conservation of ipv along isentropic surfaces. PV is conserved following an isobaric trajectory while ipv is conserved following an air parcel (Hoskins, McIntyre, and Robertson 1985).

The gradient of ipv along isentropes is related to the gradient of pv along pressure surfaces,

$$\nabla_\theta(IPV) \approx -g \frac{d\theta_{ref}}{dp} \nabla_p(PV)$$

Where $\frac{d\theta_{ref}}{dp}$ is the reference potential temperature distribution. Dividing $\nabla_\theta(IPV)$ by the gradient of IPV due to the planetary vorticity gives

$$\frac{\nabla_\theta(IPV)}{-g\frac{d\theta_{ref}}{dp}} \approx \frac{\nabla_p(PV)}{\beta}$$

The gradient of ipv along isentropes divided by the contribution due to the planetary vorticity is approximately equal to the gradient of pv along pressure surfaces divided by β.

Comparing the observations, Figure 4-2, to the equilibrated state of the model, 3-10, it is seen that the qualitative features of the observed pv distribution are resolved by the model. Quantitatively the pv gradients in the ABL are larger than the observations. This will be discussed further in the Section on static stability.

4.2   Structure of the mean temperature

Figures 4-3 compares the static stability of the control run to observations. Since the eddy diffusion coefficient is a continuous function of height, the large pv gradients in the ABL extend much higher, and the static stability peaks much higher, than in observations. The static stability in the control run below 700 is significantly smaller than observations. The magnitude and vertical profile of the static stability above 700 mb closely approximates observations.

Model runs which have diffusion coefficients which go to zero below 750 mb, discussed in Section 5.2.3, have much more realistic mean static stability and a larger region of pv homogenization. The continuous eddy diffusion coefficient has been chosen for the control run to allow the region over which the vertical eddy heat fluxes play a significant role to be a function of the other parameters in the model. Limiting the thermal diffusion to a region closer to the surface would yield a more realistic representation of a thermal capping inversion.

Figures 4-4 compares the meridional temperature gradients of the control run to observations. The large thermal damping in the ABL prevents the reduction of the meridional temperature gradients at the lowest levels by the large scale eddies. These gradients are seen to be too large relative to observations. Model runs which allow the surface temperatures to vary show that the lack of adjustment is due to the way in which the control run calculates a surface air temperature. The control run assumes that the surface air potential temperature is equal to the potential temperature at the first model level. This assumption of a well mixed layer between the first model level and the surface couples the dynamics at the first model level with the dynamics at the surface. When an equation for the surface temperature is coupled to the qg equations, the temperature at the first model level displays much more variability. The equilibrated temperatures are much closer to observations when the surface temperature is calculated from a thermodynamic balance at the surface. In these runs, fluxes of heat into (out of) the ocean cool (warm) the surface air temperature. Results from these runs are discussed in Chapter 4. In the runs without an explicit surface air temperature, fluxes of heat converge into the first model level.

Above the ABL, the pv has been homogenized (Figure 3-10). This homogenization extends along the sides of the jet, where the large scale waves have a critical level. The homogenization is a result of both increased static stability and decreased horizontal temperature gradients. This region of homogenization closely approximates the homogenization of ipv that is seen in observations (Figures 4-1 and 4-2).

Above the homogenized pv region, the pv gradients are reduced less and less with height and are relatively unchanged at the tropopause (Figure 3-10), although there is a small increase in the static stability by vertical heat fluxes at the tropopause. In the upper troposphere, the meridional temperature gradients from observations are completely different from those of the control run. The dynamics that are responsible for the observed temperature gradients in the upper troposphere are not adequately resolved in this simple process model.

4.3   Structure of the zonal mean eddy fluxes

The zonal mean eddy sensible heat fluxes of the control run have been chosen to approximate observations of the Northern Hemisphere wintertime eddy heat

fluxes. Sensible heat fluxes will be referred to as heat fluxes in what follows. Therefore, the zonal mean eddy heat fluxes from the model are compared to the zonal mean stationary plus transient eddy heat fluxes of the observations. Figure 4-5 shows the zonal mean meridional eddy heat fluxes of the equilibrated control run and observations. Figure 4-6 shows the zonal mean vertical eddy heat fluxes, of the equilibrated control run and observations. The magnitude and vertical structure of the model fluxes resemble the observed fluxes qualitatively. Both the vertical and meridional eddy heat fluxes peak at 800 mb, due to the thermal damping in the ABL. Without the thermal damping the fluxes peak at the surface.

The major inadequacy of the model fluxes is the absence of a secondary peak in the meridional eddy heat flux in the upper troposphere. A secondary peak in the vertical eddy heat flux at the tropopause is seen in the model fluxes instead. Therefore, the vertical eddy heat flux is significant in modifying the temperature structure at the tropopause instead of the meridional heat fluxes. This may be due to the limitations of the quasi-geostrophic equations in representing the dynamics at the tropopause.

Since the dynamics is this model are dry, the energy transport due to water vapor fluxes has been neglected. These fluxes are responsible for approximately 35% of the total energy transport in the lower troposphere (Peixoto and Oort 1992). In order to compensate for the neglected water vapor fluxes, the vertically averaged total eddy energy transport has been chosen to closely approximate the observed total eddy energy transport.

Figure 4-7 shows the zonal mean meridional circulation heat fluxes of the equilibrated control run and observations. The potential temperature transport has been averaged instead of the temperature transport to take into account the cancellation between the sensible heat flux and the potential energy flux. This cancellation is only significant between the mean fluxes since the eddy potential energy flux is small relative to the eddy sensible heat flux (Peixoto and Oort 1992). Given the difference between the two observational datasets, the magnitude and vertical distribution of the model's mean meridional fluxes closely approximates the observed distribution. The vertically averaged mean potential temperature flux is equal to -4.26 Km/s at the center of the channel. The ratio of the vertically averaged eddy energy flux to the mean eddy flux is equal to -17.21/4.26= -4.03 K m/s compared to -19/4= -4.75 K m/s in observations.

Figure 4-8 shows the zonal mean eddy momentum fluxes for the control run compared to observations. This figure shows that the model resembles the vertical structure and magnitude of the observations quite well, except at the surface. At the lowest level, the observations have negative momentum fluxes, while the model has positive fluxes which are very small. Since the model's fluxes were calculated using only geostrophic winds, this difference may be due to the ageostrophic winds near the surface.
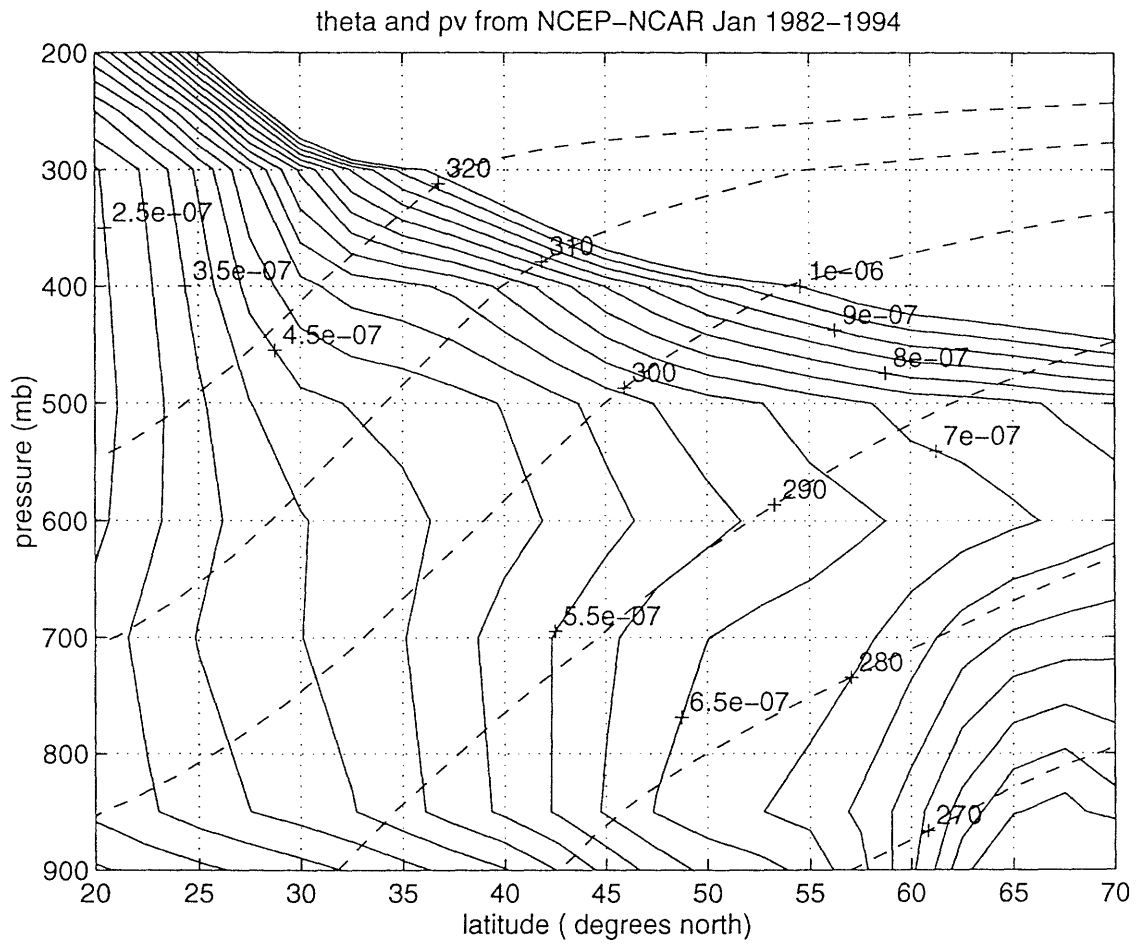
Figure 4-1: Ertel's potential vorticity and potential temperature in the Northern Hemisphere calculated from NCEP-NCAR January 1982-1994 climatology.

theta and pv gradients from NCEP–NCAR Jan 1982–1994
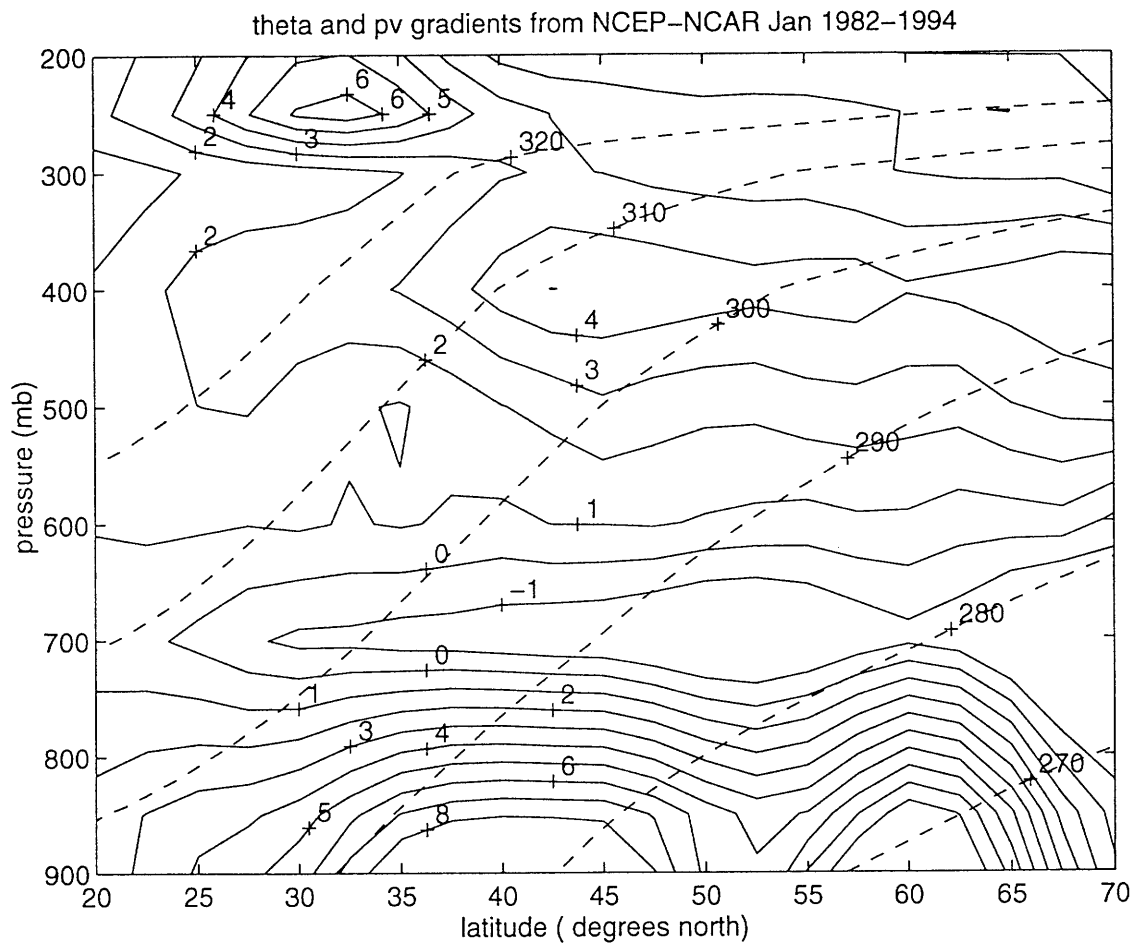
Figure 4-2: Isentropic gradients of Ertel's potential vortic-
ity, divided by the contribution from the planetary vorticity,
in the Northern Hemisphere calculated from NCEP-NCAR
January 1982-1994 climatology.
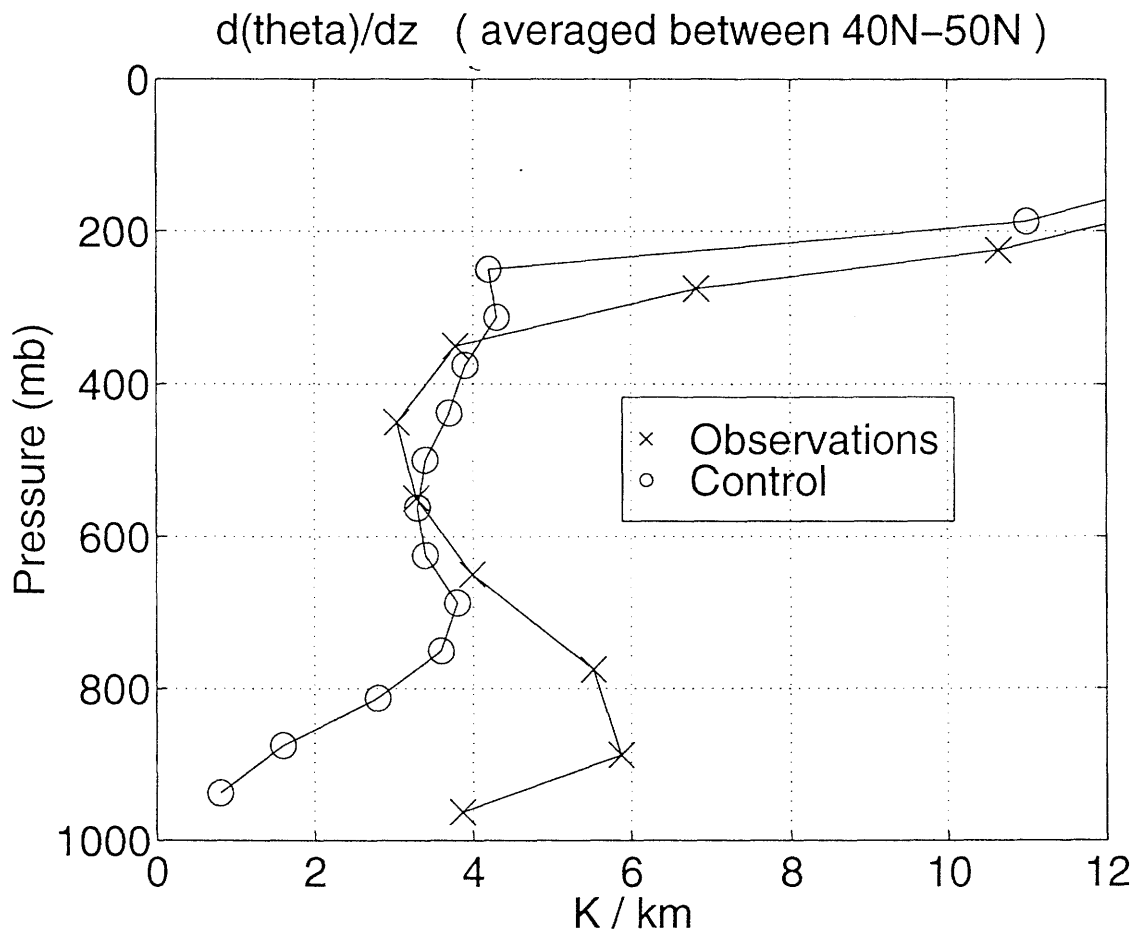
Figure 4-3: Static stability of the equilibrated state of the control run vs NCEP January 1982-1994 observations.
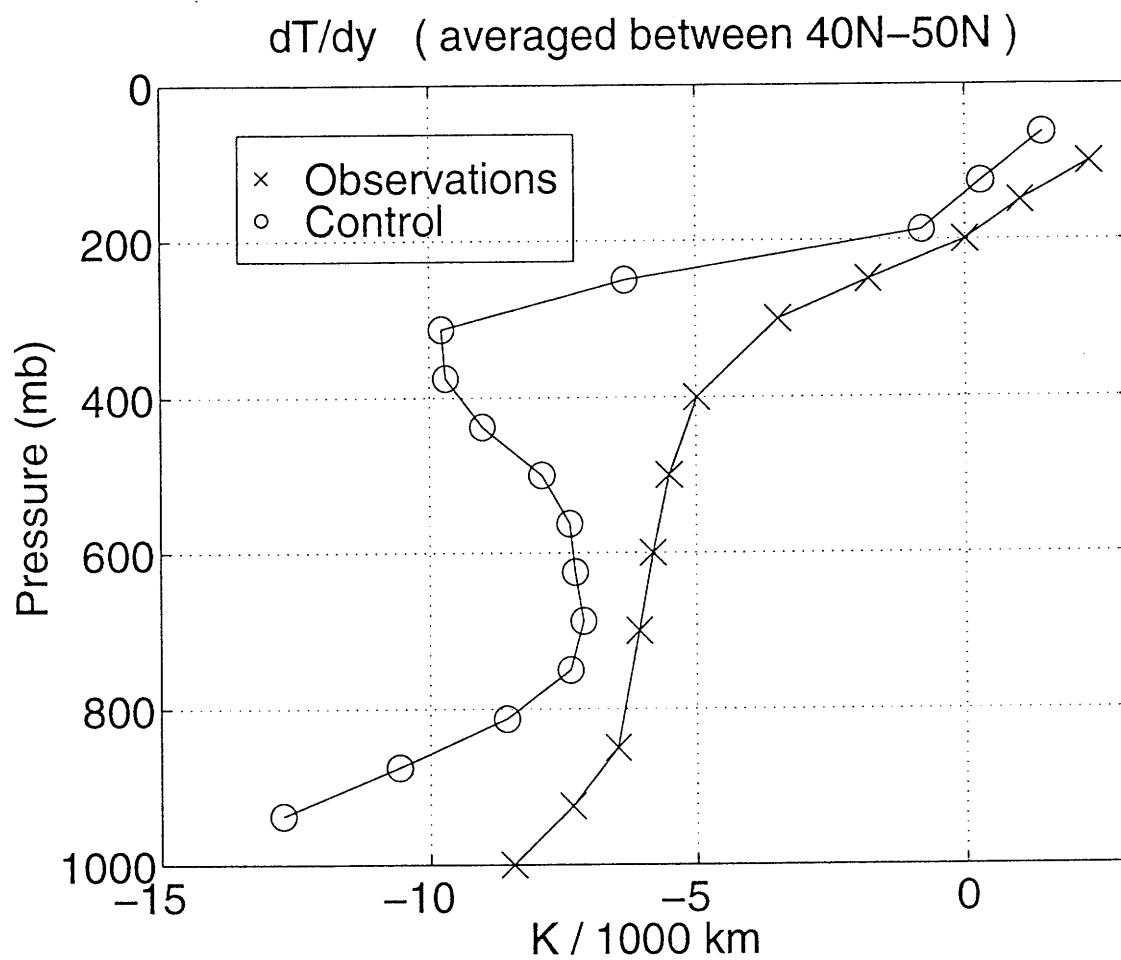
Figure 4-4: Meridional temperature gradients of the equili-
brated state of the control run vs NCEP January 1982-1994
observations.
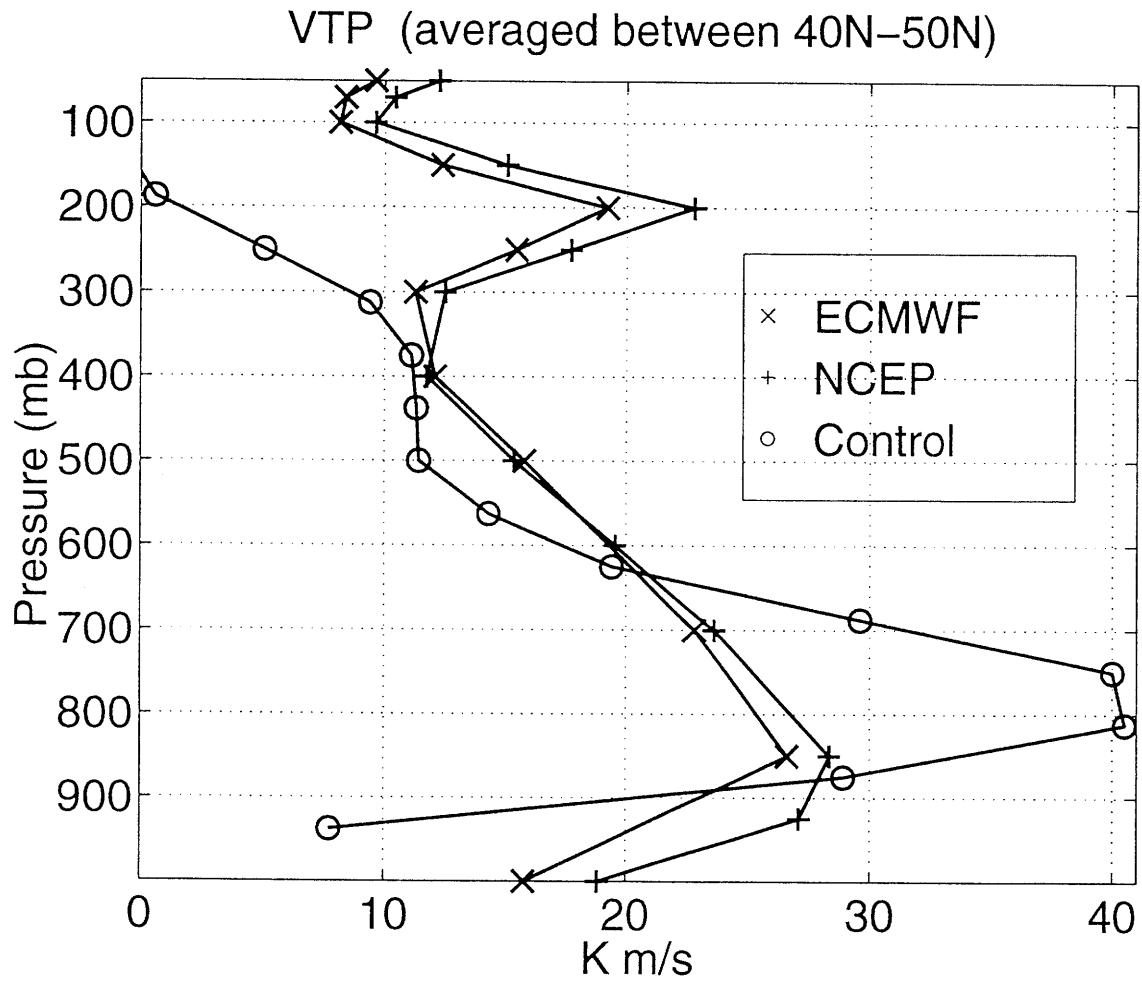
Figure 4-5: Zonal mean eddy heat fluxes of the equilibrated
state of the control run vs January ECMWF (1985-1989) and
NCEP (1982-1995) datasets.

WTP (averaged between 40N–50N)
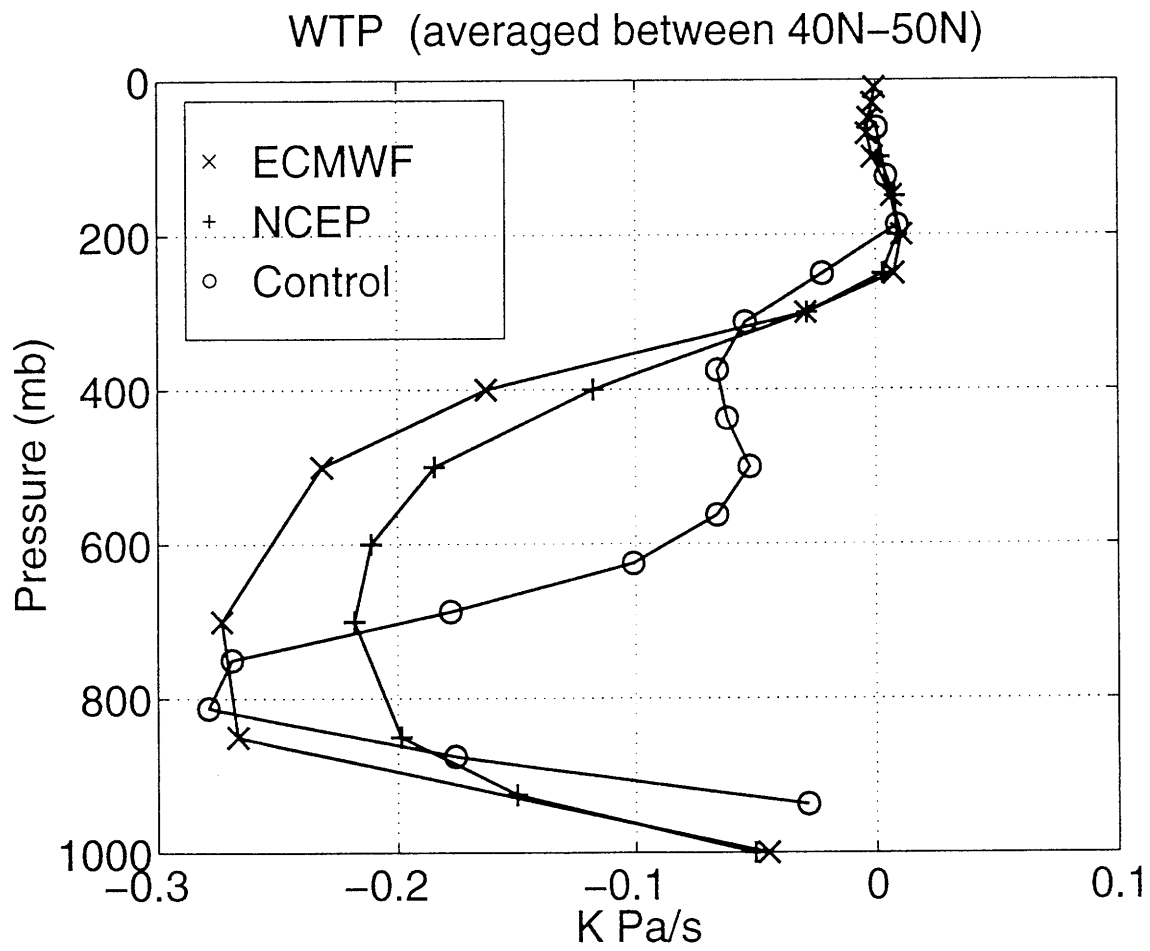
Figure 4-6: Zonal mean vertical eddy heat fluxes of the equilibrated state of the control run vs January ECMWF (1985-1989) and NCEP (1982-1995) datasets.
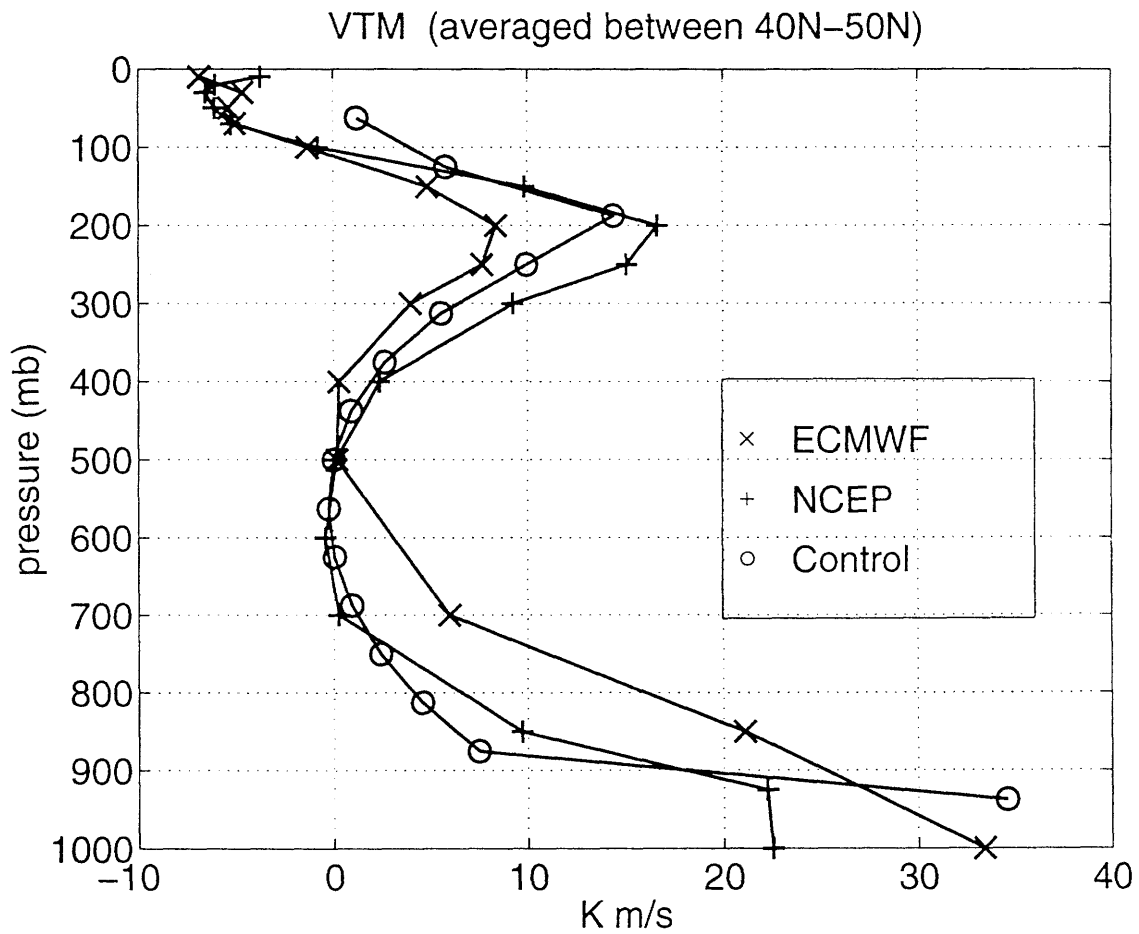
Figure 4-7: Zonal mean meridional heat fluxes of the equili-
brated state of the control run vs January ECMWF (1985-
1989) and NCEP (1982-1995) datasets.
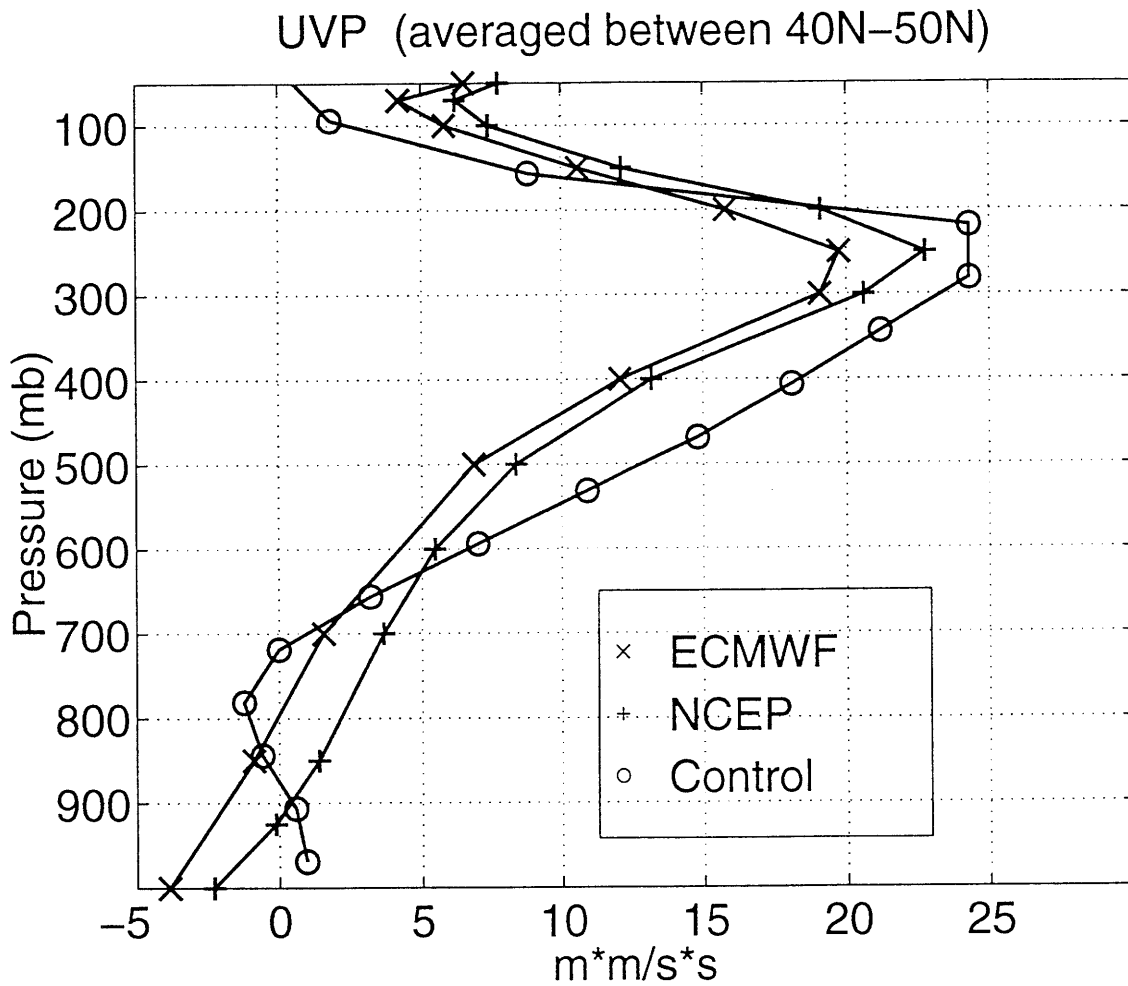
Figure 4-8: Zonal mean eddy momentum fluxes of the equi-
librated state of the control run vs January ECMWF (1985-
1989) and NCEP (1982-1995) datasets.

Chapter 5

Resolution and domain size dependence of the equilibrated states

The previous Chapter discussed the mean climate and fluxes of the control run compared to observations. In order to determine if the dynamics of the model are convergent at 17 vertical levels, the model has been run using the same parameter values but with twice the vertical resolution. In order to determine how the dynamics of the model change as a function of vertical resolution, the model has been run with 9, 5, and 3 levels in the vertical.

Since it has been found in other studies that the wave that is responsible for the most energy transport maybe the largest wave resolved by the model (Cehelsky and Tung 1991), the model has been run with 2 and 5 times the channel length of the control run, using the same resolution as the control run, and double the resolution of the control run, both meridionally and zonally, with the original channel length. The model has also been run with the jet width doubled to determine if the jet width chosen for the control run, which is close to the wavelength of the most unstable wave, artificially sets the meridional scale of the waves.

5.1 Horizontal resolution and domain size

The horizontal resolution and domain size studies have been run to determine if the dynamics are adequately resolved in the control run. The model has been run with a channel length 2 and 5 times the channel length of the control run, with the same resolution as the control run, and double the resolution of the control run, both meridionally and zonally, with the same channel length.

Figure 5-1 shows the zonal mean pv gradients of the equilibrated state of the doubled resolution run. Comparing Figure 5-1 to the pv gradients of the control run, Figure 3-10, it is seen that the two runs have similar pv gradients below 625 mb. At approximately 500 mb, the symmetric structure of the pv gradients is resolved better when the horizontal resolution is increased. This is primarily due to the increase in the zonal resolution (Figure not shown). The homogenization of pv at the center of the channel and the local peaks in the pv gradients on either side of this homogenized region are more defined. The differences in the pv gradients are primarily due to the reduction in the magnitude of the meridional temperature gradients when the horizontal resolution is increased, since the static stability for the control run and the doubled resolution run are essentially the same (Figure not shown). The reduction in the magnitude of the meridional temperature gradients is consistent with enhanced mixing of pv above the ABL. The differences between the control run and the doubled resolution run are small relative to the differences between the symmetric and equilibrated states. Qualitatively, the control run resolves the pv gradients of the doubled resolution run and is therefore considered to have adequate resolution to resolve the dynamics.

The model's equilibrated climate and mean fluxes are insensitive to a doubling of the channel length. When the channel length is increased 5 times from 5,260 km to 26,300 km, which is approximately the distance around a latitude circle at 49 degrees, the equilibrated model climate and mean fluxes change significantly. Figure 5-2 shows a comparison of the pv gradients above the ABL for a channel length of 1, 2, and 5 times the channel length of the control run. These runs will be referred to as 1X, 2X and 5X, respectively. This figure shows that, above 600 mb, the pv gradients are less adjusted as the channel length is increased. Below 600 mb, the pv gradients of the 1X and 2X runs are essentially the same. The 5X pv gradients below 600 mb are significantly reduced relatively to the 1X and 2X runs. This difference is due to the vertical structure of the meridional temperature gradients, since the vertical structure of the equilibrated static stability for the three runs are essentially the same (Figure not shown). The balance of terms in the perturbation potential entrophy equation are discussed in Chapter 3. Figure 3-26 from Chapter 3 shows the balance of terms in the perturbation potential enstrophy tendency equation for the control run. This equation is a useful diagnostic to see what processes are responsible for the maintenance of the perturbation potential vorticity. A discussion of this equation is included in Section 3.5. It is seen in this figure that between 400-500 mb the dominant balance is between the nonlinear wave-wave interactions, designated by *'s, and the Newtonian cooling, designated by x's. This is the region where the 5 times channel length results diverge from those of the control run. Figure 5-3 shows the balance of terms in the perturbation potential entrophy tendency equation for the 5 times channel length. This figure shows that all of the terms in the perturbation pe tendency equation are smaller above the ABL when the channel length is increased by a factor of five. This difference can be understood in terms of the eddy available potential energy. Wavepackets propagating along a 26,300

km latitude circle will have less eddy available potential energy than wavepackets confined to a 5,260 km channel with periodic boundary conditions.

The wavelength of the wave that is responsible for the majority of the pv transport is 5,260 km for all three runs. This is very interesting considering the results of Cehelsky and Tung (1991) which found that the dominant heat transporting wave was the largest wave resolved by the model, contrary to the results of this model study which has shown that the scale of the dominant heat transporting wave is independent to an increase in the channel length. This is due to the magnitude of the radiative forcing in this model. We have chosen radiative equilibrium temperature gradients significantly less than those chosen for the Cehelsky and Tung (1991) study. This means that equilibration mechanism in their model is not the equilibration mechanism of this model. The dominant heat transporting wave does not saturate in this model. This result has been also found in the process model study of Zhou and Stone (1992a), which used a two level primitive equation model on a sphere, and Stone and Branscome (1992), which used a two level quasi-geostrophic model on a β-plane. Our choice for the forcing appears to be more realistic, since, even with our weaker forcing, the equilibrated temperature gradients are larger than in the observations (Figure 4-4). Also as shown below, the waves that dominate the heat transport in our model are the same as in the observations.

5.2   Vertical resolution

The previous Section has shown that the dynamics of the model are not dependent upon the horizontal resolution, as long as the horizontal resolution is chosen to adequately resolve the large scale waves. The results of an earlier study of a dissipative barotropic easterly point jet, included in Appendix A, suggested that the stability of the baroclinic problem would be dependent on the vertical resolution of the model.

a. Barotropic point jet

The problem of the barotropic point jet has been shown to be mathematically homomorphic to the Boussinesq Charney problem by Lindzen *et al.* (1983). The problem of the easterly barotropic jet presents the ability to investigate the primary aspects of the impact of resolution on the linearized Charney problem in a two-dimensional model. The study of how the stability characteristics of the barotropic point jet changes as a function of the resolution was a part of the thesis proposal for this thesis and is included in Appendix A.

The supercriticality of the equilibrated state of the barotropic jet has been found to be relatively independent of the magnitude of the dissipation but very dependent on the resolution of the model. A linear stability analysis of the barotropic point jet demonstrated that the growth rates of the unstable waves and the most

doubled resolution

d(PV)/d(beta*y)

CONTOUR FROM −171 TO 84 BY CONTOUR INTERVAL 1 LABELS SCALED BY 1
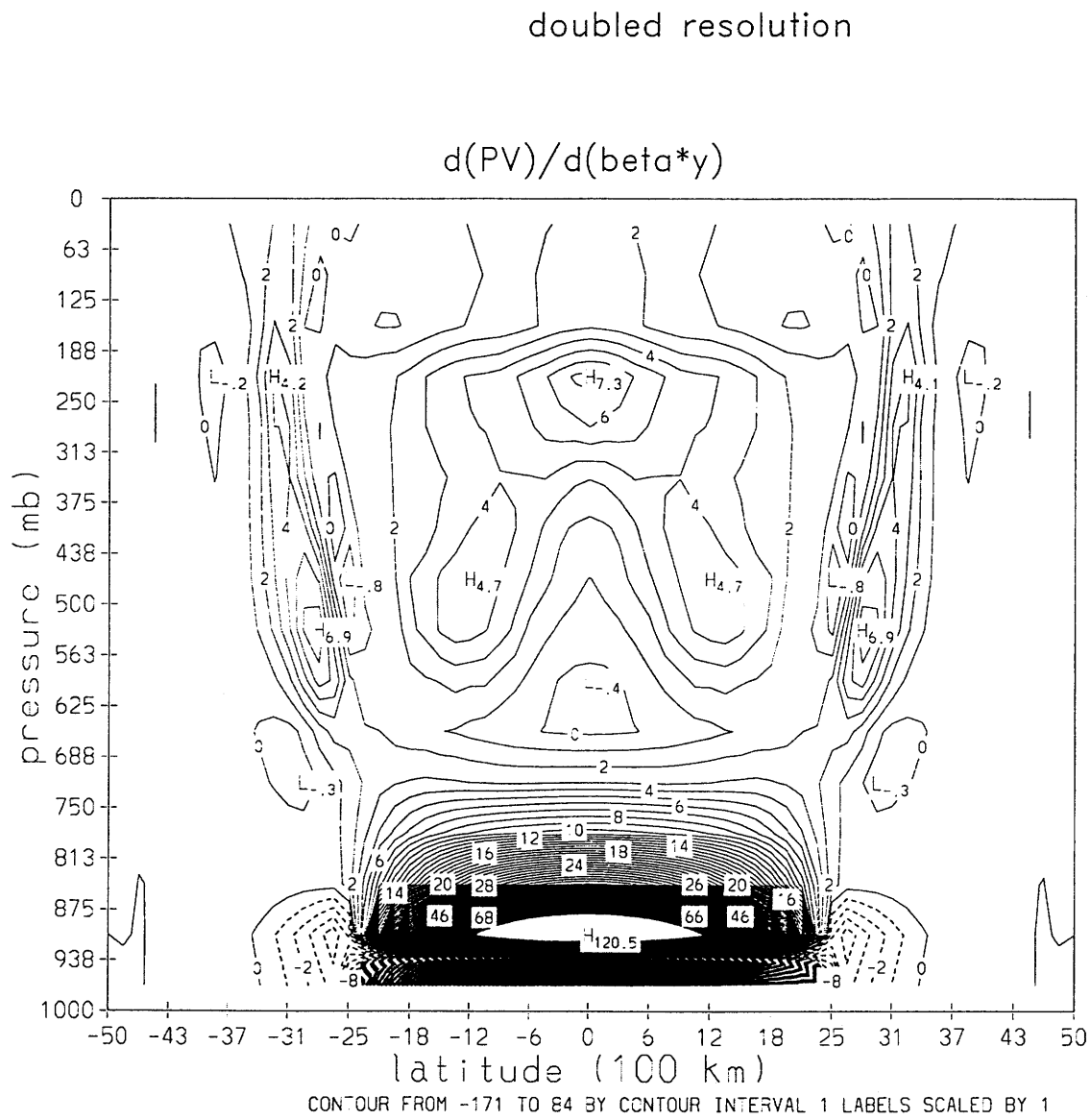
Figure 5-1: PV gradients, divided by β, of the equilibrated state of the doubled zonal resolution run, in units of β. The minimum wavelength resolved in this run is equal to 450 km (assumed to be the distance between 4 gridpoints).
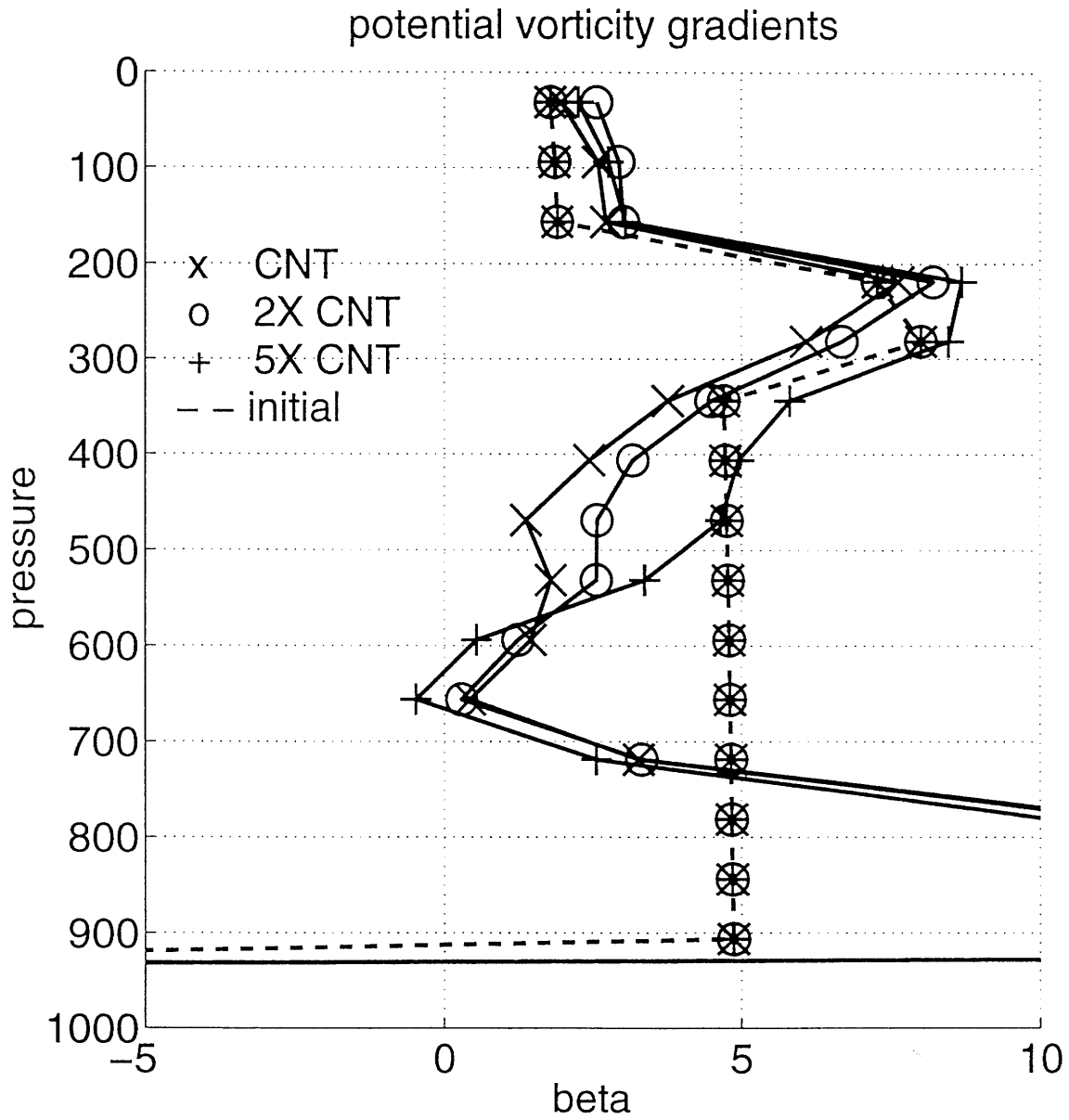
Figure 5-2: Comparison between the equilibrated meridional pv gradients at the center of the channel for the 5,260 km, 10,520 km, 26,300 km channel length runs, in units of β.
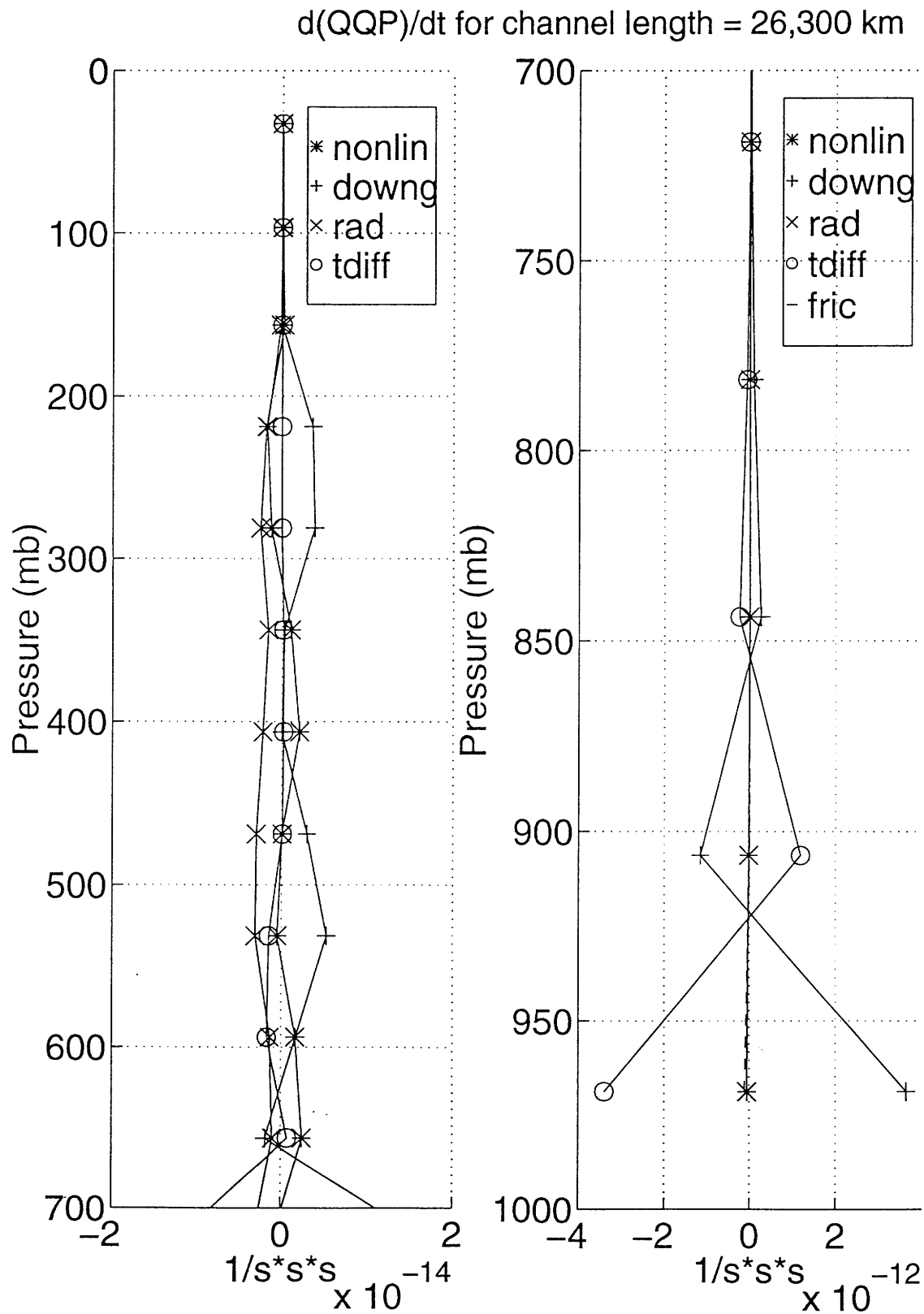
Figure 5-3: Terms in the perturbation pe tendency equation
for the 26,300 km channel length run for a) above the ABL
and b) within the ABL.

unstable wavenumbers decrease as the resolution of the model was reduced. The modification of the growth rates has been shown to have a significant impact on the equipartition of wave enstrophy in the quasi-linear neutral state. A decrease in the resolution reduced the magnitude of the jump in the potential vorticity gradient at the jet. If the magnitude of the jump in the potential vorticity gradient was reduced so that the potential vorticity gradient was positive definite, the basic state was stablized. The critical zonal wind for instability has been shown to increase as the resolution was decreased. For values of the zonal wind less than the critical zonal wind, there was no normal mode growth.

The results of the barotropic study suggest that the three-dimensional problem will also be a function of the vertical resolution. In the three-dimensional baroclinic instability problem, as in the two-dimensional problem, the magnitude of the pv gradients that are responsible for destabilizing the baroclinic Rossby waves, are a function of resolution.

b. Previous studies of variable vertical resolution

Previous studies of the impact of variable vertical resolution on the boussinesq dynamics of a mid latitude β plane channel models have concluded that it is necessary to use at least 10 to 20 levels to resolve the eddy dynamics (Pavan 1996; Hua and Haidvogel 1986). Pavan (1996) also concluded that only three levels are necessary to reproduce the general features of the response. This is interesting in light of the results of the 2D barotropic jet. Even though the pv gradients at the surface of the 3D model are also a function of the vertical resolution, the equilibrated basic state and the eddy dynamics are not. This implies that the dynamics in the 3d problem are fundamentally different from the 2D problem. The model used by Pavan (1996) did not attempt to include thermal diffusion (which dominates the diabatic heating in the ABL), the feedbacks which maintain the static stability, or an adequate representation of a tropopause. These processes may cause the model to be more resolution dependent. In particular, including a tropopause may cause the dynamics to be sensitive to the resolution since increasing the resolution causes the pv gradients at the tropopause to become more concentrated.

5.2.1   33 level model runs

This Section discusses the results of the 33 level model runs. 33 levels is most highly resolved model run in this thesis. The pressure levels are equally spaced so that there is a constant difference of 31.25 mb between the pressure levels. Three runs will be discussed in this Section. These runs are the control run with doubled vertical resolution, the control run with doubled resolution but no stratosphere/tropopause , and the control run with doubled resolution and an interactive surface air temperature. The equation used to integrate a surface air temperature is described in Section 2.2.3.

Figures 5-4 and 5-5 show the pv gradients, in and above the ABL respectively, for the three 33 level runs. Comparing the +'s with the o's shows that the pv gradients with and without a stratosphere/tropopause are very similar below 700 mb. Above 700 mb, it is seen that the runs with and without an interactive surface temperature are very similar. This is seen to be true for both the vertical and meridional temperature structure (Figure not shown). That is, in both the vertical and the meridional temperature structure, the runs with and without the stratosphere/tropopause have the same structure below 800 mb while the runs with and without the interactive surface temperature have the same structure between 300-800 mb.

A comparison of the meridional eddy heat fluxes for the three runs (Figure 5-6) shows that the eddy fluxes at the center of the channel differ even though the temperature structure is the same. This figure is a little deceiving because even though the eddy heat fluxes for the run without a stratosphere/tropopause are 20% smaller than the run with a stratosphere/tropopause, the convergence of these fluxes are actually larger than the run with a stratosphere/tropopause. This is because the eddy heat flux maximum is more concentrated meridionally without a stratosphere/tropopause. The mean vertical wind is also larger without a stratosphere/tropopause (Figure not shown). These results imply that even though the temperature structure of the ABL in the equilibrated state is independent of whether or not there is a stratosphere/tropopause. the structure of the eddies which maintain the equilibrated state is not. This may have a significant impact on the response to changes in forcing. These issues will be discussed further in a separate Section.

5.2.2   Comparison between 33, 17 and 9 level runs

Figures 5-7 and 5-8 show a comparison of the equilibrated meridional temperature gradients and static stability, respectively, of the 33, 17 and 9 level runs without an interactive surface and with an equivalent representation of a stratosphere/tropopause. These figures show that the strong thermal damping in the ABL prevents the eddies from reducing the radiative-convective equilibrium temperature gradients, and increasing the well-mixed static stability, at the first model level. Since the first model level is raised as the resolution is decreased, both the vertical and horizontal temperature structure is a function of the vertical resolution. These figures also show that the equilibrated temperature structure of the 33 level model above the ABL is approximated well by the 17 level model. Within the ABL, the 17 level model has larger meridional temperature gradients and smaller static stability, but since the focus of this thesis is on the dynamics above the ABL, the 17 level model is considered to have adequate vertical resolution to resolve the vertical structure of the equilibrated state. The dependence of the pv gradients, within and above the ABL, on the vertical resolution is seen in Figures 5-9 and 5-10, respectively. These figures show that the pv gradients of
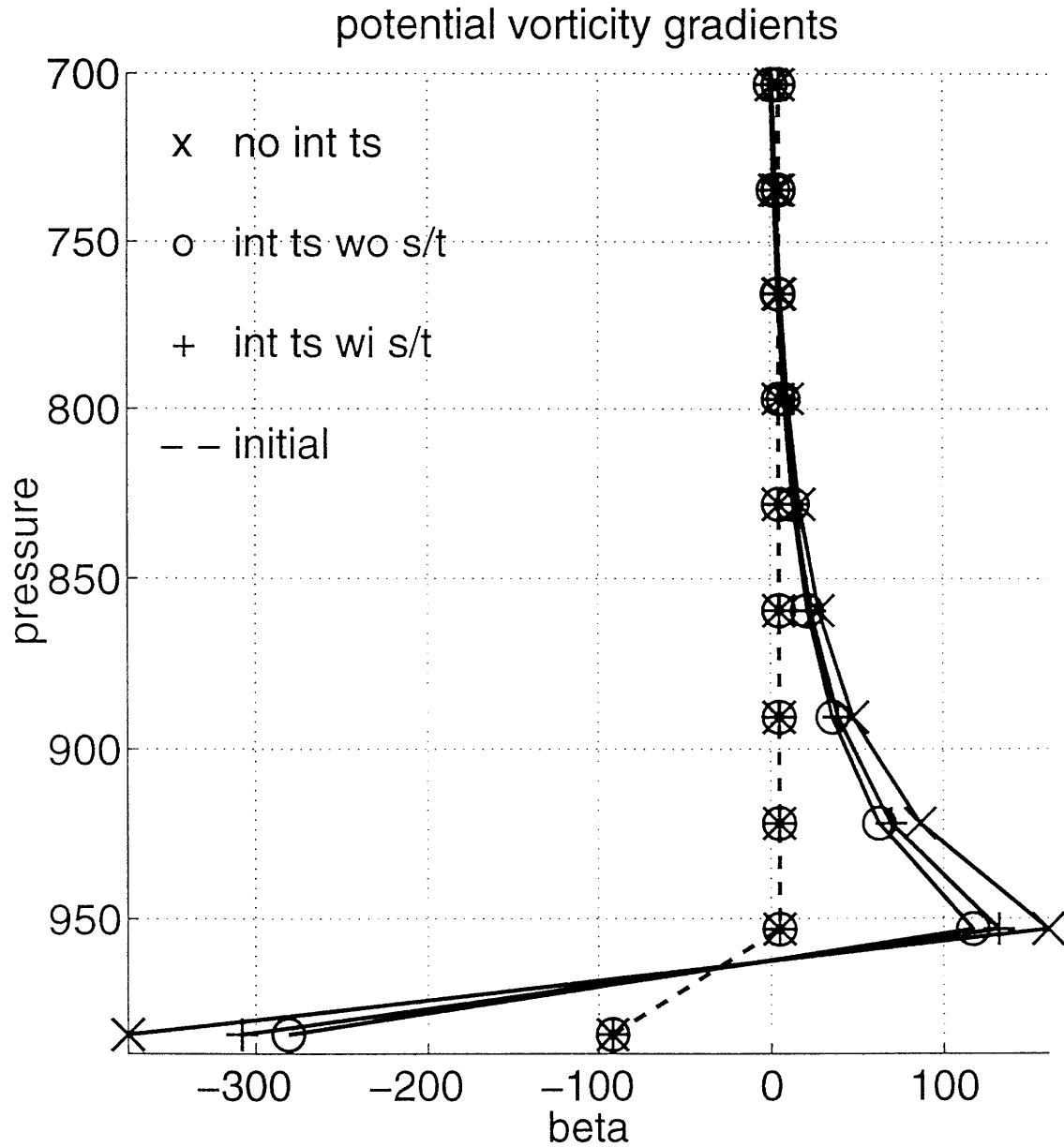
Figure 5-4: Comparison of the pv gradients in the ABL for
the 33 level runs, in units of β. x's designate the control
run (with a stratosphere/tropopause and without an inter-
active surface air temperature), o's designate the control run
without a stratosphere/tropopause and with an interactive
surface air temperature, +'s designate the control run with
an interactive surface air temperature.

potential vorticity gradients
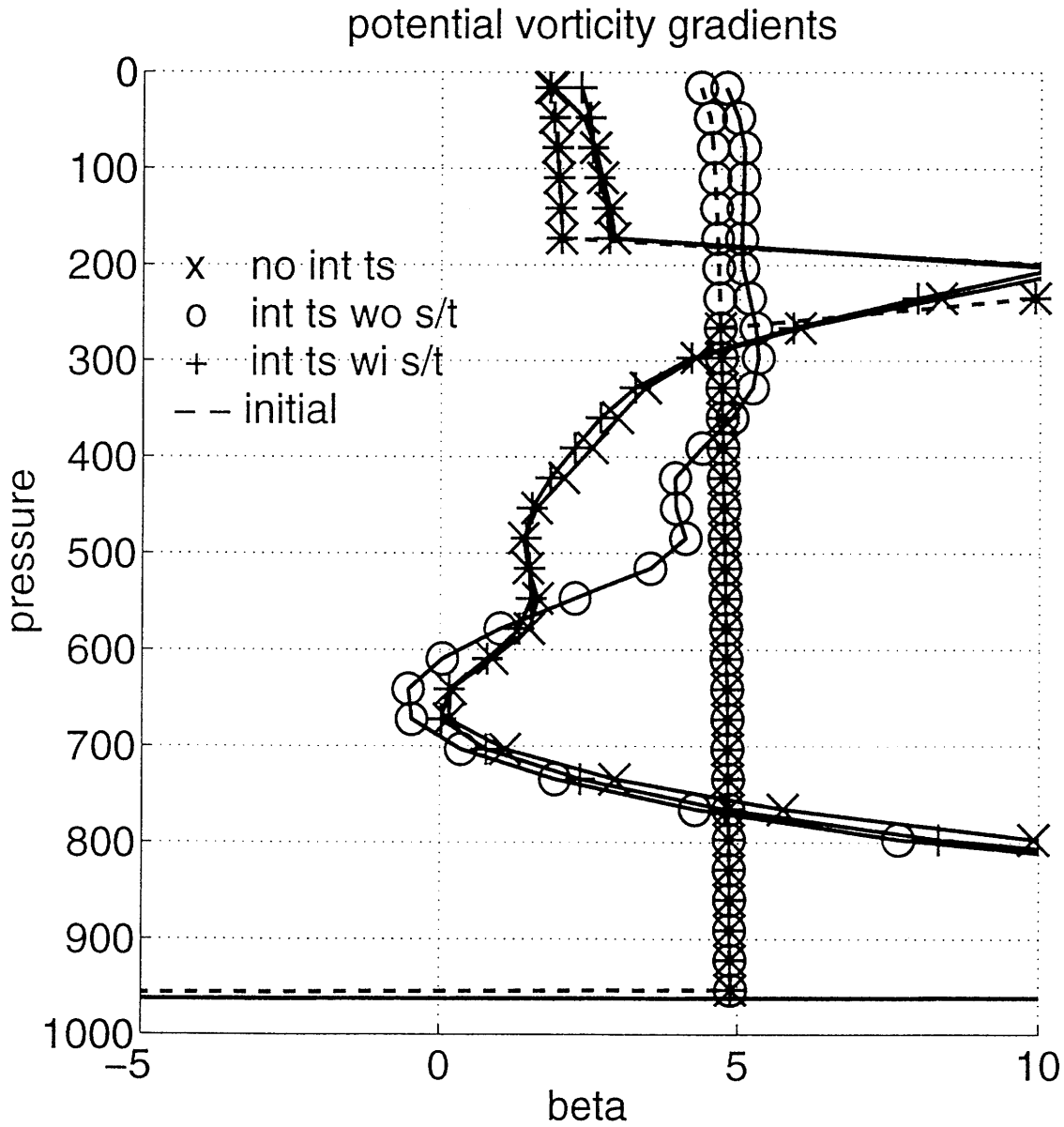
Figure 5-5: Comparison of the pv gradients above the ABL
for the 33 level runs, in units of β. x's designate the control
run (with a stratosphere/tropopause and without an inter-
active surface air temperature), o's designate the control run
without a stratosphere/tropopause and with an interactive
surface air temperature, +'s designate the control run with
an interactive surface air temperature.
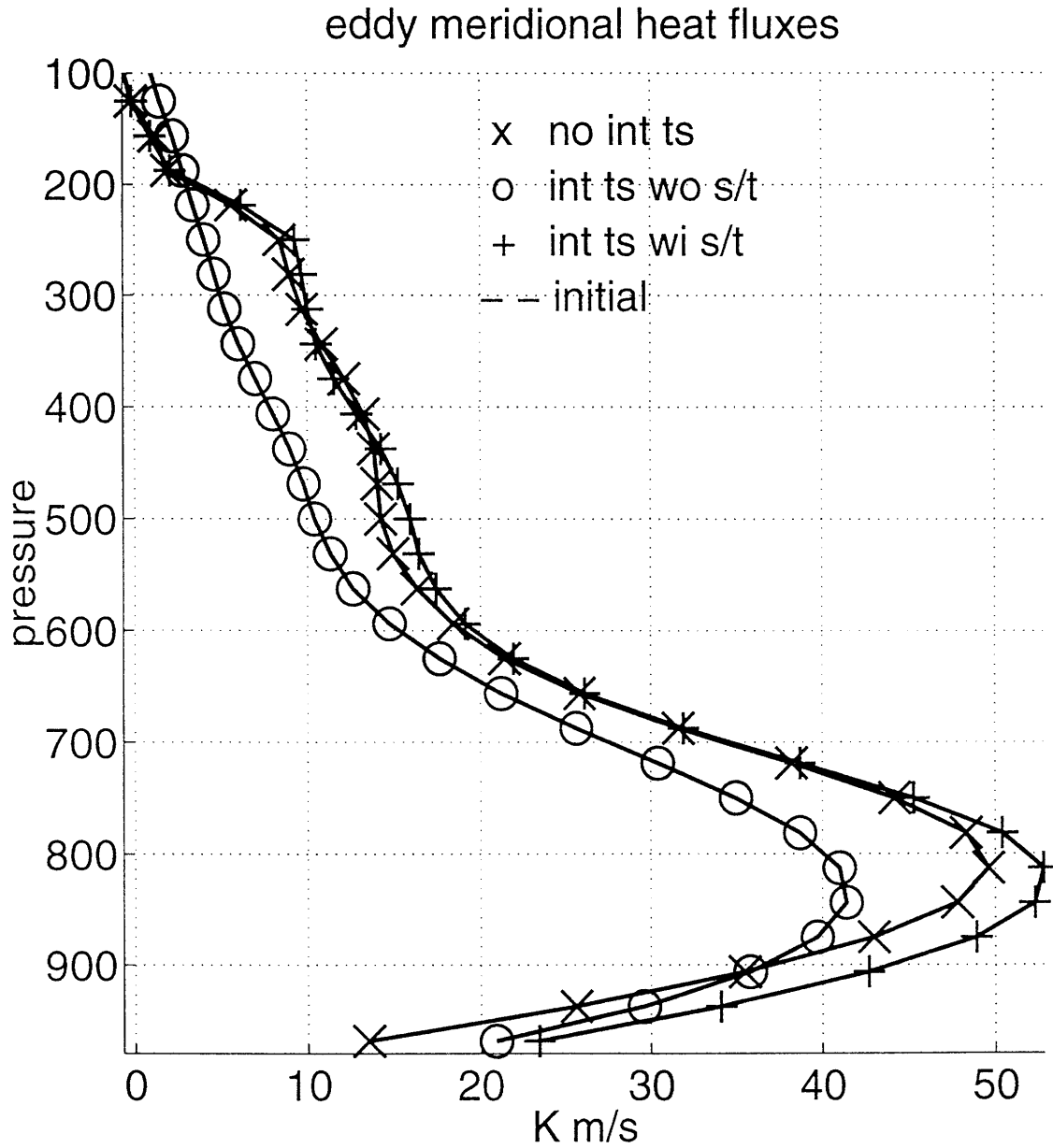
Figure 5-6: Comparison of the meridional eddy heat fluxes for the 33 level runs. x's designate the control run (with a stratosphere/tropopause and without an interactive surface air temperature), o's designate the control run without a stratosphere/tropopause and with an interactive surface air temperature, +'s designate the control run with an interactive surface air temperature.

the 33 level model are closely approximated by the 17 level model, except in the ABL where the gradients increase as the resolution is decreased.

Figures 5-11 and 5-12 show the comparison of the pv gradients, within and above the ABL respectively, of the 33, 17 and 9 level runs with an interactive surface and an equivalent representation of a stratosphere/tropopause. These figures show that when the surface temperature is interactive the pv gradients within the ABL are independent of the vertical resolution, even though the 9 level model can not resolve the large pv gradients at the second model level. Above the ABL, the pv gradients are also less dependent on the vertical resolution. Above 300 mb the pv gradients are relatively unchanged from the radiative equilibrium values. This means that the pv gradients at the tropopause increase, and become more concentrated in the vertical, when the resolution is increased. It is interesting to note that the pv gradients in the ABL are relatively insensitive to the increase in the magnitude of the pv gradients at the tropopause.

5.2.3   Sensitivity to a reduction in vertical resolution

Figures 5-13 and 5-14 display the pv gradients for the control run without a stratosphere for 3,5,9 and 17 evenly spaced pressure levels in and above the ABL, respectively. The dashed lines in the figures are the radiative equilibrium pv gradients. The dashed lines show that the magnitude of the negative pv gradients at the lowest level increases with an increase in the vertical resolution. In the symmetric state, where downgradient fluxes of heat by turbulent eddies balances the diabatic heating, the pv gradients in the ABL are larger than the pv gradients in radiative equilibrium (Figure not shown). In the ABL (Figure 5-13), the equilibrated pv gradients are larger than the RCE pv gradients. As the resolution is decreased from 17 levels, the equilibrated pv gradients differ less and less from the RCE gradients. Above the ABL (Figure 5-14), the degree of homogenization is clearly dependent on the vertical resolution of the run. The 17 level pv at 650 mb has been completely homogenized. The minimum pv gradients in the 9 level run above the ABL are approximately equal to 2.5β. The 5 level pv gradients are actually larger than the RCE pv gradients. The 3 level pv gradients above the ABL are essentially unchanged from the RCE pv gradients.

Figure 5-15 shows the meridional temperature gradients of the radiative equilibrium and equilibrated states. The dashed lines are for the radiative equilibrium states and the solid lines are for the equilibrated states. The equilibrated temperature gradients of the 9 level run have been reduced relative to radiative equilibrium , but not to the extent of the 17 level run. The lowest levels in both runs are relatively unchanged from the radiative equilibrium value. The equilibrated temperature gradients of the 5 and 3 level runs are relatively unchanged from the radiative equilibrium values. Therefore, the large equilibrated pv gradients in the 5 level model are due to changes in the static stability in the ABL, due to the ABL physics, and not to changes in the meridional temperature gradients.
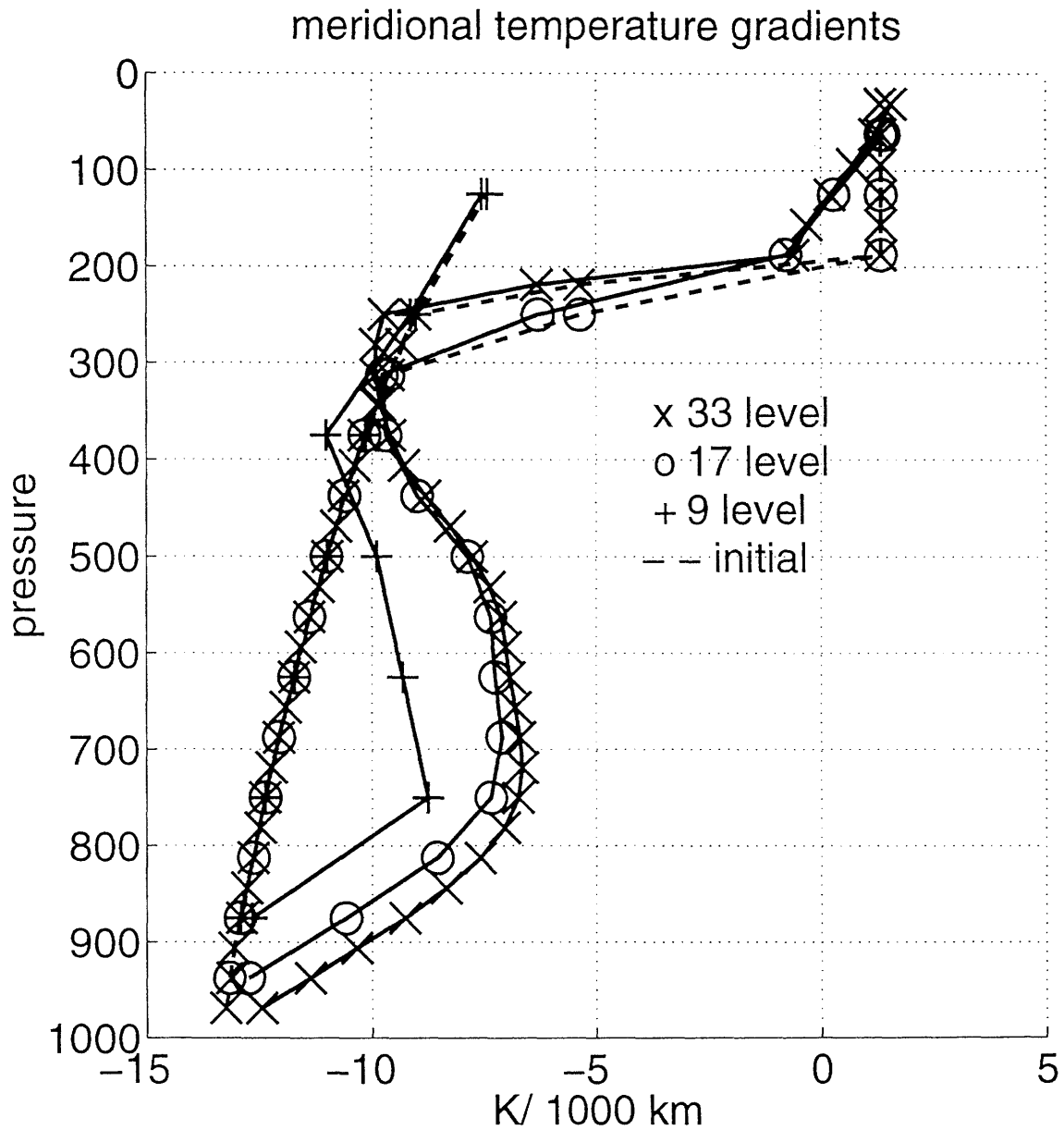
Figure 5-7: Comparison of the meridional temperature gradients at the center of the channel for the 33, 17 and 9 level runs without an interactive surface and an equivalent representation of a stratosphere/tropopause.
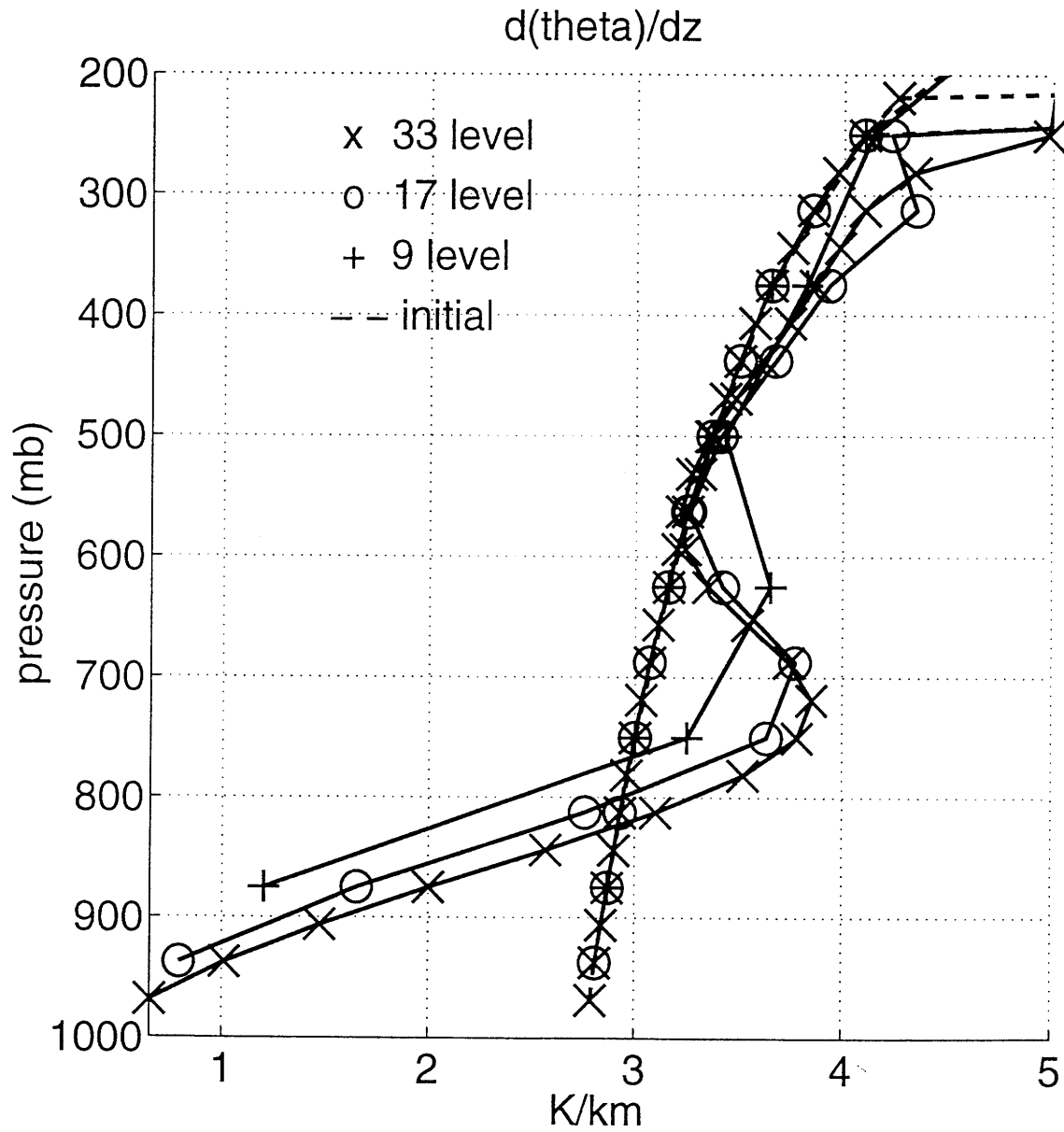
Figure 5-8: Comparison of the static stability for the 33,
17 and 9 level runs without an interactive surface and an
equivalent representation of a stratosphere/tropopause.
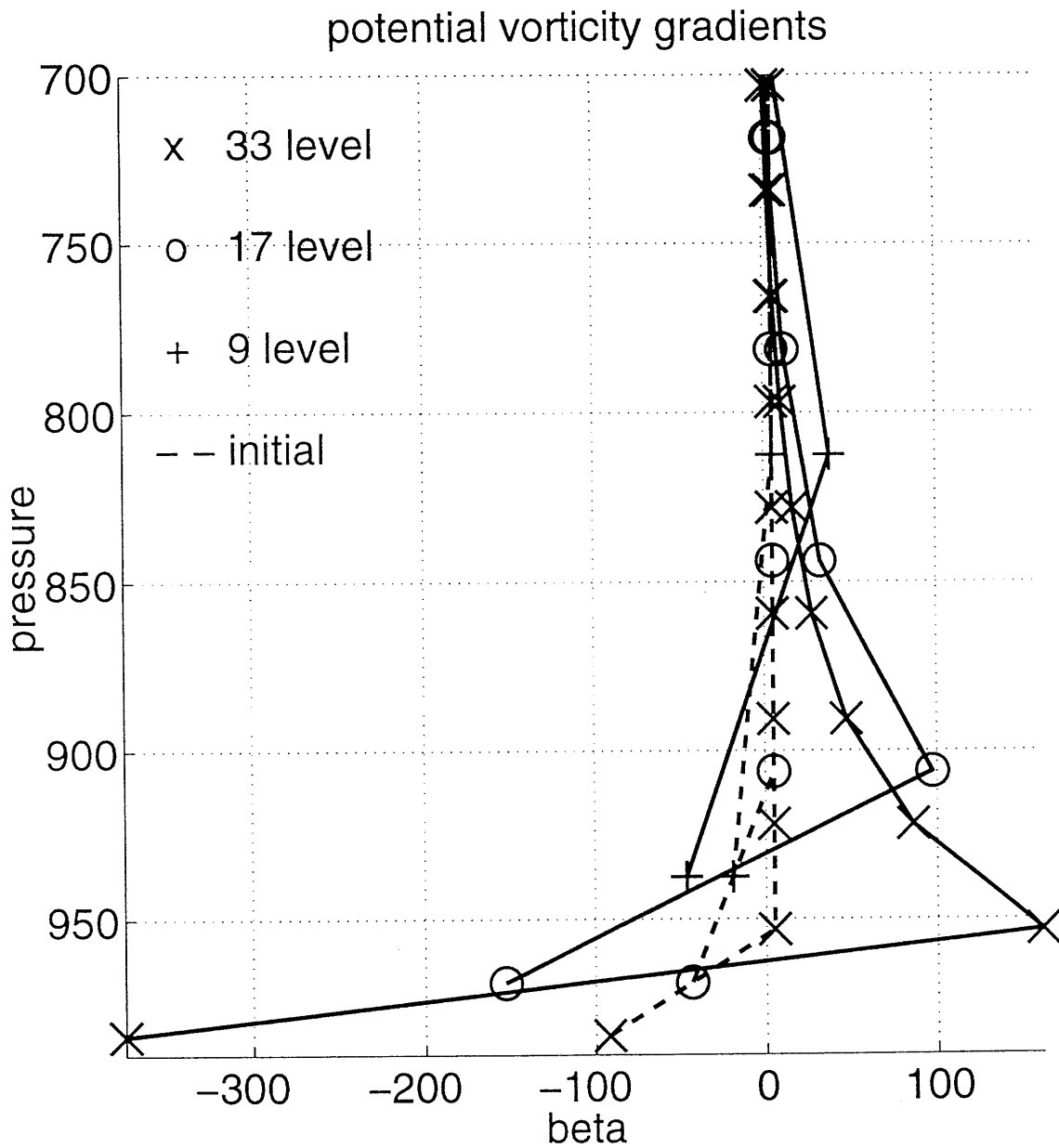
Figure 5-9: Comparison of the pv gradients in the ABL at the center of the channel for the 33, 17 and 9 level runs without an interactive surface and an equivalent representation of a stratosphere/tropopause, in units of β.
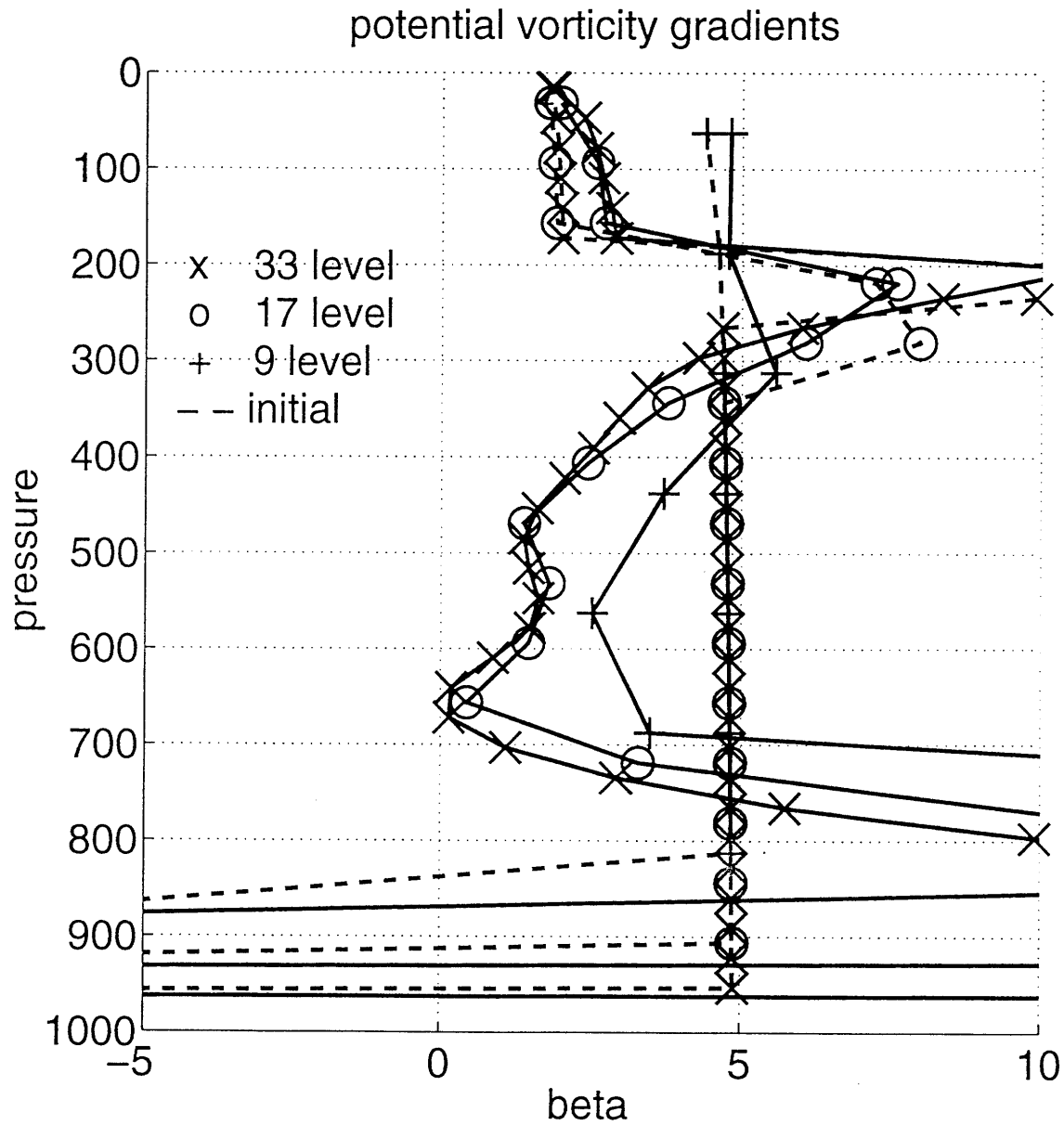
Figure 5-10: Comparison of the pv gradients above the ABL at the center of the channel for the 33, 17 and 9 level runs without an interactive surface and an equivalent representation of a stratosphere/tropopause, in units of β.

potential vorticity gradients
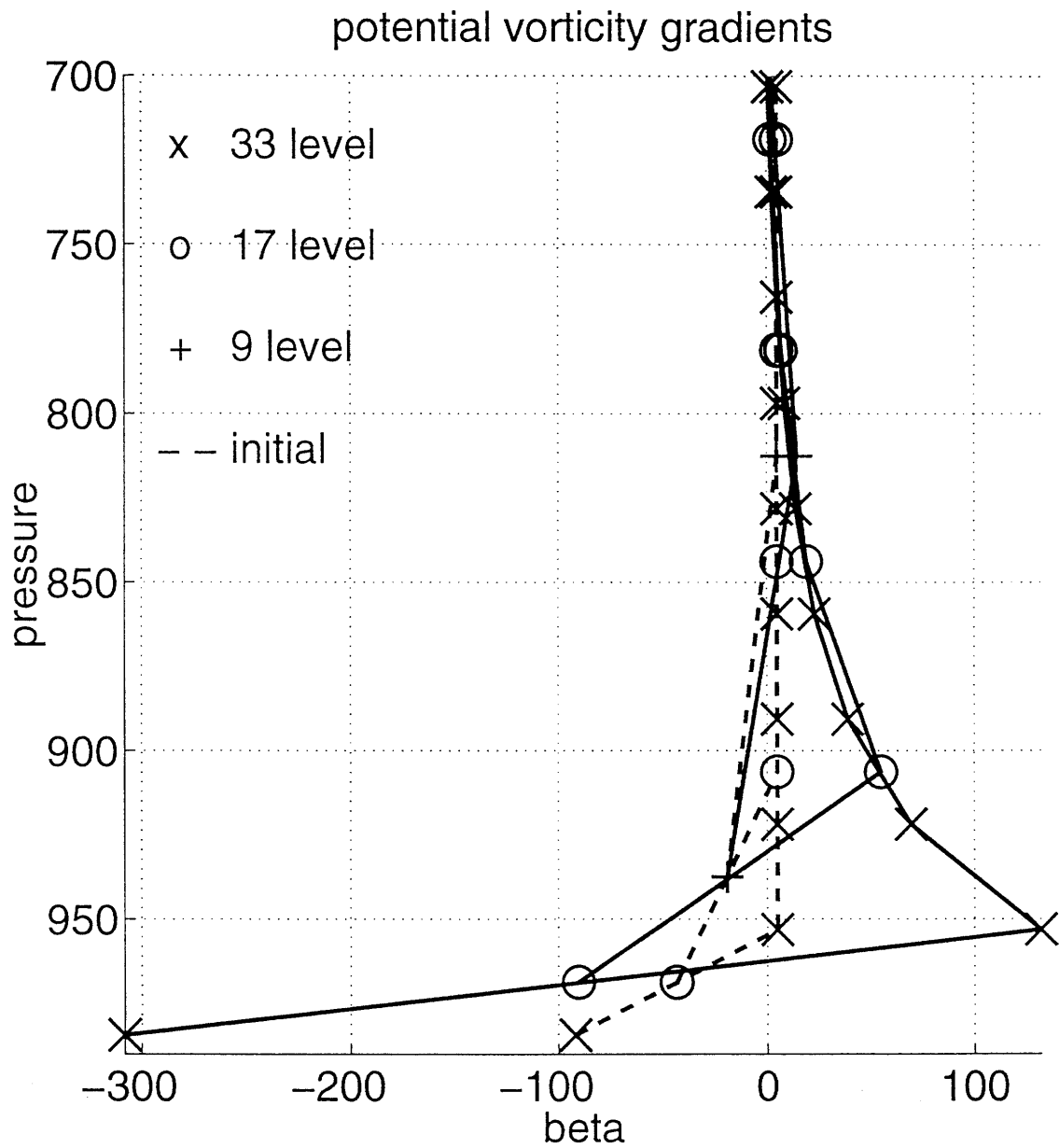
Figure 5-11: Comparison of the pv gradients in the ABL for the 33, 17 and 9 level runs with an interactive surface and an equivalent representation of a stratosphere/tropopause, in units of β.
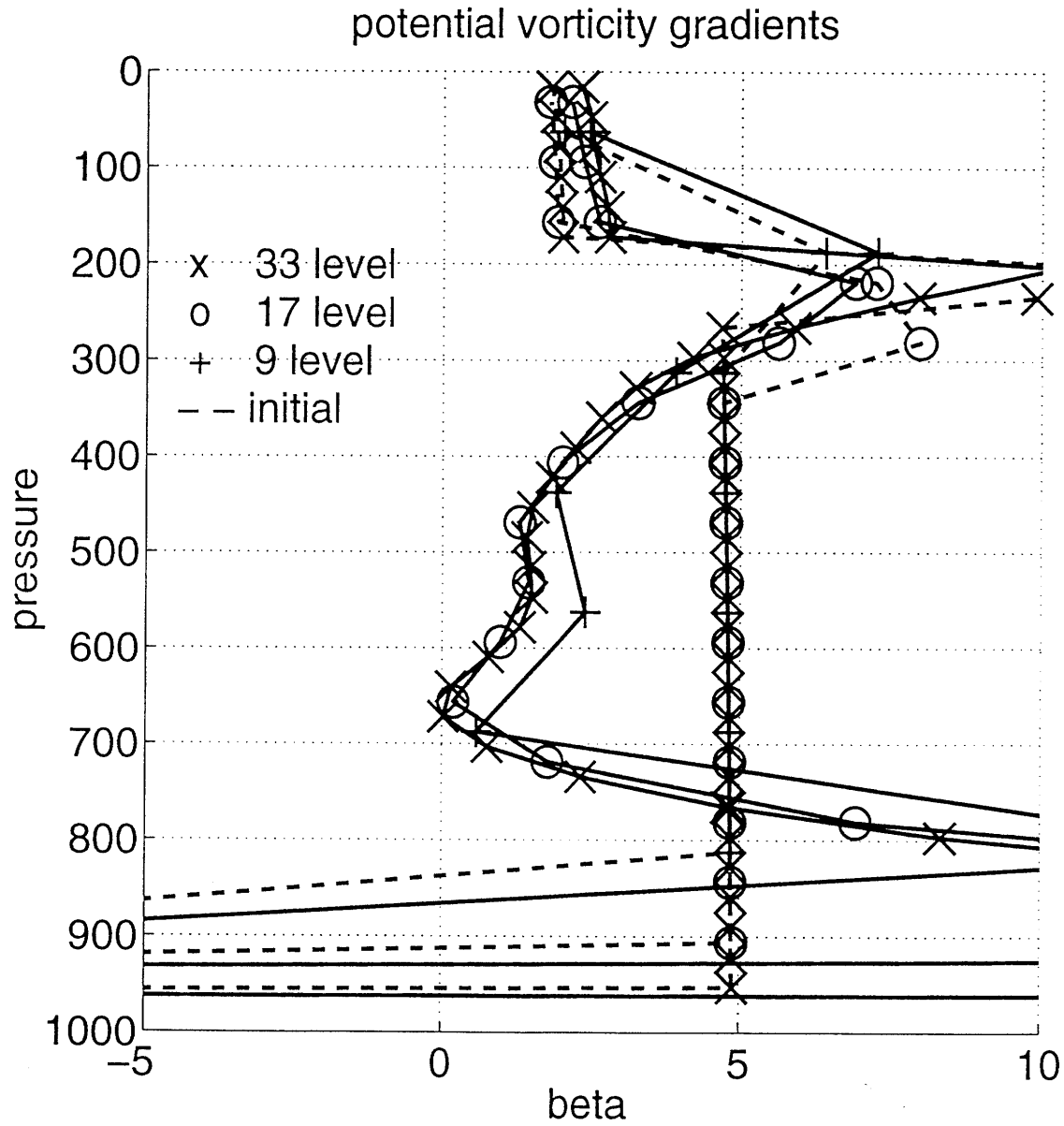
Figure 5-12: Comparison of the pv gradients above the ABL
for the 33, 17 and 9 level runs with an interactive surface and
an equivalent representation of a stratosphere/tropopause, in
units of β.

Figure 5-16 shows the dependence of the meridional eddy heat fluxes on the vertical resolution. This figure shows that the reduction in the meridional eddy heat flux is primarily in the lower troposphere. When the resolution is reduced from 17 levels to 9 levels the peak meridional eddy heat flux is reduced from 35 K m/s to 25 K m/s. The vertically averaged potential temperature flux is reduced from 14.4 K m/s to 9.6 K m/S. The 5 and 3 levels models have no large scale meridional eddy heat fluxes. The decrease in resolution causes the 5 and 3 level models to be stable to large scale waves.

Previous studies of the impact of vertical resolution on the eddy dynamics (Pavan 1996; Hua and Haidvogel 1986) did not find the stabilization of the eddies as the resolution was decreased. This is because these previous studies represented the boundary layer with Ekman pumping at the lower boundary instead of explicitly resolving the diffusion of heat and momentum at the lowest levels as a coarse representation of an ABL. In this model study, the thermal diffusion dominates over the diffusion of momentum and has a diabatic heating timescale of approximately 1 day and becomes stronger at lower resolution because the diffusive flux penetrates to a higher level.

The extreme impact of the vertical resolution on the stability of the run is due to the formulation of the thermal diffusion in the ABL. The surface drag is held fixed and is independent of the vertical resolution of the run. The potential temperature at the surface is assumed to be equal to the potential temperature at the first model level. Therefore, as the resolution is decreased, the surface temperature is calculated from model levels that are increasingly far from the surface. In the 5 level run the surface temperature is calculated from the 750 mb level, which is typically above the ABL in observations.
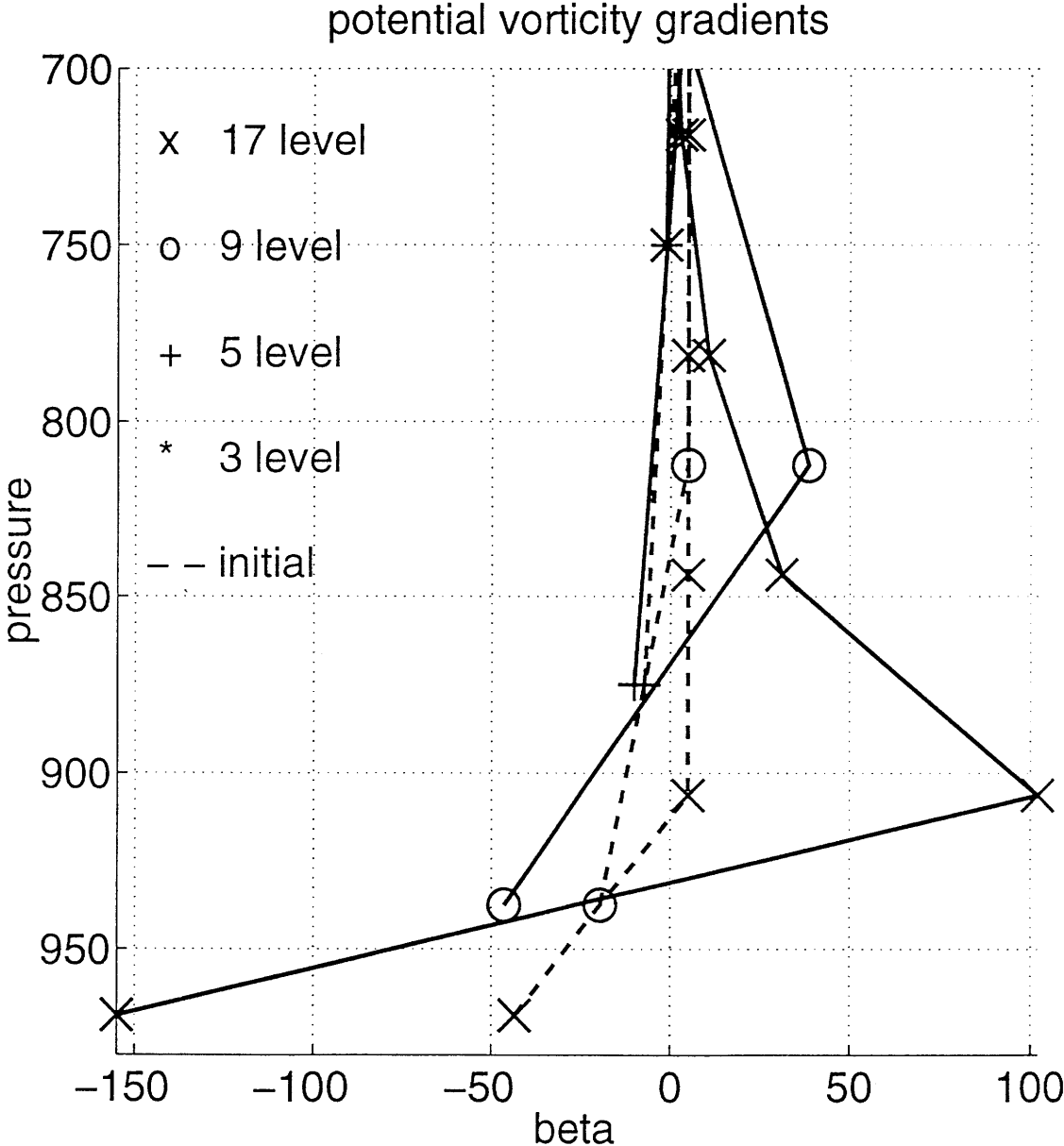
Figure 5-13: Equilibrated pv gradients in the ABL for the control run without a stratosphere for 3,5,9 and 17 evenly spaced pressure levels, in units of β.

potential vorticity gradients
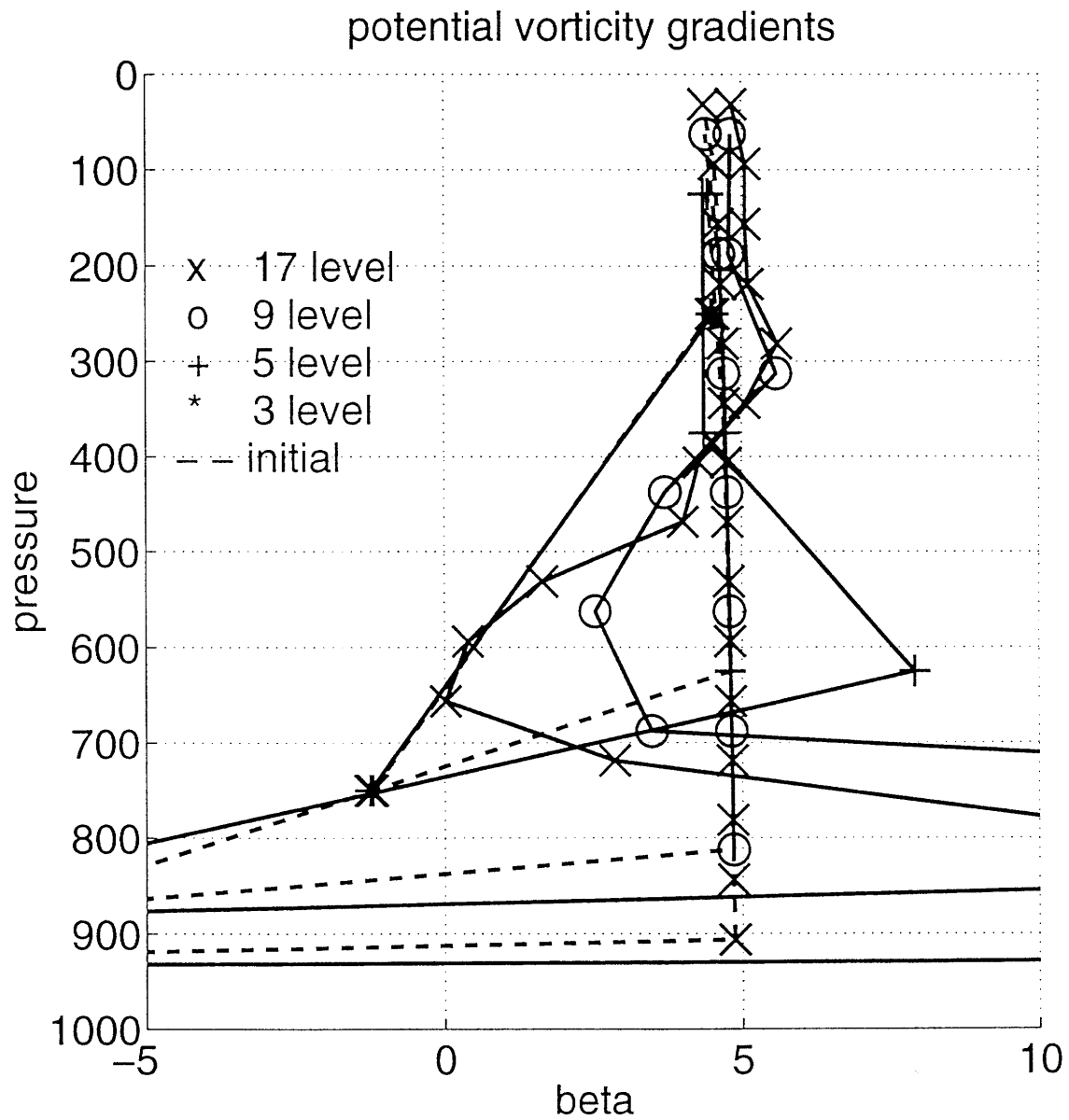
Figure 5-14: Equilibrated pv gradients above the ABL for
the control run without a stratosphere for 3,5,9 and 17 evenly
spaced pressure levels, in units of β.

meridional temperature gradients
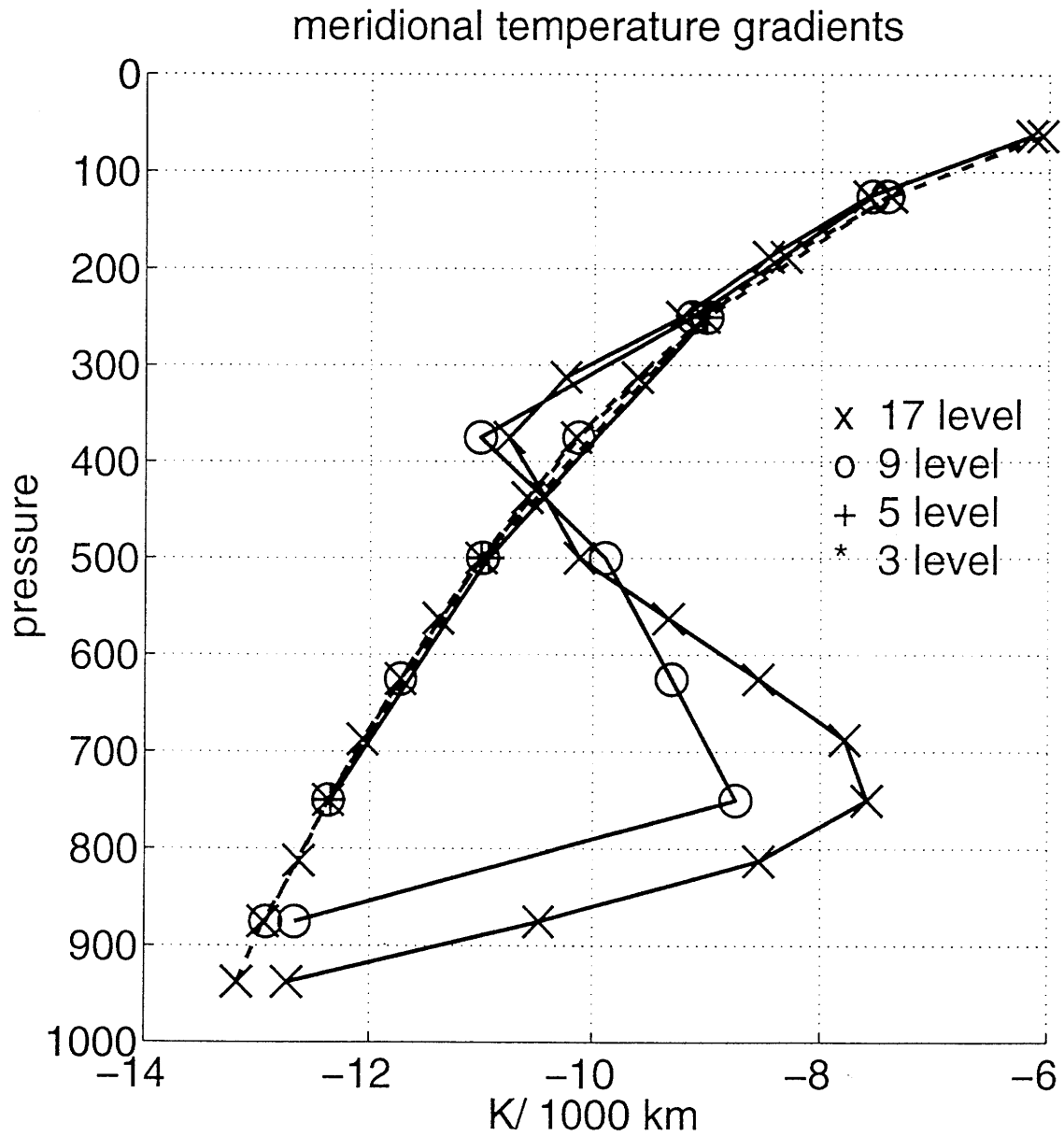
Figure 5-15: Equilibrated temperature gradients for the control run without a stratosphere for 3,5,9 and 17 evenly spaced pressure levels

meridional eddy heat fluxes
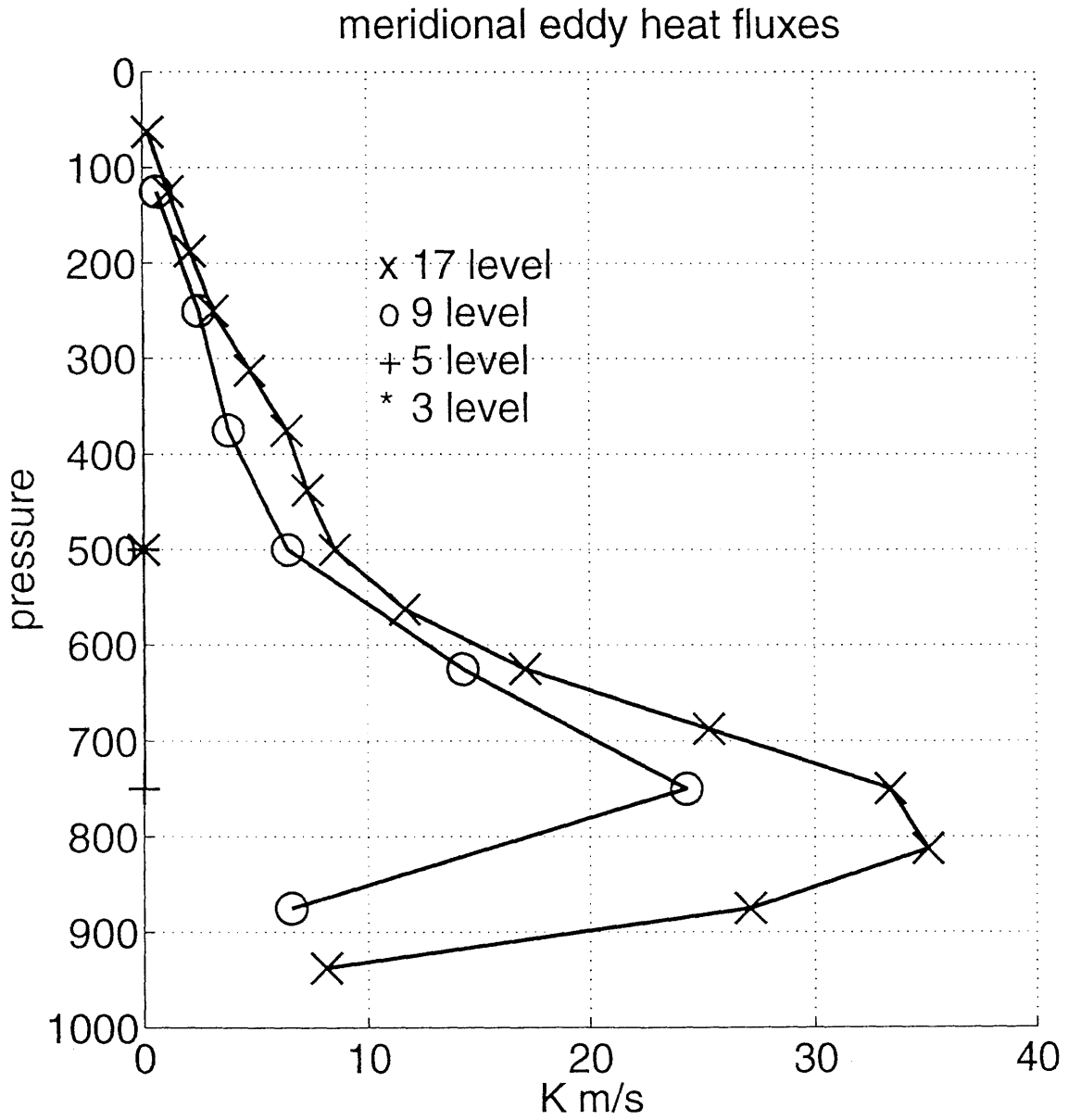
Figure 5-16: Meridional eddy heat fluxes for the control run
without a stratosphere for 3,5,9 and 17 evenly spaced pressure
levels

5.2.4 Sensitivity to vertical resolution with an interactive surface

Figure 5-18 and Figure 5-17 show the pv gradients for the control run without a stratosphere for 3,5,9 and 17 evenly spaced pressure levels. The magnitude of the pv gradients in the ABL are very large so Figure 5-17 displays the pv gradients in the free troposphere, which are of the order of β. Figure 5-17 displays the pv gradients in the ABL, which are in the range of 10-150 β. Figure 5-17 shows that the 9-level gradients coarsely resolve the 17-level pv gradients in the ABL, although there are features, like the peak in the static stability at 900 mb, that the 9 level model cannot resolve. The dashed lines in Figure 5-17 show that the pv gradients in radiative equilibrium are a function of the vertical resolution. The higher the resolution of the run, the larger the ABL pv gradients in radiative equilibrium. The equilibrated ABL gradients are also a function of the vertical resolution. The higher resolution runs have larger pv gradients in the ABL.

Above the ABL, the homogenization of the pv of the control run is resolved by the 9-level model when the surface temperature is allowed to vary. This is interesting considering that the surface temperature gradients at the center of the channel only decrease by 4% (figure not shown). The only way that the surface temperature influences the dynamics in this model is in the turbulent flux of heat into the first model level. Therefore, the way in which the turbulent fluxes are parameterized has a large impact on the equilibrated basic state and the eddy fluxes throughout the troposphere of the model.

Figure 5-19 shows the meridional temperature gradients for the control run without a stratosphere for 3,5,9, and 17-level evenly spaced pressure levels. It is seen that the 9-level model accurately resolves the temperature gradients of the control run when the surface temperature is allowed to be interactive.

Figure 5-20 shows the zonal mean static stability for the control run without a stratosphere for 3,5,9, and 17-level evenly spaced pressure levels. The equilibrated zonal mean static stability in the 9 and 17-level runs are very similar when the surface is allowed to be interactive.

The 3 and 5 level runs are unstable when the surface air temperature is allowed to be interactive. With an interactive surface temperature, the eddy fluxes of the 3 and 5 level runs closely approximate the fluxes of the higher resolution runs. Figure 5-21 shows the meridional eddy heat fluxes for the different resolutions. The numbers in the legend are the vertically averaged potential temperature flux for each resolution. This figure demonstrates how the fluxes are independent to the vertical resolution. The vertically averaged potential temperature flux shows that even though the ABL is not resolved in the 3 and 5 level runs, the vertically averaged energy transport by the eddies is robust. The same results are seen in Figures 5-23 and 5-22 which show the vertical eddy heat fluxes and the eddy momentum fluxes for the different resolutions.

The 5 and 3 level runs have inadequate resolution to resolve the large negative gradients at the first model level and the large positive gradients at the second model level. The 5 and 3 level gradients do not have these features because these runs do not have any levels in the boundary layer so the feedbacks between the vertical eddy heat fluxes and the diabatic heating in the ABL are not resolved. The 5 and 3 level runs do not resolve the vertical flux of heat out of the boundary layer which reduces the static stability below 800 mb and increases the static stability between 600-800 mb (Figure 5-20). The static stability of the 3 and 5 level runs is relatively unchanged from the initial radiative equilibrium value, but larger than the static stability in the symmetric state. The vertical fluxes of heat are responsible for bringing the static stability close to the radiative equilibrium values, but the values are still much smaller than the higher resolution runs. Just above the ABL, the meridional temperature gradients are reduced more in the 5-level run than in the higher resolution runs (Figure 5-19). Therefore, the homogenized pv above the ABL is resolved by the 5-level run even though the increased static stability is not.

The 3-level run has only one level at which the temperature gradients are defined. The adjustment to these temperature gradients is seen to be greater than that of the higher resolution runs. The large adjustment to the meridional temperature gradients in the lower troposphere can not be resolved by the 3-level run. The dashed line with the ×'s shows that the 3-level radiative equilibrium pv gradients have been almost eliminated because of the coarse resolution. The 3-level equilibrated pv gradients are seen to be very close to these radiative equilibrium values. Even though the 3-level run has significantly reduced equilibrated meridional temperature gradients, the adjustment to the pv gradients is very slight. The eddy fluxes from the 3-level run are seen to coarsely resolve the eddy fluxes of the higher resolution runs, but it is difficult to compare the adjustment to the mean climate, since the 3-level run not only fails to resolve the dynamics in the ABL but the homogenization of the pv above the ABL as well.

The results for the 3-level run are consistent with the study of Held (1978a), which investigated the response of the static stability to changes in the solar constant in a two-level primitive equation atmospheric model. The magnitude of the vertical eddy flux of potential temperature, divided by the 500 mb pressure difference between the levels, is approximately 0.1 K/day. This flux of potential temperature from the lower half of the model into the upper half of the model causes the static stability to increase. This heating is balanced in equilibrium by thermal diffusion. This thermal diffusion is dominated by the flux of heat out of the ocean into the first model level which causes the static stability to decrease. The equilibrated static stability is slightly larger than the initial radiative equilibrium value. The radiative heating is insignificant in the balance of terms in the static stability tendency equation.
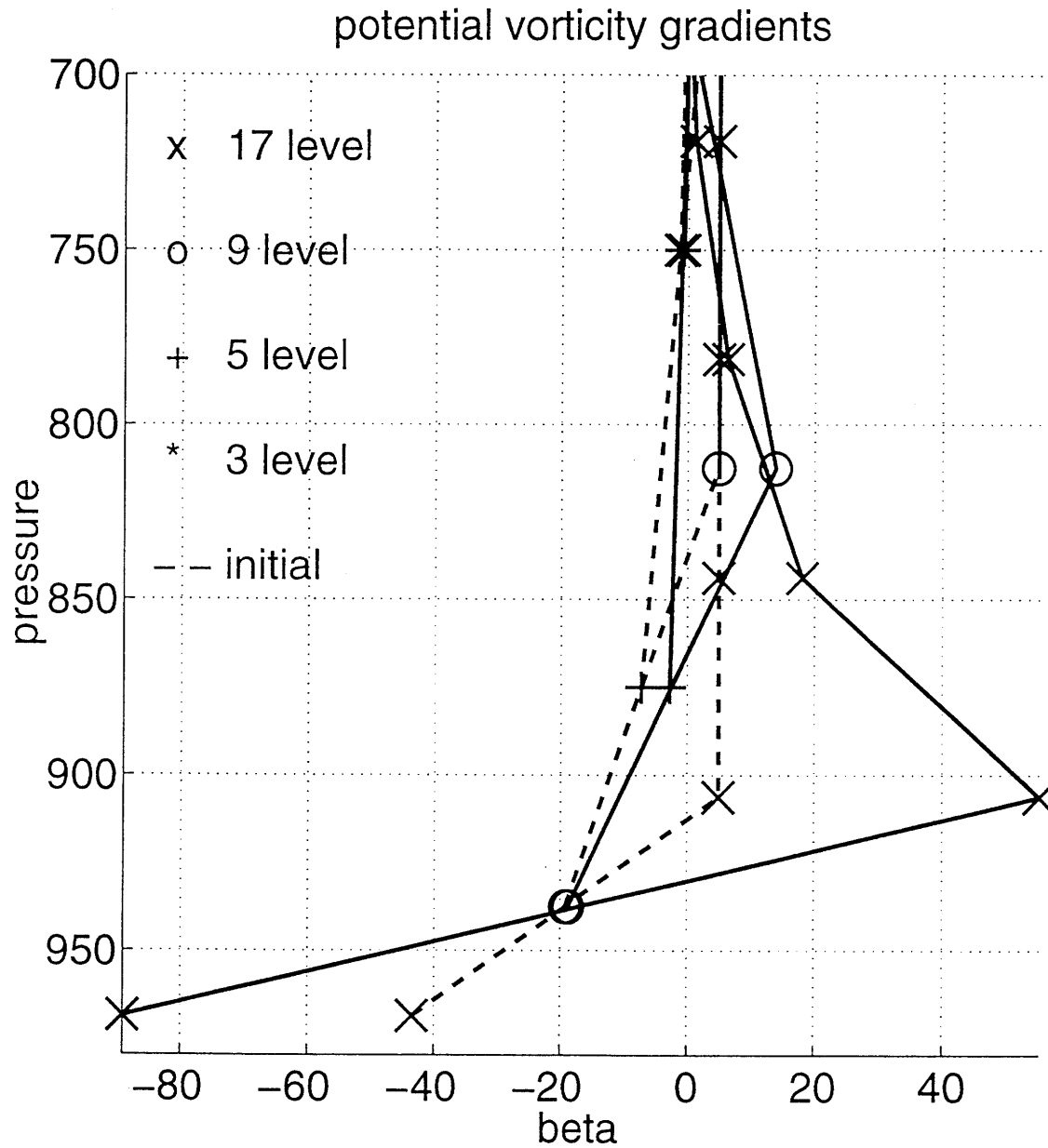
Figure 5-17: Zonal mean meridional pv gradients in the ABL with an interactive surface without a stratosphere for 3,5,9 and 17 evenly spaced pressure levels.
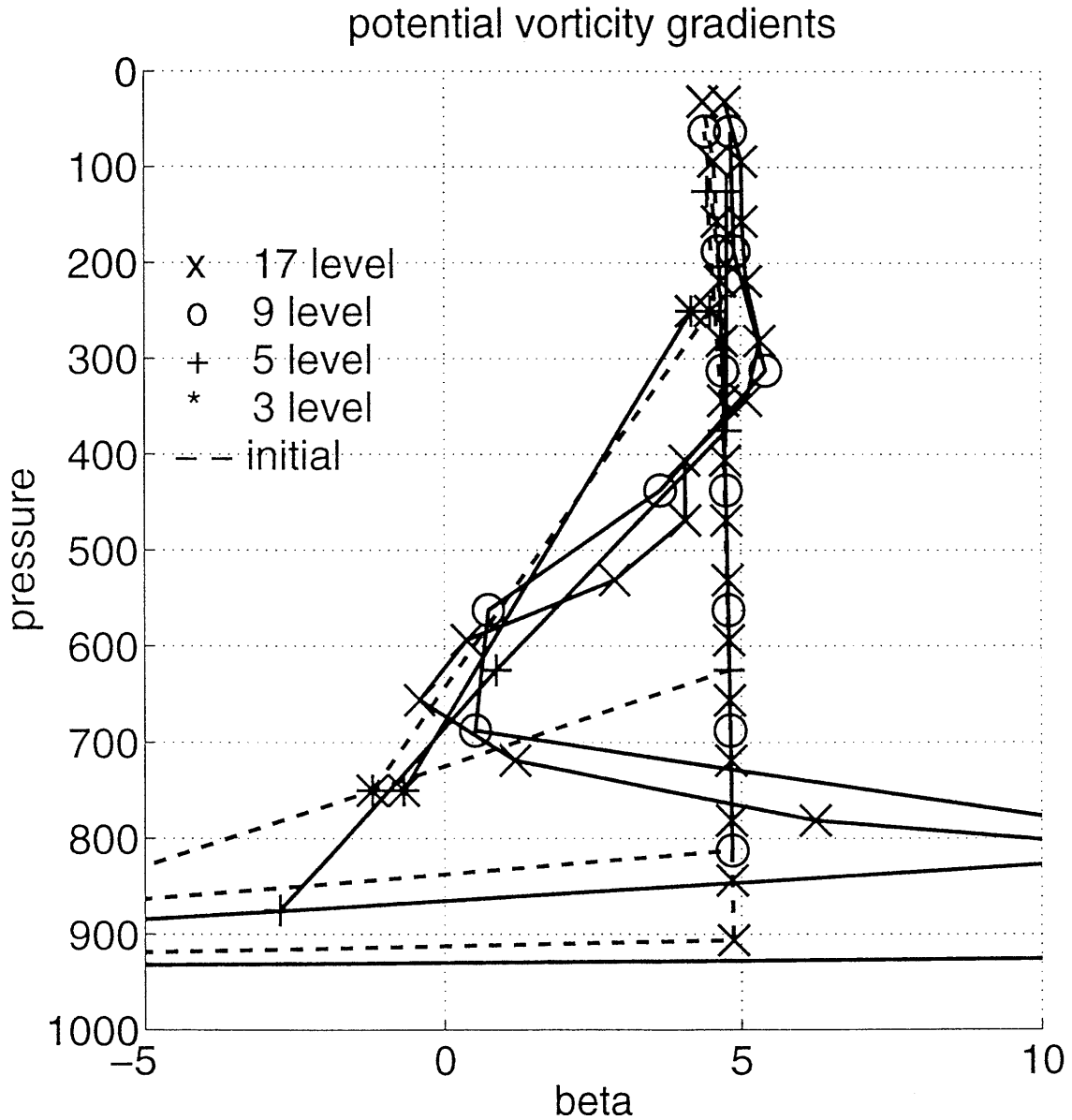
Figure 5-18: Zonal mean meridional pv gradients above the ABL with an interactive surface without a stratosphere for 3,5,9 and 17 evenly spaced pressure levels, in units of β.
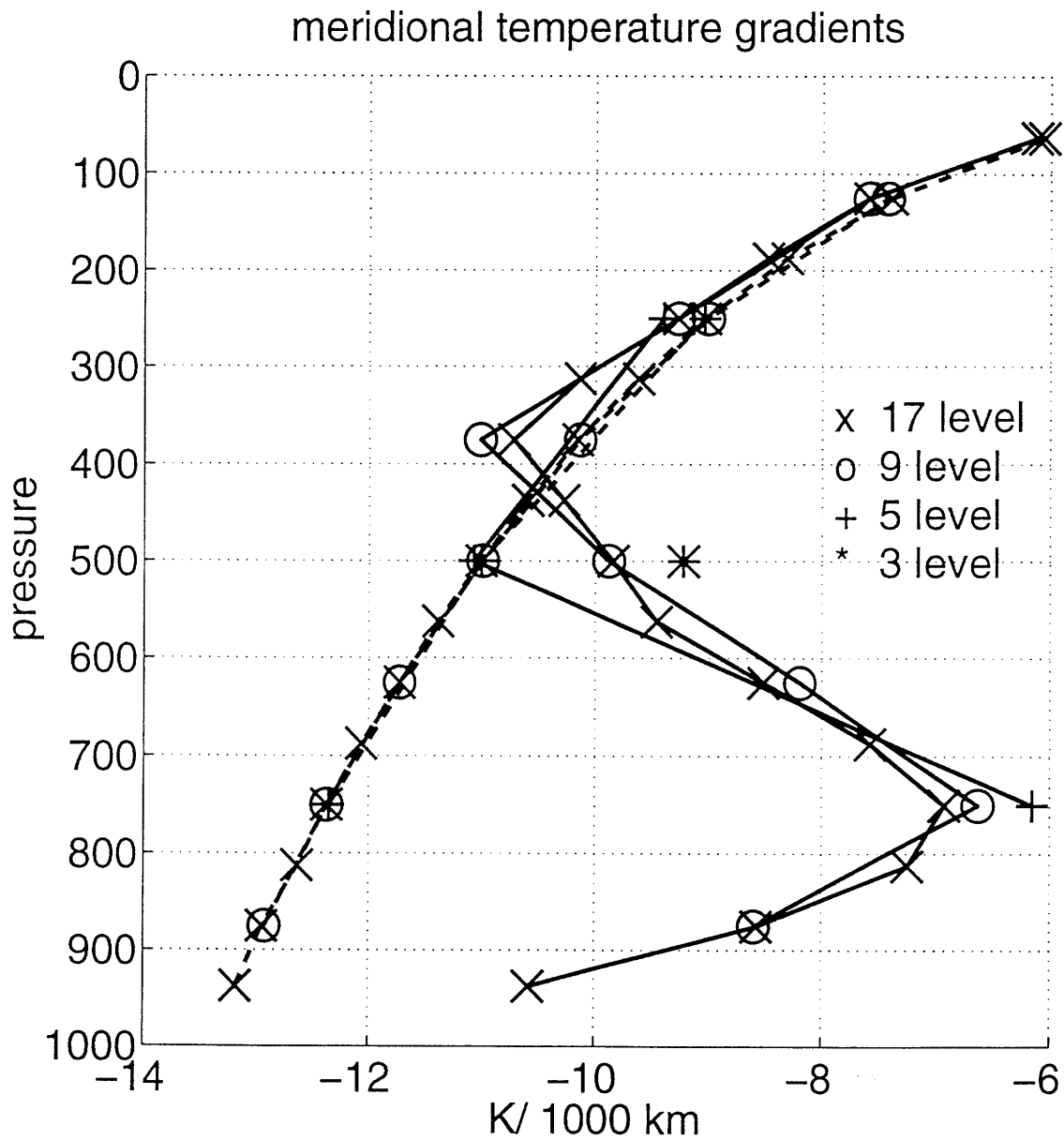
Figure 5-19: Zonal mean meridional temperature gradients
with an interactive surface without a stratosphere for 3,5,9
and 17 evenly spaced pressure levels.
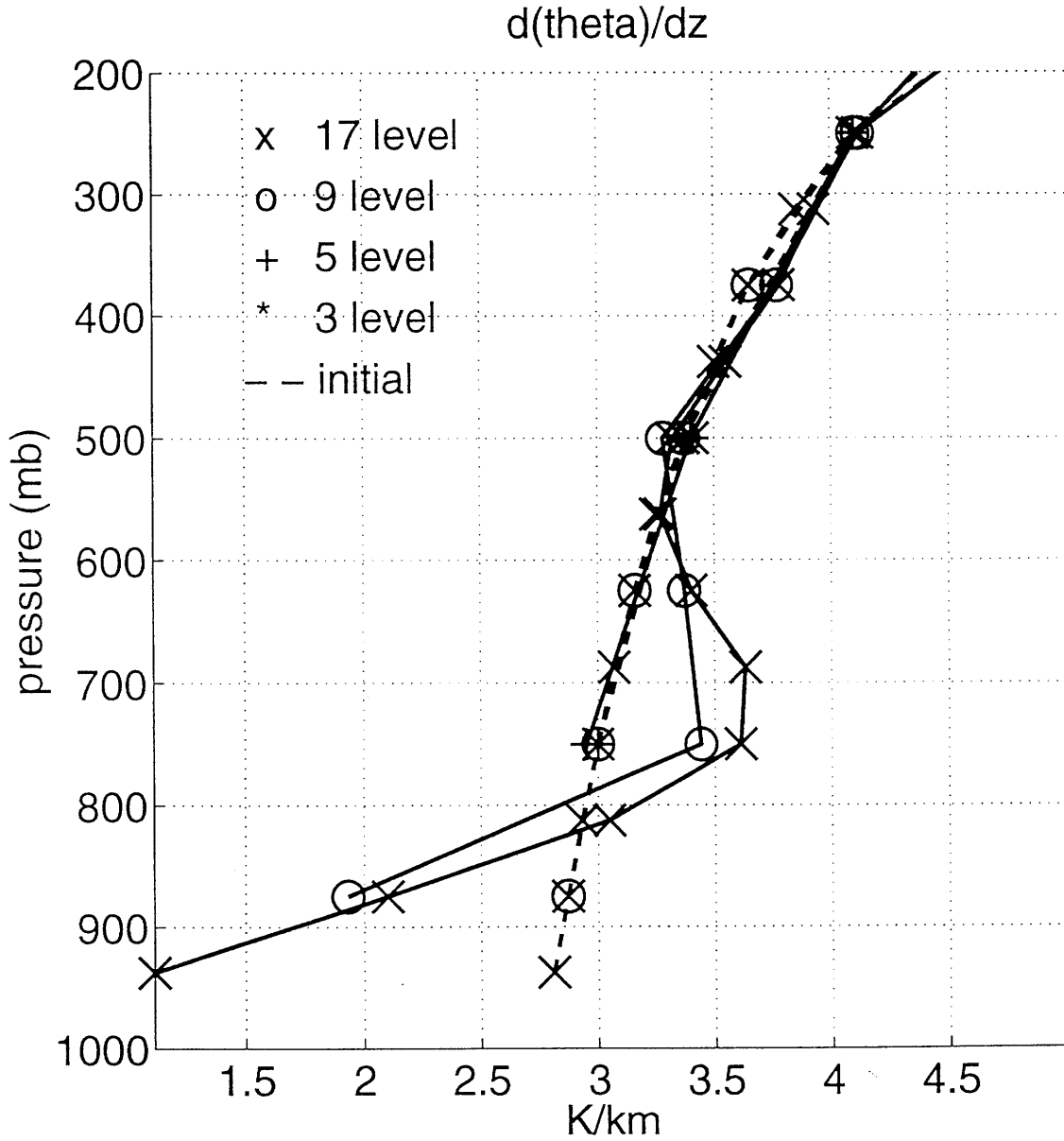
Figure 5-20: Zonal mean static stability with an interactive surface without a stratosphere for 3,5,9 and 17 evenly spaced pressure levels.
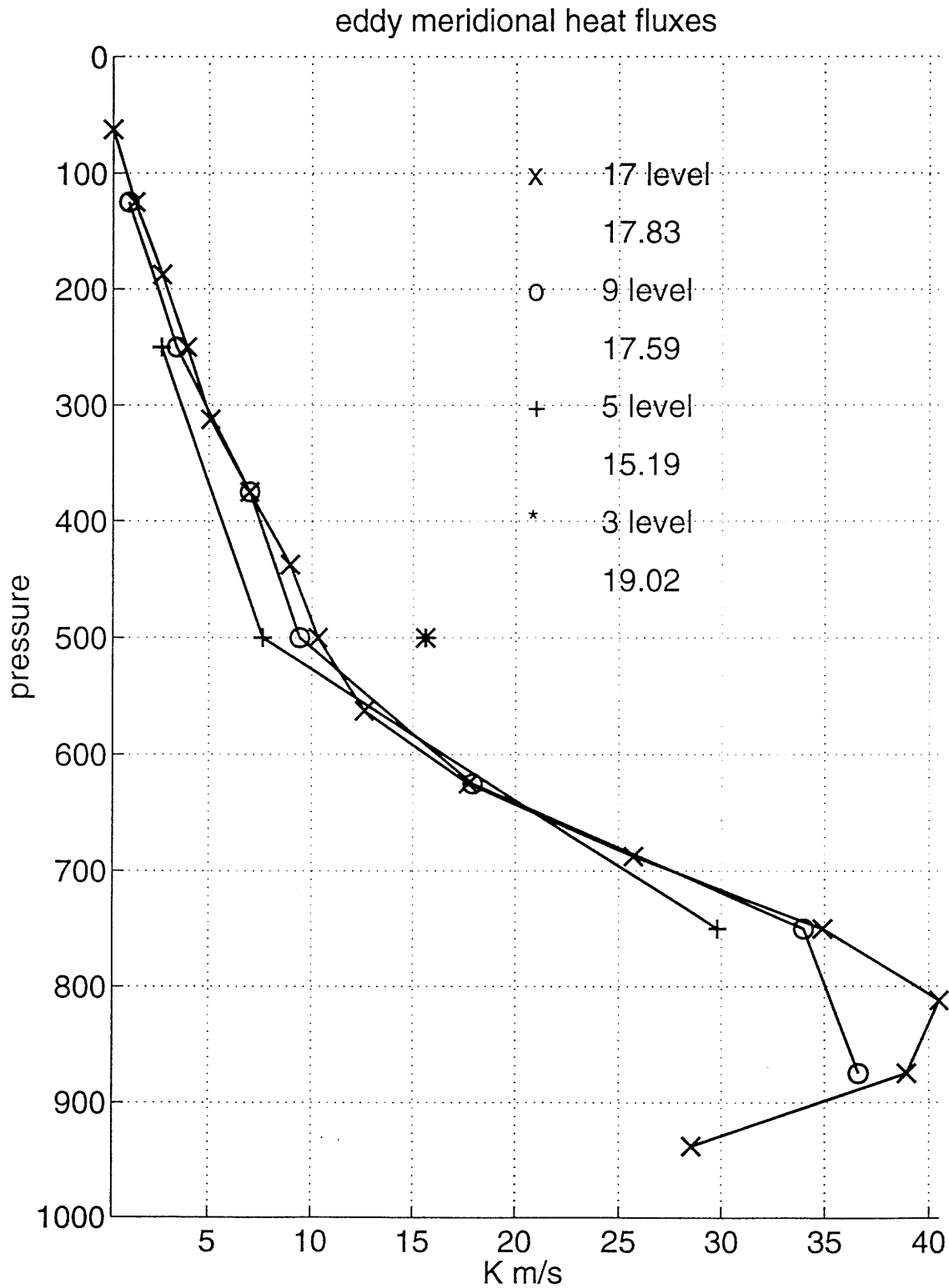
Figure 5-21: Zonal mean eddy meridional heat fluxes with an interactive surface without a stratosphere for 3,5,9 and 17 evenly spaced pressure levels. The numbers in the legend are the vertically averaged meridional eddy potential temperature fluxes at the center of the channel for each run.

eddy momentum fluxes
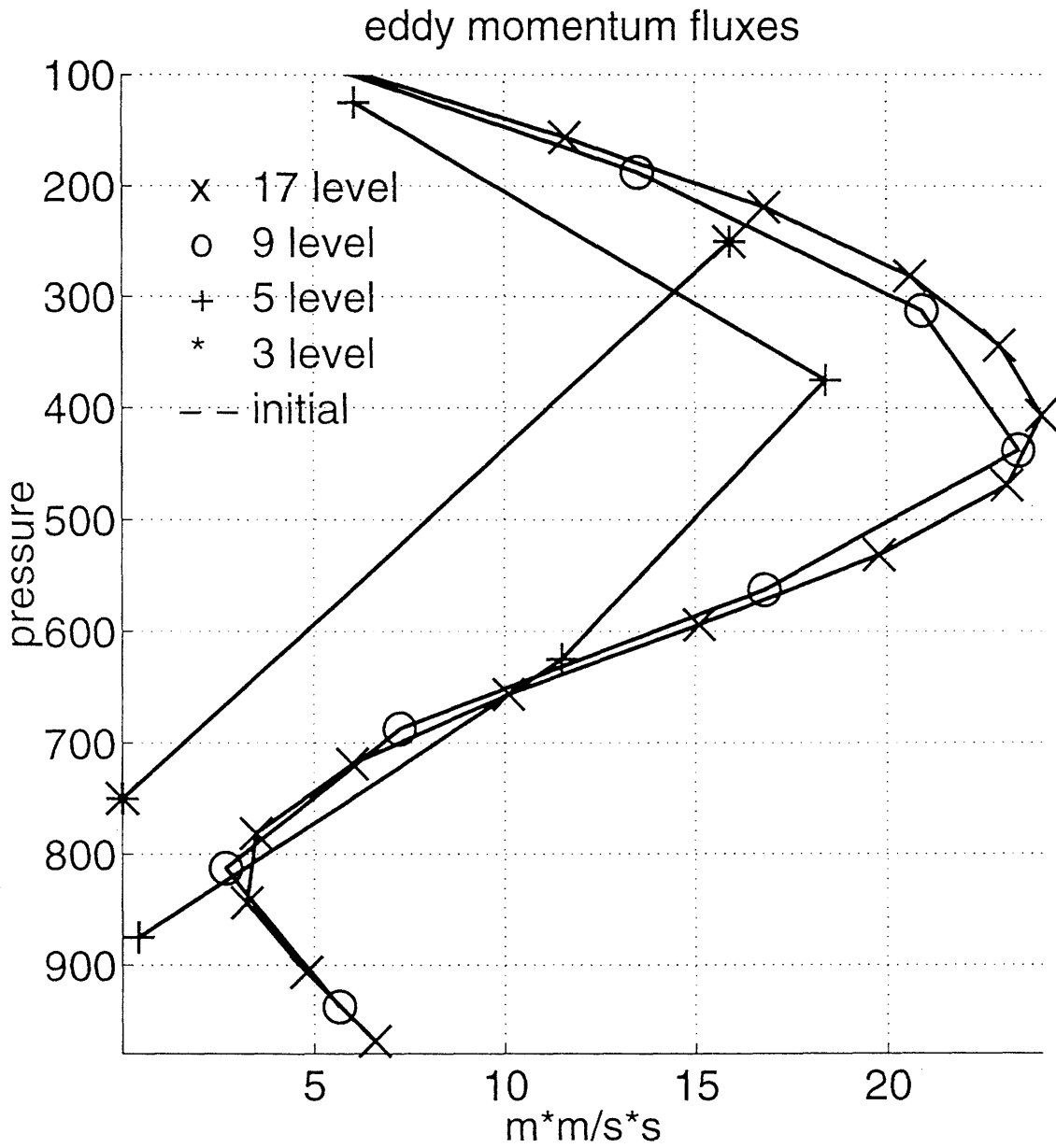
Figure 5-22: Zonal mean eddy momentum fluxes with an interactive surface without a stratosphere for 3,5,9 and 17 evenly spaced pressure levels.
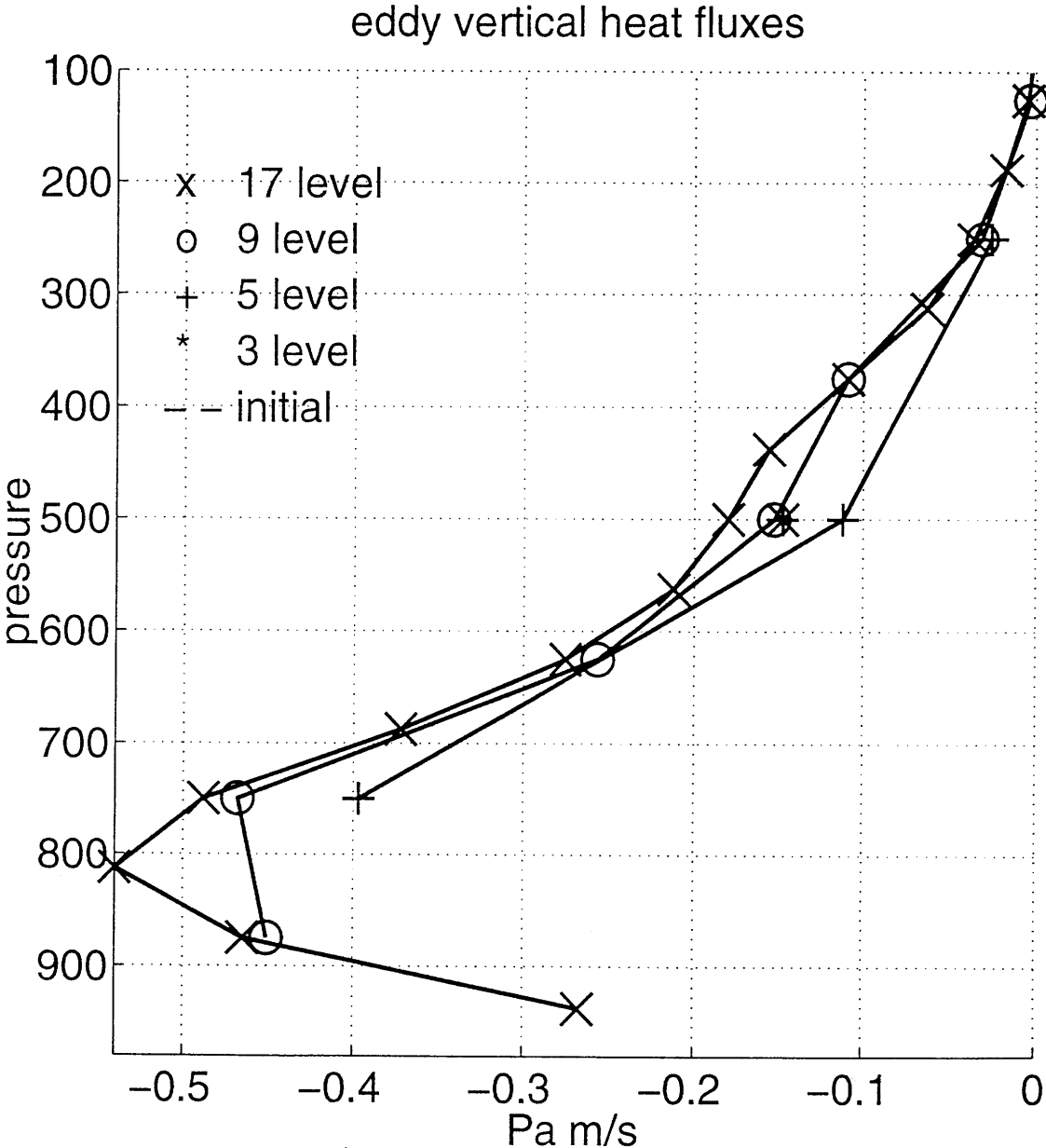
Figure 5-23: Zonal mean eddy vertical heat fluxes with an interactive surface without a stratosphere for 3,5,9 and 17 evenly spaced pressure levels.

Chapter 6

Parameter dependence of the equilibrated states

6.1 Radiative forcing

Radiative forcing in this model is parameterized with a linear Newtonian relaxation back to a radiative equilibrium temperature structure with a diabatic heating timescale which is independent of height. The radiative equilibrium temperature structure is the sum of the horizontally averaged temperature structure, which will be referred to as the radiative equilibrium lapse rate, and the quasi-geostrophic temperature structure which varies in latitude and height and will be referred to as the radiative equilibrium temperature structure. Since this model can resolve not only the horizontal but also the vertical temperature structure of the radiative forcing, there are many parameters and profiles that must be explored in order to get a complete picture of the radiative forcing parameter space. The goal of this Section is to get an idea of the sensitivity of the model's climate without exploring the whole parameter space. Therefore, only a few runs for each parameter and profile will be discussed. Table 6.1 lists the runs that will be discussed in this Section.

$d\theta_r/dy$ and dT_r/dy specify the meridional temperature gradients in the radiative equilibrium state at the center of the channel at the first model level (937.5 mb). If there are numbers in the $d\theta_r/dy$ column then the potential temperature gradients are constant with height. If there are numbers in the dT_r/dy column then the temperature structure is constant with height. These two different ways of specifying the temperature gradients have been used to look at how the eddy dynamics depend on the vertical structure of the temperature gradients. These runs will be discussed in more detail in a separate Section. dT_r/dz is the lapse rate in radiative equilibrium and is constant with height. 'jet' refers to the width of the jet. The number in this column is the width of the jet in units of $10^3 km$. τ_d is the diabatic heating timescale in units of days. S/T refers to whether or

RUN	$d\theta_r/dy$ $K/1000km$	dT_r/dy $K/1000km$	dT_r/dz K/km	jet $1000km$	S/T	τ_d days
CNT	-13.2	*****	-7.0	5.0	yes	10
TY1	-23.7	*****	-7.0	5.0	yes	10
TY2	-19.7	*****	-7.0	5.0	yes	10
TY3	-16.5	*****	-7.0	5.0	yes	10
TY4	-11.2	*****	-7.0	5.0	yes	10
TY5	-9.9	*****	-7.0	5.0	yes	10
TY6	*****	-13.2	-7.0	5.0	yes	10
TZ1	-13.2	*****	-9.0	5.0	yes	10
TZ2	-13.2	*****	-8.0	5.0	yes	10
TZ3	-13.2	*****	-5.8	5.0	yes	10
TZ4	-13.2	*****	-5.5	5.0	yes	10
WJ	-13.2	*****	-7.0	6.7	yes	10
NOST1	-13.2	*****	-7.0	5.0	no	10
NOST2	****	-13.2	-7.0	5.0	no	10
TAU1	-13.2	*****	-7.0	5.0	yes	5
TAU2	-13.2	*****	-7.0	5.0	yes	25

Table 6.1: Runs that were done to determine the sensitivity of the equilibrated climate to changes in radiative forcing.

not the run has a representation of a stratosphere and a tropopause. Different ways of parameterizing a stratosphere and tropopause have been tried. The only parameterization that will be discussed is the isothermal radiative equilibrium stratosphere which has a lapse rate equal to zero above 250 mb and meridional temperature gradients that are positive and 10 times smaller than the gradients at 300 mb.

All the runs in Table 6.1 are run for 1000 days and statistics are calculated for the last 400 days. Table 6.2 lists some characteristics of the equilibrated state for each run.

dT_e/dy is the minimum equilibrated temperature gradient at the center of the channel between 650-750 mb. $d\theta_e/dz$ is the maximum static stability at the center of the channel between 650-750 mb. EKE is the peak value of the eddy kinetic energy. ENS is the peak value of the eddy enstrophy and the pressure level at which the EKE and ENS peaks are located. $V\theta P$, $V\theta M$, and WTP are the vertically averaged meridional eddy potential temperature fluxes, mean potential temperature fluxes, and vertical temperature fluxes respectively.

RUN	dT_e/dy $K/1000km$	$d\theta_e/dz$ K/km	EKE m^2/s^2	ENS $10^{-10}/s^2$	$V\theta P$ mK/s	$V\theta M$ mK/s	WTP $10^{-2}KPa/s$
CNT(-13.2)	-7.1	3.6	497.0	42.3 (219)	17.2	-4.3	-9.0
TY1(-23.7)	-10.9	5.5	1650.0	116.0 (219)	72.1	-19.7	-83.0
TY2(-19.7)	-9.3	5.4	1250.0	86.0 (219)	49.7	-15.4	-47.0
TY3(-16.5)	-7.3	4.6	969.0	65.9 (219)	32.4	-6.5	-19.2
TY4(-11.2)	-10.0	2.5	1.6	0.6 (656)	0.5	0.1	-0.9
TY5(-9.9)	RCE	RCE	0.0	0.0	0.0	0.1	0.0
TY6(-13.2)	-6.0	4.0	813.0	58.5 (219)	24.4	-4.7	-11.7
TZ1(-9.0)	-9.2	2.1	615.0	117.0 (219)	21.0	-11.9	-32.6
TZ2(-8.0)	-7.6	2.7	584.0	56.7 (219)	22.2	-7.4	-18.9
TZ3(-5.8)	-10.0	4.7	94.9	6.0 (406)	8.4	-3.2	-7.9
TZ4(-5.5)	RCE	RCE	0.0	0.0	0.0	0.5	0.0
WJ(6.7)	-5.4	3.3	499.0	33.1 (219)	19.9	-6.4	-8.4
NOST1	-7.4	3.7	132.0	9.2 (343)	14.5	-4.5	-17.0
NOST2	-10.0	3.4	72.8	4.7 (343)	8.5	-2.3	-12.9
TAU1(5)	-8.1	3.6	412.0	35.8 (219)	20.7	-6.0	-11.9
TAU2(25)	-7.1	3.6	518.0	42.2 (219)	13.1	-3.0	-7.3

Table 6.2: Characteristics of the equilibrated states of the runs that were done to determine the sensitivity to changes in radiative forcing.

6.1.1   Equilibrated state

Figures 6-1 and 6-2 show a comparison of the vertical derivative of the slope of the isentropes, S_p, which, assuming $\frac{\partial^2 \bar{u}}{\partial y^2}$ is small, is proportional to the pv gradients minus β, for all of the runs in Table 6.1 except for runs NOST1 and NOST2, in and above the ABL, respectively. These latter two runs are not included in the comparison because these equilibrated states differ from the runs with a stratosphere/tropopause. The dashed lines in the figure are the radiative equilibrium states that the model is forced towards. The thick solid lines are the equilibrated profiles at the center of the channel. Four runs with the largest forcing have been highlighted with markers. Lines with +'s are for run TZ1. This is the run with the smallest static stability in radiative equilibrium. Lines with *'s are for run TY1, which is the run with the largest temperature difference across the channel in radiative equilibrium. Lines with x's are for run TZ2, the run with the second smallest static stability in radiative equilibrium. Lines with the o's are for run TY2, the run with the second largest radiative equilibrium temperature difference across the channel. The dashed lines show the range of the radiative equilibrium basic states that are used in this series of runs. The solid lines show that the equilibrated S_p is relatively robust in the 800-500 mb layer.

In all of the runs that have been done with this model it is S_p which is found to be a robust field, not the slope of the isentropes. If pv is completely homogenized in the model then S_p would be equal to a constant, equal to $\beta/f_o = 2e - 7$ for this beta plane model. This is clearly not the case for this model. PV is only homogenized above the ABL, between 600-700mb. The equilibrated S_p profile is composed of 5 distinct regions. The first region is the ABL, Figure 6-1, where S_p is of order 100 times larger than above the ABL. The second region is between 550-650mb where S_p linearly increases with pressure. The third region is between 550-400mb where S_p is equal to a constant. The fourth region is between 400mb-200mb where S_p again linearly increases with pressure. The fifth region is above 200mb, where S_p is equal to the radiative equilibrium S_p. One very important feature to note is that there is a very robust value of S_p at the tropopause. except for the TZ1 run.

Figures 6-3 and 6-4 are the comparison plots of $d\theta_e/dz$ and dT_e/dy, respectively , for all runs except NOST1 and NOST2. These figures show that the equilibrated profiles of $d\theta_e/dz$ and dT_e/dy are not as robust as S_p . There is no clear division of adjustment between dT_e/dy and $d\theta_e/dz$. This is because the vertical profile of S_p is the vertical derivative of the slope of the isentropes. so the robust profile seen in figure 6-2 can be accomplished by a wide variety of $d\theta_e/dz$ and dT_e/dy profiles. The four runs described above, that have been marked with markers, have more of an adjustment in the upper troposphere, relative to the adjustment in the lower troposphere, than the runs with weaker radiative forcing.

Figures 6-5 and 6-6 display the vertical profiles of the meridional and vertical eddy heat fluxes, respectively, for all the runs except NOST1 and NOST2. These figures show that an increase in the temperature gradients across the channel results in increased meridional as well as vertical eddy heat fluxes, the o's and ×'s, whereas a decrease in the lapse rate has a much smaller impact on the fluxes, the +'s and x's. In fact a decrease in the lapse rate from -8 K/km to -9 K/km results in almost no change in the meridional eddy heat fluxes and an increase in the magnitude of the vertical eddy heat fluxes, but this increase is still significantly smaller than the fluxes for the increased temperature gradient runs, * and o runs. This can be seen in Figures 6-3 and 6-4 where the adjustment to the static stability and the meridional temperature gradients is far larger for an increase in the RCE temperature gradients, the * and o runs, than for a decrease in the lapse rate, the + and x runs. Looking at Figure 6-1 shows that the initial distribution of S_p are very similar for the *, o and x runs. The vertical profiles of the equilibrated S_p shows that the adjustments to S_p are also comparable. These results show that the same adjustment to S_p is accomplished in two very different ways when the RCE lapse rate is decreased and when the RCE meridional temperature contrast is increased. This can be clearly illustrated by comparing the x and o lines. These two runs have essentially the same initial and equilibrated S_p distribution but very different lapse rates and meridional temperature gradients. The run with the decreased lapse rate, the x's, has much less of an adjustment to the lapse rate and the meridional temperature gradients but the vertical profiles of these

fields are adjusted to attain the robust equilibrated S_p distribution that is seen in Figure 6-2.

The difference between the two ways of attaining the equilibrated S_p can also be seen in a comparison of the eddy kinetic energy for the runs (Table 6.2). Varying the lapse rate results in a very small change in the EKE, relative to the large changes that results when the meridional temperature contrast is varied.

6.1.2   Varying the jet width

The control run has a radiative equilibrium jet width which is 5,000 km wide. This distance is very close to the wavelength of the linearly most unstable wave. Previous wave-mean flow studies have shown that an important equilibration process is the barotropic governor (James and Gray 1986). The waves equilibrate by not only reducing the shear but also by modifying the barotropic structure of the mean jet. Imposing the jet structure that the eddies would have otherwise created should result in a large change in the eddy fluxes. In order to determine whether the results of the control run are robust and relatively independent of the imposed jet width, the model has been run with a RCE jet width of 6,700 km, run WJ. The temperature gradients at the center of the channel are chosen to be equal to those of the control run. The wider jet has a temperature difference of 53.7K across the center 5,000 km of the channel, compared to 43K in the control run.

Table 6.2 shows that the equilibrated state of WJ has similar static stability to the control run but the magnitude of the temperature gradients at the center of the channel significantly increase. The width of the equilibrated jet is approximately equal to the width of the RCE jet at the tropopause and narrower than the RCE jet in the lower troposphere (Figure not shown). The eddies do not cause the width of the equilibrated jet to tighten to the width of the wavelength of the most unstable wavelength. Therefore, in these model runs, the barotropic governor was not found to be an important equilibration mechanism.

6.1.3   Varying the vertical structure of dT/dy

TY6 has been run to test the sensitivity of the equilibrated state to changes in the vertical structure of the RCE temperature structure. The potential temperature gradients of the control run are constant with height. TY6 holds the temperature gradients constant with height. The temperature gradients at the surface are equal to 43K over the center 5000 km of the channel, for both TY6 and CNT. Therefore, the temperature gradients of the control run decrease with height and are equal to 30.8K/5000km at 312 mb. This is a 28% reduction in the temperature gradients in the upper troposphere. This vertical structure has been chosen as a simple
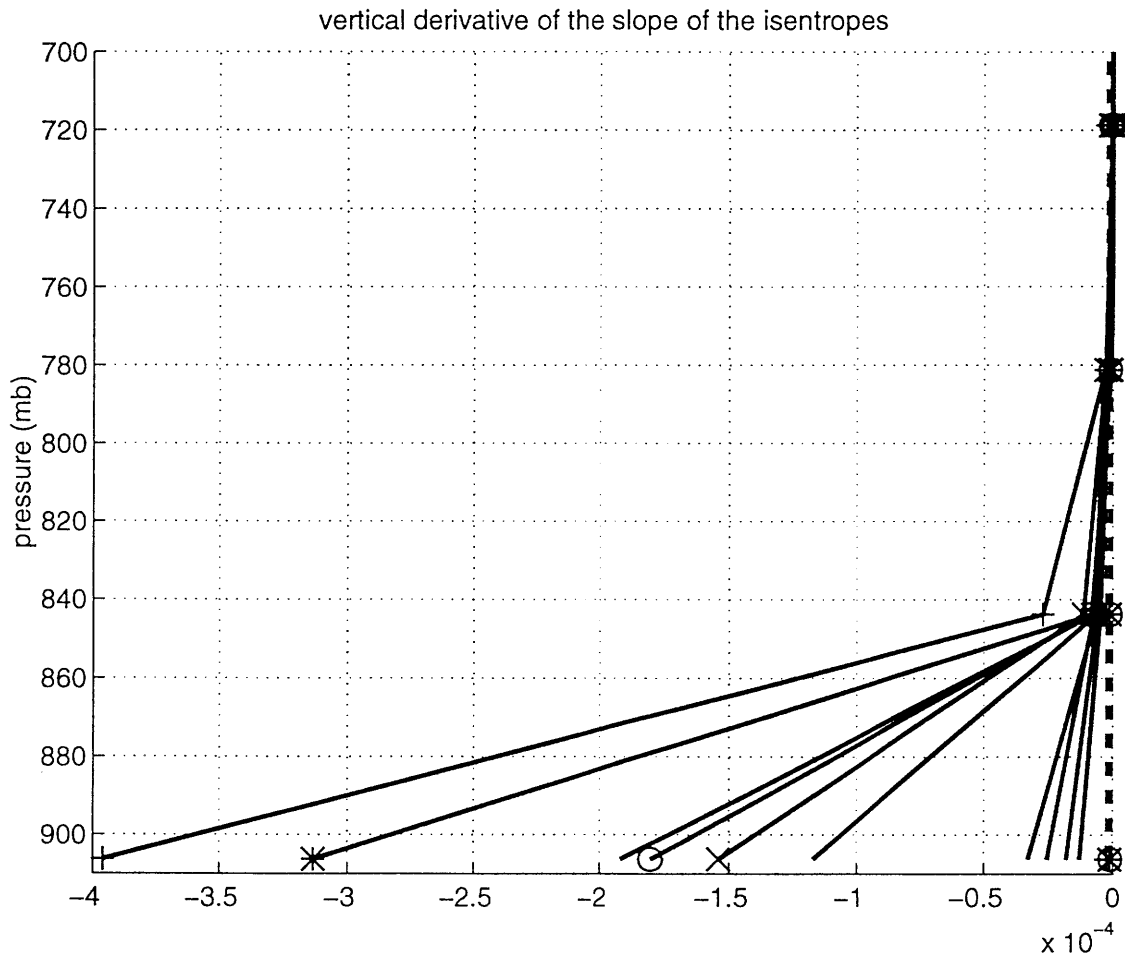
Figure 6-1: Equilibrated S_p in the ABL for all cases listed
in Table 5.1 except NOST1 and NOST2. Where +'s are for
TZ1, *'s are for TY1, x's are for TZ2, and o's are for run
TY2. Dashed lines show the range of radiative equilibrium
basic states used in this series of runs.

vertical derivative of the slope of the isentropes
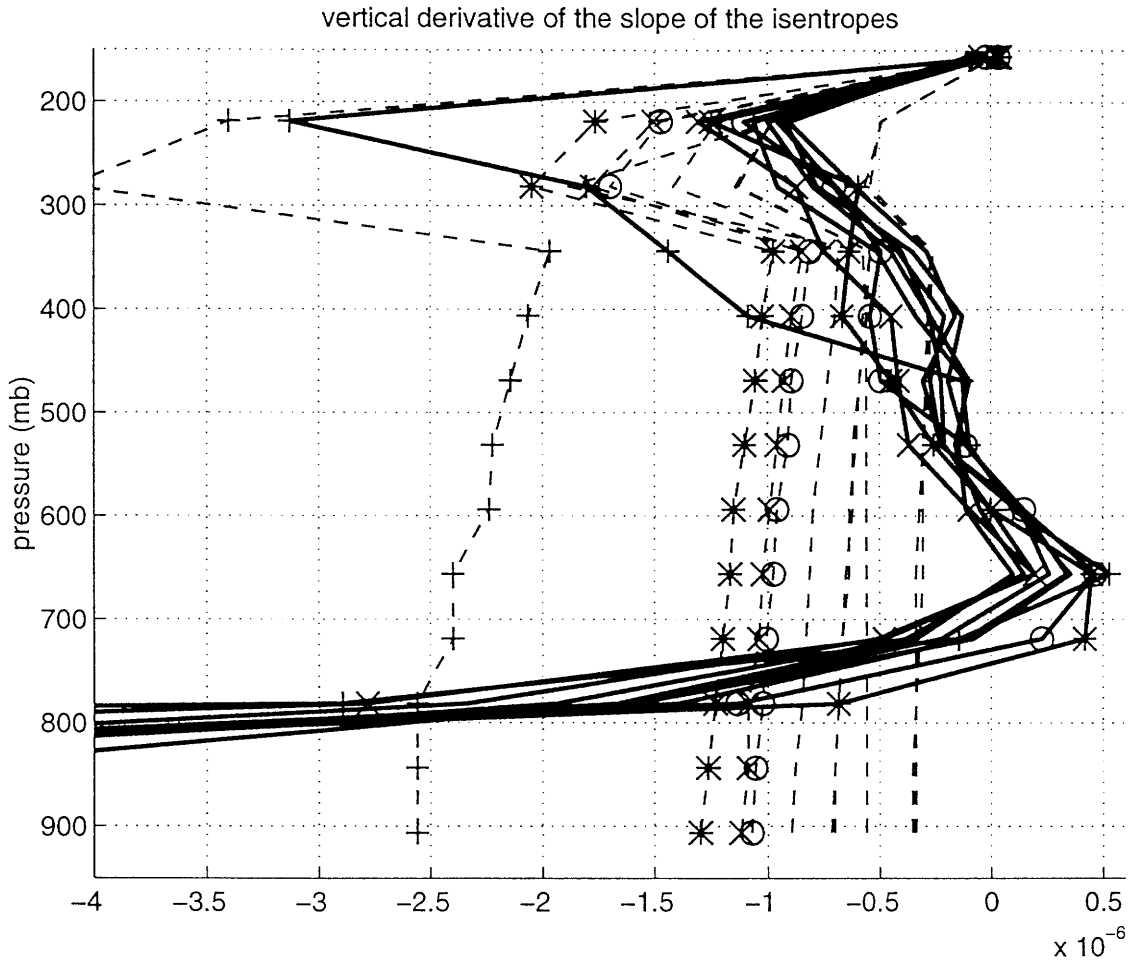
Figure 6-2: Equilibrated S_p above the ABL for all cases listed in Table 5.1 except NOST1 and NOST2. Where +'s are for TZ1, *'s are for TY1, x's are for TZ2, and o's are for run TY2. Dashed lines show the range of radiative equilibrium basic states used in this series of runs.
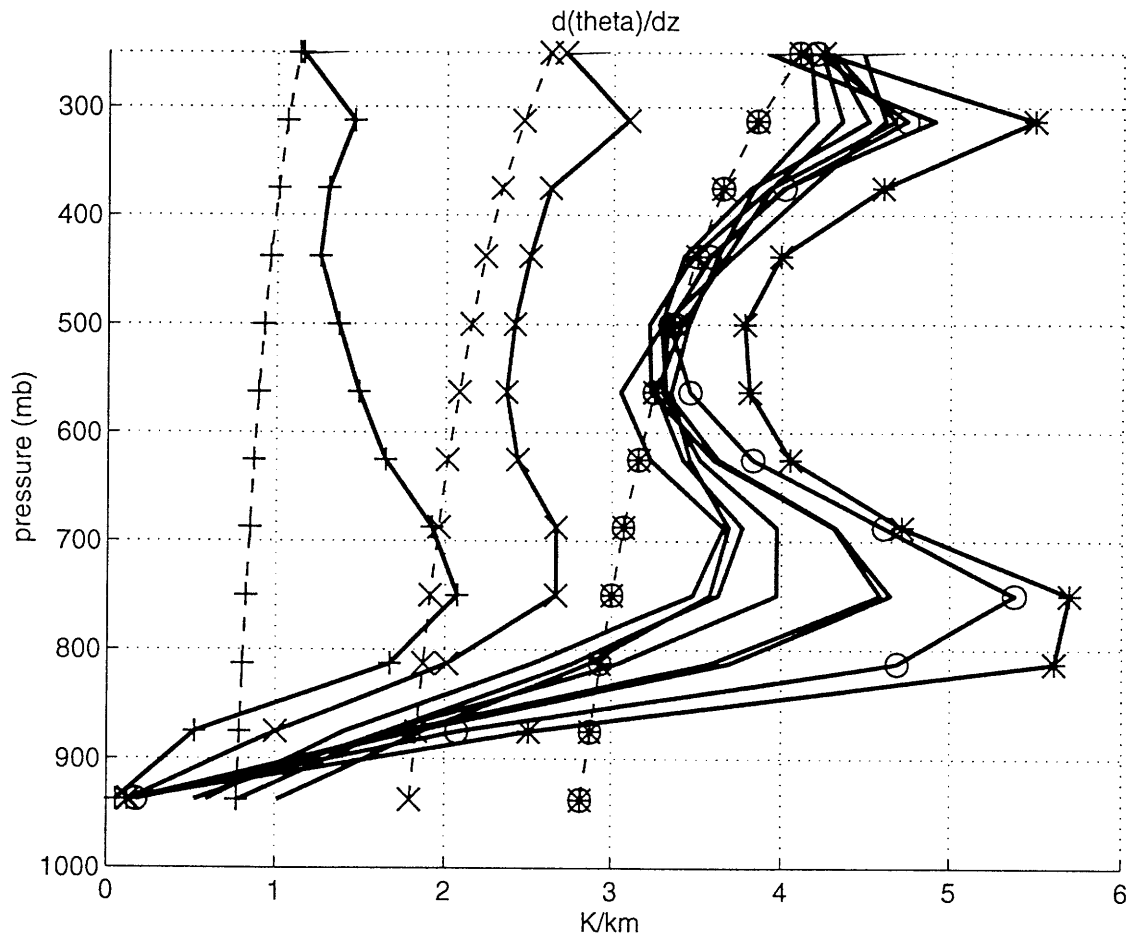
Figure 6-3: Equilibrated static stability for all cases listed in Table 5.1 except NOST1 and NOST2. Where +'s are for TZ1, *'s are for TY1, x's are for TZ2, and o's are for run TY2. Dashed lines show the range of radiative equilibrium basic states used in this series of runs.
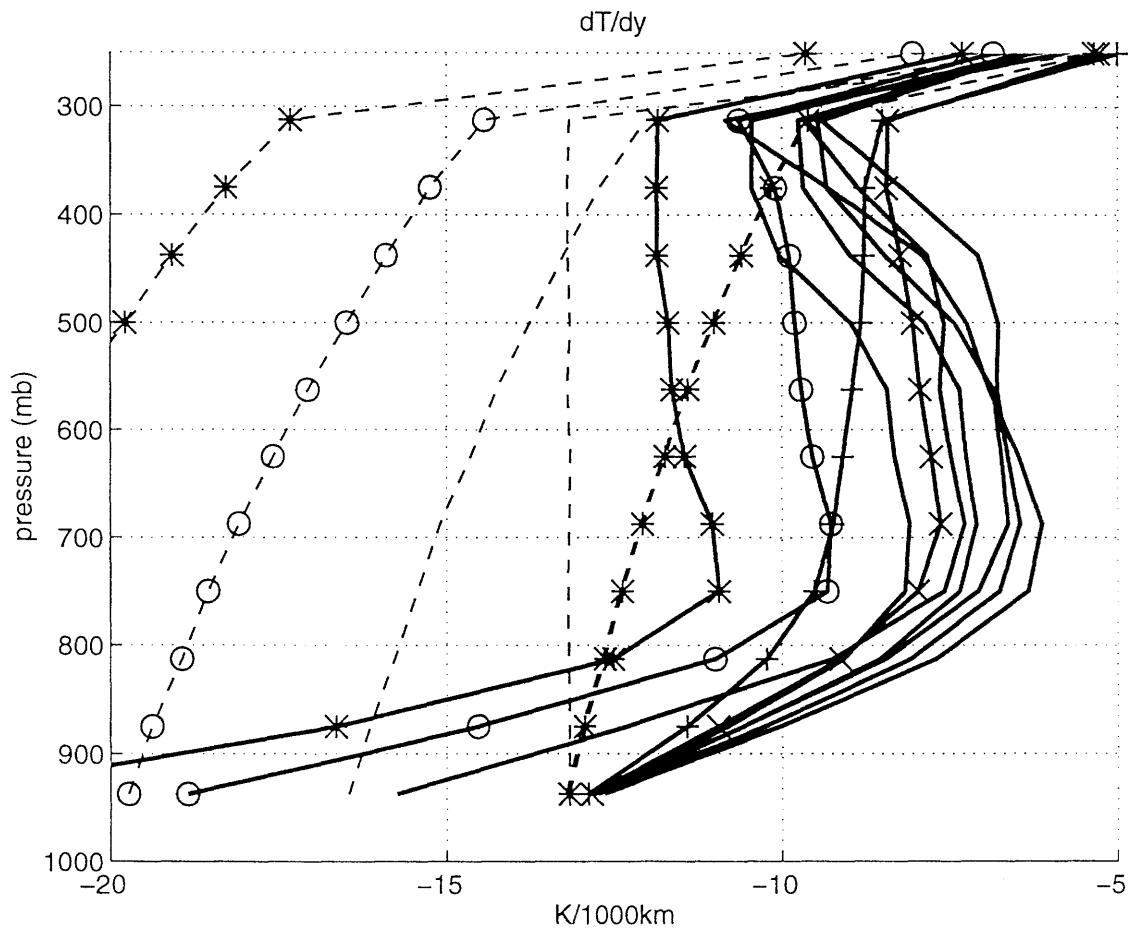
Figure 6-4: Equilibrated meridional temperature gradients for all cases listed in Table 5.1 except NOST1 and NOST2. Where +'s are for TZ1, *'s are for TY1, x's are for TZ2, and o's are for run TY2. Dashed lines show the range of radiative equilibrium basic states used in this series of runs.

comparison with the control run and as a test of the sensitivity of the temperature structure in the lower troposphere to changes in the RCE temperature structure in the upper troposphere.

Table 6.2 shows that the run with the larger temperature gradients in RCE, TY6, has smaller equilibrated temperature gradients. The magnitude of the TY6 pv gradients are larger in the ABL and smaller up to the tropopause, than the pv gradients of the control run (figure not shown). The TY6 ENS, EKE, and the eddy fluxes significantly increase (Table 6.2). An important difference between these two runs is that, in TY6 thermal diffusion is acting to change the vertical structure of the RCE temperature structure because the potential temperature increases with height. Since the thermal diffusion is limited to the lower troposphere and the RCE temperature structures differ primarily in the upper troposphere, the pv gradients in the symmetric state are very similar in the ABL and the mid troposphere. Another important point is that the TY6 pv gradients at the tropopause are 1.5 times larger than the CNT pv gradients at the tropopause. A more detailed study of the eddy response to changes in the vertical structure of the RCE temperature structure will be discussed in chapter 7.

6.1.4   Including a stratosphere/tropopause

Runs NOST1 and NOST2 are not included in the comparison of the equilibrated state because these runs equilibrate differently than the runs with a stratosphere/tropopause. Runs without a stratosphere/tropopause have a RCE lapse rate that is independent of height and meridional temperature gradient with either constant RCE temperature or potential temperature gradients.

Table 6.2 shows that the EKE and ENS of NOST1 and NOST2 peak lower in the troposphere than the runs with a stratosphere. The table also shows that the magnitude of the ENS and EKE are significantly reduced when the stratosphere is not present. A comparison between CNT and NOST1 shows that the meridional temperature gradients and static stability above the ABL are relatively independent of whether or not the stratosphere is resolved. A comparison between TY6 and NOST2 shows that this is not the case when the RCE temperature structure has temperature gradients that are constant with height, as opposed to the runs that have a RCE temperature structure with constant potential temperature gradients. TY6 and NOST2 have completely different equilibrated temperature structure and eddy fluxes. These runs highlight the impact of the stratosphere on the structure of the eddies. These runs also highlight the response of the eddies to a change in the RCE temperature structure. These four runs show that the eddy fluxes and the response to a change in the radiative forcing are very sensitive to the inclusion of a stratosphere/tropopause.

Figure 6-7 shows the time evolution of the amplitude of the perturbation pv at the center of the channel for NOST2. This figure shows that the perturbation pv is not steady when the stratosphere/tropopause is removed. In all of the cases

with a stratosphere/tropopause the perturbation pv was steady after the model became equilibrated. Figure 6-7 shows that there is a peak in the perturbation pv at the surface a few days before the peak at 400 mb, after which the perturbation pv decays away. The cycle repeats itself with a period of 40 days. The vertical distribution of the perturbation pv at the time of the peak at 400 mb closely approximates the distribution of the perturbation pv in the control run.

Figure 6-8 shows the time evolution of the zonal mean pv gradients at the center of the channel for the same time period as Figure 6-7, in units of β. This figure shows that there are large pv gradients that are associated with the pulses in the perturbation pv at the surface. In the mid troposphere, the zonal mean pv gradients oscillate between periods of large pv gradients and periods of homogenized pv gradients between 700-500 mb. The periods of homogenization in the mid troposphere closely approximate the zonal mean pv gradients in the mid troposphere from the control run.
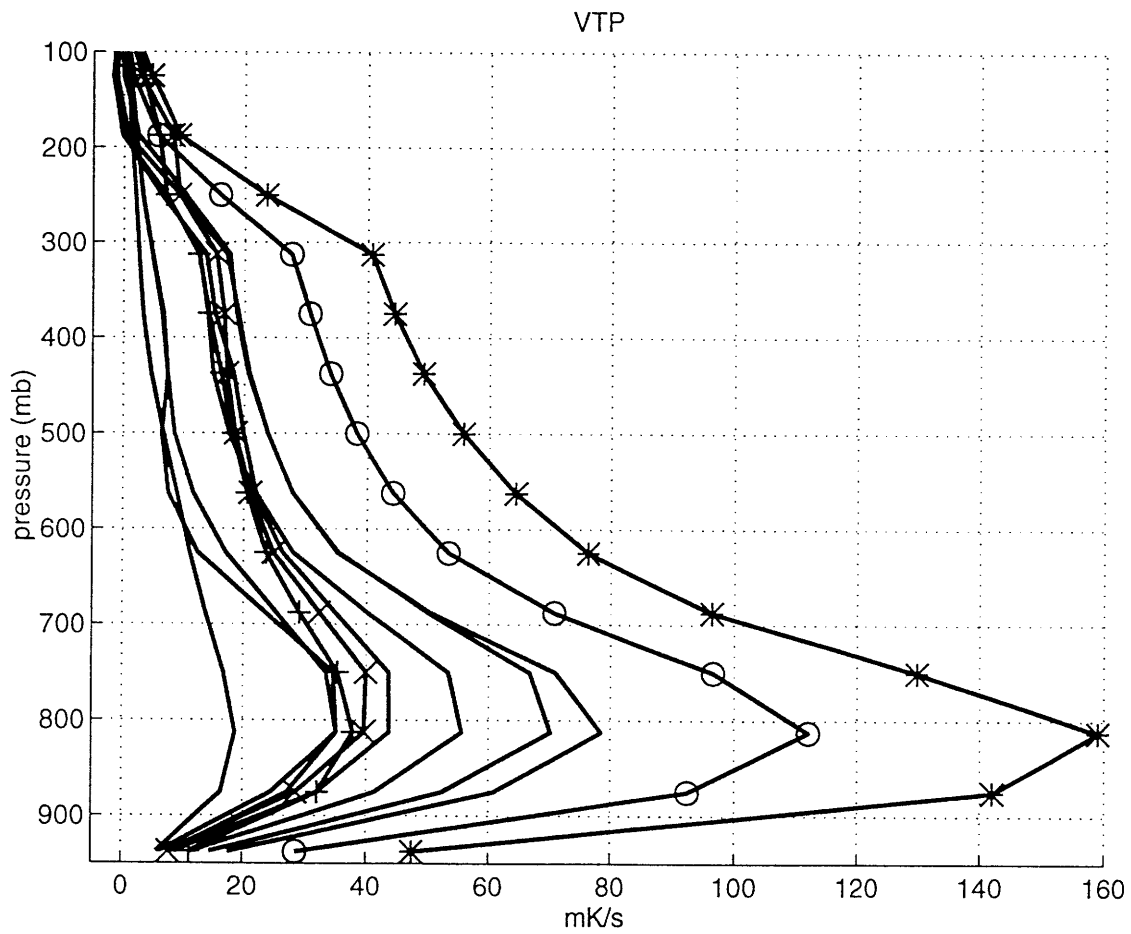
Figure 6-5: Equilibrated meridional eddy heat fluxes for all cases listed in Table 5.1 except NOST1 and NOST2. Where +'s are for TZ1, *'s are for TY1, x's are for TZ2, and o's are for run TY2.
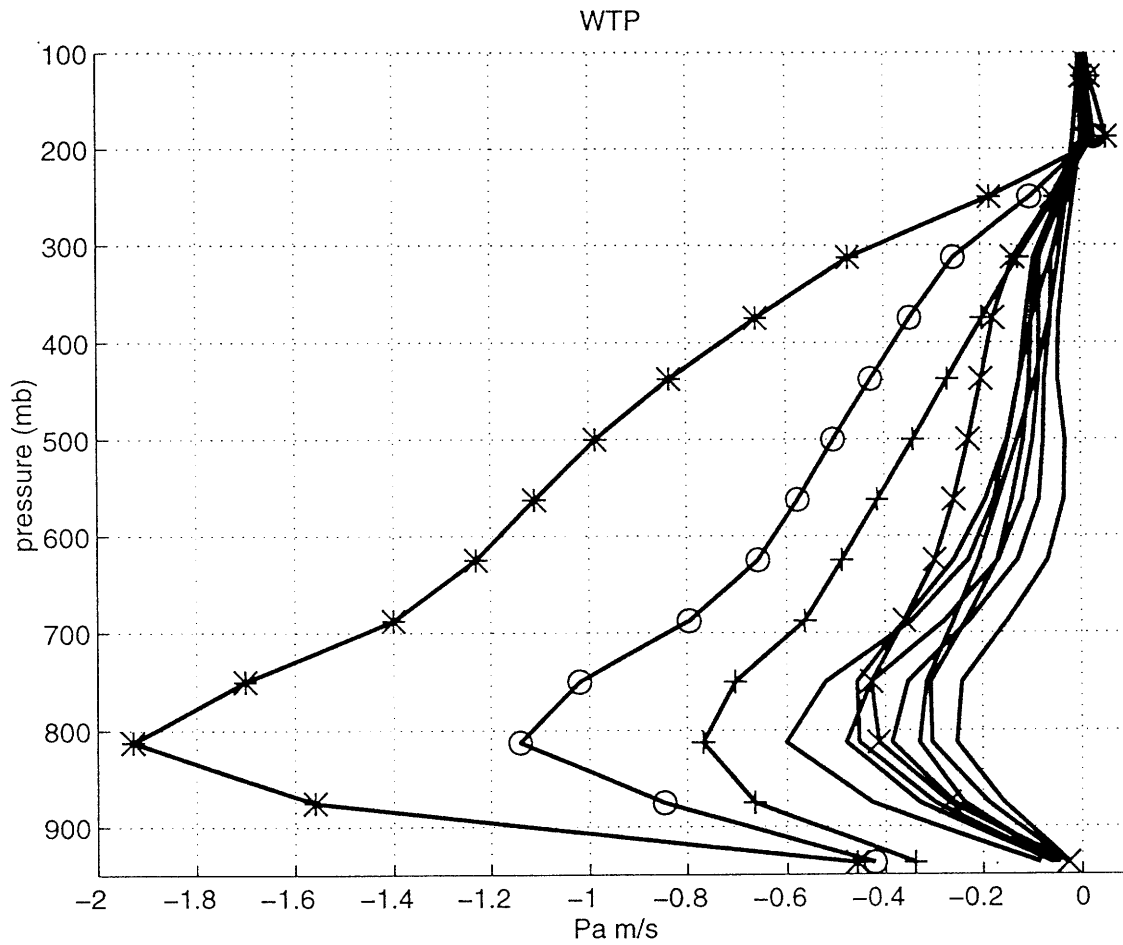
Figure 6-6: Equilibrated vertical eddy heat fluxes for all cases listed in Table 5.1 except NOST1 and NOST2. Where +'s are for TZ1, *'s are for TY1, x's are for TZ2, and o's are for run TY2.

amplitude of the perturbation pv for NOST2
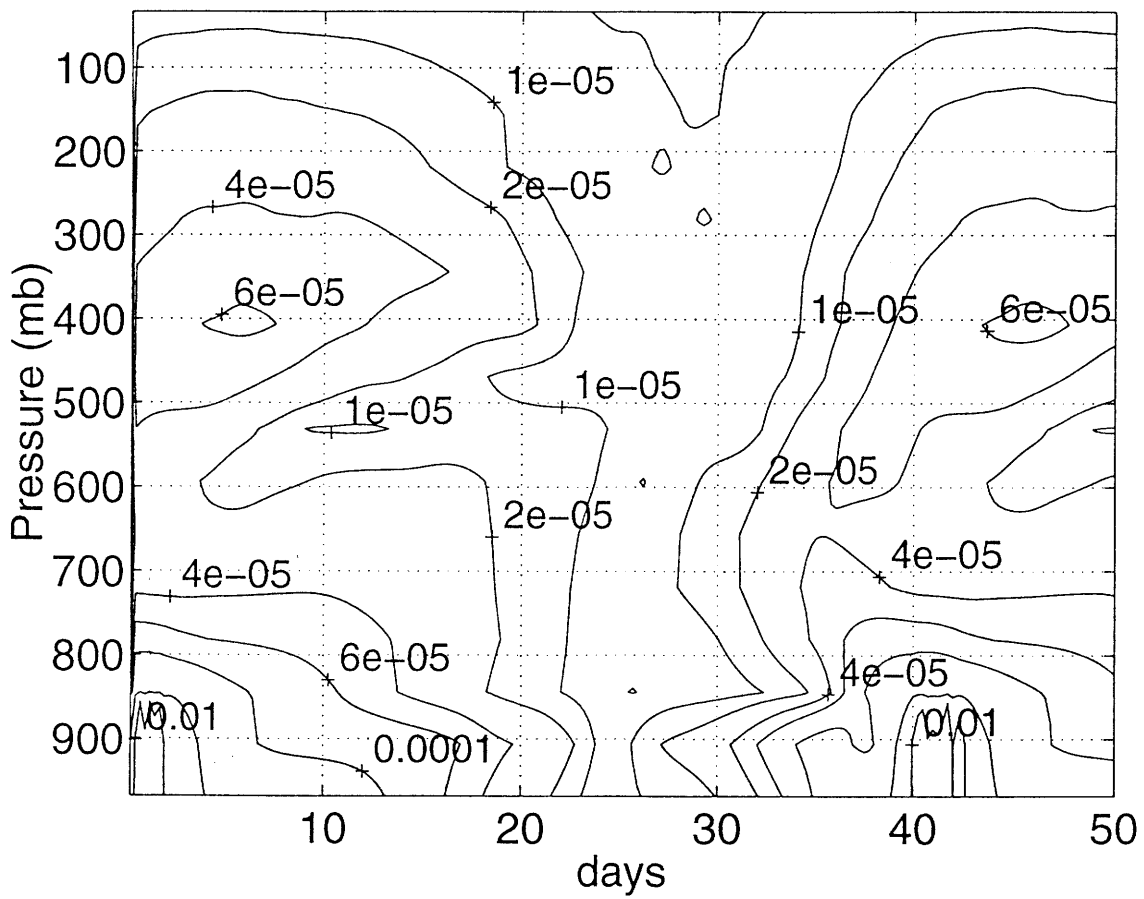
Figure 6-7: Amplitude of the perturbation pv at the center of the channel in the equilibrated state of NOST2.
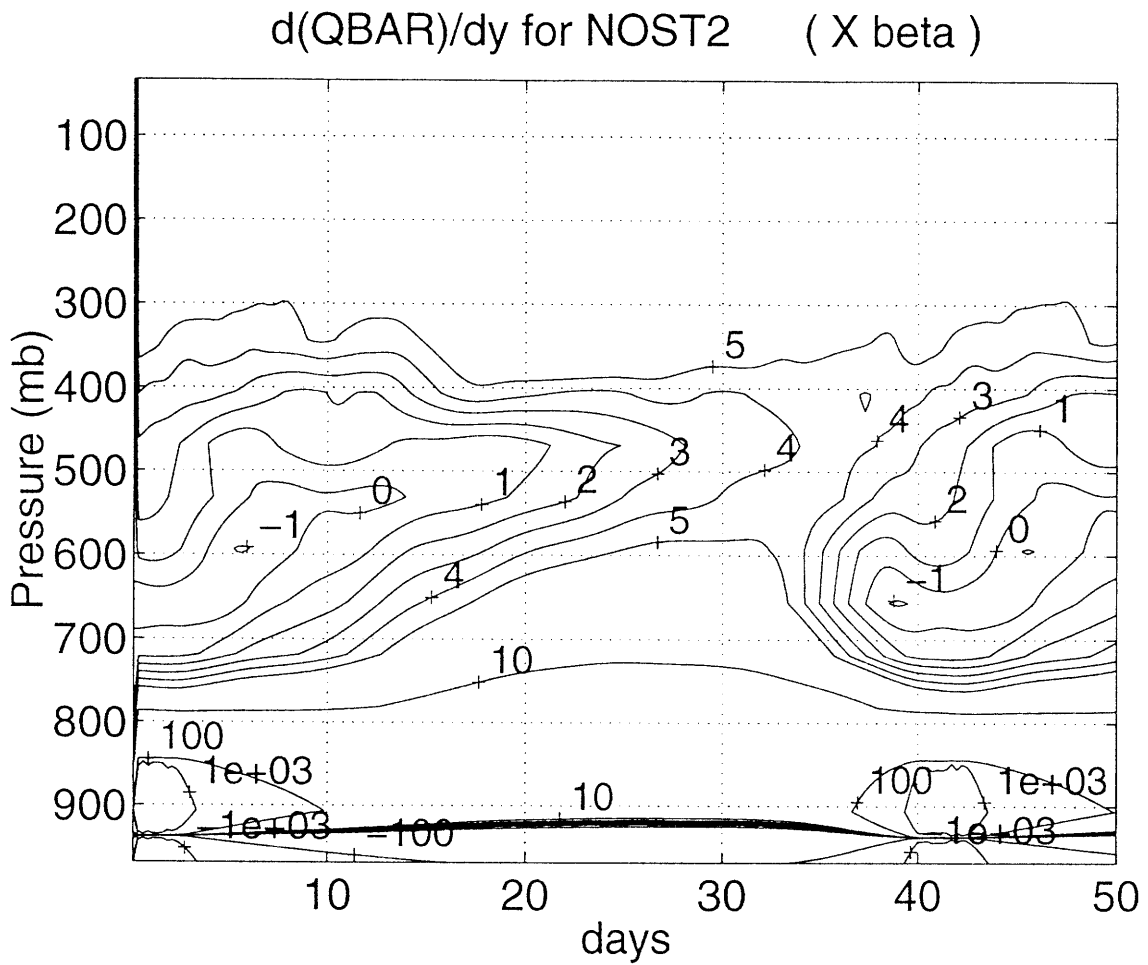
Figure 6-8: Zonal mean pv gradients at the center of the channel in the equilibrated state of NOST2, in units of β.

6.2   Turbulent fluxes of heat and momentum

The goal of this Section is to determine how the equilibrated mean state and fluxes depend upon the way in which the ABL is parameterized in the model. The turbulent fluxes of heat and momentum in the ABL are defined in this model by a surface drag, which determines the fluxes that cross the air-sea interface, and vertical diffusion, which is a function of the eddy diffusion coefficients, $\nu_T(p)$ and $\nu_M(p)$. All of the runs in this Section hold the temperature of the ocean to be fixed. Therefore, the ocean is assumed to be an infinite reservoir of heat.

The turbulent mixing has been varied in three different ways. The first way is to vary the strength of the surface drag coefficient. These runs are specified by CD1-CD7. The drag coefficient discussed in this Section is the product of surface drag coefficient and the ambient surface wind, which will be referred to as cd from here on, and is varied from 6×10^{-3} to 0.1 m/s. The vertical profile and magnitude of the vertical diffusion coefficients are held fixed and equal to that of the control run.

The second way is to vary the vertical extent of the eddy diffusion coefficients. In this series of runs, BL1-BL3, the eddy diffusion coefficients are set equal to zero above some specified pressure level. The pressure at which the eddy diffusion coefficient goes to zero is specified in Table 6.3 in the column titled BLH. The magnitude of the eddy diffusion coefficents are specified to be equal to the control run at the first model level and then decrease to zero as a function of the square of the pressure, not the cube of the pressure as has been done in the control run.

The third way is to vary the magnitude of the vertical diffusion coefficients. This series of runs is specified by NU1-NU4. NU1 and NU2 vary the eddy diffusion coefficients of heat and momentum together. NU3 and NU4 vary the eddy diffusion coefficients separately to determine their relative importance.

Table 6.3 lists the runs that will be discussed in this Section.

All of the runs listed above are run for 1000 days. Statistics are calculated from the last 400 days of the run.

RUN	cd	$\nu_T(p)$ $m*m/s$	$\nu_M(p)$ $m*m/s$	BLH mb
CNT	0.06	$10.0(P/P_0)^3$	$10.0(P/P_0)^3$	0.0
CD1	.006	$10.0(P/P_0)^3$	$10.0(P/P_0)^3$	0.0
CD2	0.01	$10.0(P/P_0)^3$	$10.0(P/P_0)^3$	0.0
CD3	0.02	$10.0(P/P_0)^3$	$10.0(P/P_0)^3$	0.0
CD4	0.04	$10.0(P/P_0)^3$	$10.0(P/P_0)^3$	0.0
CD5	0.05	$10.0(P/P_0)^3$	$10.0(P/P_0)^3$	0.0
CD6	0.07	$10.0(P/P_0)^3$	$10.0(P/P_0)^3$	0.0
CD7	0.08	$10.0(P/P_0)^3$	$10.0(P/P_0)^3$	0.0
CD8	0.10	$10.0(P/P_0)^3$	$10.0(P/P_0)^3$	0.0
BL1	0.06	$15.0(P/P_0)^2$	$15.0(P/P_0)^2$	750.0
BL2	0.06	$15.0(P/P_0)^2$	$15.0(P/P_0)^2$	687.5
BL3	0.06	$15.0(P/P_0)^2$	$15.0(P/P_0)^2$	625.0
NU1	0.06	0.0	0.0	0.0
NU2	0.06	$2.0(P/P_0)^3$	$2.0(P/P_0)^3$	0.0
NU3	0.06	$15.0(P/P_0)^3$	$15.0(P/P_0)^3$	0.0
NU4	0.06	$20.0(P/P_0)^3$	$20.0(P/P_0)^3$	0.0
NU5	0.06	$2.0(P/P_0)^3$	$10.0(P/P_0)^3$	0.0
NU6	0.06	$10.0(P/P_0)^3$	$2.0(P/P_0)^3$	0.0

Table 6.3: Runs that were done to determine the sensitivity of the equilibrated climate to changes in the turbulent fluxes of heat and momentum in the ABL.

Table 6.4 lists some characteristics of the equilibrated state for each run.

6.2.1   Varying the surface drag

Changing the drag coefficient changes the fluxes across the air-sea interface in three different ways. The same drag coefficient is used to calculate the turbulent fluxes of heat in both the static stability tendency equation and the qg thermodynamic equation. It is also used to determine the turbulent flux of momentum at the ground. Therefore it is not straightforward to diagnose the response of the model to changes in this parameter. In order to get an idea of the robust features of the equilibrated state, a comparison of the equilibrated states of CD1-CD7 has been created.

Figure 6-9 compares the pv gradients above the ABL at the center of the channel for runs CD1-CD7. This figure shows that all of the runs have a minimum in the pv gradients at the top of the ABL (750mb). This minimum is between 0 and

RUN	dT_e/dy $K/1000km$	$d\theta_e/dz$ K/km	EKE m^2/s^2	ENS $10^{-10}/s^2$	$V\theta P$ mK/s	$V\theta M$ mK/s	WTP KPa/s
CNT(0.06)	-7.1	3.6	497.0	42.3 (219)	17.2	-4.3	-0.090
CD1(.006)	-6.5	3.7	367.0	38.9 (984)	23.6	0.4	-0.227
CD2(0.01)	-6.3	3.6	487.0	35.5 (219)	26.6	-3.3	-0.226
CD3(0.02)	-6.6	4.0	726.0	56.5 (219)	29.6	-6.0	-0.178
CD4(0.04)	-5.3	3.9	789.0	51.4 (219)	24.1	-3.9	-0.078
CD5(0.05)	-6.0	3.8	632.0	48.2 (219)	20.4	-4.0	-0.078
CD6(0.07)	-8.8	3.6	327.0	27.1 (219)	13.3	-4.3	-0.097
CD7(0.08)	-8.9	3.6	262.0	21.8 (219)	11.7	-4.2	-0.103
CD8(0.10)	RCE	RCE	0.0	0.0	0.0	0.3	0.0
BL1(750)	-5.9	5.0	694.0	48.6 (219)	14.2	-1.8	-0.028
BL2(688)	-6.5	4.2	498.0	44.4 (219)	15.5	-4.2	-0.082
BL3(625)	-10.3	5.3	5.6	1.3 (719)	1.0	-0.1	-0.027
NU1(0)	-4.6	4.2	713.0	49.5 (219)	22.4	-7.5	-0.074
NU2(2)	-4.8	4.4	797.0	50.6 (219)	18.5	-2.4	-0.109
NU3(15)	-7.7	3.6	405.0	35.7 (219)	16.8	-4.6	-0.017
NU4(20)	-10.4	2.8	15.9	3.4 (594)	2.9	-0.3	-0.076
NU5(2)	-4.9	4.5	761.0	47.6 (219)	18.2	-1.5	-0.022
NU6(10)	-6.9	3.8	524.0	44.1 (219)	17.4	-4.1	-0.081

Table 6.4: Characteristics of the equilibrated states of the runs that were done to determine the sensitivity to changes in the turbulent fluxes of heat and momentum in the ABL.

1.53, depending on the magnitude of the surface drag. This figure also shows that varying the drag coefficient has a large impact on the degree of homogenization of pv above the ABL. An increase in the surface drag causes a decrease in the homogenization of pv above the ABL. For example, when the drag is equal to 0.08 m/s (o's), the significant reduction in the magnitude of the pv gradients is limited to a narrow region between 600-670 mb. When the drag is reduced to 6×10^{-3} m/s (*'s), the pv gradients has a very different vertical structure from the runs with larger drag coefficients. This run has pv gradients above the ABL that are larger than runs with larger values of the surface drag. Figure 6-10 shows the pv gradients in the ABL. This figure shows the nonlinear dependence of the pv gradients at the surface on the value of the drag. The run with the smallest surface drag (*'s) has significantly smaller pv gradients at the surface than the other runs. Figures 6-9 and 6-10 together suggest that the surface drag plays a large role in determining the magnitude of the equilibrated surface pv gradients. These surface pv gradients appear to play a role in modifying the stability of the eddies which determine the degree and extent of the homogenization of pv above the ABL. The

surface drag also plays a large role in the magnitude of the pv gradients at the tropopause. The magnitude of the pv gradients at the tropopause can be larger or smaller than the RCE pv gradients at the tropopause. Larger for larger values of the surface drag, smaller for smaller values of the surface drag.

The division of the adjustment between the static stability and the horizontal temperature gradients can be seen in Figures 6-11 and 6-12, respectively. Figure 6-11 shows that the equilibrated static stability in the ABL is very dependent upon the value of the surface drag. Large surface drag corresponds to a strong coupling between the air and sea temperatures. This coupling prevents the increase in the static stability by vertical fluxes of heat of the baroclinically unstable eddies. In fact, with a strong coupling between the ocean and atmosphere, the vertical fluxes of heat by the baroclinic eddies actually causes the static stability at the surface to be smaller than in the absence of eddies. Above the ABL the equilibrated static stability is relatively independent of the value of the drag at the surface.

Figure 6-12 shows the horizontal temperature gradients for CD1-CD7. All the runs have the same qualitative behaviour except for CD1 and CD2 which have much smaller temperature gradients in the ABL and, in the case of CD1 also much smaller at the tropopause than all of the other runs. This figure shows that a small change in the drag at the surface can result in a large change in the horizontal temperature gradients throughout the troposphere. Figure 6-13 shows the meridional eddy heat fluxes for CD1-CD7. This figure shows the increase in the heat flux as the surface drag is decreased for runs CD2-CD7. This figure also shows that when the surface drag is reduced to less than 0.02 m/s, the heat fluxes peak at the surface (*'s). This profile is similar to results of model studies which neglect surface heat fluxes, such as, Gutowski, Branscome and Stewart (1989).

6.2.2   Varying the vertical diffusion

Figures 6-14 and 6-15 show the equilibrated pv gradients at the center of the channel above and within the ABL, respectively, for the NU1-NU4 runs. Figure 6-14 shows that a reduction in the eddy diffusion coefficients (o's) causes the pv to be almost completely homogenized at 780-850 mb, instead of at 650 mb for the control run (dash-dot). A reduction in the eddy diffusion coefficient also has a large impact on the pv gradients near the tropopause. When the eddy diffusion coefficients are reduced by a factor of five, the pv gradients at the tropopause are reduced by 30%. Therefore, decreasing the eddy diffusion coefficient results in increased pv mixing throughout the troposphere. When the eddy diffusion coefficients are increased by a factor of two (*'s), the eddies are essentially damped out by the thermal diffusion.

The division of the adjustment between the static stability and the meridional temperature gradients is seen in Figures 6-16 and 6-17. Figure 6-16 shows that a smaller eddy diffusion coefficient results in much smaller static stability at the surface and much larger static stability at the top of the ABL, than the static

stability in the control run. The top of the ABL is lowered and more sharply peaked in these runs (NU1 and NU2). The equilibrated mean temperature of the surface air is smaller than the ocean temperature so that there is a net flux of heat out of the ocean into the atmosphere (figure not shown). This is the process that is responsible for warming the surface air that has been cooled by the vertical flux of heat by the large scale eddies. In the control run the equilibrated surface air temperature is larger than the ocean temperature so there is a net flux of heat into the ocean in the equilibrated state. The warmer surface air temperature is due to the downward heat transport by the turbulent eddies. The vertical structure of NU2 is closer to observations than the static stability of the control run. The static stability of NU4 is essentially that of the symmetric state. The static stability at the tropopause is relatively independent to the magnitude of the eddy diffusion coefficients and is a maximum when the eddy diffusion coefficients are equal to zero.

Figure 6-17 shows that the meridional temperature gradients are also sensitive to the magnitude of the eddy diffusion coefficients. Decreasing the eddy diffusion coefficients allows the eddies to be more efficient at reducing the meridional temperature gradients in the ABL. The vertical profile of the meridional temperature gradients above the ABL appear to be dependent upon the magnitude of the meridional temperature gradients at the top of the ABL. The vertical profile is similar for both NU2, NU3, and CNT, with the meridional temperature gradients at the top of the ABL as a lower boundary condition for the temperature gradients above the ABL. The run with eddy diffusion coefficients equal to zero (NU1) has a different vertical profile than the other runs, essentially because the top of the ABL is much lower in this run.

Figure 6-15 shows that even though the temperature gradients are reduced when the eddy diffusion coefficients are reduced, NU1 and NU2, the small static stability causes the pv gradients in the ABL to become large. Increasing the eddy diffusion coefficients, NU3 and NU4, does not have a very large impact on the static stability so the decrease in the pv gradients in the ABL is modest relative to the control run.

The meridional eddy heat fluxes for NU1-NU4 and CNT are shown in Figure 6-18. This figure shows that when the eddy diffusion coefficients are increased to 20 m^s/s (*'s) the heat fluxes are reduced by a factor of four in the ABL and essentially equal to zero above the ABL. The nonlinear dependence of the stability of the large scale waves on the magnitude of the eddy diffusion coefficients is seen in the comparison between NU3,NU4, and CNT. Increasing the eddy diffusion coefficients by $5m^2/s$ has little impact on the heat fluxes. Increasing the coefficients an additional $5m^2/s$ stabilizes the waves above the ABL. Setting the vertical diffusion coefficient to zero causes the heat fluxes to peak at the second level above the surface (NU1), whereas all runs with nonzero eddy diffusion coefficients peak higher up. The meridional eddy heat flux at the center of the channel is relatively insensitive to a decrease in the eddy diffusion coefficients (NU2). This is interesting considering that the meridional temperature gradients are highly dependent

upon the magnitude of the eddy diffusion coefficients (Figure 6-17).

Since NU1-NU4 and CNT vary the eddy diffusion coefficient for heat and momentum together, it is not clear if the diffusion of one is dominant over the other. Therefore, two other cases have been run. NU5 and NU6 vary the two diffusion coefficients in order to determine if one process is dominant over the other. It is found that the thermal diffusion dominates over the vertical diffusion of momentum (figure not shown). The equilibrated meridional eddy heat flux, zonal mean static stability, pv gradients, and meridional temperature gradients of NU5 are equal to NU2 and equivalently for NU6 and CNT. Therefore, the mean state and fluxes of the run are determined by the value of the thermal diffusion coefficient and are relatively independent to the vertical diffusion of momentum, for this range of the eddy diffusion coefficients.

6.2.3   Varying the ABL height

Figure 6-20 shows the equilibrated meridional temperature gradients. This figure shows that, except for BL3, the magnitude of the temperature gradients in the ABL are relatively independent of the height at which the eddy diffusion coefficient goes to zero. The magnitude of the temperature gradients fall off rapidly up to 750 mb for BL1, BL2 and CNT. BL3 has equilibrated meridional temperature gradients that differ from RCE only in the ABL.

Figure 6-19 shows the equilibrated static stability for BL1-BL3 and CNT. This figure shows that for all runs. even BL3, the static stability peaks at the level just below where the eddy diffusion goes to zero. The adjustment to the static stability and meridional temperature gradients in BL3 are sufficient to stabilize the large scale waves. This is seen in Figure 6-21 which shows the meridional eddy heat fluxes for BL1-BL3 and CNT. The heat fluxes for BL3 are seen to be equal to zero above the ABL. It is not clear why setting the boundary layer height in this way causes such dramatic results.

Figures 6-22 and 6-23 shows the equilibrated pv gradients at the center of the channel above and within the ABL, respectively, for the BL1-BL3 runs. Figure 6-22 shows that BL1 and BL2 have minimum pv gradients at the level above where the vertical diffusion coefficient goes to zero. BL3 has a very different vertical profile. This run has negative pv gradients of close to -3β and very little pv mixing above 500 mb. Figure 6-23 shows that the large decrease in the static stability, that results when the boundary layer height is lowered, causes the magnitude of the pv gradients within the ABL to increase substantially.
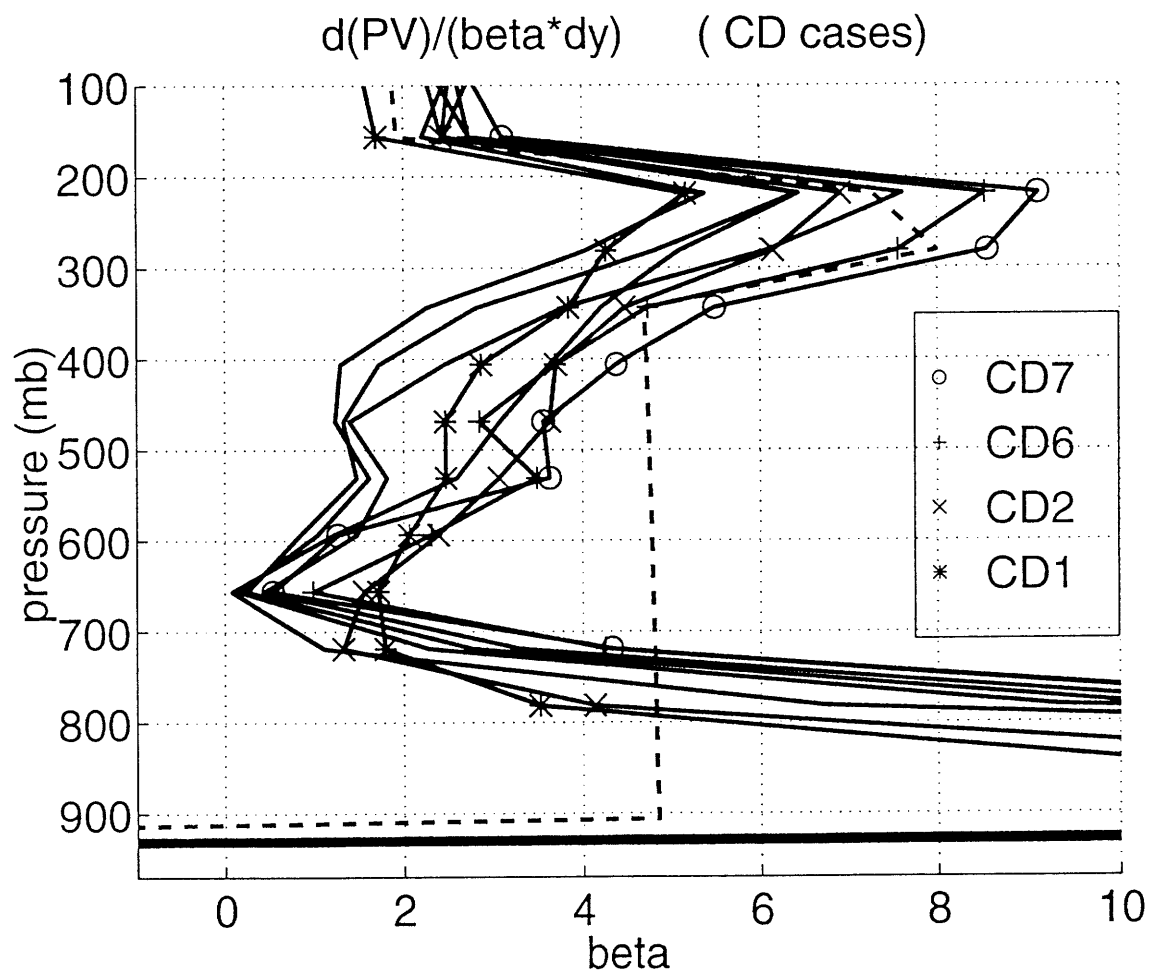
Figure 6-9: Comparison of the equilibrated pv gradients
above the ABL at the center of the channel for runs CD1-
CD7, in units of β.
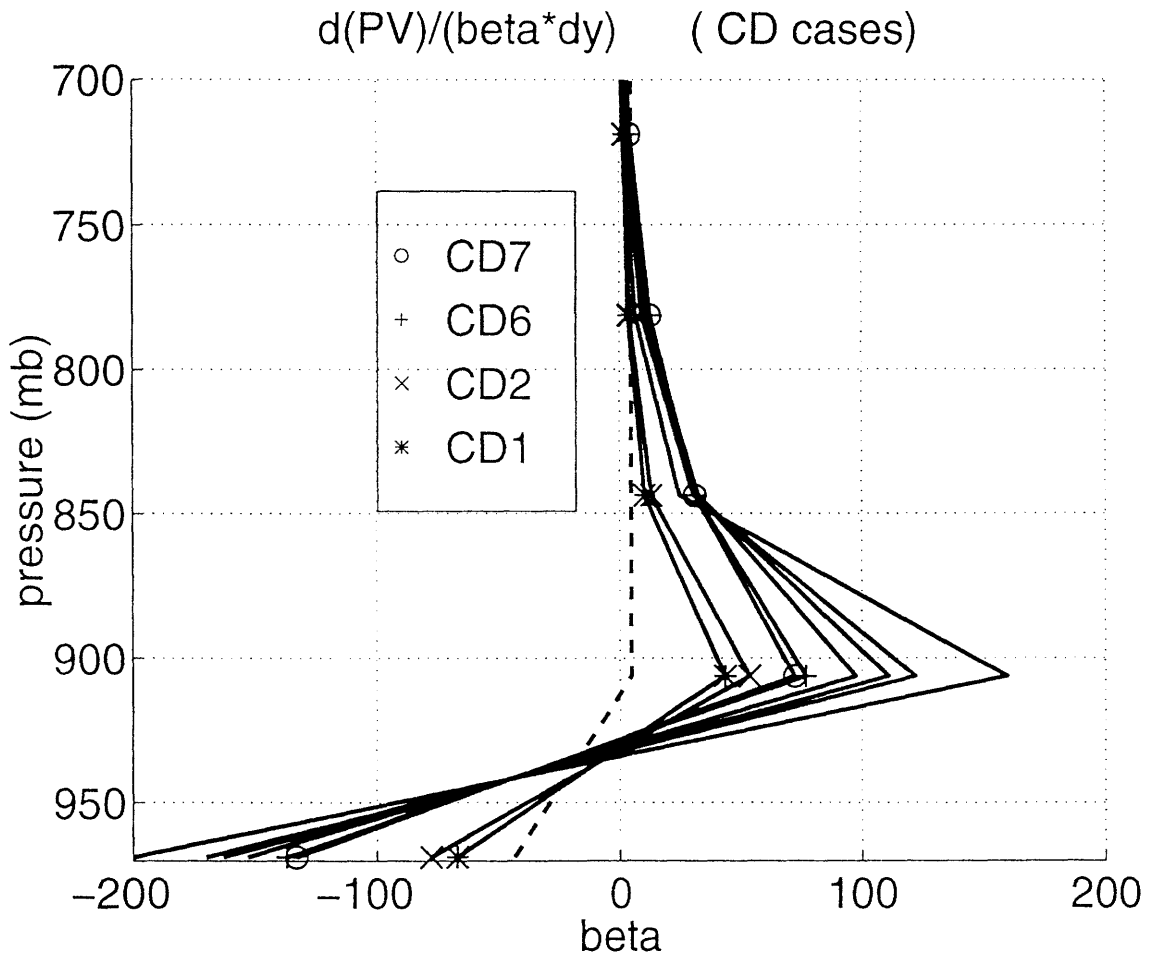
Figure 6-10: Comparison of the equilibrated pv gradients within the ABL at the center of the channel for runs CD1-CD7, in units of β.
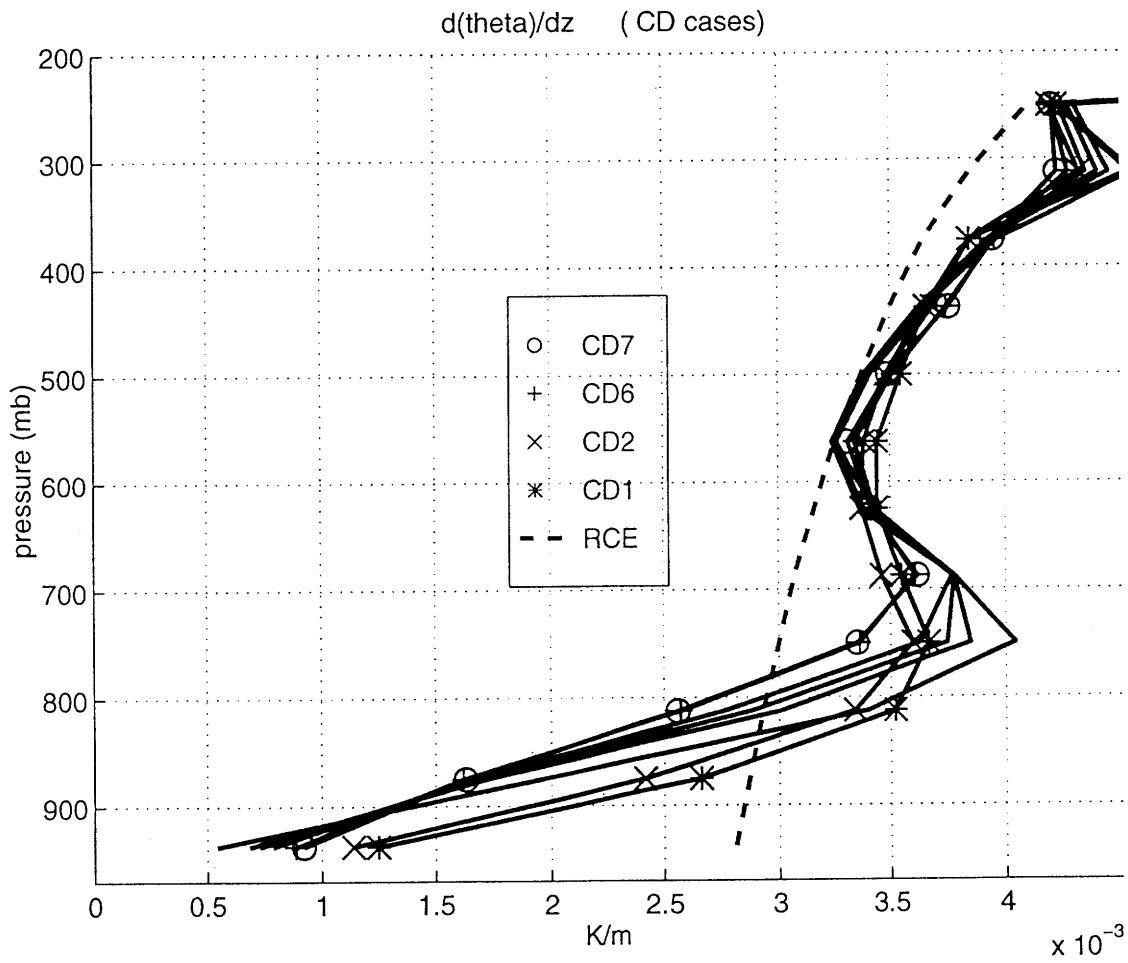
Figure 6-11: Comparison of the equilibrated static stability
at the center of the channel for runs CD1-CD7.
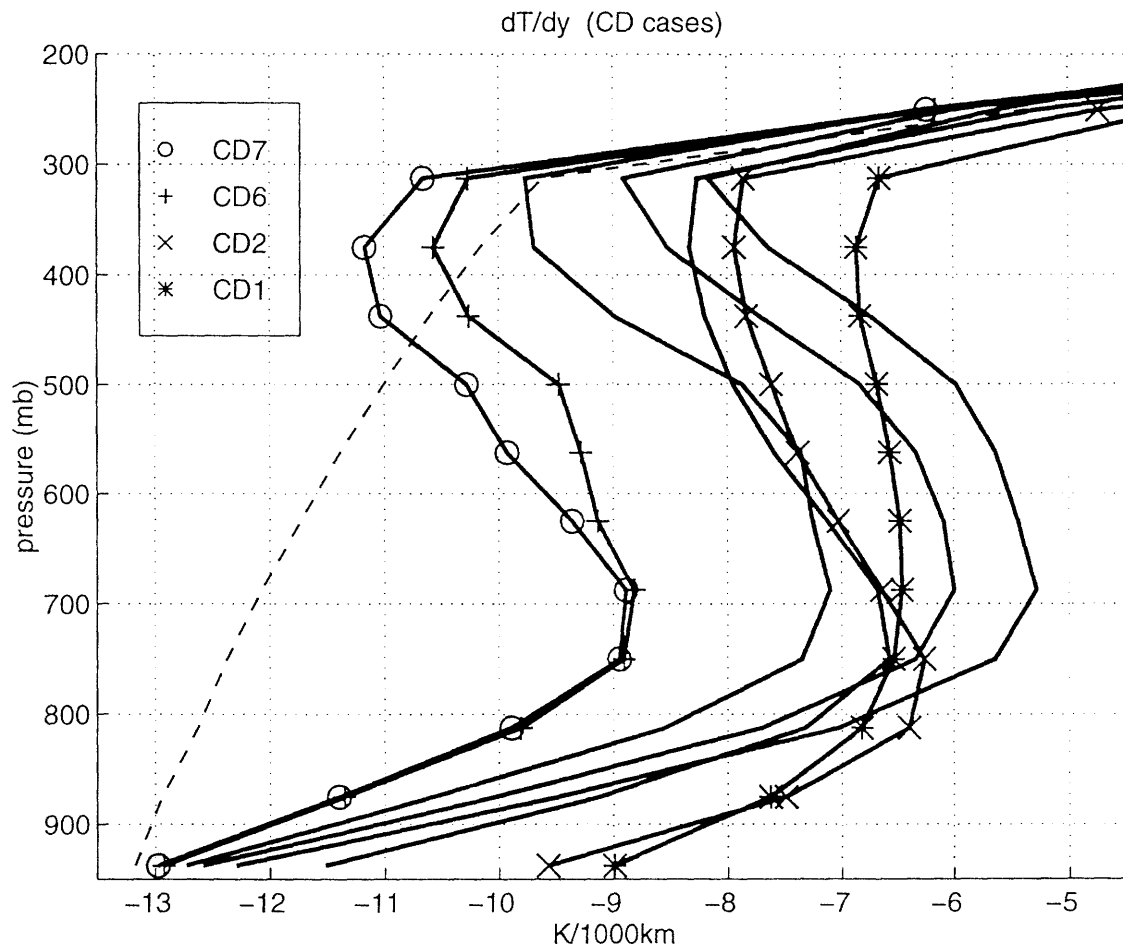
Figure 6-12: Comparison of the equilibrated meridional temperature gradients at the center of the channel for runs CD1-CD7.
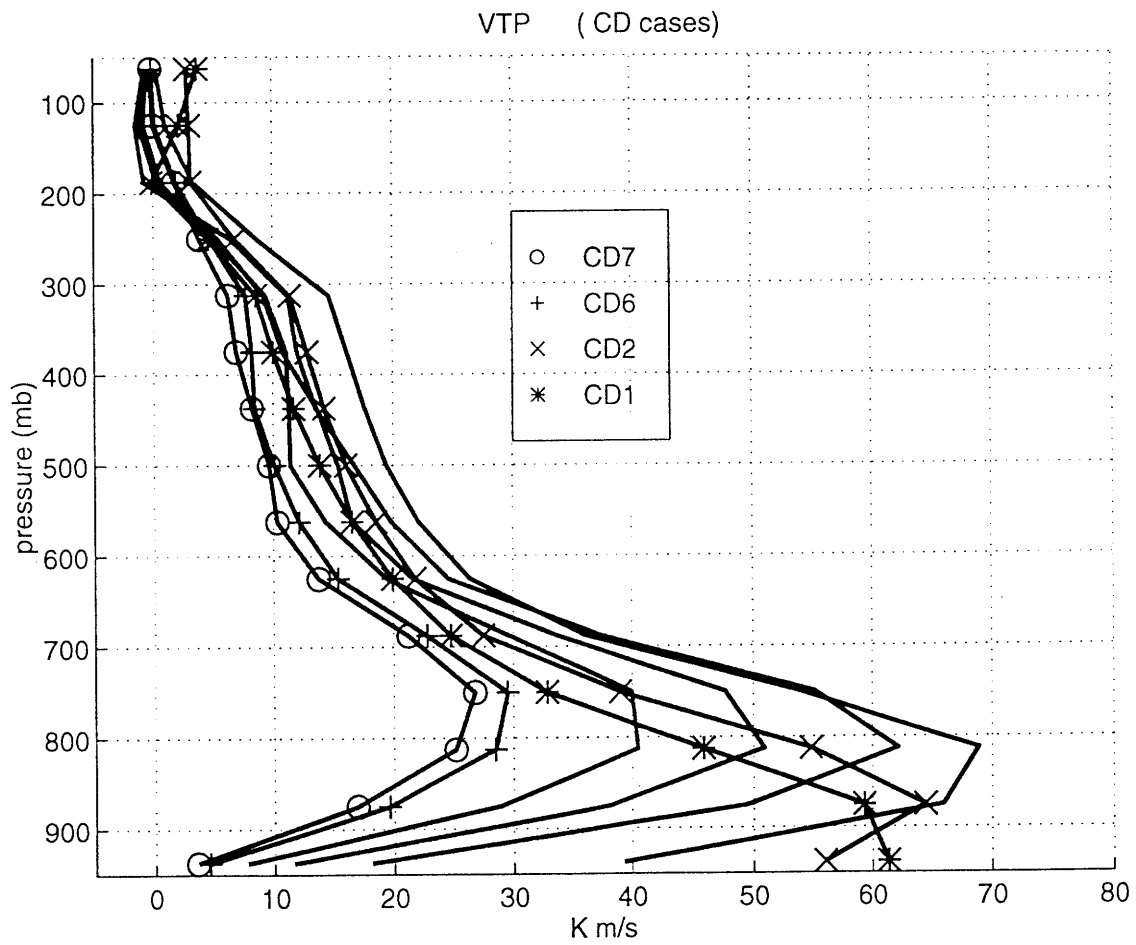
Figure 6-13: Comparison of the equilibrated meridional eddy
heat fluxes at the center of the channel for runs CD1-CD7.
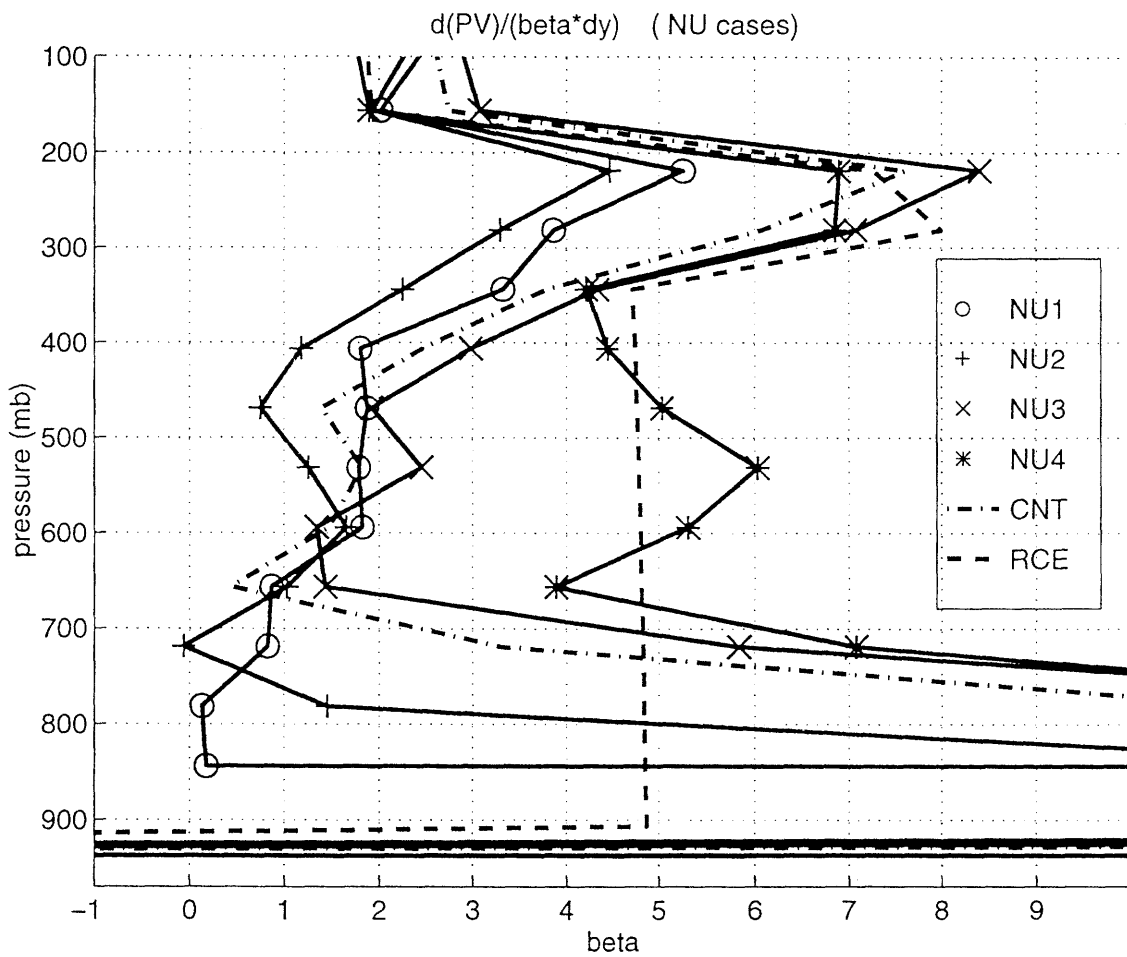
Figure 6-14: Comparison of the equilibrated pv gradients above the ABL at the center of the channel for runs NU1-NU4, in units of β.
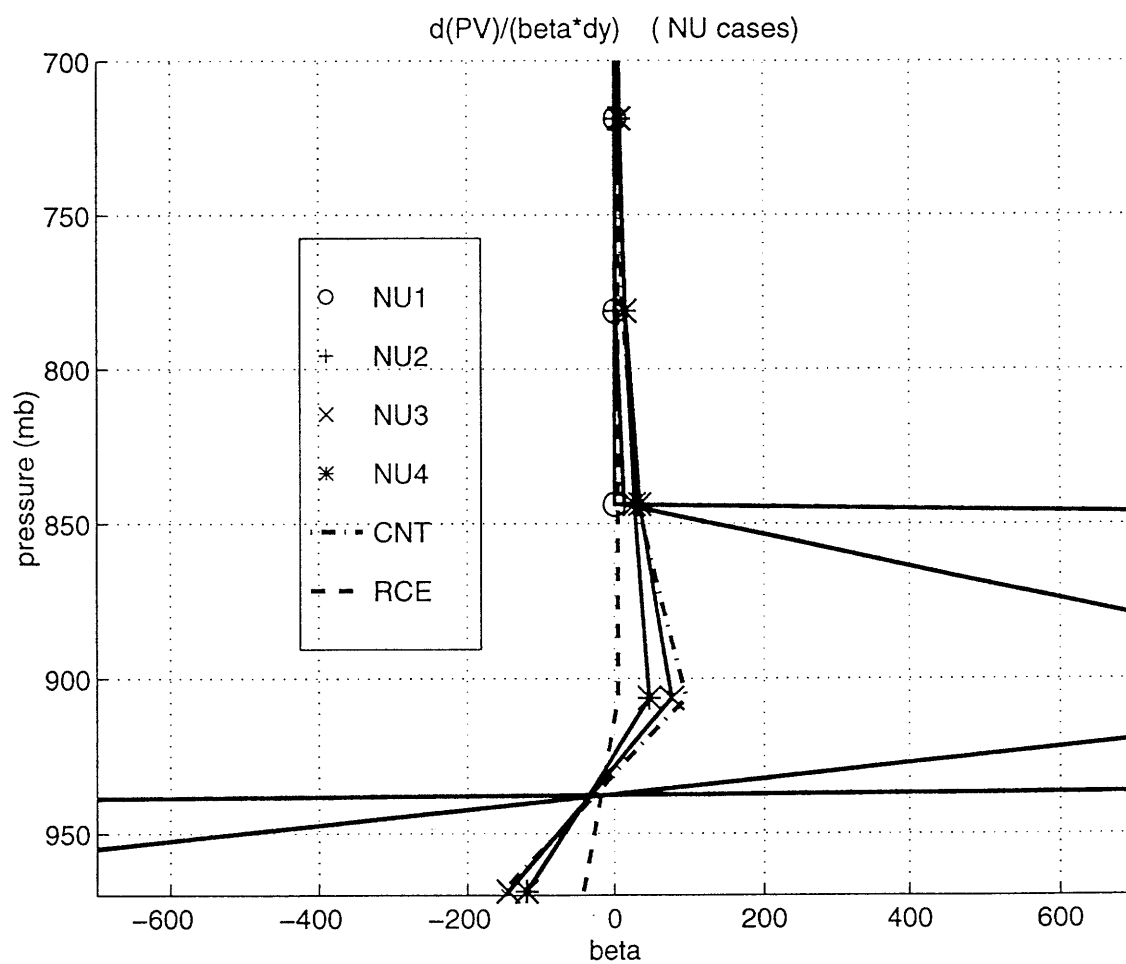
Figure 6-15: Comparison of the equilibrated pv gradients in the ABL at the center of the channel for runs NU1-NU4, in units of β.
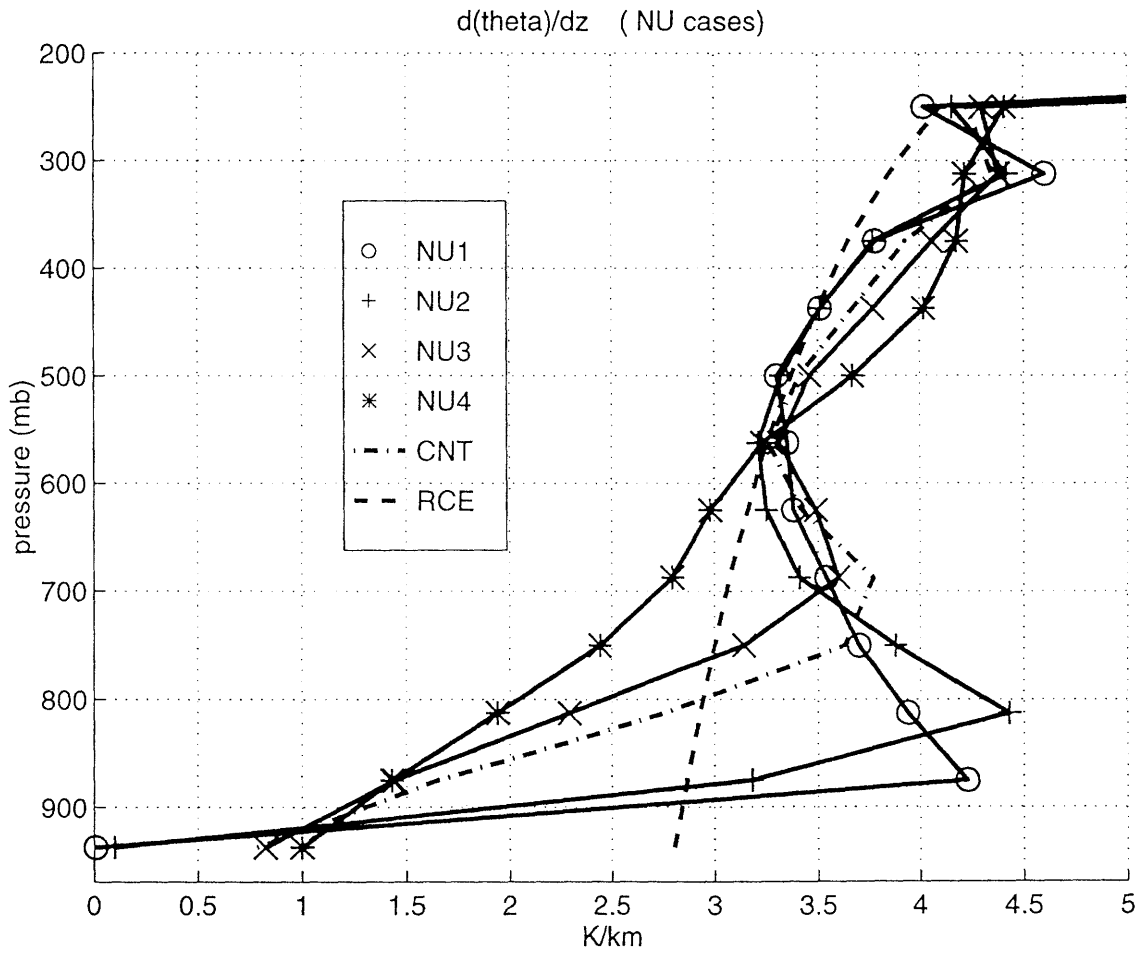
Figure 6-16: Comparison of the equilibrated static stability
at the center of the channel for runs NU1-NU4.
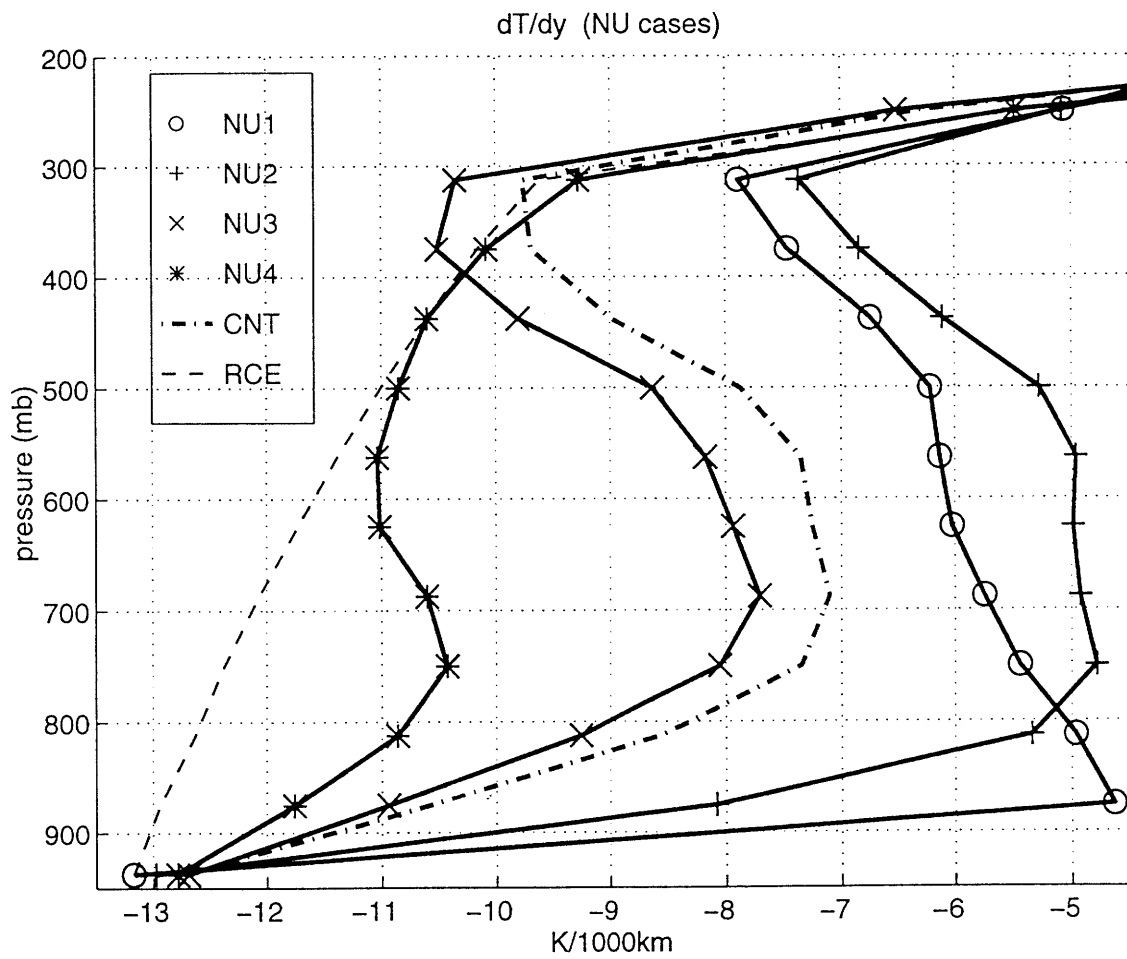
Figure 6-17: Comparison of the equilibrated meridional temperature gradients at the center of the channel for runs NU1-NU4.
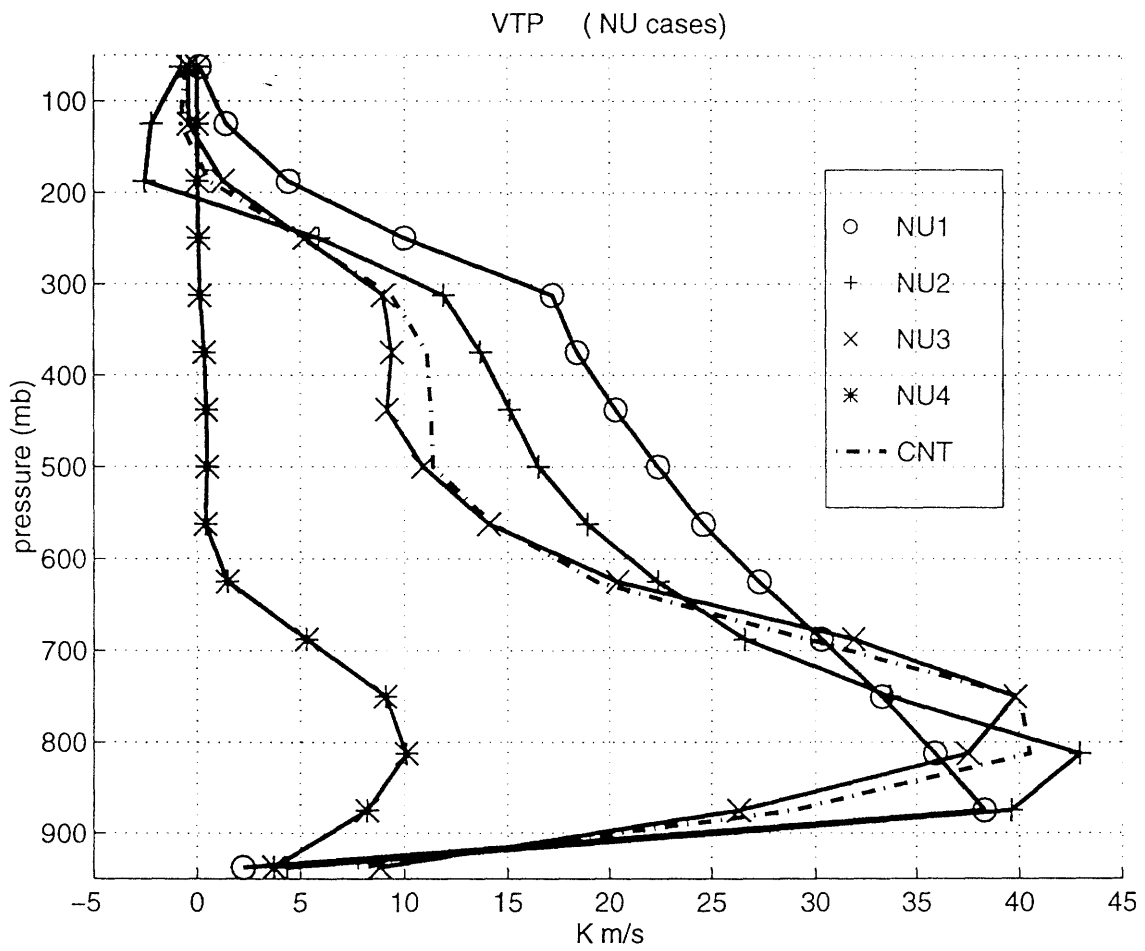
Figure 6-18: Comparison of the equilibrated meridional eddy
heat fluxes at the center of the channel for runs NU1-NU4.
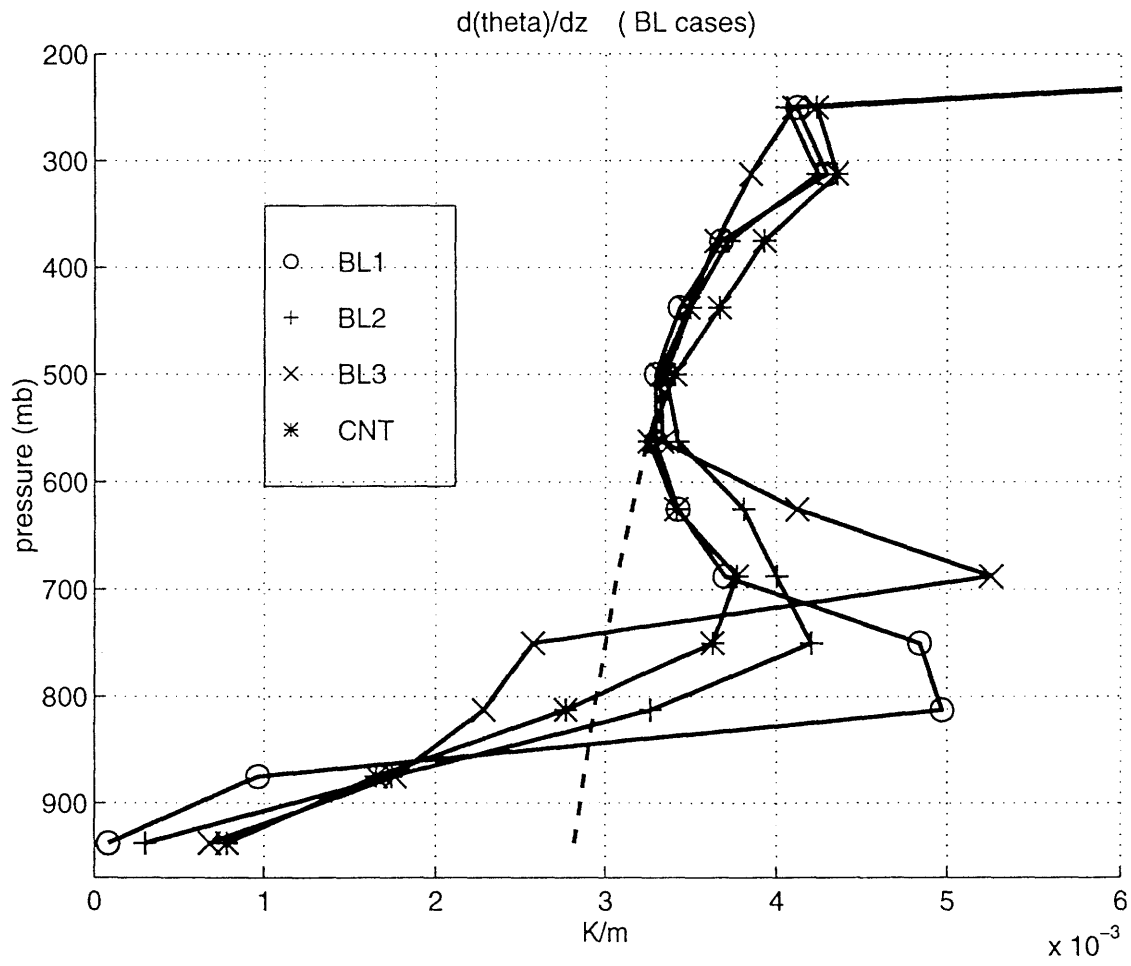
Figure 6-19: Comparison of the equilibrated static stability
at the center of the channel for runs BL1-BL3.
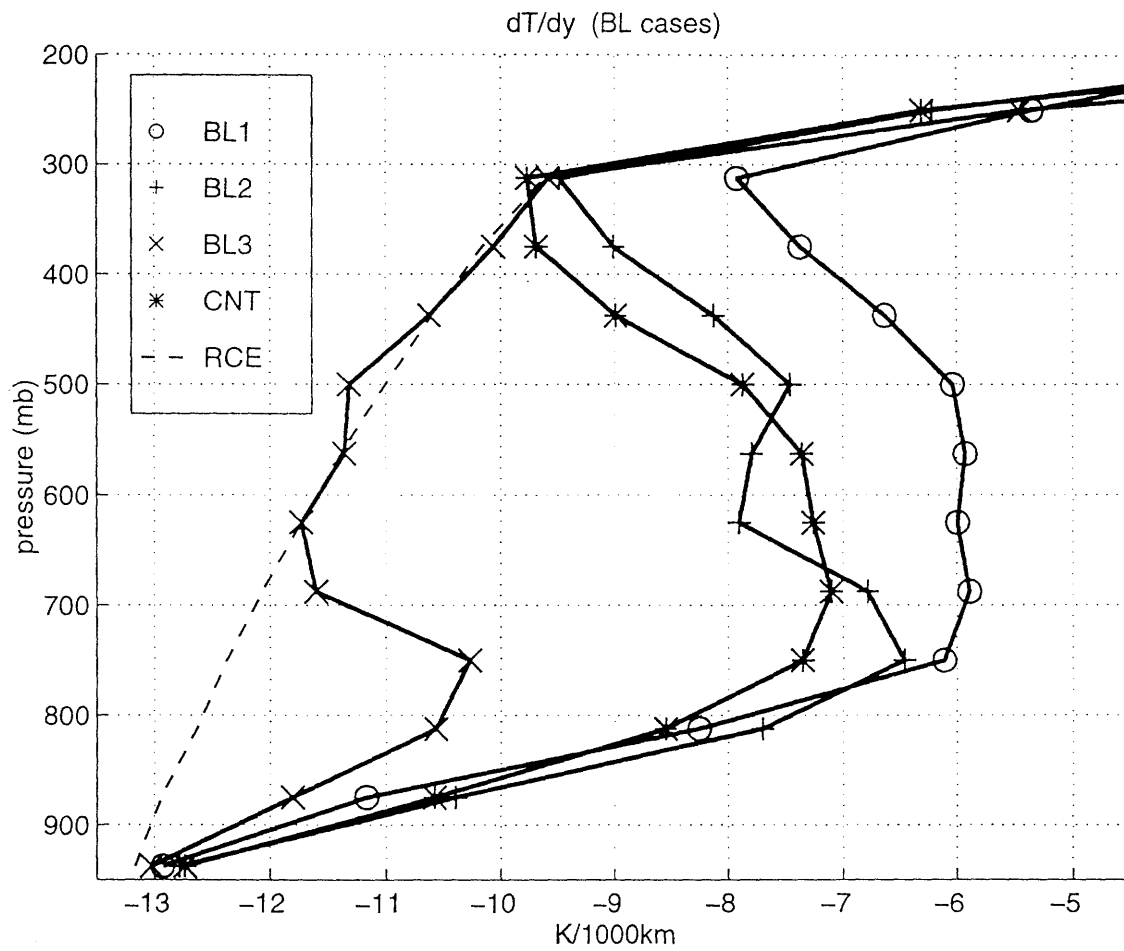
Figure 6-20: Comparison of the equilibrated meridional temperature gradients at the center of the channel for runs BL1-BL3.
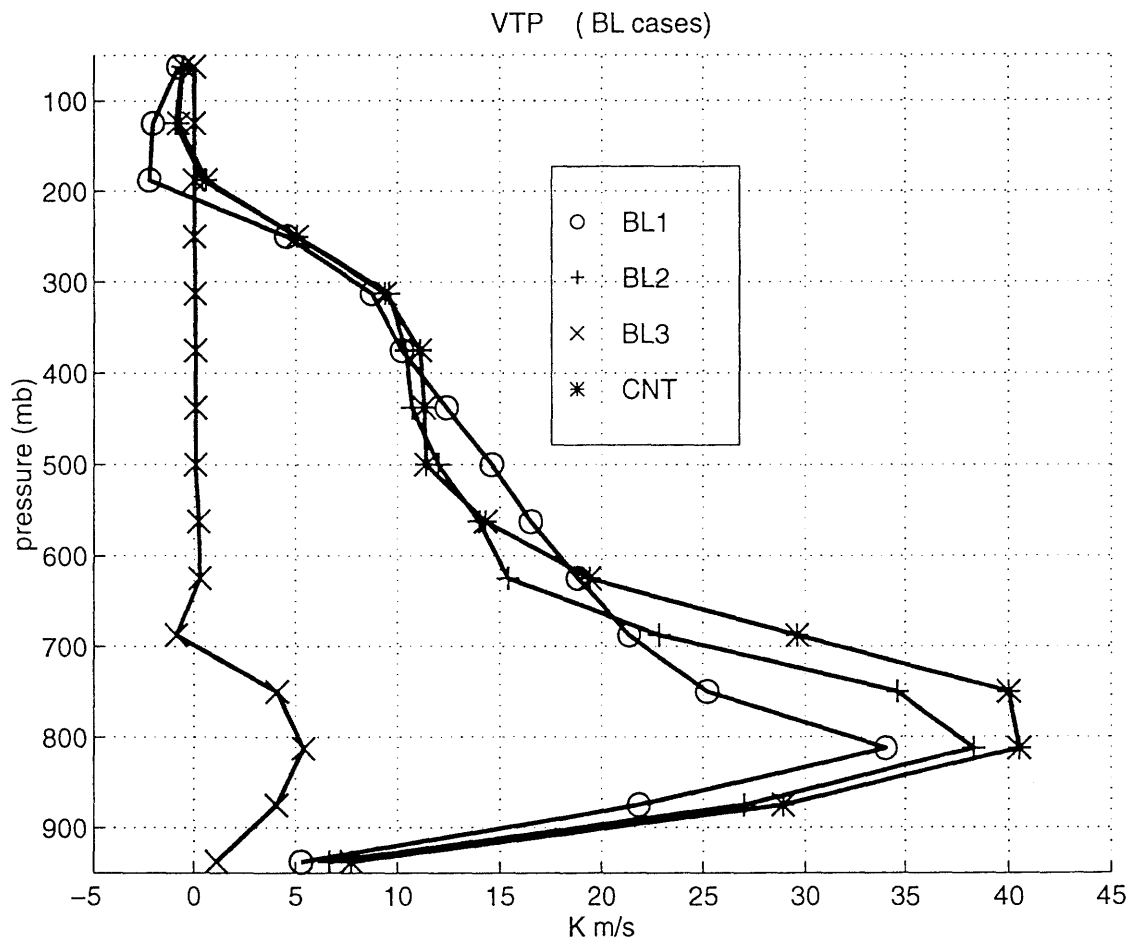
Figure 6-21: Comparison of the equilibrated meridional eddy
heat fluxes at the center of the channel for runs BL1-BL3.
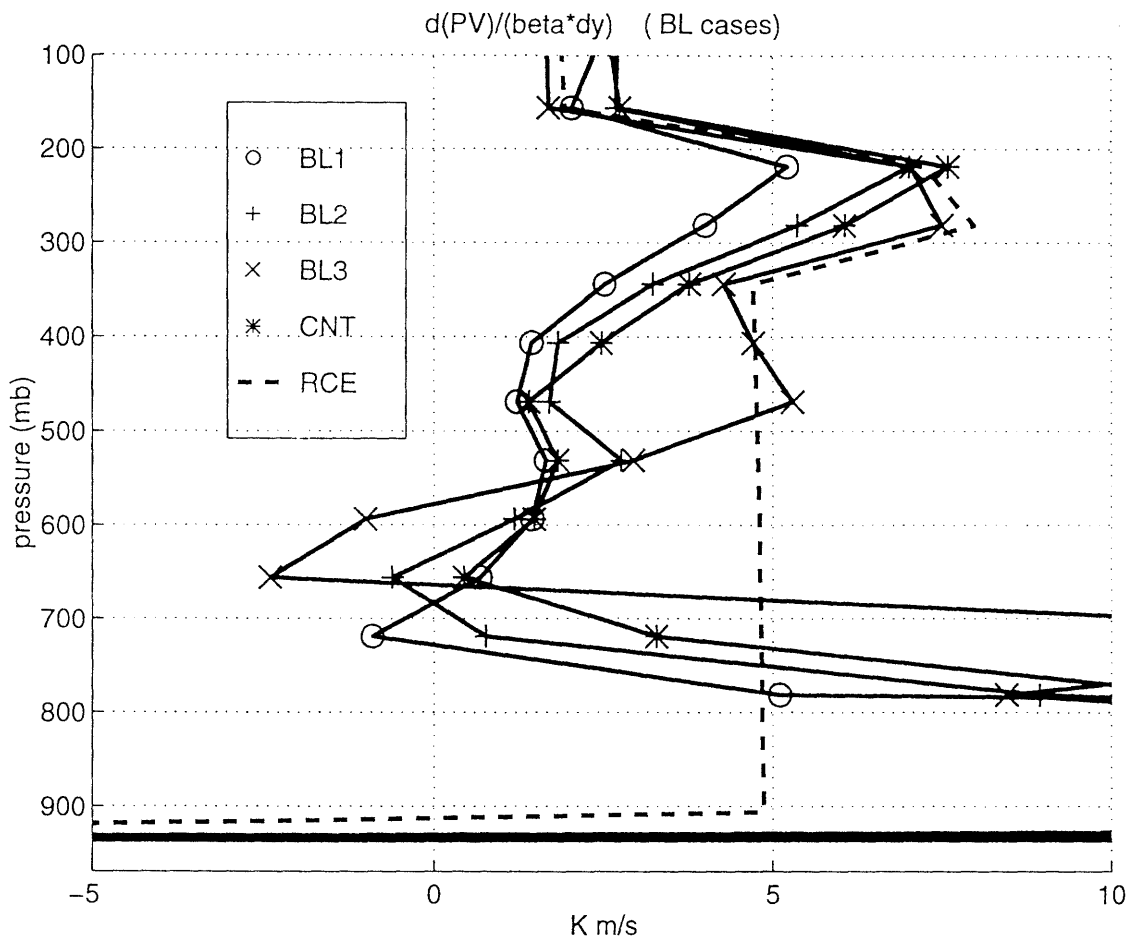
Figure 6-22: Comparison of the equilibrated pv gradients above the ABL at the center of the channel for runs BL1-BL3, in units of β.
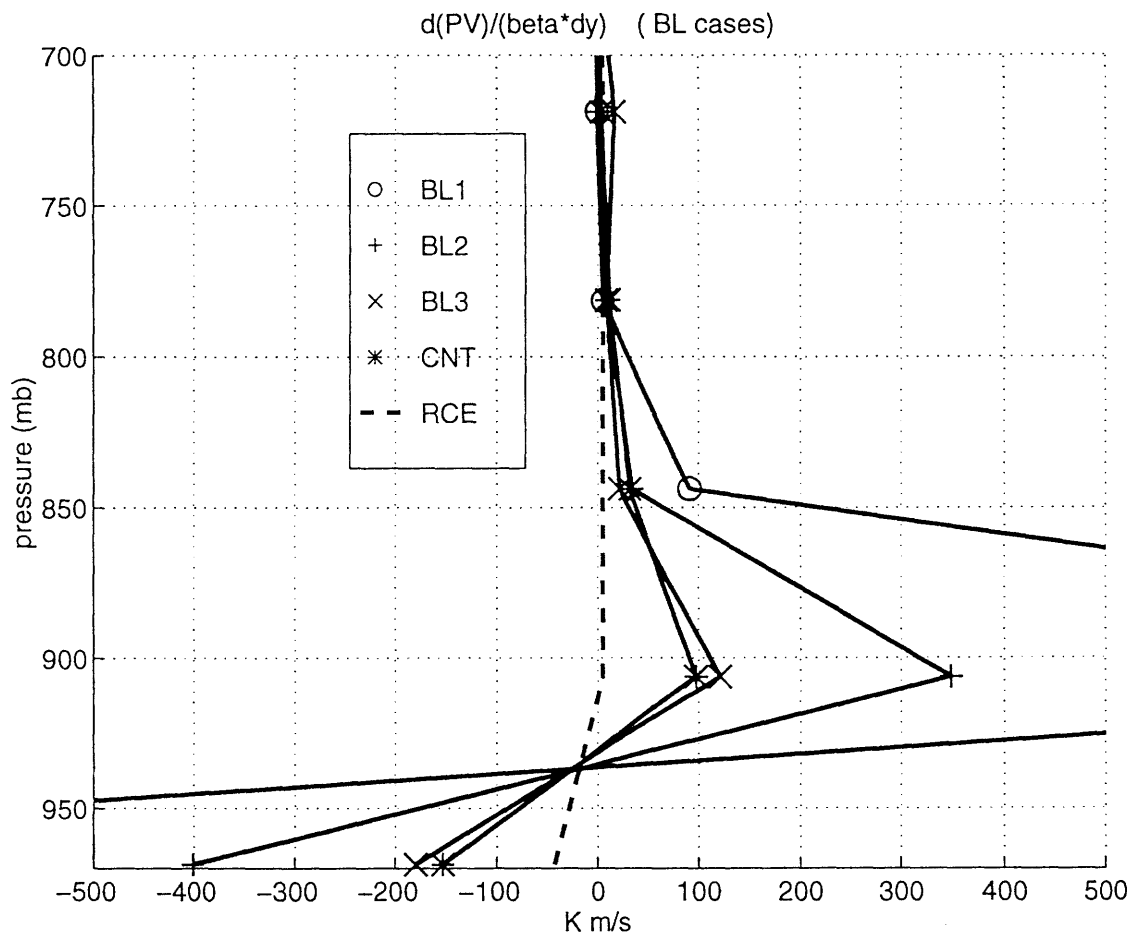
Figure 6-23: Comparison of the equilibrated pv gradients in the ABL at the center of the channel for runs BL1-BL3, in units of β.

6.3   Winds and temperature in the ABL

6.3.1   The Ekman momentum approximation

This Section shows how including the ageostrophic terms in the ABL which are necessary to resolve an Ekman spiral modify the results of the control run. Figures 6-24, 6-25, and 6-26 show the terms in the qg vorticity equation. The equation is divided into the first-order terms in the equation within the ABL, which are, the coriolis force, and the vertical diffusion due to the geostrophic winds, and the vertical diffusion due to the ageostrophic winds, respectively. The other terms in the equation are found to be at least an order of magnitude smaller than these terms (figure not shown). These figures show that the ageostrophic winds cause the total friction to be reduced by a factor of two. The ageostrophic winds are only significant in the friction at the first model level.

Figure 6-27 shows the latitudinal pressure cross-section of the pv gradients in the equilibrated state with the ageostrophic winds included in the vertical diffusion of momentum. This figure shows that the vertical structure at the center of the channel is qualitatively the same as the control run (Figure 3-10). Compared to the control run, the pv gradients are larger in the ABL and more broadly distributed near the tropopause. Otherwise, the general features of large pv gradients within the ABL, complete homogenization just above the ABL, and pv gradients close to radiative equilibrium near the tropopause are robust. The zonal mean geostrophic winds increase by a factor of two at the surface.

Although, the zonal mean state was found to be relatively insensitive to the ageostrophic winds in the friction, the mean fluxes are not. The vertical eddy heat flux. the meridional eddy heat flux, and the momentum flux all increase by 50% (figures not shown), but the vertical distribution of these fluxes are unchanged.

All of these results, the increase the magnitude of the fluxes, the larger geostrophic wind and pv gradients within the ABL, are consistent with a decrease in the drag coefficient by a factor of two. In order to demonstrate this conclusion Figures 6-28 and 6-29 show the pv gradients within and above the ABL, respectively, for two values of the surface drag, cd = 0.05 designated by x's and cd = 0.03 designated by o's, and the control run including ageostrophic winds in the vertical diffusion of momentum, designated by +'s. These figures show that the pv gradients of the control run, which has a surface drag equal to 0.06, with the Ekman momentum approximation in the ABL are bracketed by the two runs without the Ekman momentum approximation and a surface drag equal to 0.03 and 0.05. This is true above the first two model levels. At the first two model levels the control run with the Ekman momentum approximation has pv gradients that are slightly larger than the other two runs. Figure 6-30 shows same comparison for the meridional heat fluxes. This figure shows that the meridional heat fluxes of the control run plus the Ekman momentum approximation above the ABL are closely approximated by the run which has a surface drag equal to 0.03. Within the ABL, the meridional heat fluxes of the control run plus the

Ekman momentum approximation are bracketed by the two runs which vary the surface drag.

Figures 6-31 and 6-32 show the total wind vectors at the surface with and without the ageostrophic friction, respectively. Therefore, both of the figures include the ageostrophic winds but only Figure 6-31 includes the ageostrophic winds in the evaluation of the vertical diffusion of momentum. The winds in Figure 6-31 have a turning angle of 38 degrees at the center of the channel, while the winds from the control run have a turning angle of 28 degrees at the center of the channel. The control run has significant turning of the winds at the surface, but this turning is enhanced when the ageostrophic winds are included in the vertical diffusion of momentum.

Although the control run does not include the first-order balance which defines an Ekman layer, this Section has shown that including the contribution of the ageostrophic winds to the vertical diffusion of momentum does not qualitatively change the equilibrated state of the control run. Including the ageostrophic winds in the vertical diffusion was found to be equivalent to decreasing the surface drag by a factor of two.

6.3.2 Surface wind and temperature formulations

In order to demonstrate the significance of including an equation for the surface air temperature tendency and an equation which explicitly resolves an Ekman layer, three different runs are compared in this Section. The first run is the control run which neglects both the interactive surface air temperature tendency equation and the terms which are needed to explicitly resolve an Ekman layer. The second run is the control run coupled to an equation for the surface air temperature tendency. The third run looks at the combined impact of both the interactive surface air temperature tendency equation and the Ekman momentum approximation. Figure 6-33 shows a comparison of the meridional eddy heat fluxes for these three different runs. Figure 6-33 shows that the meridional eddy heat fluxes in the ABL are sensitive to the treatment of the surface air temperature, the fluxes being larger at the lowest model level when the surface temperature is allowed to vary independently. All of the runs have peak fluxes at 800 mb but the fluxes from the interactive surface air temperature run are significantly larger below 750 mb than the fluxes of the control run. The interactive fluxes are much less damped in the boundary layer. Above 750 mb, the fluxes of the runs with interactive surface air temperatures are closer to the fluxes of the control run.

Figure 6-34 shows a comparison of the vertical profile of the temperature gradient at the center of the channel for the three runs. This figure shows that the fluxes are not simply related to the meridional temperature gradients. It is seen that the temperature gradients throughout the ABL and lower troposphere are significantly reduced when the surface temperature is allowed to be interactive.

with ageo winds

fdw/dp ZM (1/s*s)

CONTOUR FROM -24 TO 24 BY CONTOUR INTERVAL 2 LABELS SCALED BY 10^{-11}
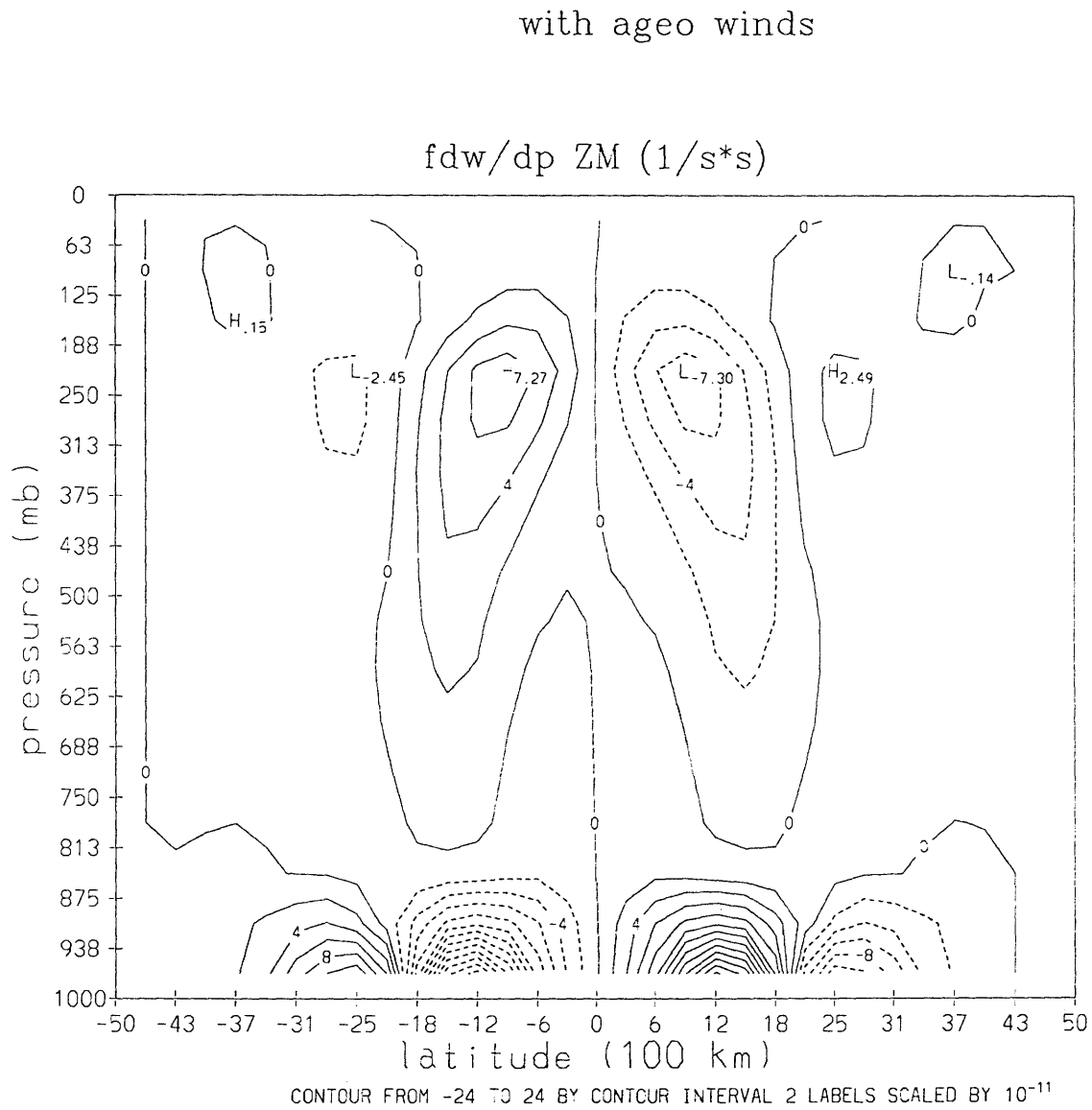
Figure 6-24: The vorticity tendency contribution from the coriolis force, when the ageostrophic winds contribute to the vertical diffusion of momentum.

with ageo winds

Geostrophic Friction   ZM (1/s*s)

CONTOUR FROM −60 TO 60 BY CONTOUR INTERVAL 10 LABELS SCALED BY 10^{-11}
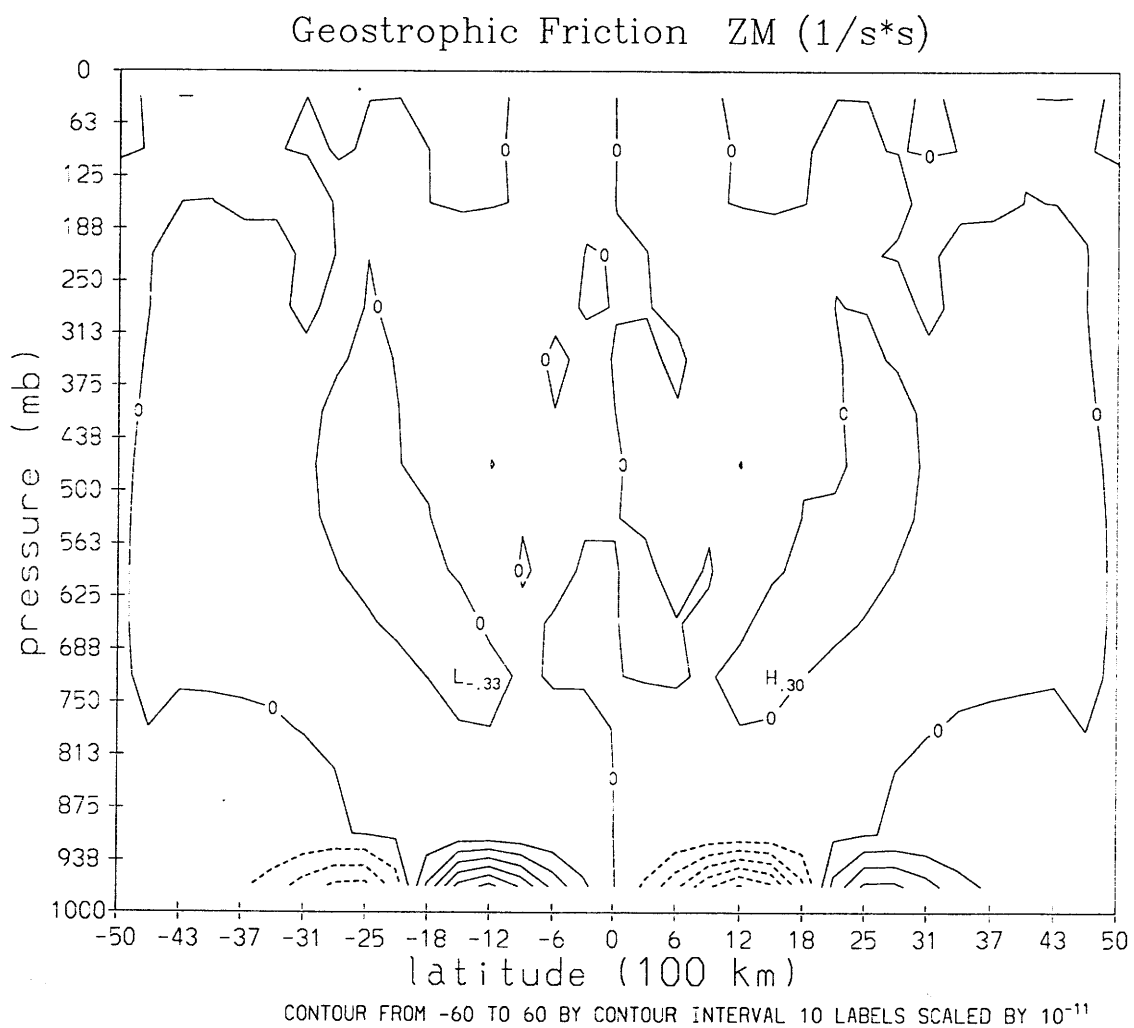
Figure 6-25: The vorticity tendency contribution from the geostrophic friction, when the ageostrophic winds contribute to the vertical diffusion of momentum.

with ageo winds

Ageostrophic Friction   ZM (1/s*s)

CONTOUR FROM -30 TO 30 BY CONTOUR INTERVAL 10 LABELS SCALED BY 10^{-11}
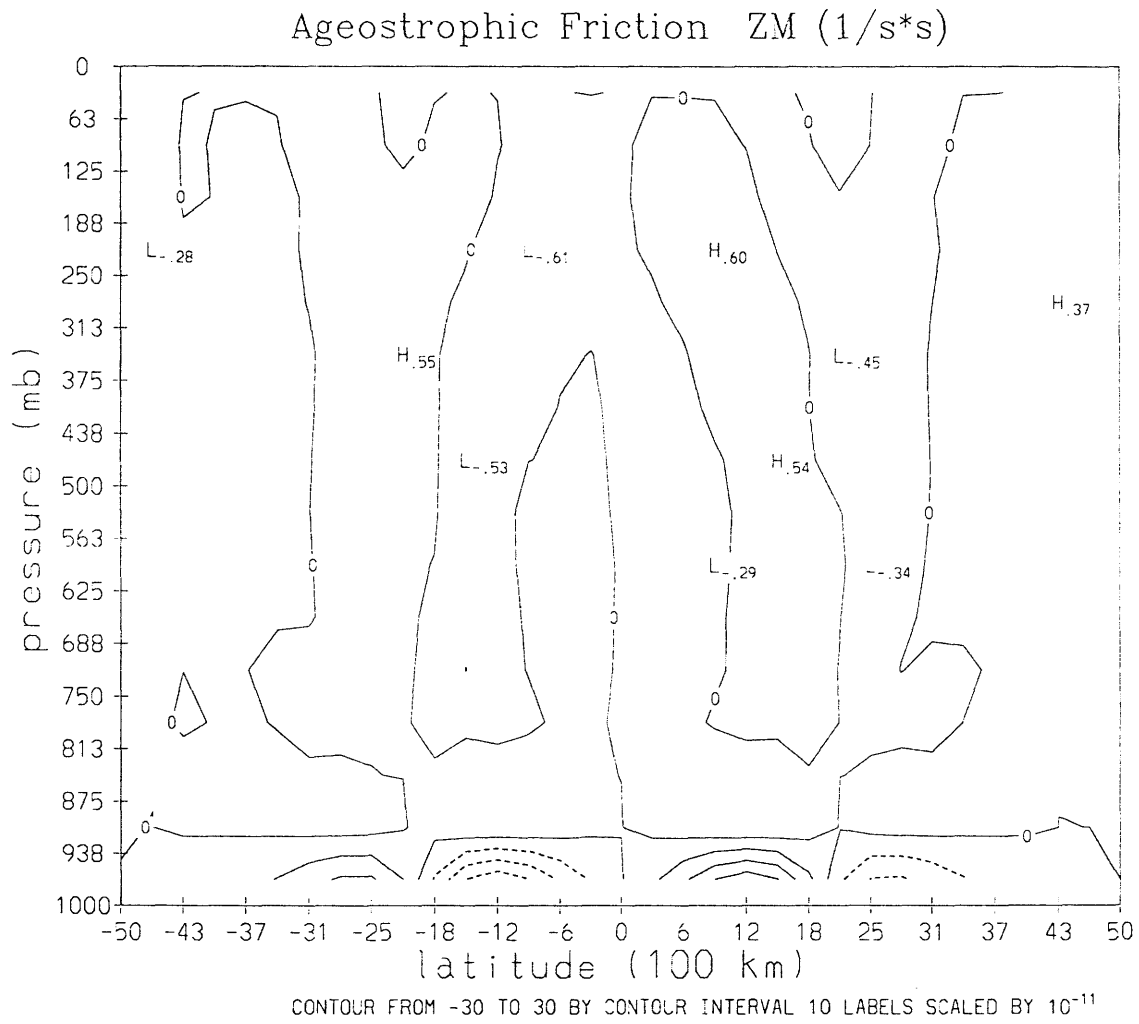
Figure 6-26: The vorticity tendency contribution from the ageostrophic friction, when the ageostrophic winds contribute to the vertical diffusion of momentum.

with ageo winds

d(PV)/d(beta*y)

CONTOUR FROM -171 TO 84 BY CONTOUR INTERVAL 1 LABELS SCALED BY 1
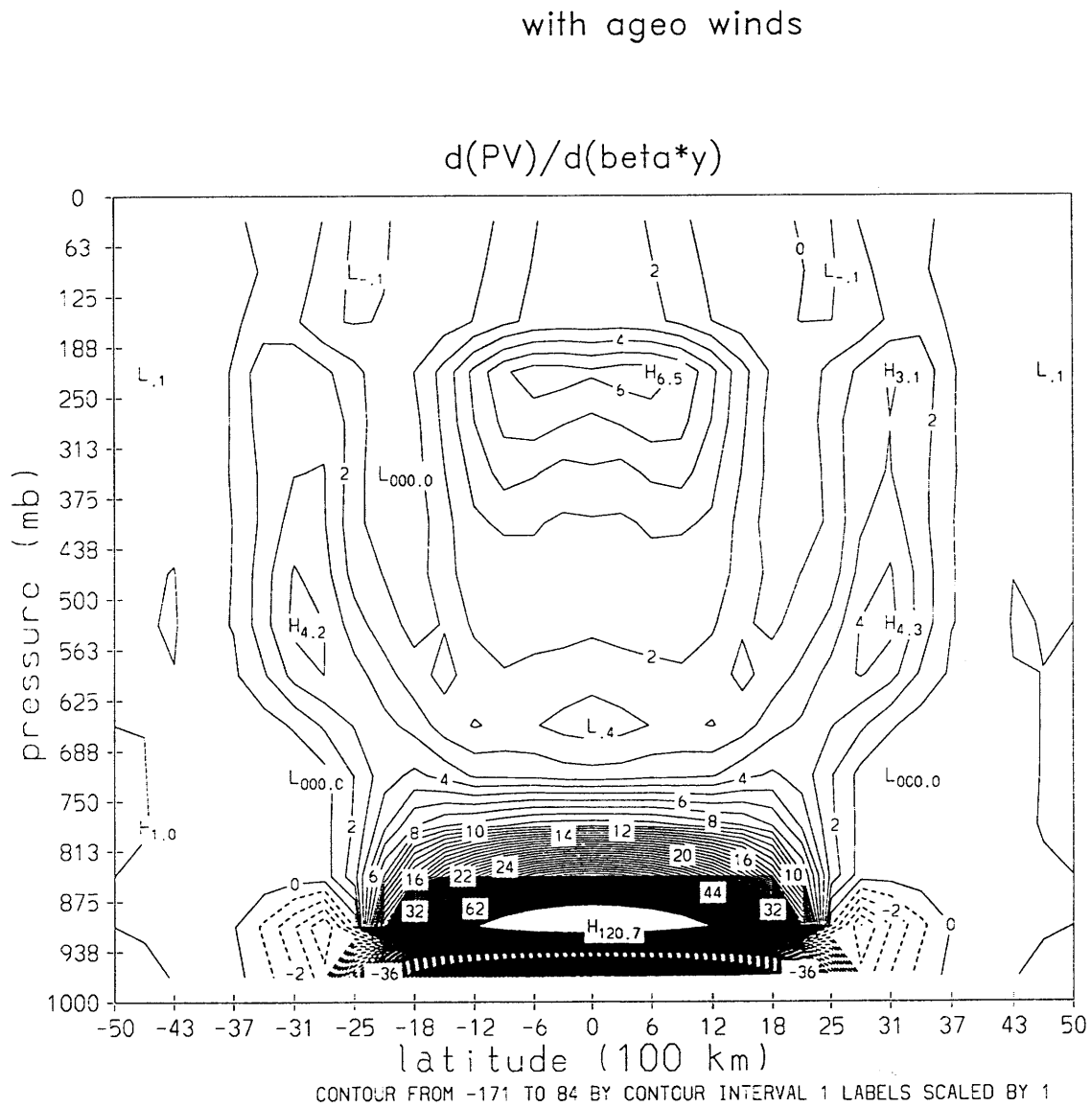
Figure 6-27: Latitudinal pressure cross-section of the equilibrated pv gradients, when the ageostrophic winds contribute to the vertical diffusion of momentum.
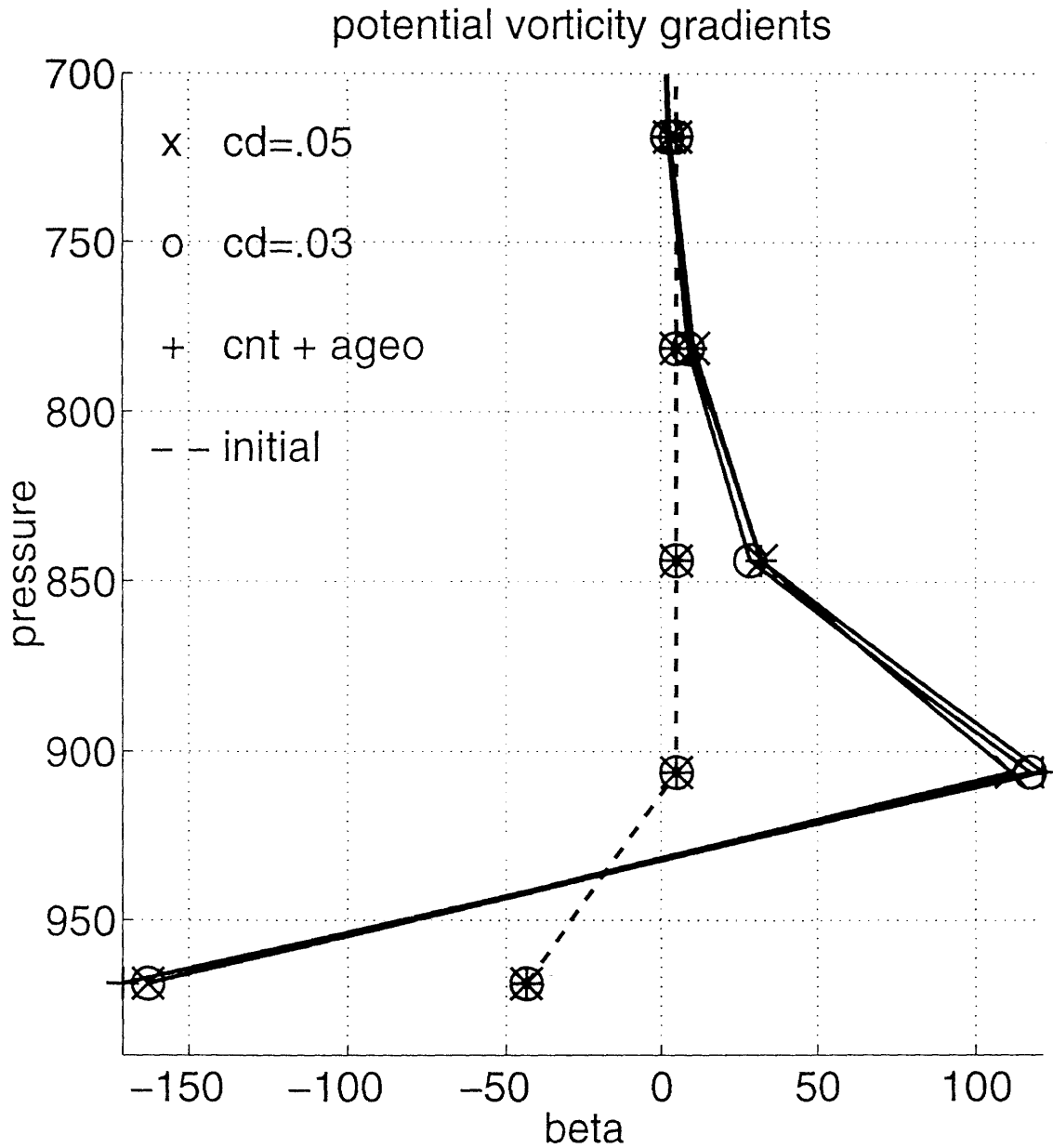
Figure 6-28: Comparison of the equilibrated pv gradients in
the ABL at the center of the channel for two values of the
surface drag (0.05 = x's, 0.03 = o's) and the control run
including ageostrophic winds in the vertical diffusion of mo-
mentum (+'s), in units of β.
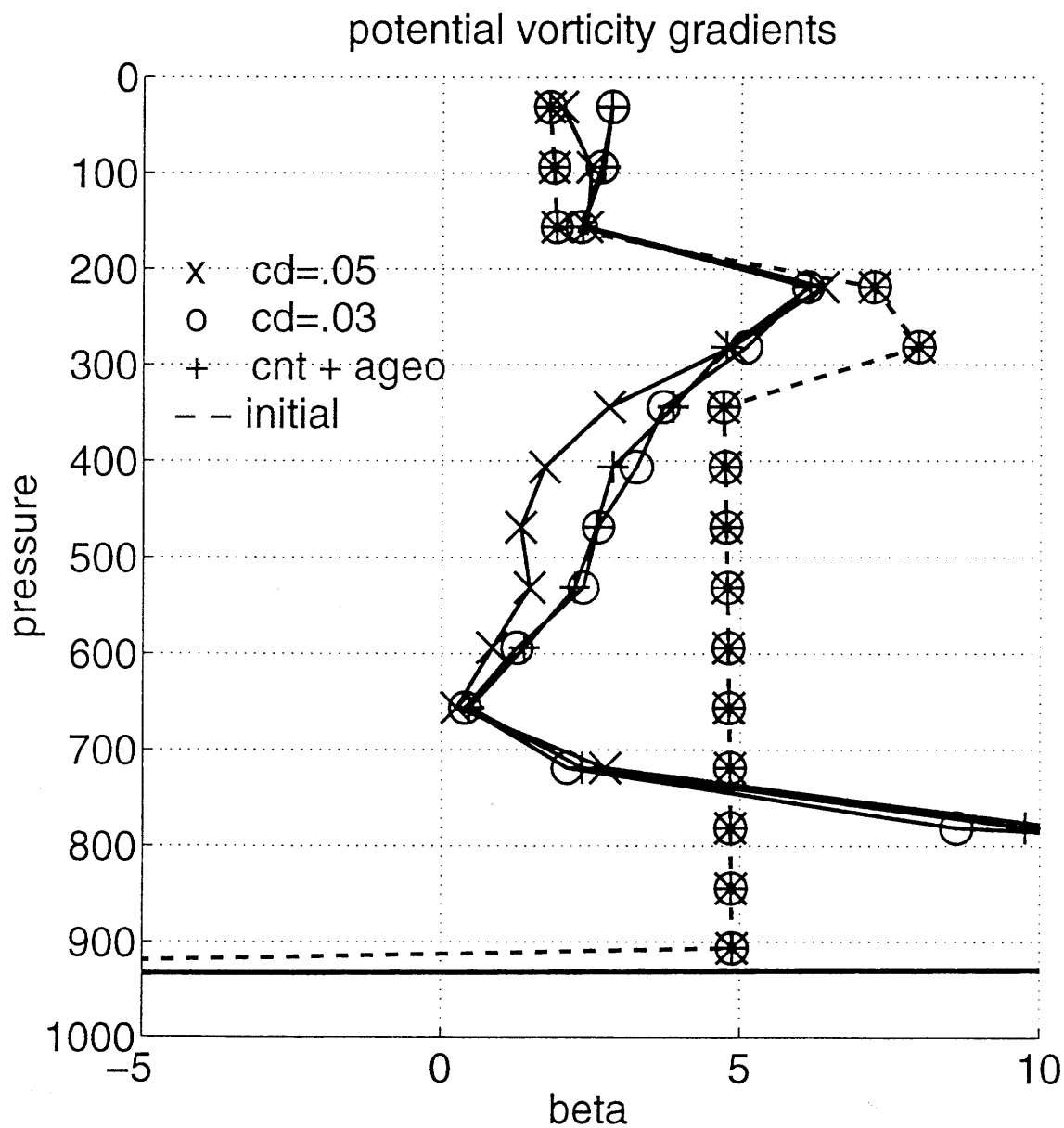
Figure 6-29: Comparison of the equilibrated pv gradients above the ABL at the center of the channel for two values of the surface drag (0.05 = x's, 0.03 = o's) and the control run including ageostrophic winds in the vertical diffusion of momentum (+'s), in units of β.
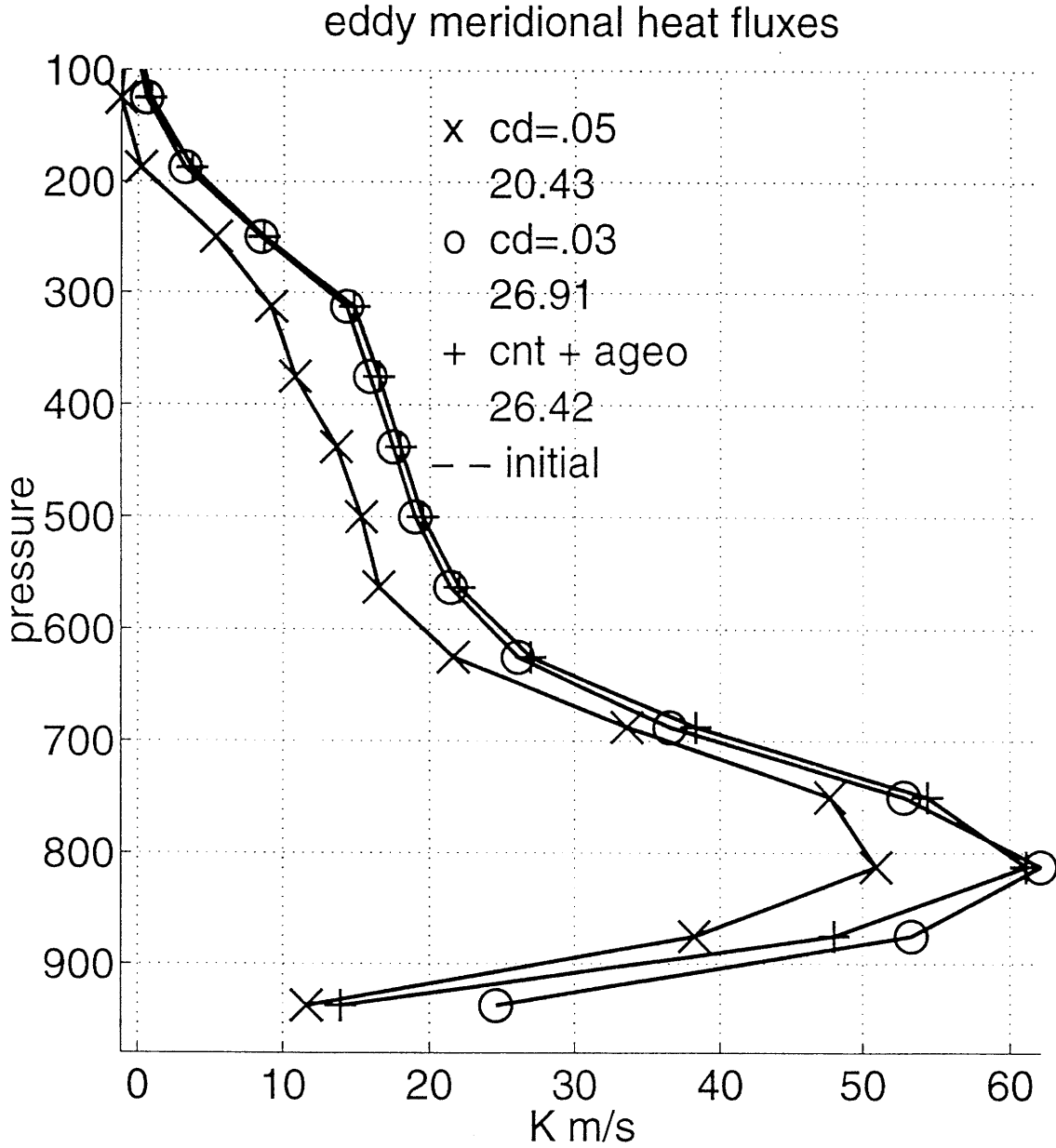
Figure 6-30: Comparison of the meridional eddy heat fluxes at the center of the channel for two values of the surface drag (0.05 = x's, 0.03 = o's) and the control run including ageostrophic winds in the vertical diffusion of momentum (+'s). The numbers in the legend are the vertically averaged meridional eddy potential temperature fluxes at the center of the channel for each run.

with ageo winds

Wind (m/s) 1000.0 m, day   1.0

0.102E+02
MAXIMUM VECTOR
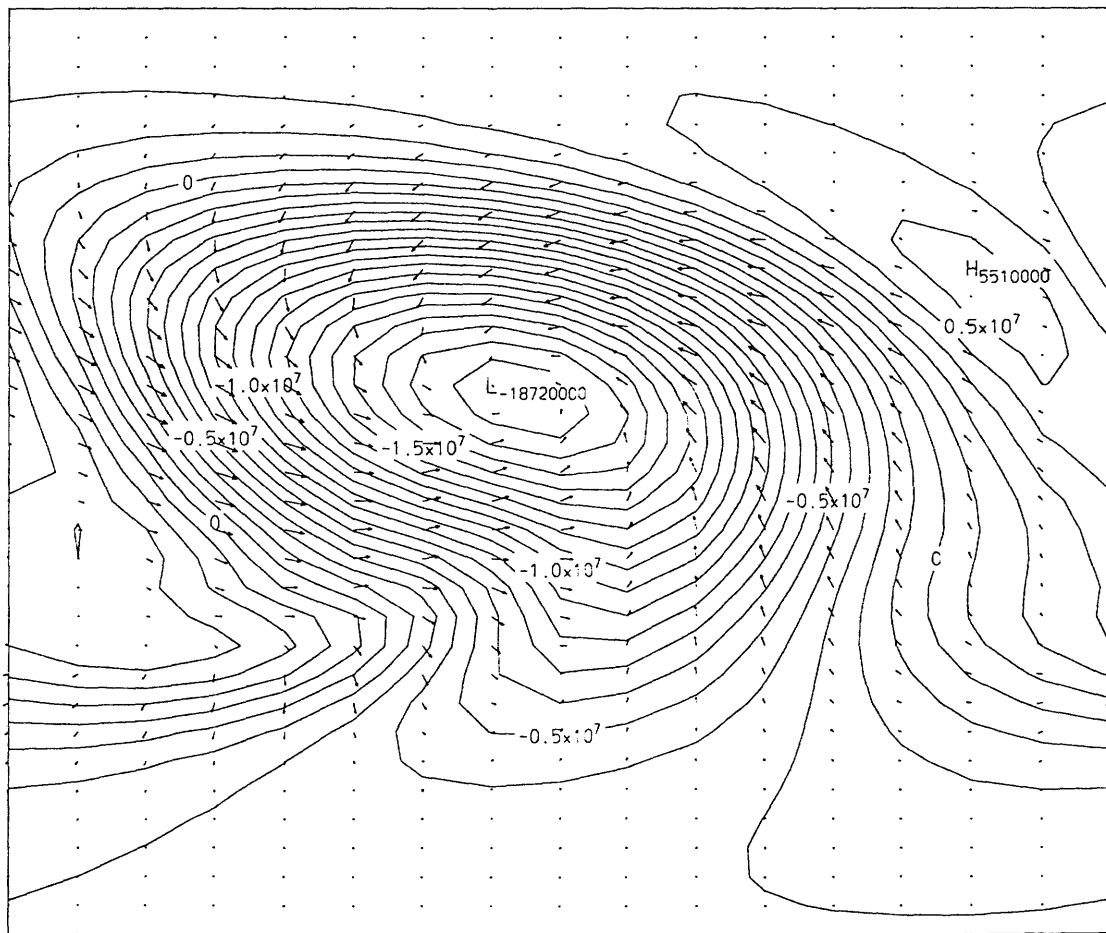
Figure 6-31: Total winds vector on geopotential contours, in units of meters, at 1000 mb, when the ageostrophic winds contribute to the vertical diffusion of momentum.

control run

Wind (m/s) 1000.0 m, day   1.0
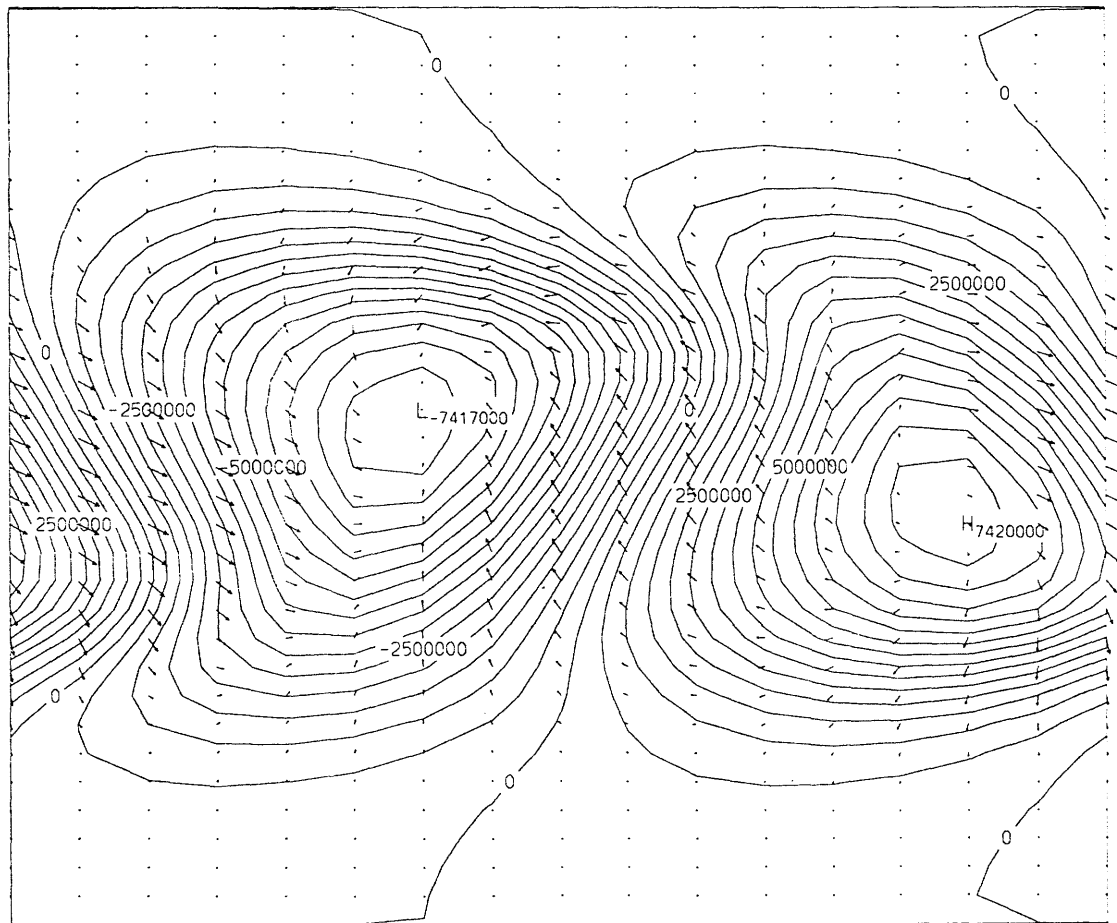
0.171E+02
→
MAXIMUM VECTOR

Figure 6-32: Total winds vector on geopotential contours, in
units of meters, at 1000 mb, for the control run.

The meridional temperature gradients in the ABL are much closer to observations when the surface air temperature is allowed to be interactive.

Figures 6-35 and 6-36 show a comparison of the vertical profile of the pv gradients at the center of the channel for the three runs. The reduction in the temperature gradients with an interactive surface temperature causes the large pv gradients in the ABL to be reduced by a factor of two. The homogenized pv above the ABL is relatively unchanged when the surface temperature is allowed to be interactive. This means that, although the meridional temperature gradients are closer to observations, the static stability is adjusted farther from observations.

This series of runs has shown that the pv and temperature gradients in the ABL are very sensitive to the treatment of the surface air temperature. The pv and temperature gradients above the ABL were shown to be independent to the treatment of the surface air temperature.

eddy meridional heat fluxes

x control
   17.21
o int surf temp (ageo)
   29.47
+ int surf temp
   21.53
– initial

pressure

K m/s
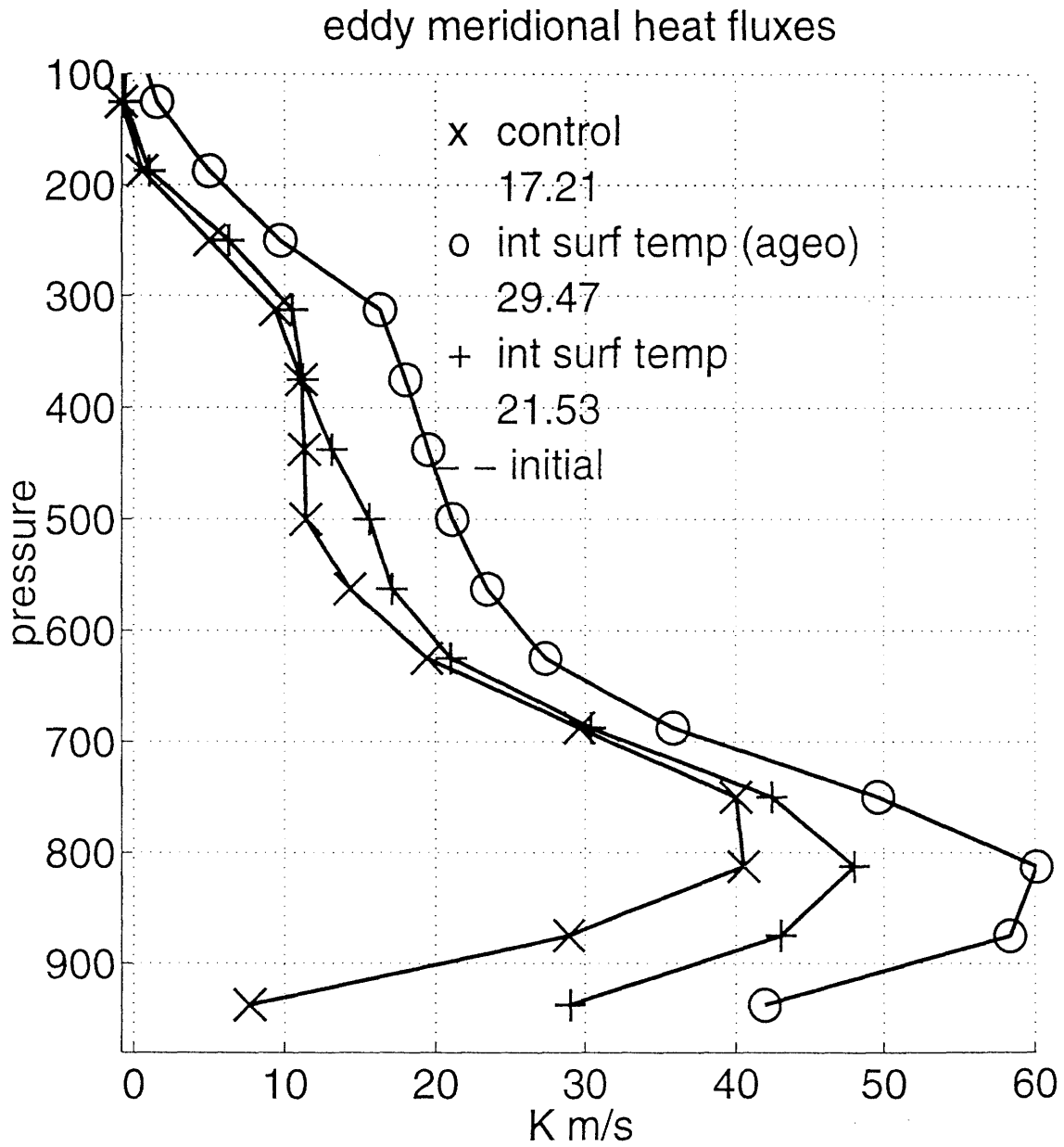
Figure 6-33: Comparison of the meridional eddy heat fluxes for the control and the interactive surface air temperature, with and without ageostrophic friction, runs. The numbers in the legend are the vertically averaged meridional eddy potential temperature fluxes at the center of the channel for each run.
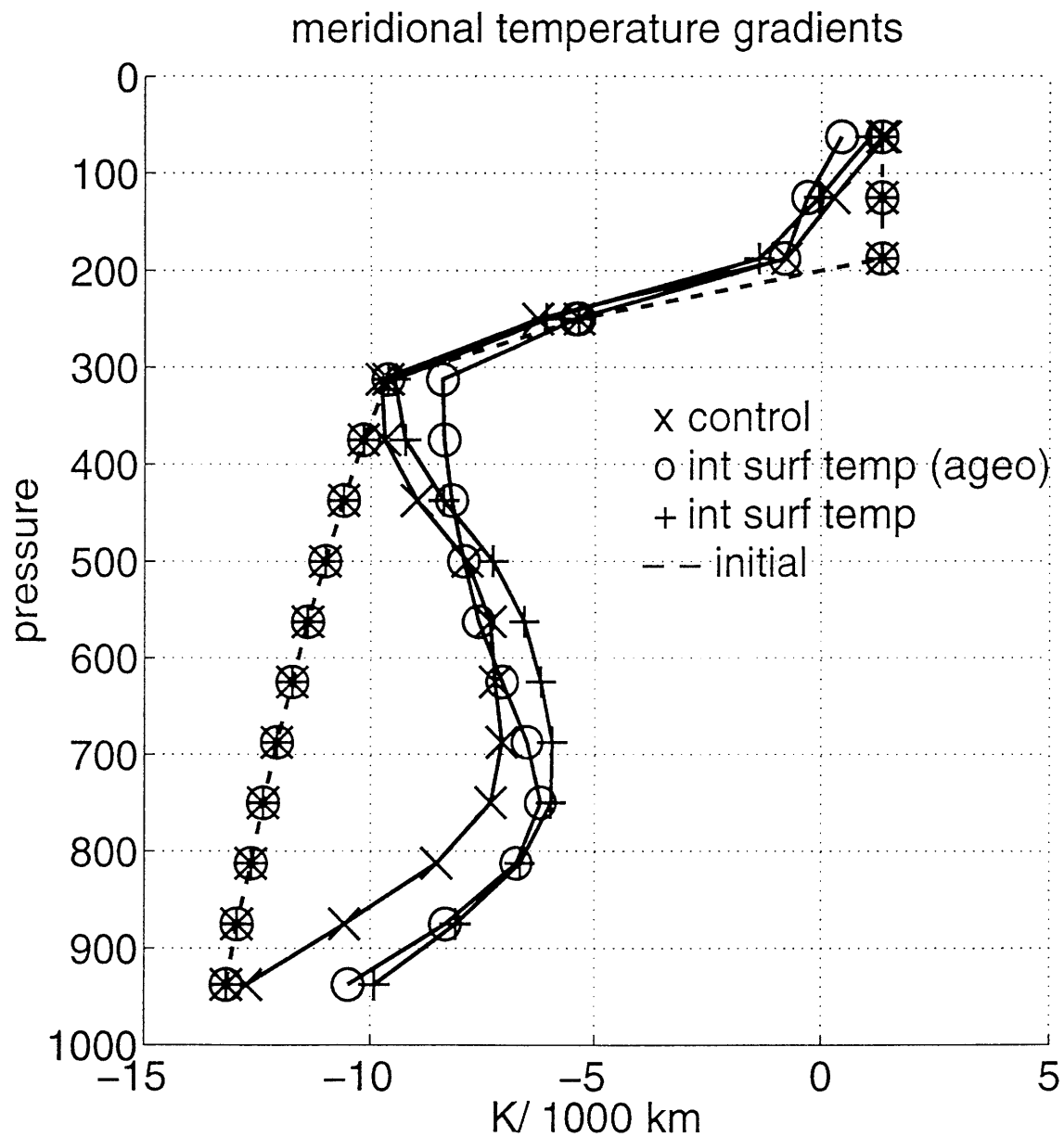
Figure 6-34: Comparison of the meridional temperature gradients for the control run and the interactive surface air temperature, with and without ageostrophic friction, runs.
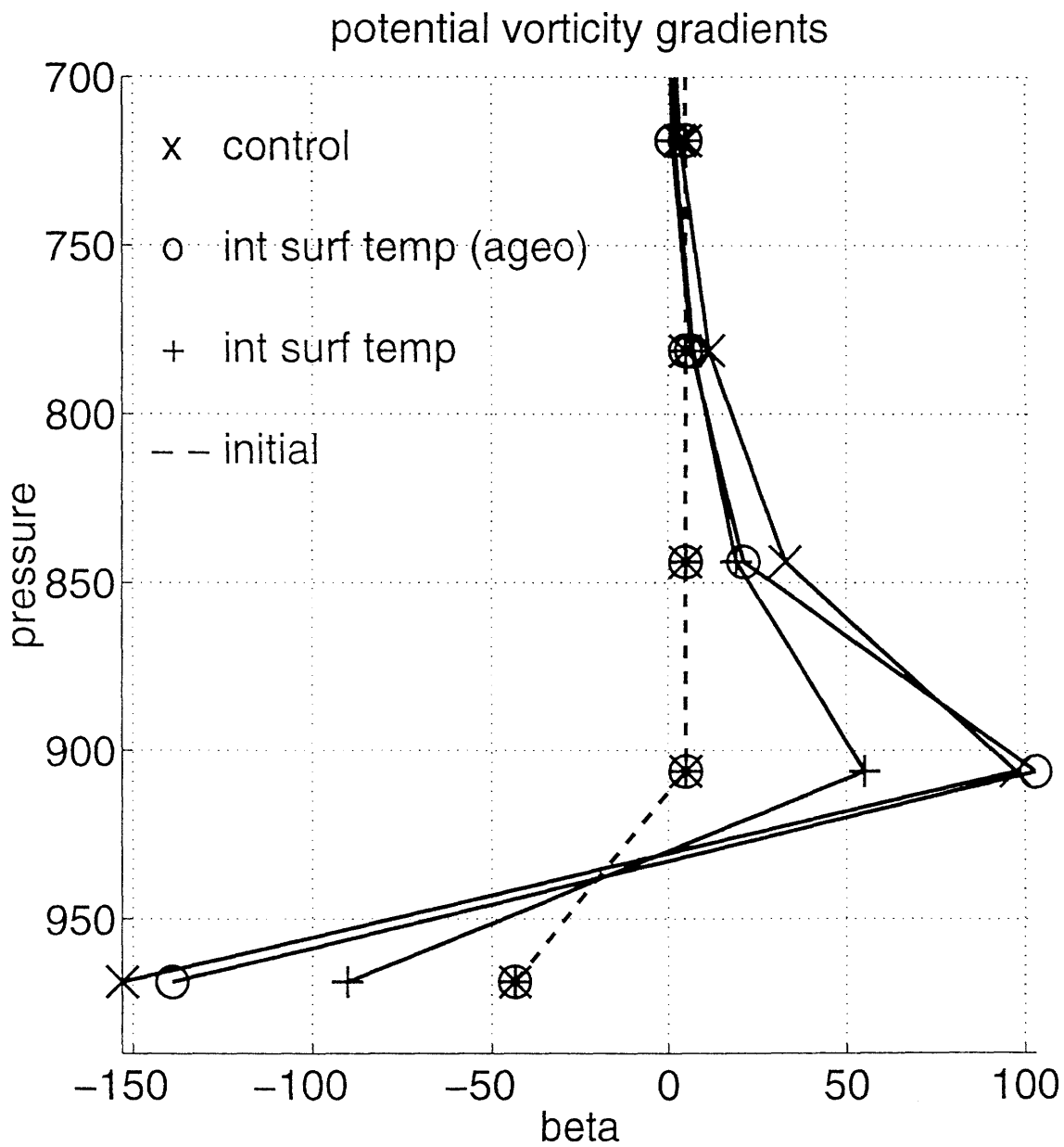
Figure 6-35: Comparison of the meridional pv gradients in the ABL for the control run and the interactive surface air temperature, with and without ageostrophic friction, runs, in units of β.
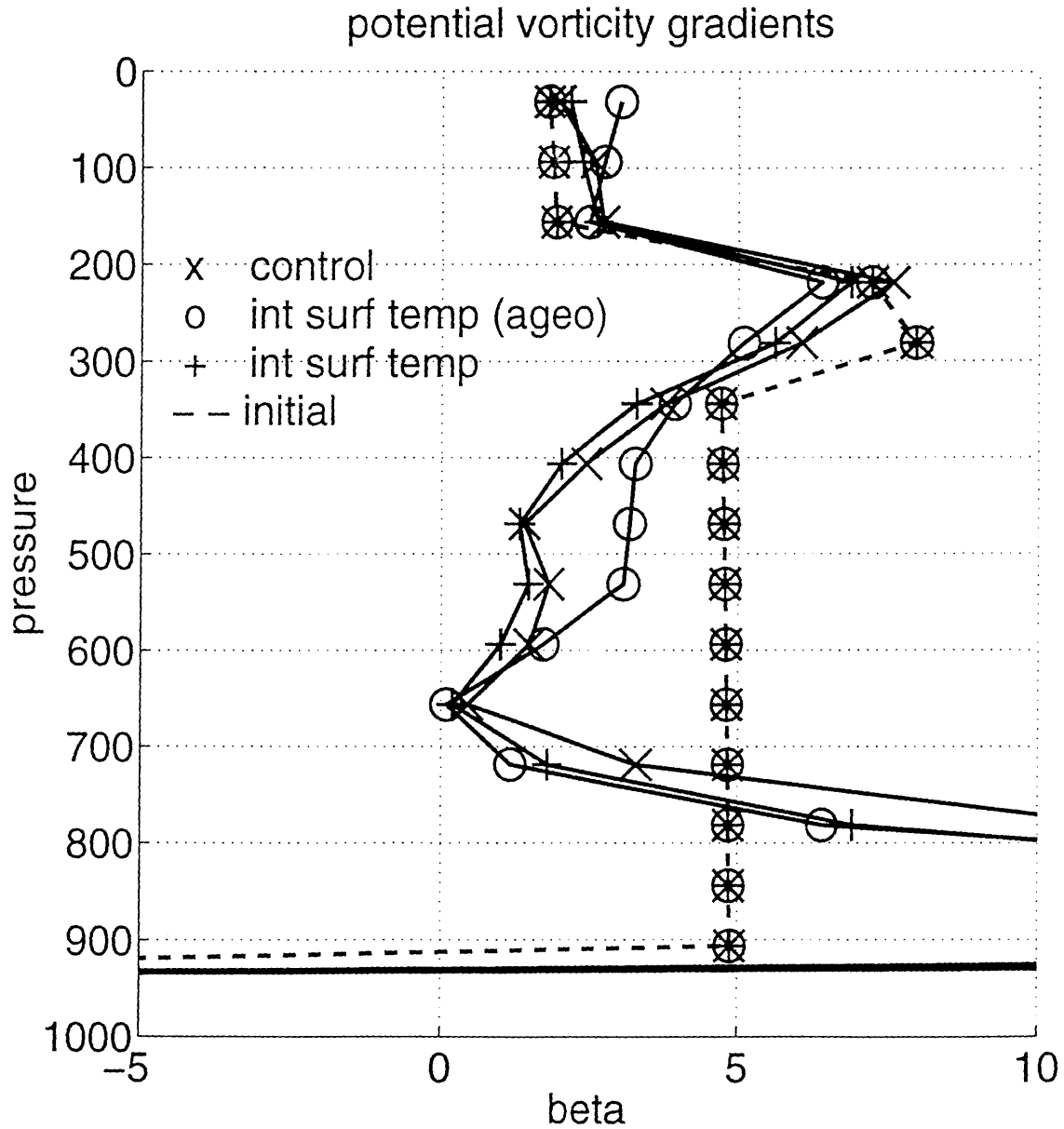
Figure 6-36: Comparison of the meridional pv gradients above the ABL for the control run and the interactive surface air temperature, with and without ageostrophic friction, runs, in units of β.

Chapter 7

The role of variable static stability

7.1 Introduction

Previous studies have shown that it is necessary to include the processes and feedbacks that are responsible for the maintenance of the static stability in order to model the observed zonal mean static stability and eddy fluxes. Both observational and model studies have demonstrated that the feedbacks which determine the vertical temperature structure of the troposphere are as significant in determining the observed mean fluxes and temperature structure as the feedbacks which determine the horizontal temperature structure. Gutowski, Branscome, and Stewart (1989) included both surface heat fluxes and surface friction in a multi-level primitive equation baroclinic lifecycle study. This study found that it is necessary to include both surface friction and surface heat fluxes in order to get realistic eddy heat flux distributions and mean temperature profiles. A recent observational study by Swanson and Pierrehumbert (1997) has shown that the lower tropospheric heat transport is characterized by strong thermal damping of temperature anomalies back to the underlying oceanic surface temperature with characteristic timescales of one day. This study suggests that thermal diffusion would also be a significant process in the dynamical balance which determines the mean static stability.

This model has been shown in Chapter 3 to have equilibrated zonal mean potential vorticity gradients that resemble the observed structure of the potential vorticity in the mid latitude troposphere. It has also been shown in Chapter 5 that the model has equilibrated zonal mean potential vorticity gradients that are relatively insensitive to changes in radiative forcing. It is of interest to determine to what extent the interactive static stability is responsible for these results.

The model used in this study was designed to include the wave-mean flow feedbacks which maintain both the horizontal and vertical temperature structure.

Therefore, this Chapter addresses the following questions. To what extent is the equilibrated state of the model, and its resemblance to observations, due to the interactive static stability? In what way does allowing for an interactive static change the model's equilibrated climate? Does this change in the model's equilibrated climate play a significant role in the insensitivity of the model's potential vorticity gradients to changes in external forcing?

7.2   Fixed versus interactive static stability runs

7.2.1   Equilibrated state with fixed static stability

The model has been shown to resemble the observed potential vorticity structure of the wintertime mid latitude troposphere. The large scale eddies that maintain this equilibrated state were shown in the previous Section to extend throughout the depth of the model's troposphere. This Section looks at the role of the interactive static stability in these results.

Figure 7-1 shows the latitude pressure cross-section of the zonal mean potential vorticity gradients, in units of β, in the equilibrated state with the static stability held fixed at -7K/km. This Figure shows that holding the static stability fixed results in smaller pv gradients in the ABL, compared to the pv gradients in the equilibrated state of the control run Figure 3-10. The characteristic homogenization of pv above the ABL, that was seen in the runs when the radiative forcing was varied, is not seen in the equilibrated state when the static stability is held fixed. This is only true in the region just above the ABL since there is still homogenized pv on the sides of the jet. Therefore, the complete homogenization of the pv just above the ABL is dependent upon the adjustment due to both the meridional temperature gradients and static stability.

Figure 7-2 shows the terms in the perturbation pe tendency equation when the static stability is held fixed. Compared to Figure 3-26, which shows the terms for the control run, the fluxes in the lower troposphere are an order of magnitude smaller when the static stability is held fixed. In the control run, the vertical fluxes of heat in the upper troposphere cause the static stability to increase. This increase in the static stability and stabilization of the large scale eddies is prevented when the static stability is held fixed. These feedbacks may be the reason why the wave-wave interactions are insignificant in the upper troposphere of the control run, but are as important as the quasi-linear fluxes when the static stability is held fixed.

7.2.2   Sensitivity to changes in external forcing

The previous Section has shown that the feedbacks which maintain the static stability play a significant role in the homogenization of pv above the ABL. This homogenization of pv was shown to be consistent with the pv structure of the observed wintertime mid latitude climate. It is of interest to determine how this modification to the equilibrated state changes the model's sensitivity to changes in external forcing. Previous studies which hold static stability fixed have concluded that the eddies which maintain the equilibrated climate are shallow and are insensitive to changes in the upper tropospheric temperature gradients, (Pavan 1996; Held and O'Brien 1992). Pavan (1996) used a multi-level qg β-plane channel model to study the sensitivity of the model's equilibrated climate to changes in the vertical structure of the radiative equilibrium temperature gradients. There are many significant differences between the model that Pavan (1996) used and the model that has been used for this thesis. Pavan's model has an ABL that is parameterized by Ekman pumping at the lower boundary, a diabatic heating timescale of 30 days, and a static stability that is independent of height. The runs done in this section are motivated by this study but the large differences between the model's make it difficult to directly compare the results.

It is not clear how allowing for an interactive static stability, and a more realistic equilibrated pv structure, will change the model's sensitivity to changes in external forcing. This Section investigates how holding the static stability fixed changes the model's sensitivity to changes in external forcing.

The RCE state chosen to test the sensitivity to changes in external forcing is shown in Figure 7-3. This figure shows the comparison between the RCE and equilibrated meridional temperature gradients at the center of the channel, for the two runs which include an interactive static stability, the control run and the run with increased upper tropospheric RCE temperature gradients (IUT). The dashed lines in the Figure show the RCE states for the control and IUT temperature gradients. The solid lines show the equilibrated temperature gradients. The x's are for the control run. The o's are for the IUT runs. The IUT RCE state has a 2% increase in the vertically averaged lower tropospheric temperature gradients and a 10% increase in the vertically averaged upper tropospheric temperature gradients.

These temperature gradients were chosen because of the results of modeling studies, such as Manabe and Wetherald (1975), which predict that increased concentration of greenhouse gases would result in smaller lower tropospheric temperature gradients but larger upper tropospheric gradients, relative to the current climate. A profile with an increase in the temperature gradients at all levels was chosen, instead of increases in just the upper troposphere, to prevent large jumps in the pv gradients in the mid troposphere which may have an impact on the stability of the large scale waves. A few runs were done with various modifications to the IUT RCE temperature gradients to determine if the response is due to the changes in the upper troposphere or due to the changes in the lower troposphere.

It was determined that the response, which will be discussed below, is primarily due to the increase in the temperature gradients in the upper troposphere.

Figure 7-4 shows the comparison between the RCE and equilibrated meridional temperature gradients at the center of the channel, for the runs that hold the static stability fixed. Comparing Figure 7-4 to Figure 7-3 it is seen that within the ABL, the meridional temperature gradients are independent of whether or not there is an interactive static stability. Above the ABL, the run with an interactive static stability is more adjusted, smaller equilibrated meridional temperature gradients, when the radiative equilibrium upper tropospheric temperature gradients are increased, but these differences are relatively small.

Figure 7-5 shows the comparison of the magnitude of the perturbation pv at the center of the channel, with and without the increased upper tropospheric temperature gradients, including an interactive static stability. The line with the x's is from the control run. The line with the o's is for the run which is relaxed towards the IUT RCE state. The dash line shows the difference between the two runs. The dashed line shows that the primary response of the perturbation pv to the IUT RCE is in the ABL. The amplitude of the perturbation pv at the tropopause is relatively unchanged. The vertical fluxes of heat in the upper troposphere cause the static stability to increase. This increase in the static stability and stabilization of the large scale eddies causes the amplitude of the perturbation pv to be relatively independent to changes in forcing in the upper troposphere.

Figure 7-6 shows the same comparison as Figure 7-5, holding the lapse rate fixed at -7 K/km. The primary peak at the surface, that was observed when the static stability was allowed to vary, is absent. The perturbation pv peaks instead away from the surface, at the second model level. The dash line shows that when the static stability is held fixed, the primary response to the IUT RCE is at the tropopause. This is consistent with the previous studies that were discussed in the introduction that looked at the response to an increase in upper tropospheric temperature gradients with a fixed static stability.

Figure 7-7 shows the same comparison as Figure 7-6, except that the static stability is held fixed using the static stability of the equilibrated state of the control run. This comparison was done to determine if choosing a more realistic vertical profile for the static stability will cause the perturbation pv in the ABL to be more sensitive to changes in the upper level RCE temperature gradients when the static stability is held fixed. The dashed line shows the difference between the control run and the control run with increased upper tropospheric RCE temperature gradients, as in Figure 7-6. This was discussed in the previous paragraph. The dash-dot line shows the difference between the control run and the run with increased upper tropospheric RCE temperature gradients and a static stability which was held fixed to the control run values. This line shows that, although the pv gradients above the ABL are small in this run, the perturbation pv is still relatively insensitive to a change in the upper tropospheric RCE temperature gradients when the static stability is held fixed.

Figure 7-8 is a comparison of the initial and equilibrated static stability for the same three runs as in Figure 7-7. This figure shows that, given the small change in the forcing in the upper troposphere, the static stability within and above the ABL is sensitive to a change in the upper tropospheric RCE temperature gradients, although the equilibrated meridional temperature gradients are not (Figure 7-9).

This Section has shown that the feedbacks which maintain the static stability are responsible for the sensitivity of perturbation pv in the ABL to changes in the upper tropospheric temperature gradients. This sensitivity is absent when the static stability is held fixed, even if the fixed static stability is chosen to have a more realistic vertical profile. Therefore, the feedbacks which maintain the static stability, and couple the model's atmosphere to the surface, play an important role in coupling the model's ABL with the upper troposphere.

fixed static stability
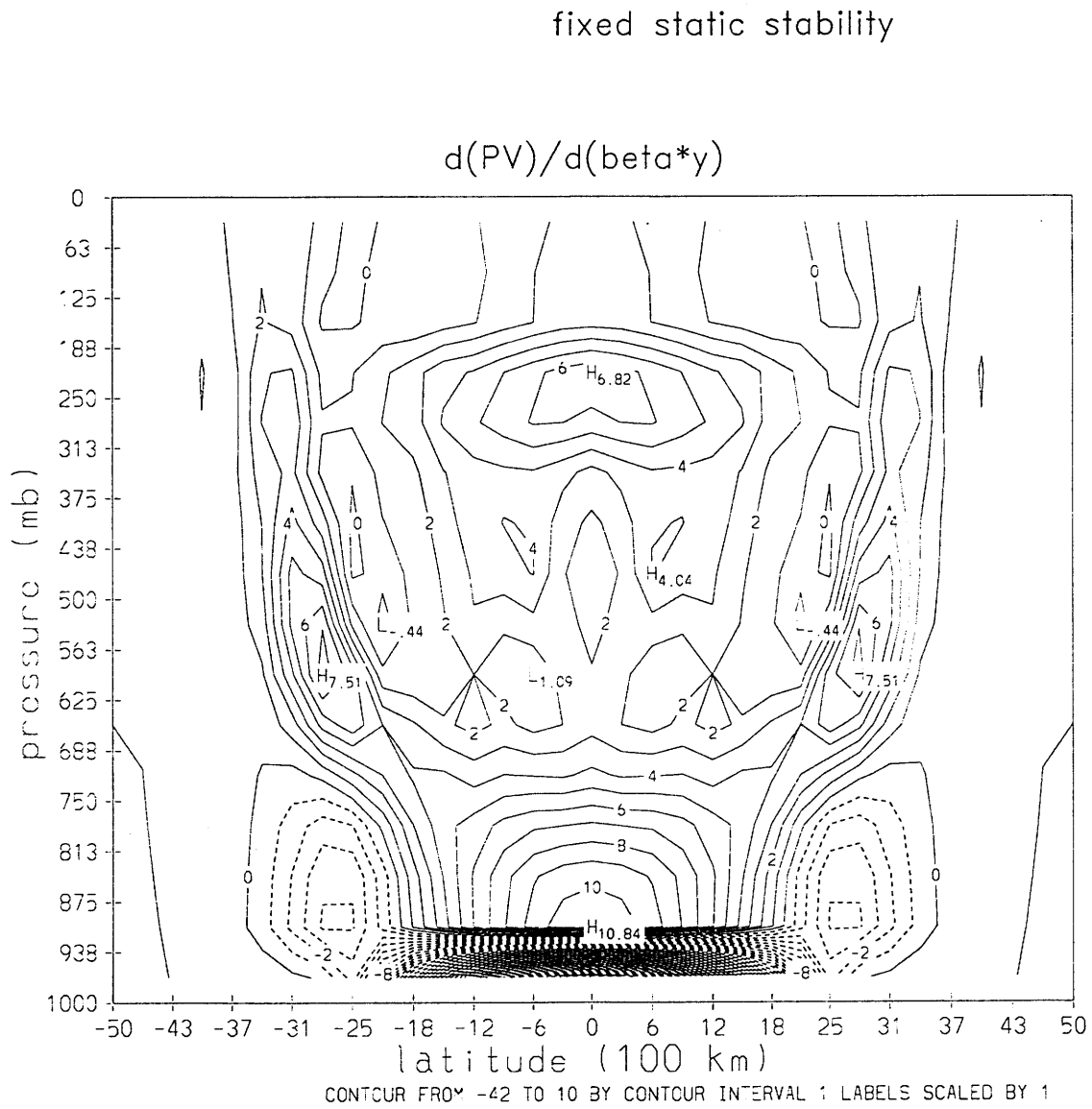
Figure 7-1: Latitude pressure cross-section of the zonal mean
potential vorticity gradients, in units of β, in the equilibrated
state with fixed static stability.
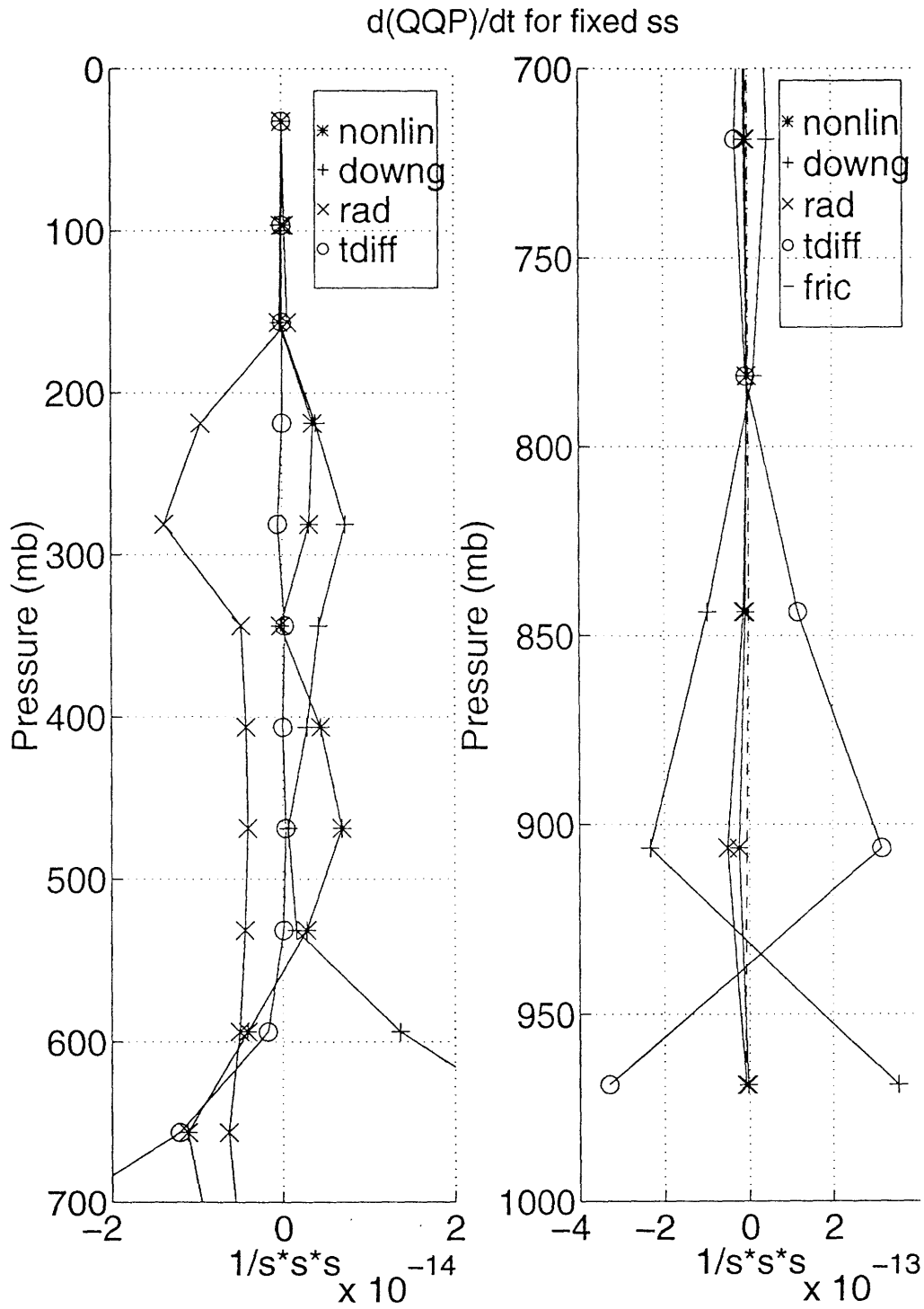
Figure 7-2: The terms in the perturbation pe tendency equation for the run with fixed static stability for a) above the ABL and b) within the ABL.
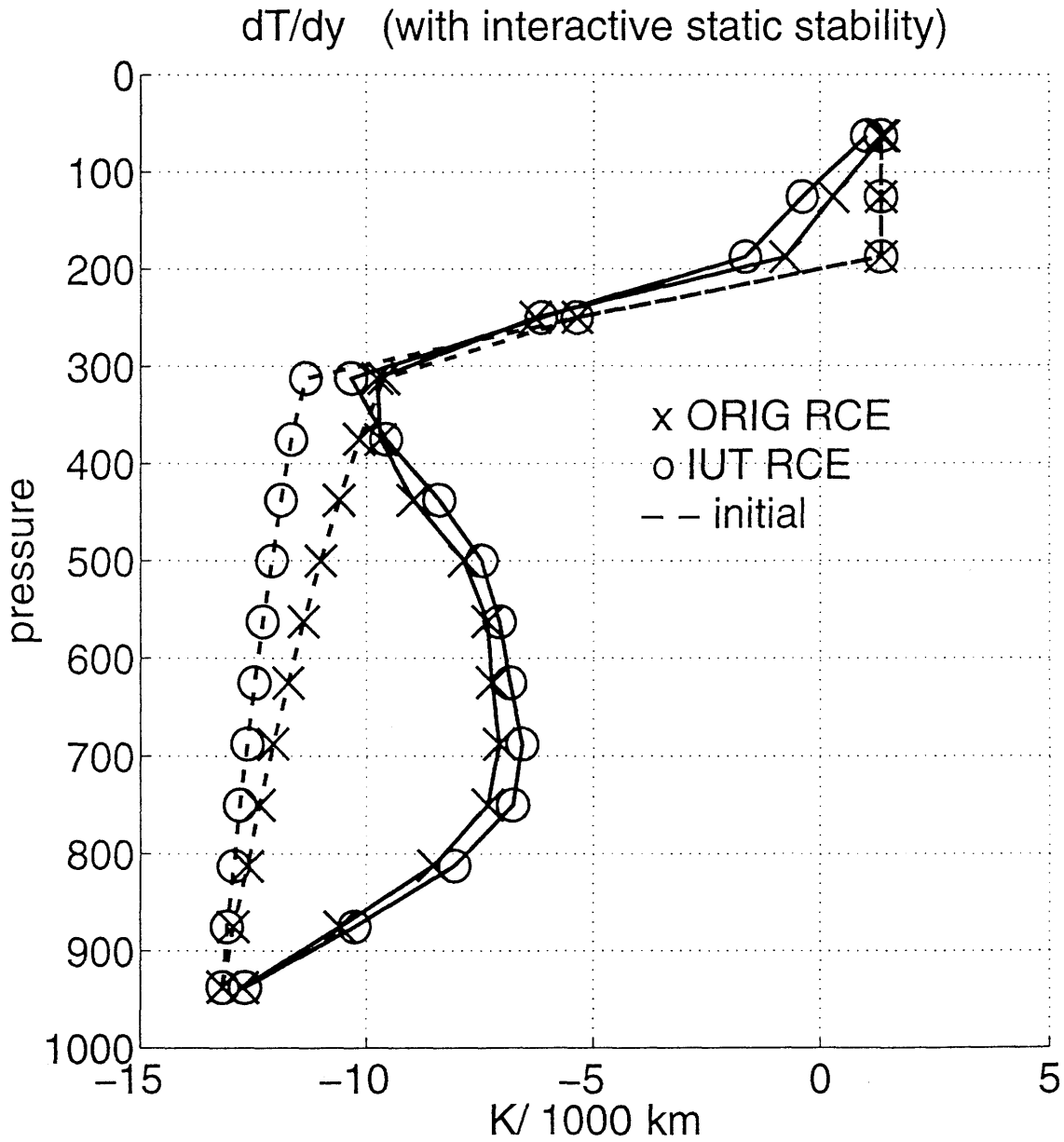
Figure 7-3: Comparison between RCE and the equilibrated meridional temperature gradients, at the center of the channel for the runs which include an interactive static stability.
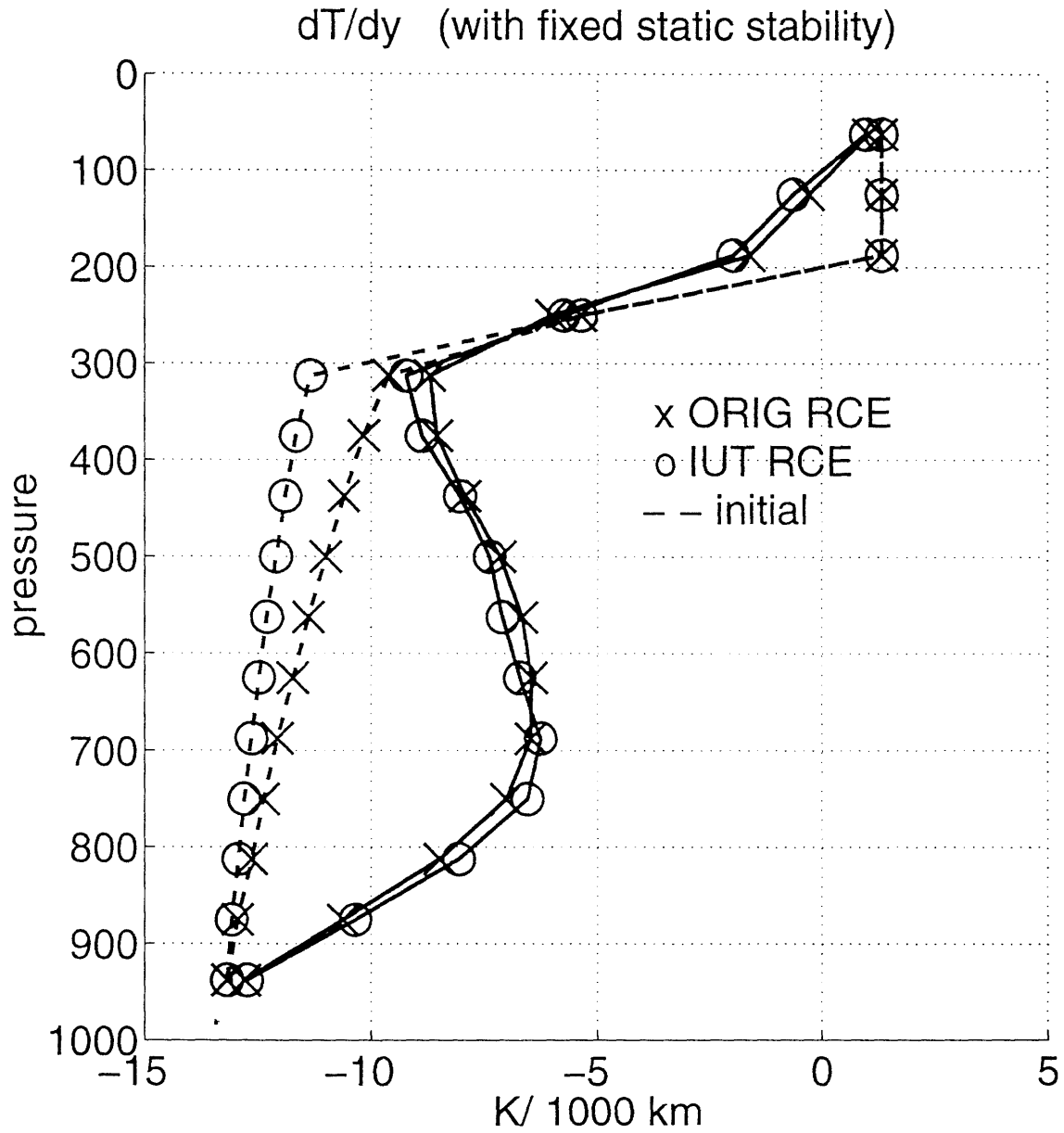
Figure 7-4: Comparison between RCE and the equilibrated meridional temperature gradients, at the center of the channel, for the runs which hold the static stability fixed.
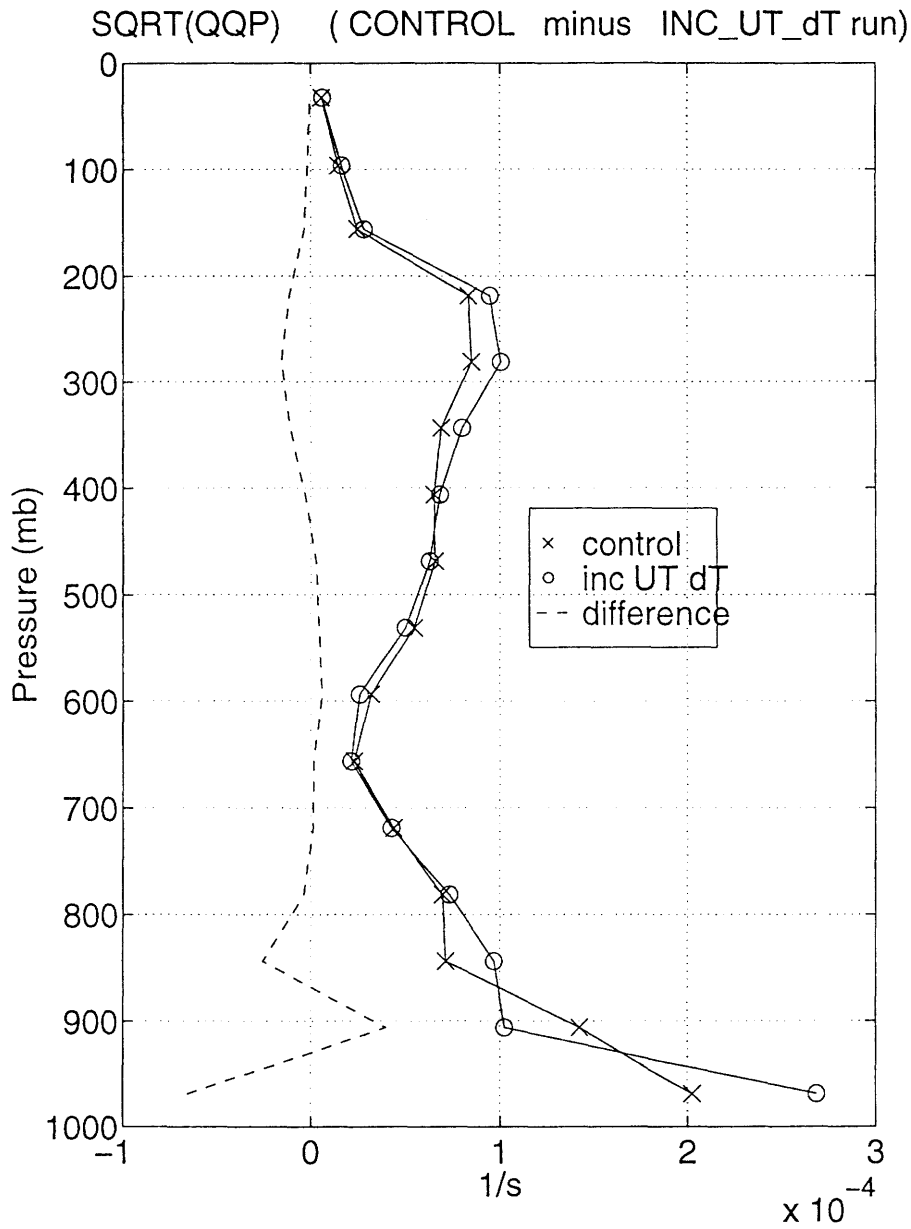
Figure 7-5: Comparison of the magnitude of the perturbation pv at the center of the channel, with and without the increased upper tropospheric temperature gradients, including an interactive static stability.
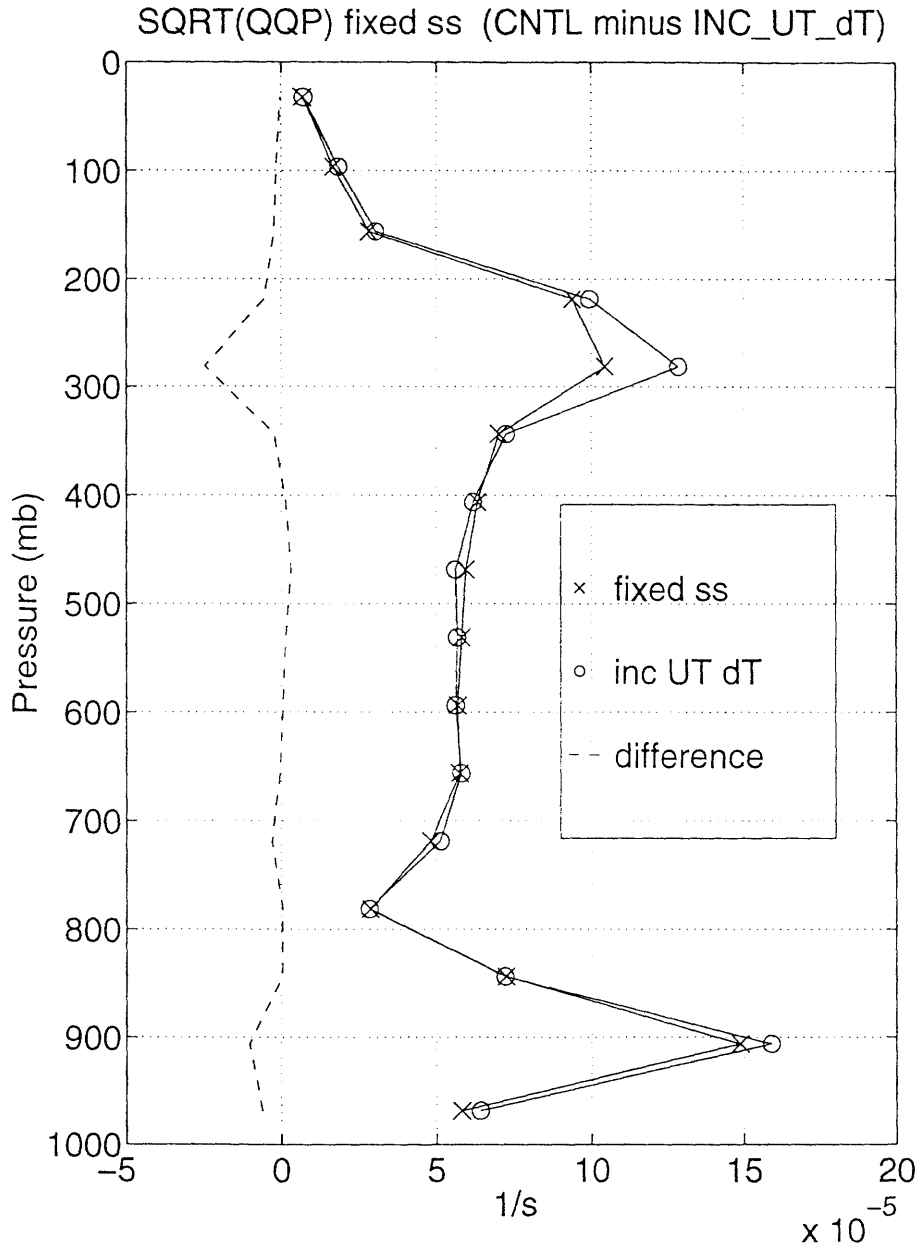
Figure 7-6: Comparison of the magnitude of the pertur-
bation pv at the center of the channel, with and without
the increased upper tropospheric temperature gradients, with
static stability held fixed at -7 K/km.
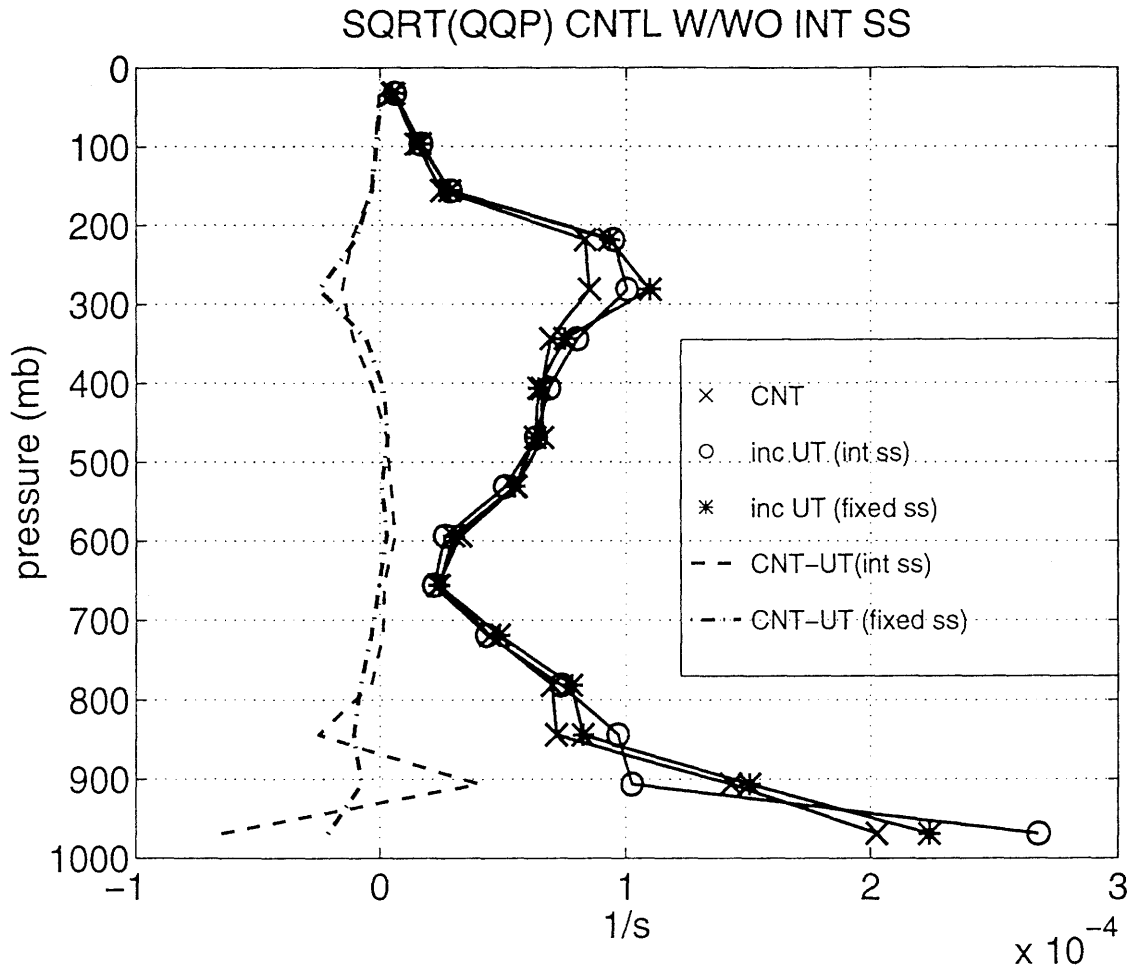
Figure 7-7: Comparison of the magnitude of the perturba-
tion pv at the center of the channel, with and without the in-
creased upper tropospheric temperature gradients, with and
without interactive static stability. Line with x's mark the
control run with interactive static stability. Line with o's
mark the control run with interactive static stability and in-
creased upper tropospheric RCE temperature gradients. Line
with *'s mark the run with increased upper tropospheric RCE
temperature gradients and static stability held fixed at the
values of the equilibrated state of the control run
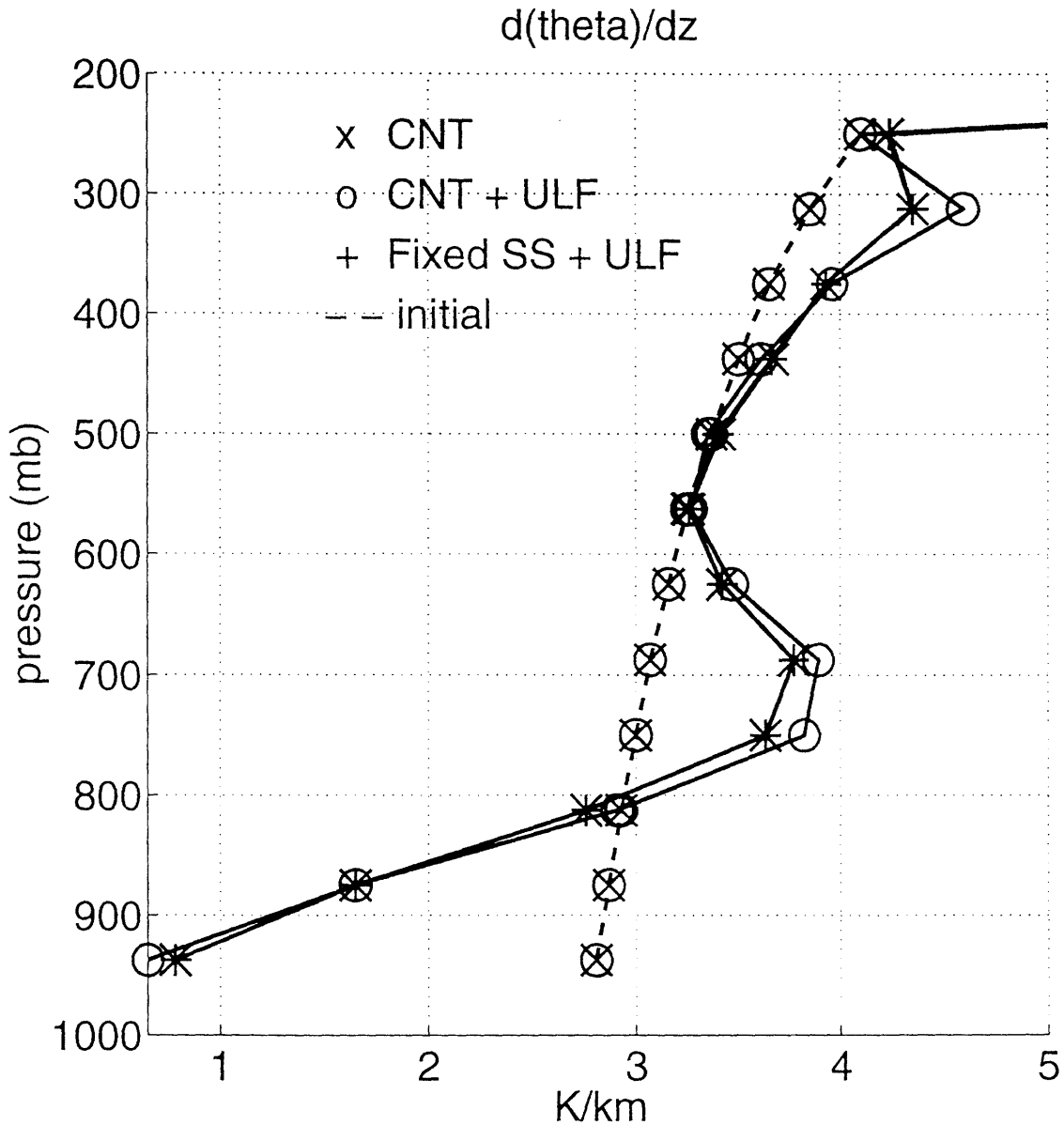
Figure 7-8: Comparison of the equilibrated static stability, with and without the increased upper tropospheric temperature gradients, with and without interactive static stability. Line with x's mark the control run, with interactive static stability. Line with o's mark the control run with interactive static stability and increased upper tropospheric RCE temperature gradients. Line with +'s mark the run with increased upper tropospheric RCE temperature gradients and static stability held fixed at the values of the equilibrated state of the control run
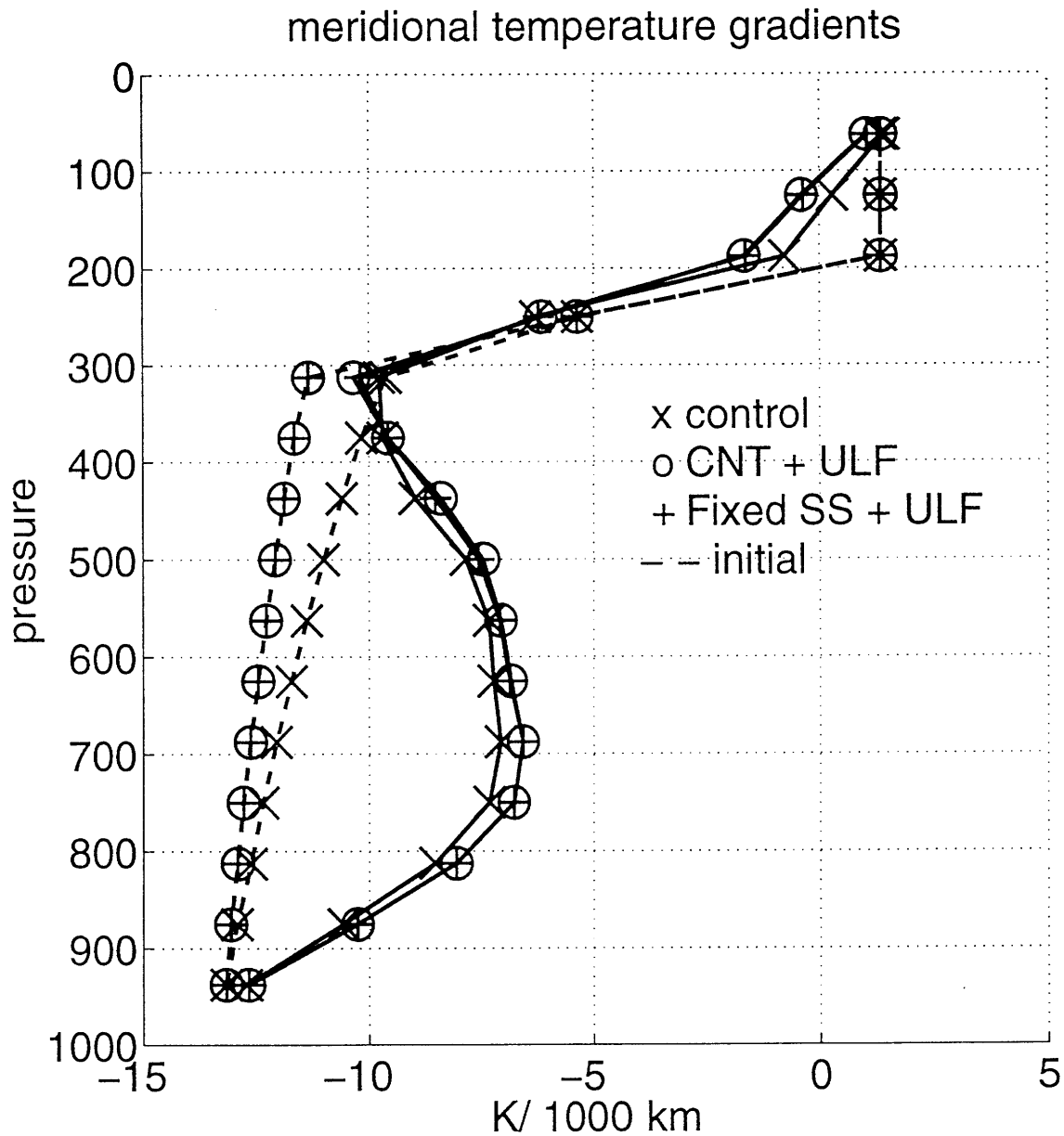
Figure 7-9: Comparison of the equilibrated meridional temperature gradients at the center of the channel, with and without the increased upper tropospheric temperature gradients, with and without interactive static stability. Line with x's mark the control run, with interactive static stability. Line with o's mark the control run with interactive static stability and increased upper tropospheric RCE temperature gradients. Line with +'s mark the run with increased upper tropospheric RCE temperature gradients and static stability held fixed at the values of the equilibrated state of the control run

Chapter 8

Summary

A multi-level quasi-geostrophic mid-latitude β-plane channel model with simple representations of heating and friction has been described and used to study the sensitivity of the model's equilibrated climate to changes in radiative forcing and mixing by turbulent eddies within the ABL.

This model has been shown to have an equilibrated climate and mean fluxes that resemble the observed wintertime tropospheric climate. This equilibrated climate has been shown to be linearly stable to small amplitude perturbations. A 1D linear stability analysis was found to give inaccurate results due to the sensitivity of these results on the estimate of the meridional structure of the eddies.

The model's equilibrated climate was found to be stabilized by a decrease in the vertical resolution. This sensitivity on the vertical resolution was found to be eliminated when an interactive surface temperature was coupled to the model. The model was found to be insensitive to an increase in the resolution at the tropopause, which results in an increase in the pv gradients at the tropopause.

The equilibrated meridional temperature gradients at the lowest model level were found to be fixed to the RCE temperature gradients because of the damping by the thermal diffusion, in agreement with the observational study by Swanson and Pierrehumbert (1997). The vertical diffusion of heat was also responsible for the mixing of heat across the air-sea interface which kept the static stability small. Qualitatively, the static stability and meridional temperature gradients were consistent with observations.

Above the ABL, the pv gradients were found to be relatively independent to the changes in radiative forcing and mixing within the ABL, however the static stability and the meridional temperature gradients were not. The magnitude and vertical structure of the static stability and the meridional temperature gradients were found to be very sensitive to changes in radiative forcing and the parameters that define the mixing with the ABL.

This study has shown that it is important to include both an interactive static stability and a representation of a tropopause/stratosphere in order to model the

dynamics in the boundary layer. The lack of a tropopause or an interactive static stability caused the large-scale eddies that maintain the equilibrated to become shallow. Including a representation of a tropopause and an interactive static stability resulted in deep eddies which extend throughout the troposphere. Deeper eddies caused dynamics within the ABL to be more sensitive to changes in forcing in the upper tropopause.

The vertical eddy heat fluxes that maintain the static stability were found to play a significant role in the modification of the mean climate throughout the troposphere. The feedback between the vertical fluxes of heat and the thermal diffusion near the lower boundary caused the vertical temperature to be well mixed. Above the boundary layer, the vertical eddies played an important role in the homogenization of the pv. The homogenization of pv just above the ABL was absent when the vertical eddy heat fluxes were not allowed to modify the static stability, although the homogenization on the sides of the jet was unchanged. At the tropopause, the feedback between the vertical eddy heat fluxes and the radiative forcing played an important role in the maintenance of the amplitude of the eddy pe.

Appendix A

Model study of the barotropic point jet

A.1   The Barotropic Point Jet

An analytical prototype problem developed to investigate the modification of the neutral state, in the presence of external forcing in a continuous atmosphere, is the problem of the barotropic point jet. Lindzen *et al.* (1983) showed that the barotropic easterly jet problem is mathematically homomorphic to the Boussinesq Charney problem. The linearized equation for the time rate of change of the perturbation potential vorticity , on a basic zonal flow , is

$$\frac{\partial q'}{\partial t} + \bar{u}\frac{\partial q'}{\partial x} + v'\frac{\partial \bar{q}}{\partial y} = -Dq'. \qquad (1)$$

where the meridional potential vorticity gradient is,

$$\frac{\partial \bar{q}}{\partial y} = \beta - \bar{u}_{yy}.$$

and D^{-1} is the dissipation time constant. In the quasi-linear integrations, this term acts to both dissipate the waves and dissipate/force the mean flow. In the barotropic problem, the perturbation potential vorticity is equal to the perturbation vorticity,

$$q' = \frac{\partial^2 \psi}{\partial y^2} + \frac{\partial^2 \psi}{\partial x^2}, \qquad (2)$$

where ψ is the perturbation streamfunction. Assuming normal mode solutions, the equation governing the linearized perturbations reduces to,

$$\psi_{yy} + \left[\frac{\beta - \overline{u}_{yy}}{\overline{u} - c} - k^2\right]\psi = iD\frac{(-k^2\psi + \psi_{yy})}{k(\overline{u} - c)}, \qquad (3)$$

where solutions are assumed to be of the form $\Psi = \psi(y)exp[ik(x - ct)]$.

Figure A-1 shows the initial jet structure and the potential vorticity gradient of the basic state for the barotropic jet and for the Charney problem. In a numerical simulation of this problem, Schoeberl and Lindzen (1984; hereafter, SL) demonstrated that, in the absence of forcing, an unstable jet evolved to a steady-state that was neutral to the eddies. This neutral state was the neutral state as defined by the Charney-Stern criterion for stability. The shear of the flow was modified by the waves as predicted by the linear adjustment theory. The jet evolved from a point to a parabola such that,

$$\overline{q}_y = \beta - \overline{u}_{yy} = 0. \qquad (4)$$

When dissipation was added to the system, the neutral state was found to be supercritical by the Charney-Stern theorem, even though the growth of the waves had been suppressed. The steady-state in the presence of dissipation was found to be independent of the magnitude of the dissipation. The supercritical neutral state was found to have a balance between the generation of vorticity by the mean-flow and the dissipation of vorticity due to the eddies. SL note that the neutral state would not be independent of the magnitude of the dissipation if a form other than linear damping had been used.

The problem of the easterly barotropic jet presents the ability to investigate the primary aspects of the impact of resolution on the linearized Charney problem in a two-dimensional model. A two-dimensional model can be used to derive analytic dispersion relations as a function of β, zonal wind and resolution.

Since the barotropic jet is two-dimensional it can not be used to investigate the full three dimensional nonlinear baroclinic problem. The analogy between the linearized barotropic jet and the linearized Boussinesq Charney problem assumes that the meridional wavenumber is equal to zero. Even though this is the most unstable wavenumber for the Charney problem, it is most likely not the dominant meridional wavenumber that would be found in the presence of a jet. Lindzen (1993) notes that a meridional jet of width L would impose a meridional wavenumber of $l = 1/L$ on the baroclinic instabilities. For a characteristic winter subtropical jet with a width of 0.15a, where a is the radius of the earth, this meridional wavenumber is found to be close to global wavenumber 6. Observations of the mid-latitude winter indicate that this is the wavenumber associated with the maximum normal mode growth.

Ioannou and Lindzen (1986) studied the impact of the meridional structure of barotropically stable jets on baroclinic instability. This analysis studied the linear stability of quasi-geostrophic perturbations on a mid-latitude β-plane. The jet structure was found to meridionally contain the baroclinic instabilities. It was found that the growth rates of the unstable modes could be estimated from

models without barotropic jets, if the appropriate vertical shear and meridional wavenumber was chosen.

A further result of the Ioannou and Lindzen paper was that heat and momentum fluxes associated with the unstable waves tended to increase the barotropicity of the flow while reducing the baroclinicity. The increase in the barotropicity is due to the convergence of momentum fluxes at the jet and the resultant increase in the curvature of the meridional jet structure. The barotropic effects on baroclinic instability can not be investigated in a two dimensional model. These dynamics will be investigated in the proposed full three dimensional model.

A.2   Linear results

In order to derive boundary conditions for the barotropic jet that are analogous to the Charney problem, symmetry of the perturbation streamfunction was required at the point of the jet. SL, Schoeberl and Nielsen (1984; hereafter, SN) and Nielsen and Schoeberl (1986: hereafter, NS) studied the full one-point jet and imposed the boundary condition that there be no mass flux into the jet at the walls sufficiently far from the jet maximum. This formulation of the problem does not exclude the asymmetric modes from the solution and therefore does not strictly satisfy the requirement that the solution be symmetric about the jet. This was found to be an adequate formulation to the problem that was investigated by these previous studies because, for the values of the zonal mean wind and β that were used, the asymmetric modes were found to be small relative to the symmetric modes. This may not be true generally. Therefore, this study will only look at the half jet so that the symmetric boundary condition is strictly satisfied.

The linearized equation for the perturbation streamfunction, equation (3) has been solved numerically as an eigenvalue problem for the phase speed, c. The linear problem has been solved numerically for two different schemes. The first scheme is the numerical set-up of the barotropic problem. In the studies of SN and NS, the barotropic problem is solved numerically with the perturbation and mean streamfunction at the same meridional levels. The mean zonal wind is calculated using a centered finite difference scheme so that the perturbation streamfunction and the mean zonal wind are placed at the same meridional level. When this numerical scheme is used to set-up the two-level formulation of the barotropic problem, the use of the centered finite difference scheme introduces a computational mode into the equilibrium solution. Therefore, a second scheme has been formulated. The second scheme is called the staggered barotropic scheme. The staggered scheme places the mean streamfunction at the mid-level so that the mean zonal wind is calculated at the level. The use of this scheme in the numerical integration of the barotropic problem removes the computational mode. This scheme can not be used to calculate the barotropic wave-wave interaction terms, therefore the first scheme is used for the nonlinear integrations.

n	u_c	Γ_c
pts	m/s	$10^{-5}/s$
3	60.0	2.4
5	30.0	1.2
9	15.0	0.6
17	7.5	-0.3

Table A.1: Values of the critical zonal wind for resolutions used in this study of the barotropic point jet.

The staggered barotropic scheme has been for all of the linear and quasi-linear calculations described in this paper. The boundary condition on the perturbation streamfunction at $y = 0$ is that $v' = 0$. This is the requirement that there be no mass flux into the half jet from outside the channel. The boundary condition at $y = L$, the point of the half jet, is $u' = 0$. This is the requirement that the perturbation streamfunction be symmetric about the point of the jet. This is the boundary condition that must be imposed in order to make this barotropic problem analogous to the linearized Charney problem. The barotropic problem which is equivalent to the two-level baroclinic problem has three levels where the perturbation streamfunction is defined. If the numerical problem is solved using adequately high resolution, then the results are independent of the scheme used. In all of the calculations, there are 129 points in the zonal direction and the length of the channel is kept fixed at 20,000 km. The width of the half jet is held fixed at 2500 km. In all of the integrations $\beta = 1.9 \times 10^{-11}\frac{1}{ms}$.

A.2.1   Critical zonal mean wind

In a dissipationless system, there is no normal mode growth when the Charney-Stern criteria for stability is satisfied. This condition is met when the meridional potential vorticity gradient does not change sign and can be written,

$$\beta - \frac{\Gamma}{\Delta y} > 0. \quad (5)$$

Where Γ is the constant zonal mean shear of the basic state and is equal to ,$\Gamma = \frac{u_0}{L}$. In this problem L is equal to the width of the half jet. Equation (5) can be solved for the critical zonal mean wind for instability. Table A.1 lists the values of the critical zonal wind for resolutions used in this study.

Γ_c is the critical shear and n is the number of meridional gridpoints in the half jet. For the same value of the zonal mean wind, an increase in resolution will make the problem more unstable. This is because the delta function in the

meridional gradient of the potential vorticity becomes better defined when the resolution is increased. This decreases the value of the potential vorticity gradient at the point of the jet. A decrease in resolution can increase the value of the potential vorticity gradient to the point where the waves have been completely stabilized. When $\Delta y \to 0$, the system is always unstable and $\Gamma_c \to 0$. With the given parameters, The 3 pt system, which is equivalent to the two-level model, is stable for all mean zonal winds less that 60 m/s.

The critical zonal mean wind and shear that is calculated in Table A.1 is not the critical zonal mean wind and shear that is predicted by the Charney-Stern Theorem for the quasi-linear neutral state. This is due to the initial zonal wind profile used in the staggered barotropic scheme. In order for the two different numerical schemes to be consistent, the initial mean streamfunction of the staggered barotropic sheme was calculated from the initial mean streamfunction of the original scheme. The mean streamfunction of the staggered scheme at the midpoint is the average of the mean streamfunction of the original scheme at the gridpoint. The critical shear predicted for the quasi-linear neutral state is equal to $\Gamma_c/2$.

A.2.2   Linear parameter study

The linear stability of the Charney problem was studied by Held (1978a). This study derived the vertical scale height of linear quasi-geostrophic waves that were destabilized by surface temperature gradients. This vertical scale height, h, is only relevant when $h << H$, where H is equal to the geometric height of the model and

$$h = \frac{f_0^2 \frac{\partial \overline{u}}{\partial z}}{N^2 \frac{\partial \overline{q}}{\partial y}},$$

and the potential vorticity gradient is evaluated at the jet. The shear and static stability are constant. The horizontal wavelength of the most unstable wave was derived to be proportional to

$$\lambda_h = Nh/f_0.$$

Held (1978a) assumed that the horizontal phase speed of the waves was scaled by $\frac{\partial \overline{u}}{\partial z}h$. When h is the relevant scale height,

$$\frac{\partial \overline{u}}{\partial z}h = \frac{u_0}{H}h << u_0.$$

The horizontal phase speed, c, is $O(u_0)$ in the barotropic point jet problem, NS. Therefore, c will be scaled by u_0 instead of the scaling used by Held (1978a). Using this scaling, the growth rate of the waves would be $O(kc) = O(\frac{u_0 f_0}{Nh})$. This scaling analysis can be applied to the barotropic point jet by replacing $-\frac{f_0}{N}\frac{\partial}{\partial z}$ with $\frac{\partial}{\partial y}$. The meridional scale height of the waves, for the barotropic point jet, is calculated

to be,

$$l = -\frac{\partial \overline{u}}{\partial y} \Big/ \frac{\partial \overline{q}}{\partial y}$$

$$= \frac{-\Gamma}{\beta - \frac{\Gamma}{\Delta y}}$$

$$= (\frac{(n-1)}{L} - \frac{\beta}{\Gamma})^{-1}.$$

Since $\frac{\Gamma}{\Delta y} > \beta$ for instability, a decrease in the resolution will increase the scale height of the waves. When $l >> L$, the scale height of the waves is replaced by L. The zonal wavelength of the most unstable wave is proportional to l. This means that the most unstable wavelength will increase when the resolution is decreased. The growth rate of the most unstable wave is $O(kc)$ and is proportional to $\frac{u_0}{l} = L\frac{\partial \overline{q}}{\partial y}$. Decreasing the resolution, decreases the jump in the potential vorticity gradient at the jet and decreases the growth rate of the most unstable wave.

Figures A-2, A-3, and A-4 show the growth rates calculated using the staggered scheme for the half jet that is defined by 9 gridpoints. Figure 2 is the growth rates of waves 1-10 when the zonal mean wind is increased from 0 to 56 m/s. Increasing the zonal mean wind increases the growth rate of the most unstable wave. This plot also shows that the wavelength of the most unstable wave increases when the zonal mean wind is increased. This result is inconsistent with the scaling analysis and is being studied at this time. The most unstable wave for a zonal mean wind of 20 m/s is wave 5. When the zonal mean wind is increased to 40 m/s the most unstable wave is reduced to wave 3. The range in the growth rates for the unstable waves also increases as the zonal mean wind is increased. This means that the most unstable wave will grow much faster than the other unstable waves when the zonal mean wind is increased. This may have a significant impact on the partitioning of enstrophy among the waves in the quasi-linear and nonlinear integrations. Figure A-3 is the growth rates of waves 1-10 when β is increased from $0.2 \times 10^{-11}\frac{1}{ms}$ to $4.0 \times 10^{-11}\frac{1}{ms}$. For physically relavent values of β, the growth rates of the long waves are continuously reduced as β is increased. The most unstable wavenumber is continuously increased as β is increased. Figure A-4 shows how this behaviour is modified when the zonal mean is increased from 30 m/s to 70 m/s. For physically relevant values of β, the growth rates of the waves increases as β is increased. (The very large value of 70 m/s for the 9pt problem is being studied for the sake of comparison with the 3pt problem.) The most unstable waves shifts from wave 2 to wave 3 when $\beta > 2. \times 10^{-11}$.

The parameter studies for 5 point resolution are shown in Figures A-5 and A-6. Figure A-5 is the growth rates of waves 1-10 when the zonal mean wind is increased from 30 m/s to 87 m/s. For a zonal mean wind of 39 m/s , wave 3 is the most unstable wavenumber for the 5 point, as well as, the 9 point resolution

study. For this value of the zonal wind, the reduction in resolution stabilizes both the long waves and the short waves. The growth rates have been reduced by a factor of 2. Figure A-6 is the 5 pt β parameter study with the same parameters as Figure A-4. The growth rates are reduced as resolution is decreased and β is increased. The growth rates are decreased by a factor of 2 relative to the 9 point resolution study. Wave 2 is consistently the most unstable wave.

The parameter studies using 3 point resolution are shown in Figures A-7, A-8, and A-9. Figure A-7 is the growth rates for waves 1-3. All of the waves except waves 1 and 2 have been stabilized. Wave one is the most unstable wave for all values of the zonal mean wind. The problem becomes complete stable for $u_0 \leq 60m/s$ The growth rates for wave two are less than $0.1/day$ for all values of the zonal mean wind. The growth rates for wave one are $\leq 0.2/day$ and are approximately 2 times smaller than the growth rates of the 5 point study with the same parameters. Figure A-8 is the 3 pt β parameter study with the same parameters as Figure A-4. As was seen in the 5 point study, reducing the resolution by a factor of two reduces the growth rates by a factor of two. Figure A-9 is the 3 pt β parameter study with the same parameters as Figure A-4, except that the dissipation time scale, D^{-1} has been set equal to zero. The growth rates are increased by a factor of 2 relative to Figure A-8, but the structure is the same.

In all of the studies without dissipation, the critical zonal wind for instability was the zonal wind at which the potential vorticity gradient changed sign. For all basic states that had a positive definite potential vorticity gradient, the basic state was stable. For all basic states with a change of sign in the potential vorticity gradient, the basic state was unstable. This was not true for the studies that had dissipation. When the potential vorticity gradient changed sign, the basic state did not become unstable. The magnitude of the potential vorticity gradient that is needed to make the dissipative study unstable is supercritical relative to the nondissipative study.

A.3   Quasi-linear integration results

The quasi-linear problem retains the nonlinear terms that modify the mean flow while neglecting the nonlinear terms which modify the waves. Therefore, the waves can only act to modify themselves indirectly, through changes in the mean flow. In the wave-mean flow system there are no cascades of energy and enstrophy. Equation (1) is the equation that governs the waves. The equation that governs the changes in the mean flow is,

$$\frac{\partial \overline{q}}{\partial t} + \frac{\partial}{\partial y}(\overline{v'q'}) = -D(\overline{q} - q_0), \qquad (6)$$

where q_0 is the initial potential vorticity and $\bar{q}$ is the zonally averaged potential vorticity. The dissipation time constant, D, is found in equations (1) and (6). The quasi-linear integrations are initialized with a small perturbation in waves 1 through 6. The initial enstrophy in the waves has a negligible effect on the final state.

A.3.1   Limits on integrated wave enstrophy

SL derived the limits on the integrated wave enstrophy in a nondissipative system. Using conservation of enstrophy on constant pressure surfaces and assuming that the initial wave enstrophy is equal to zero, the integrated wave enstrophy in the final state is

$$< q_f'^2 > = < \bar{q}_i^2 > - < \bar{q}_f^2 >, \qquad (7)$$

where $<> = L^{-1} \int_0^L () dy$.

The final state of the wave-mean flow system is assumed to be defined by the Charney-Stern criteria for instability. In the final state, the wave-mean flow interactions have modified the mean flow such that all mean potential vorticity gradients are greater than or equal to zero. Following the work of SL, the mean flow is assumed to be modified to a distance, y_c, from the jet maximum. For $0 \leq y < y_c$, the mean potential vorticity is assumed to be unchanged from the initial state. Therefore, y_c is calculated as the intersection between the initial and the final mean potential vorticity. The final state which minimizes the adjustment to the mean flow, and maximized the integrated wave enstrophy, is the state where the mean potential vorticity is equal to zero for $y_c < y < L$. y_c is then found to be equal to Γ/β. The curvature of the jet in this final state is

$$\frac{\partial^2 \bar{u_f}}{\partial y^2} = \beta.$$

For this model the initial potential vorticity is

$$q = \beta y - \frac{\Gamma}{2}, \qquad y = L - \frac{\Delta y}{2}$$

$$q = \beta y - \Gamma, \qquad y < L - \frac{\Delta y}{2}.$$

Letting n_c be the gridpoint closest to y_c,

$$n_c = 0.5 + \frac{\Gamma}{\beta \Delta y}.$$

This gives an estimate of the integrated wave enstrophy for a given number of

n	y_c	$< q'^2_f >$
pts	km	$10^{-11}/s^2$
3	625	0.2
3	1875	3.0
5	1563	5.0
9	1406	7.0
17	1484	12.0

Table A.2: Integrated wave enstrophy for $\Gamma = 2.8 \times 10^{-5}/s$, which corresponds to a zonal mean wind at the point of jet of 70 m/s.

gridpoints, n,

$$< q'^2_f >= \frac{1}{n-1} \left[\sum_{i=2}^{n_c} (\frac{(2i-1)}{2}\beta\Delta y - \Gamma)^2 + (\frac{\beta\Delta y}{2} - \frac{\Gamma}{2})^2 \right].$$

Table A.2 lists the integrated wave enstrophy for $\Gamma = 2.8 \times 10^{-5}/s$, which corresponds to a zonal mean wind at the point of jet of 70 m/s.

The analytic limit derived by SL for these parameters is

$$< q'^2_f >= \frac{\Gamma^3}{3L\beta} = 15 \times 10^{-11}/s^2.$$

The analytic value for $y_c = \frac{\Gamma}{3}$ is 1474 km. The increase in the integrated wave enstrophy for an increase in the resolution is due to the increase in magnitude of the jump in the meridional gradient of the potential vorticity gradient at the point of the jet. This increase means that more integrated wave enstrophy is needed to stabilize the waves. The 3 point calculation for the integrated wave enstrophy in the equilibrated state is 87 percent smaller than the analytic calculation. The closest gridpoint to y_c in the 3 gridpoint configuration is 399 km away from y_c. The calculation for the 3pt case assumes that since this is the closest gridpoint to y_c, it will be modified by the adjustment to equilibrium. This may not be a good assumption. If the closet gridpoint to y_c on the side of the jet maximum is the only gridpoint to be modified by the adjustment to the neutral state, then the integrated wave enstrophy would be equal to $2 \times 10^{-12}/s^2$. So the neutral state of the 3 pt formulation is predicted to have an integrated wave enstrophy between $2 \times 10^{-12}/s^2$ and $3 \times 10^{-11}/s^2$. This is a very large range. It is not clear how a model that does not resolve y_c well, will adjust to neutrality. The values for the integrated wave enstrophy in the quasi-linear neutral state, in units of s^{-2}, are listed in Table A.3.

The 3 pt and 5 pt integrated wave enstrophy values are very close to the

n pts	$< q_f'^2 >$ $10^{-11}/s^2$
3	0.3
5	6.0
9	12.0

Table A.3: Values of the integrated wave enstrophy in the quasi-linear neutral state, in units of s^{-2}.

analytically calculated values. The 3pt calculation shows that it is primarily the closest gridpoint on the side of the jet that is modified. The 9 pt value is close to the analytically calculated value for 17 pts. These values for $< q_f'^2 >$ are larger than the values that were calculated analytically for a neutral state defined by the Charney-Stern theorem, even though the quasi-linear neutral state is still supercritical by the Charney-Stern theorem.

Figures A-10, A-11, and A-12 show the partitioning of the integrated wave enstrophy among waves 1-6, in a dissipationless system. Figure A-10 is for a resolution of 9 points. Waves 1 through 6 are all unstable initially. Waves 2 and 3 grow the fastest and modify the mean flow such that all of the waves, except wave 1, become stabilized at approximately the same time. Since there is no exchange of energy or enstrophy among the waves in the quasi-linear integration, the enstrophy of the waves changes very little after the waves have become stabilized. Figure A-10 shows that there is not an equipartition of enstrophy in this neutral state. This is because of the large differences in the growth rates of the waves. An increase in resolution reduces this difference and causes the waves to grow at approximately the same rate. Therefore, enstrophy is distributed more equally as resolution is increased. The enstrophy in wave one continues to increase after the other waves have become saturated. This is because wave 1 is still unstable in a mean flow that is stable to the higher wavenumbers. Figure A-11 is for the 5 point quasi-linear integration. Only waves 1 and 2 are unstable. As in the 9 pt integration, wave 1 continues to grow after wave 2 has become saturated. The linear parameter studies showed that the growth rates of the waves was reduced as the resolution was decreased. This explains why it takes the waves longer to become stabilized as the resolution is decreased. Figure A-12 shows the 3 point quasi-linear integration. Only wave 1 is unstable. The contribution to the integrated wave enstrophy by the other waves is negligible. Wave 1 doesn't become saturated until day 100.

Figure A-13, A-14, and A-15 show the effect of adding dissipation. It is seen that the most unstable wave decays away with the higher wavenumbers. Wave one grows slowly but becomes the dominant wave, even for a large dissipation time constant of 60 days. Therefore it is not only the growth rate of the waves that determines whether a wave will dissipate away.

When dissipation is added, the integrated wave enstrophy of the neutral state is reduced from $1 \times 10^{-10}/s^2$ to $3 \times 10^{-11}/s^2$, independent of the magnitude of the dissipation. This result was also found in the SL study. These results were found to be true for the 5 pt study, Figure A-15. The 3 pt study had a similar reduction of integrated wave enstrophy, when the dissipation was added.

A.3.2 Equilibrated states

The meridional gradient of the potential vorticity at the jet is shown in Figure A-16 for the 9pt study, Figure A-17 for the 5pt study, Figure A-18 for the 3pt study. These Figures show that the magnitude of the oscillations increases as the resolution is increased. The neutral states are all supercritical, relative to the Charney-Stern criteria, even though there is no dissipation. The zero line appears to be an upper bound for the oscillations, therefore the larger the resolution is, the larger the supercriticality of the potential vorticity gradients. Similar behaviour is found in the SL study of the wave-mean flow interaction (their Figure 3). When dissipation is added to the system, the magnitude of the oscillation decreases but the average supercritical value which it oscillates about, changes very little. For smaller values of the zonal mean wind, the potential vorticity gradients are seen to oscillate about the zero line more closely, Figure A-19, even though the system has a dissipation time constant of 20 days. The supercriticality of the neutral state increases when the resolution is increased. For 3 points in the half jet, the neutral state has a jump of $-0.2 \times 10^{-11}/ms$ in $\frac{\partial \bar{q}}{\partial y}$ at the point of the jet, for the case described above. This is compared to a value of $-1 \times 10^{-11}/ms$ for 5 point resolution and $-2 \times 10^{-11}/ms$ for 9 point resolution. A parameter study of the jump in $\frac{\partial \bar{q}}{\partial y}$ for a resolution of 19 points, the resolution used in the SL study, is shown in Figure A-20. This Figure shows that the magnitude of the potential vorticity gradient increases as β is decreased and/or the zonal mean wind is increased.

The time rate of change of the zonally averaged wave enstrophy was derived by SL to be

$$\frac{1}{2}\frac{\partial(\overline{q'^2})}{\partial t} = -(\overline{v'q'})\frac{\partial \bar{q}}{\partial y} - D(\overline{q'^2}). \qquad (7)$$

If the time rate of change of the zonally averaged wave enstrophy goes to zero then the zonally averaged transport of the perturbation potential vorticity down the gradient of mean potential vorticity must balance the dissipation of the zonally averaged wave enstrophy. An increase in the zonally averaged wave enstrophy of the neutral state, or a decrease in the dissipation time constant, must be accompanied by either an increase in the magnitude of the mean potential vorticity gradient or an increase in the zonally averaged transport of perturbation potential vorticity. If the system is dissipationless and the meridional gradient of the potential vorticity is not equal to zero, then the potential vorticity transport goes to zero as the time rate of change of the wave enstrophy goes to zero.

n	$\overline{v'q'}$	$\partial\bar{q}/\partial y$	$\overline{q'^2}$	Γ_f
pts	$10^{-6}m/s^2$	$10^{-11}/ms$	$10^{-11}/s^2$	$10^{-5}/s$
3	0.4	-0.2	0.2	1.3
5	2.3	-1.1	4.7	1.0
9	4.2	-1.8	12.8	0.6

Table A.4: Quasi-linear values at the jet, where u0 has been set equal to 70 m/s and D^{-1} has been set equal to 20 days.

Figures A-21 and A-22 show the zonally averaged transport of perturbation potential vorticity at the jet for a resolution of 9 points. Figure A-21 is for a dissipation time constant of 20 days while Figure A-22 was calculated with a dissipation time constant of 60 days. It is seen that the frequency of the oscillations increases as the dissipation time constant is increased. The magnitude of the transport is the same until day 60. After day 60, the oscillations observed in Figure A-21 start damping out to a constant value of $4 \times 10^{-6}m/s^2$. The pv transport for the less dissipative case has large oscillations throughout the integration and oscillates about a value of $1 \times 10^{-6}m/s^2$. As the dissipation time constant is increased the pv transport oscillates about a value closer to zero, approaching the nondissipative neutral state where the pv transport goes to zero.

When the resolution is decreased to 5 points and D^{-1} is equal to 20 days, the pv transport at the jet approaches a value of $2 \times 10^{-6}m/s^2$, Figure A-23. Therefore, reducing the resolution by a half, reduces the pv transport at the jet by a half. When the resolution is reduced again by a half, to 3 points, Figure A-24, the pv transport at the jet approaches a value of $0.4 \times 10^{-6}m/s^2$ The relationships described above are illustrated in Table A.4. Table A.4 lists the quasi-linear values at the jet, where u0 has been set equal to 70 m/s and D^{-1} has been set equal to 20 days.

When the resolution has been reduced from 9 points to 3 points, the pv transport and the jump in the mean potential vorticity gradient are reduced by an order of magnitude. Since this reduces the transport of perturbation potential vorticity down the mean potential vorticity gradient, the zonally averaged enstrophy at the jet needed to balance this change must increase. These relationships were found to be independent of the magnitude of the dissipation. The shear of the equilibrated state is very close to the critical shear of the analytic problem for the 3 point resolution The equilibrated state of the 5 and 9 point resolution studies have a shear which are larger than the analytic critical shear by a factor of 2.

n	$\overline{v'q'}$	$\partial\overline{q}/\partial y$	$\overline{q'^2}$
pts	$10^{-6}m/s^2$	$10^{-11}/ms$	$10^{-11}/s^2$
5	11.2	-0.35	5.9
9	7.3	-1.09	14.1

Table A.5: Values of the nonlinear neutral state at the jet, where u0 is equal to 70 m/s and D^{-1} is equal to 20 days.

A.4 Nonlinear integration results

The nonlinear integrations were formulated with a different numerical scheme than the quasi-linear integrations. This is because of the inability to use a centered finite difference method when the barotropic problem is formulated in two levels. Therefore, the nonlinear integrations will be used to determine whether the results of the 5 and 9 point quasi-linear integrations change significantly when wave-wave interaction is allowed.

Including the wave-wave interactions does not change the balance defined by equation (7), at the jet. Therefore, the mean potential vorticity gradient at the jet can be calculated from the wave terms at the jet, when the system has reached equilibrium. Using this relationship to calculate $\frac{\partial\overline{q}}{\partial y}$, Table A.5 lists the values of the nonlinear neutral state at the jet, where u0 is equal to 70 m/s and D^{-1} is equal to 20 days.

The wave enstrophy is approximately $\frac{5}{4}$ times the quasi-linear results. The largest change is in the mean potential vorticity gradient at the jet. Table A.5 shows that the nonlinear integrations equilibrate to a state that is less supercritical than the quasi-linear neutral state. This reduction in the supercriticality is balanced by a increase in the pv transport. The supercriticality increases with an increase in the resolution, in agreement with the quasi-linear results. The pv transport changes by 35 percent when the resolution is doubled. This is much less than the 2 fold increase that was calculated in the quasi-linear integrations. The nonlinear integrations have shown that the neutral state of the quasi-linear closely approximates the nonlinear neutral state. The quasi-linear neutral state overestimates the supercriticality at the jet. This is accompanied by a proportional decrease in the pv transport. The wave enstrophy at the jet changes very little when the nonlinear terms are included in the integration.

A.5 Baroclinic interpretation of barotropic results

The linearized barotropic jet is analogous to the linearized Charney model. This equivalence does not hold when the nonlinear terms grow to be of the same order as the linear terms. This is because of the fundamentally three dimensional nature of the baroclinic problem. The nonlinear neutral state was found to have potential vorticity gradients that were 3 times smaller than those calculated in the quasi-linear neutral state. All of the nonlinear and quasi-linear neutral states were supercriticality, relative to the Charney-Stern criteria. This supercriticality was found to be relatively independent of the magnitude of the dissipation but very dependent on the resolution of the model.

The linear barotropic results can be extended to the baroclinic problem when the nonlinear terms are small relative to the linear terms. Therefore, in the linearized Boussinesq Charney model, the most unstable wavenumber will shift to lower wavenumbers when the resolution is decreased. The growth rates of the waves will decrease and the shortwaves will become stabilized as the resolution is decreased. The critical mean zonal wind for instability will double when the resolution is reduced by a half. A reduction in resolution will stabilize the waves by increasing the critical zonal mean wind for instability.

The extension of the quasi-linear results to the baroclinic problem assumes that the baroclinic system is stabilized by wave-mean flow interactions and that the wave-wave interactions are negligible. It also assumes that there are no barotropic feedbacks onto the baroclinic instability. The momentum fluxes are neglected and the meridional structure of the jet is assumed to be unchanged by the waves. Stabilization of the waves due to feedbacks associated with a variable static stability are also neglected in this extension. The significance of these feedbacks and their modification by changes in resolution will be investigated in the proposed baroclinic model study. As a prototype problem, concerned exclusively with the purely baroclinic quasi-geostrophic problem, this study reveals the impact of resolution on the wave-mean flow interactions. This may prove to be significant in the full three-dimensional study.

The potential vorticity transports and the potential vorticity gradients change significantly when the nonlinear terms are included in the equations. The zonally averaged enstrophy at the jet appears to be more robust. The enstrophy is maximized while the potential vorticity transport and gradient are modified by variations in the resolution.

The barotropic problem assumes that the zonal wind is symmetric about the point of the jet. This means that the shear and the zonal mean potential vorticity are equal to zero at the point of the jet. In the analogous baroclinic problem the point of the jet corresponds to the lower boundary. This lower boundary in the baroclinic problem represents the surface of the earth. The meridional shear in the barotropic problem corresponds to the vertical shear in the baroclinic problem.

n	u_c	Γ_c	$\partial\bar{\theta}_c/\partial y$
pts	m/s	$10^{-4}/s$	$10^{-3} K/km$
3	5.2	7.0	-2.1
5	2.6	3.5	-1.0
9	1.3	1.8	-0.5

Table A.6: Critical shears and temperature gradients for the linear baroclinic model, that have been calculated from the values of the linear barotropic model in Table A.1 .

By the thermal wind relation, the vertical shear is proportional to the meridional temperature gradient. Since the shear goes to zero at the lower boundary of the baroclinic problem, the surface temperature gradient also goes to zero at the lower boundary. This is very unrealistic, since the largest temperature gradients in the troposphere are observed to be at the surface of the earth. The critical shear is the shear necessary to eliminate the negative potential vorticity gradients in the model and is expressed as,

$$\Gamma_c = \frac{\beta N^2}{f_0^2}\frac{H}{(n-1)}$$

Where N^2 is the Brunt-Vaisala frequency and has been set equal to $1. \times 10^{-4}/s^2$, f_0 is the Coriolis parameter and is set equal to $1. \times 10^{-4}/s$, H is the vertical scale height of the troposphere and is set equal to 7.4 km. n is the resolution of the model. The critical zonal wind, assuming a constant initial shear is expressed as, $\Gamma_c H$. The critical shears and temperature gradients for the linear baroclinic model, that have been calculated from the values of the linear barotropic model in Table A.1, are listed in Table A.6.

The temperature gradient is calculated using the equation,

$$\frac{\partial\bar{\theta}}{\partial y} = -\frac{f_0\theta_0}{g}\frac{\partial\bar{u}}{\partial z}.$$

These temperature gradients correspond to a temperature difference across a distance of 40 degrees of, -9.2 K for n=3, -4.6 K for n=5 and -2.3 K for n=9. These values are for an unforced and dissipationless model. The continuous formulation of the point jet has no critical shear or critical temperature gradient. The critical shear that is calculated in Table A.6 is strictly due to the truncation of the model. The predicted critical shear for the quasi-linear neutral state is 0.5× this critical shear. As the resolution is increased the critical shear is reduced. For a resolution of 3 points, which is equivalent to the two-level model, the critical shear and critical temperature gradients are of the order of observed mid-latitude surface shears and temperature gradients. Observations, Peixoto and Oort (1993), yield an annual mean temperature gradient of -4×10^{-3} K/km and an annual mean

n	$\overline{v'q'}$	$\overline{v'\theta'}$	Γ_f	$\partial\overline{\theta_c}/\partial y$
pts	$10^{-5}m/s^2$	Km/s	$10^{-4}/s$	$10^{-3}K/km$
3	0.5	0.3	3.8	-1.1
5	2.6	0.7	2.8	-0.8
9	4.8	0.7	1.7	-0.5

Table A.7: Characteristics of the baroclinic equilibrium state calculated from the values of the barotropic quasi-linear neutral state.

zonal wind shear of 7×10^{-4} s^{-1}, for the Northern Hemispheric mean at approximately 800 mb. The characteristics of the baroclinic equilibrium state calculated from the values of the barotropic quasi-linear neutral state, listed in Table A.4, for $D^{-1} = 20$ days, are listed in Table A.7.

Where $\frac{\partial}{\partial y} = -\frac{f_0}{N}\frac{\partial}{\partial z}$ and

$$\overline{v'q'}_{baroclinic} = \frac{f_0^2}{N^2}\frac{L^2}{H^2}\overline{v'q'}_{barotropic},$$

$$\overline{v'\theta'} = \frac{N^2\theta_0 H}{2f_0 g(n-1)}\overline{v'q'}.$$

The temperature flux and the critical shear are evaluated at $\Delta z/2$. A decrease in the resolution decreases the potential temperature flux and increases the shear of the equilibrated state. The potential temperature flux at $\frac{\Delta z}{2}$ changes very little when the resolution is decreased from 9 points to 5 points. When the resolution is decreased from 5 points to 3 points, the potential temperature flux decreases by a factor of two. A comparison of the two-dimensional results with the results of the proposed three-dimensional model will determine whether the modification of the dynamics, due to a reduction in resolution in the two-dimensional problem, is significant in the full three-dimensional problem.
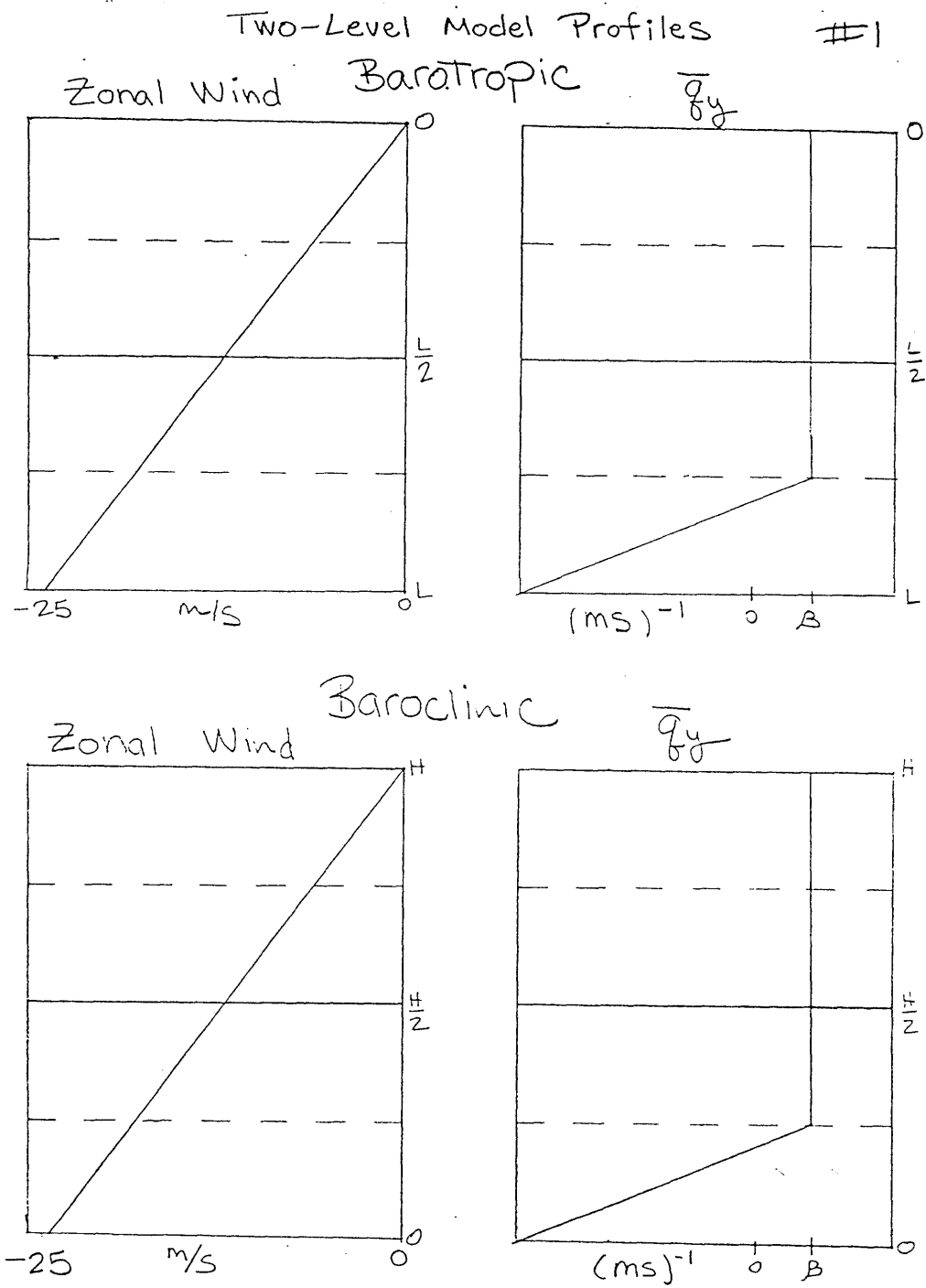
Two-Level Model Profiles   #1

Zonal Wind   Barotropic $\overline{q}_y$

Figure A-1: The initial jet structure and the potential vorticity gradient of the basic state for the barotropic jet and for the Charney problem.

Numerical Configuration
beta = 1.9e−11/ms
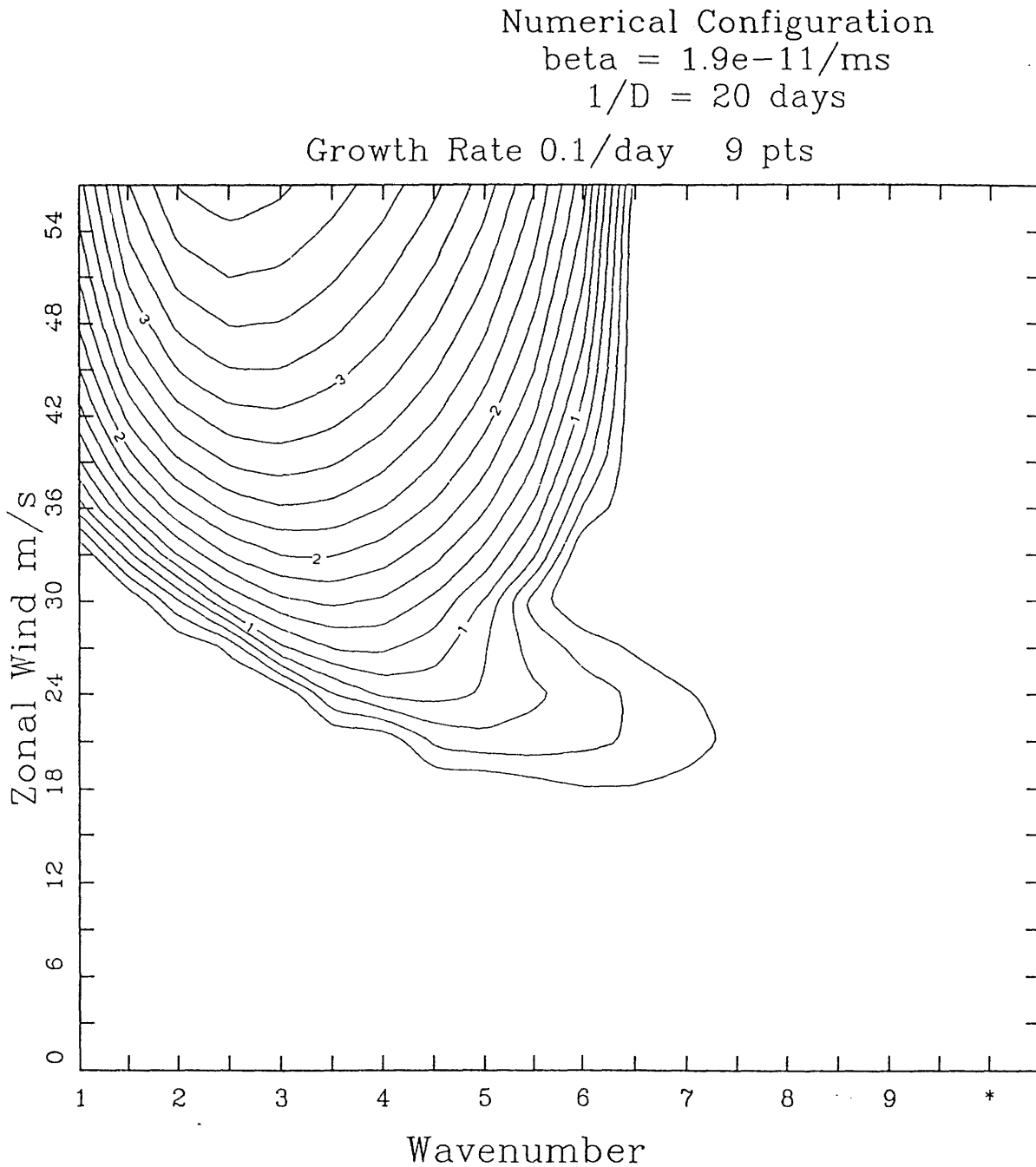1/D = 20 days

Growth Rate 0.1/day   9 pts

Figure A-2: The growth rates of waves 1-10 when the zonal mean wind is increased from 0 to 56 m/s, from the model run using the staggered scheme for the 9 gridpoint half jet.
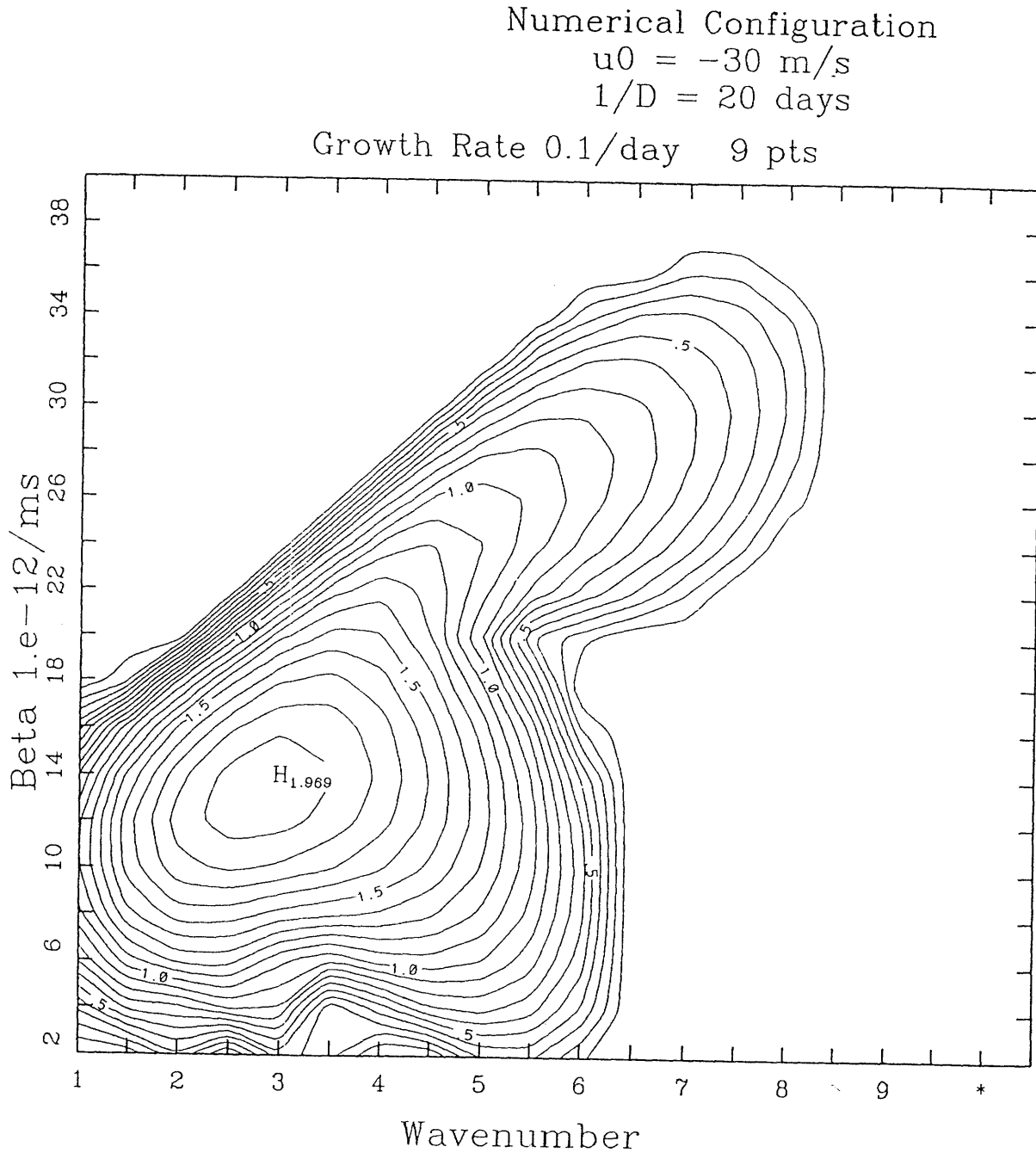
Figure A-3: The growth rates of waves 1-10 when β is increased from $0.2 \times 10^{-11} \frac{1}{ms}$ to $4.0 \times 10^{-11} \frac{1}{ms}$, from the model run using the staggered scheme for the 9 gridpoint half jet.
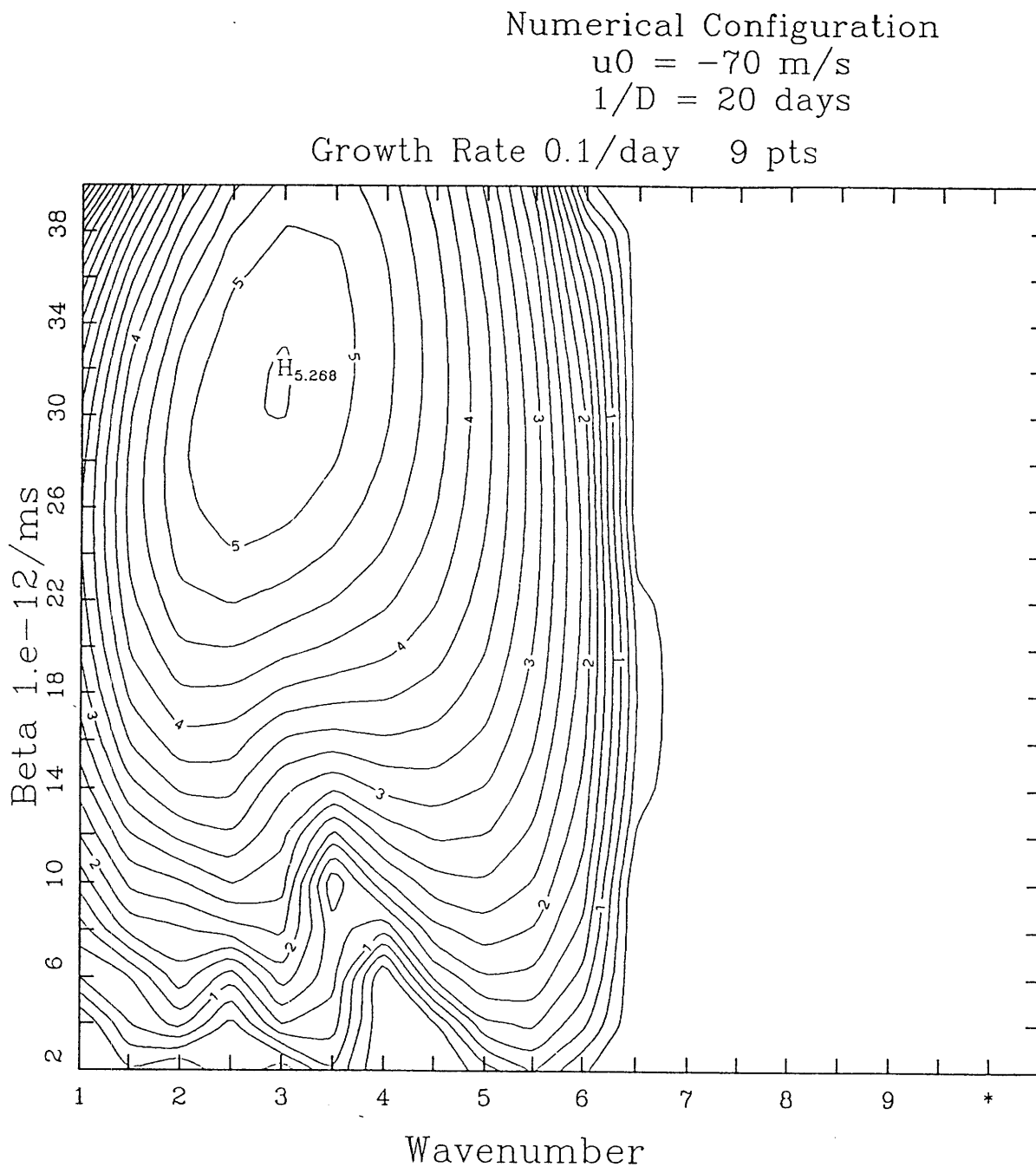
Numerical Configuration
u0 = −70 m/s
1/D = 20 days

Growth Rate 0.1/day   9 pts

Figure A-4: The growth rates of waves 1-10 when β is increased from $0.2 \times 10^{-11}\frac{1}{ms}$ to $4.0 \times 10^{-11}\frac{1}{ms}$ when the zonal mean wind is increased from 30 m/s to 70 m/s, from the model run using the staggered scheme for the 9 gridpoint half jet.
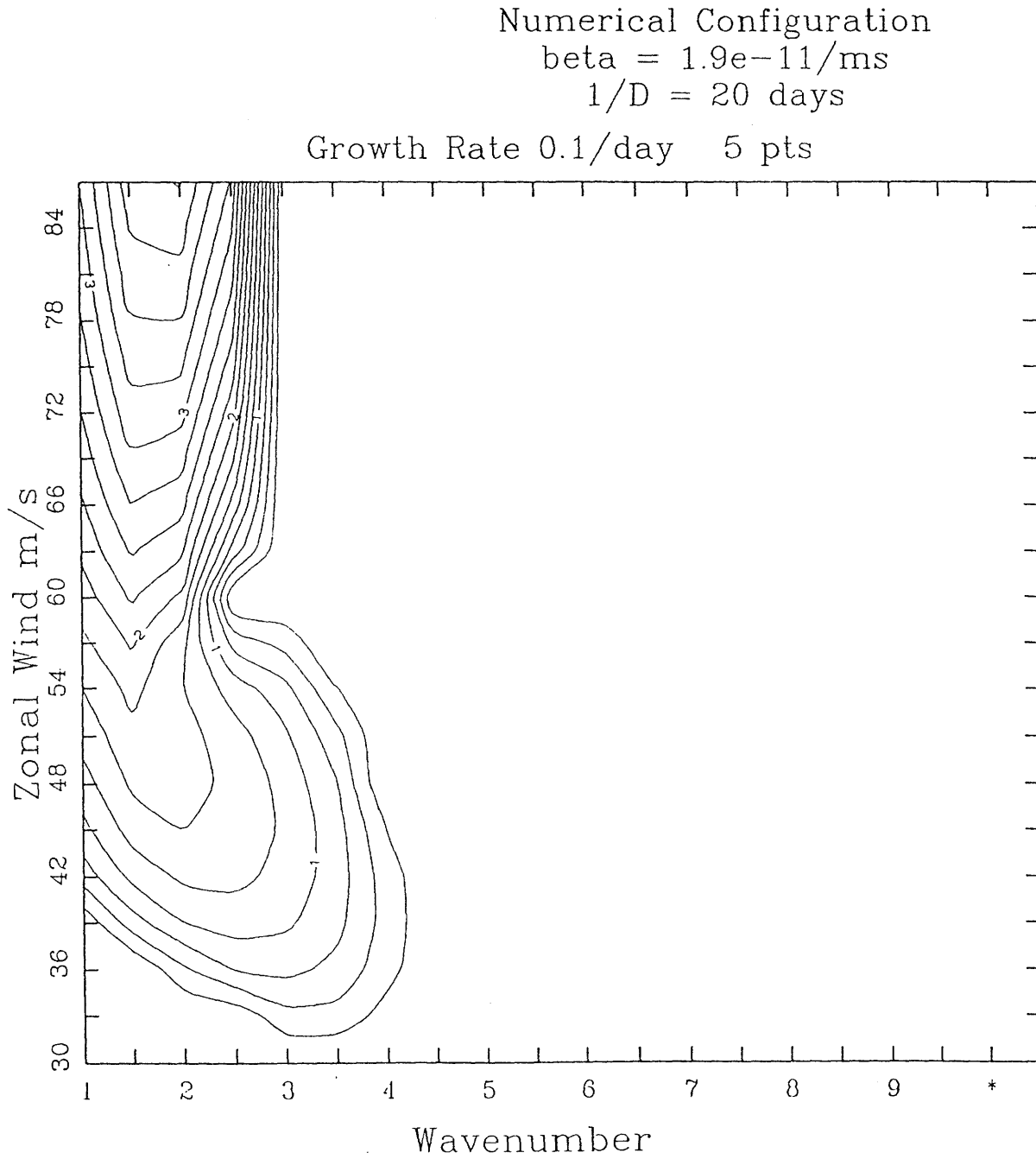
Figure A-5: The growth rates of waves 1-10 when the
zonal mean wind is increased from 30 m/s to 87 m/s,
from the 5 gridpoint staggered half jet model run.

Figure A-6: The growth rates of waves 1-10 when β is increased from $0.2 \times 10^{-11}\frac{1}{ms}$ to $4.0 \times 10^{-11}\frac{1}{ms}$ when the zonal mean wind is increased from 30 m/s to 70 m/s, from the 5 gridpoint staggered half jet model run.

Numerical Configuration
beta = 1.9e−11/ms
1/D = 20 days

Growth Rate 0.1/day   3 pts

Figure A-7: The growth rates of waves 1-10 when the
zonal mean wind is increased from 30 m/s to 120 m/s,
from the 3 gridpoint staggered half jet model run.

Numerical Configuration
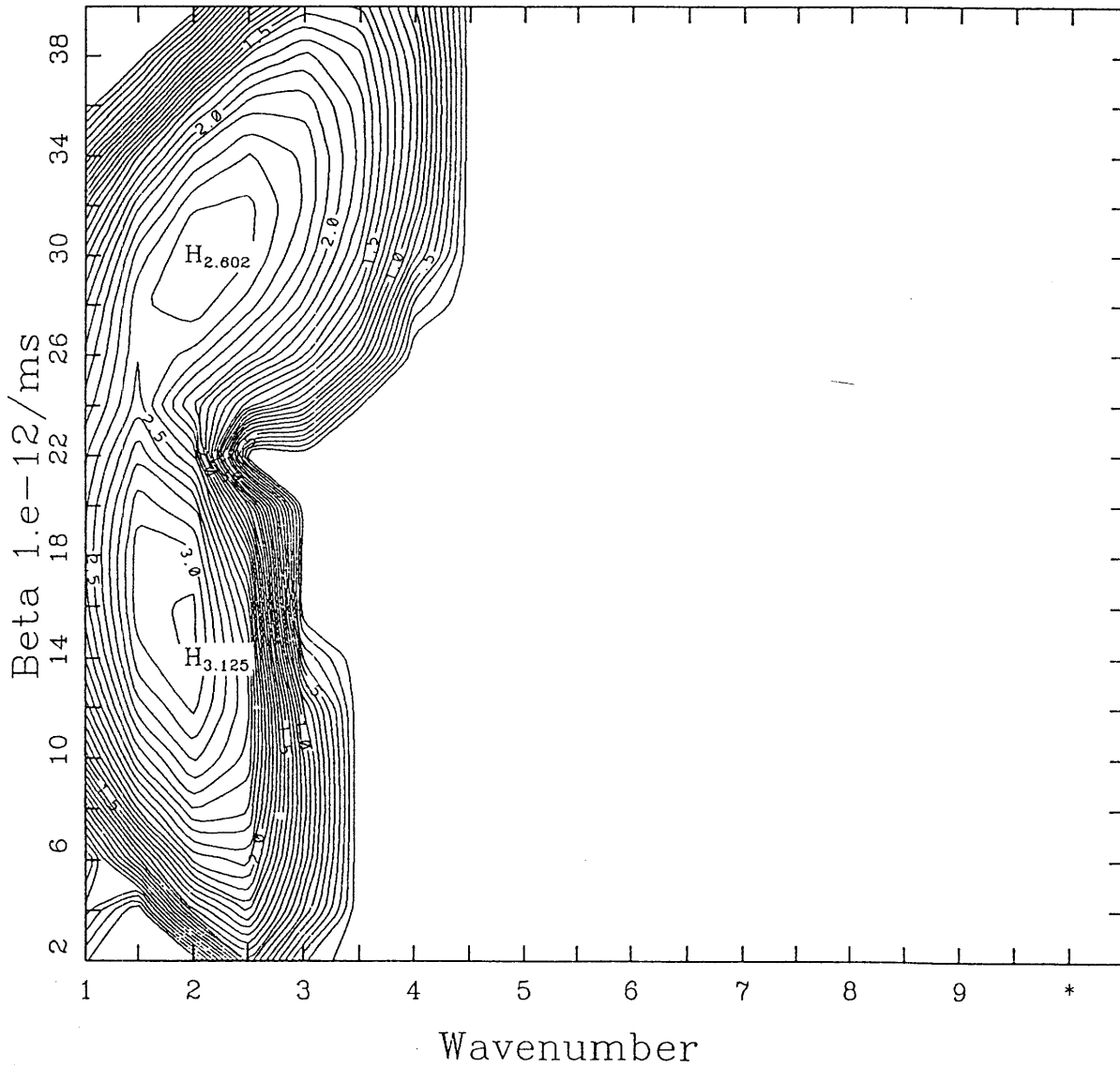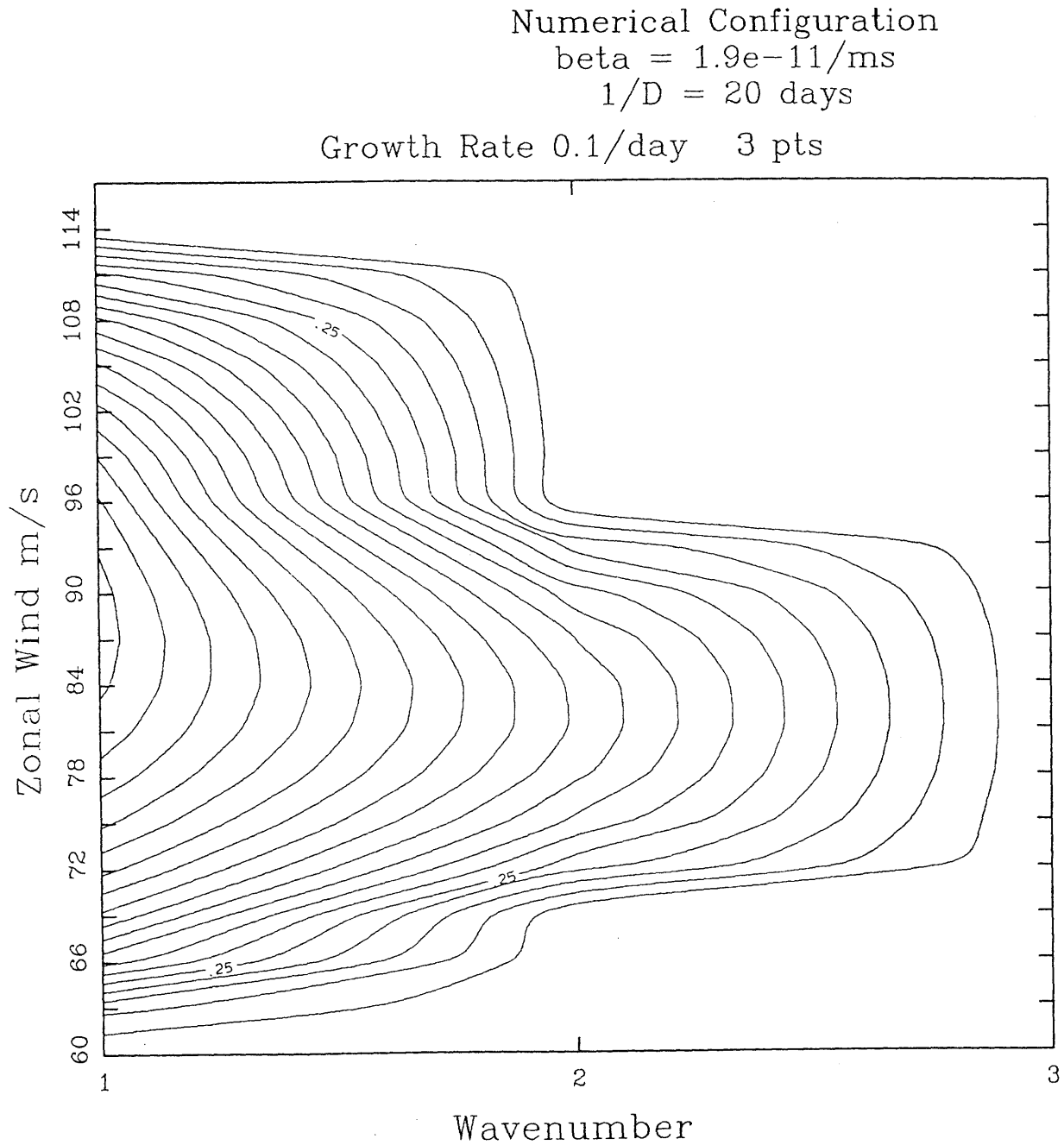u0 = −80 m/s
1/D = 20 days

Growth Rate 0.1/day   3 pts

Figure A-8: The growth rates of waves 1-10 when β is increased from $0.2 \times 10^{-11}\frac{1}{ms}$ to $4.0 \times 10^{-11}\frac{1}{ms}$ when the zonal mean wind is increased from 30 m/s to 80 m/s, from the 3 gridpoint staggered half jet model run.

Numerical Configuration
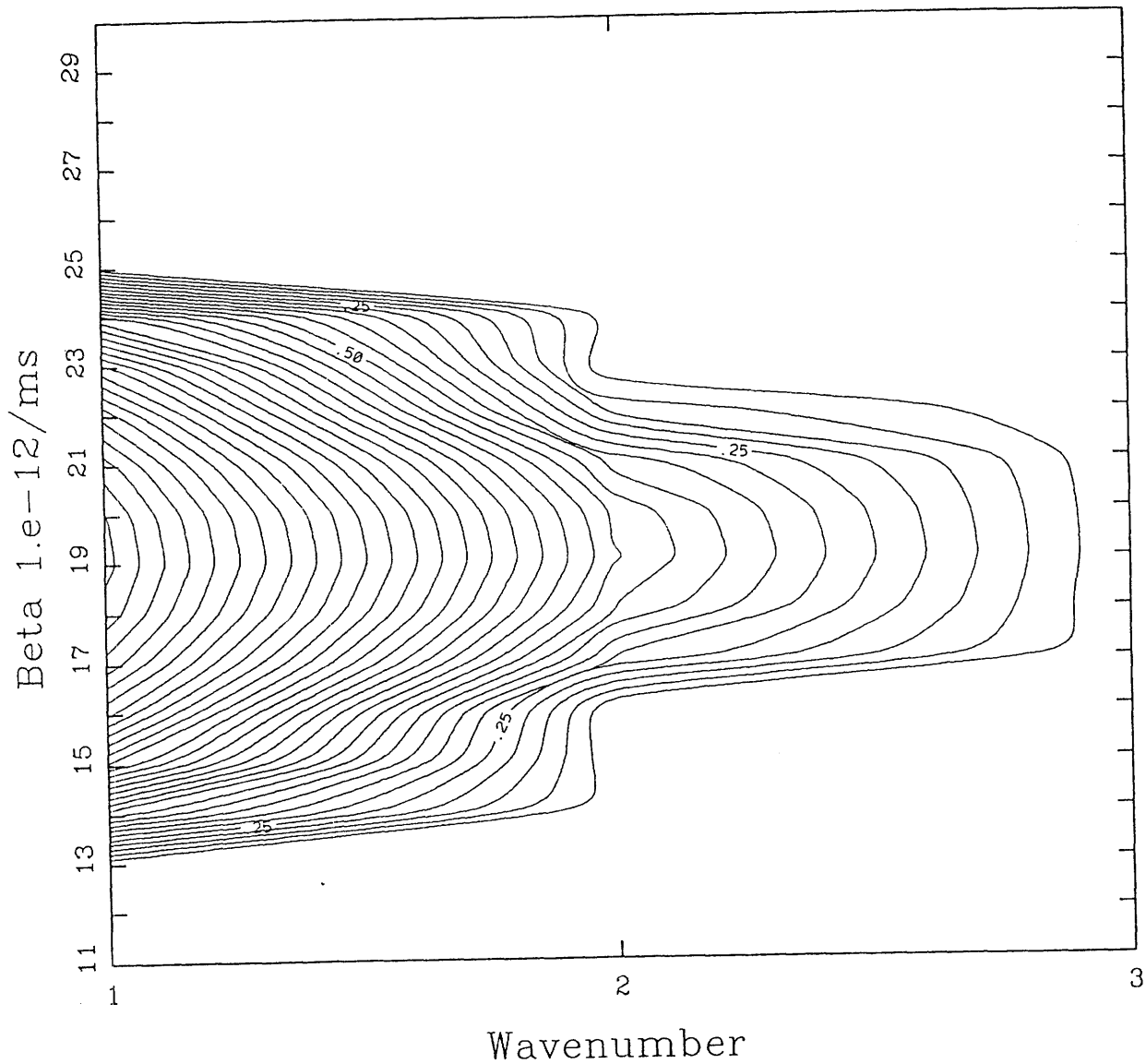## u0 = −80 m/s
1/D = 0 days

Growth Rate 0.1/day   3 pts

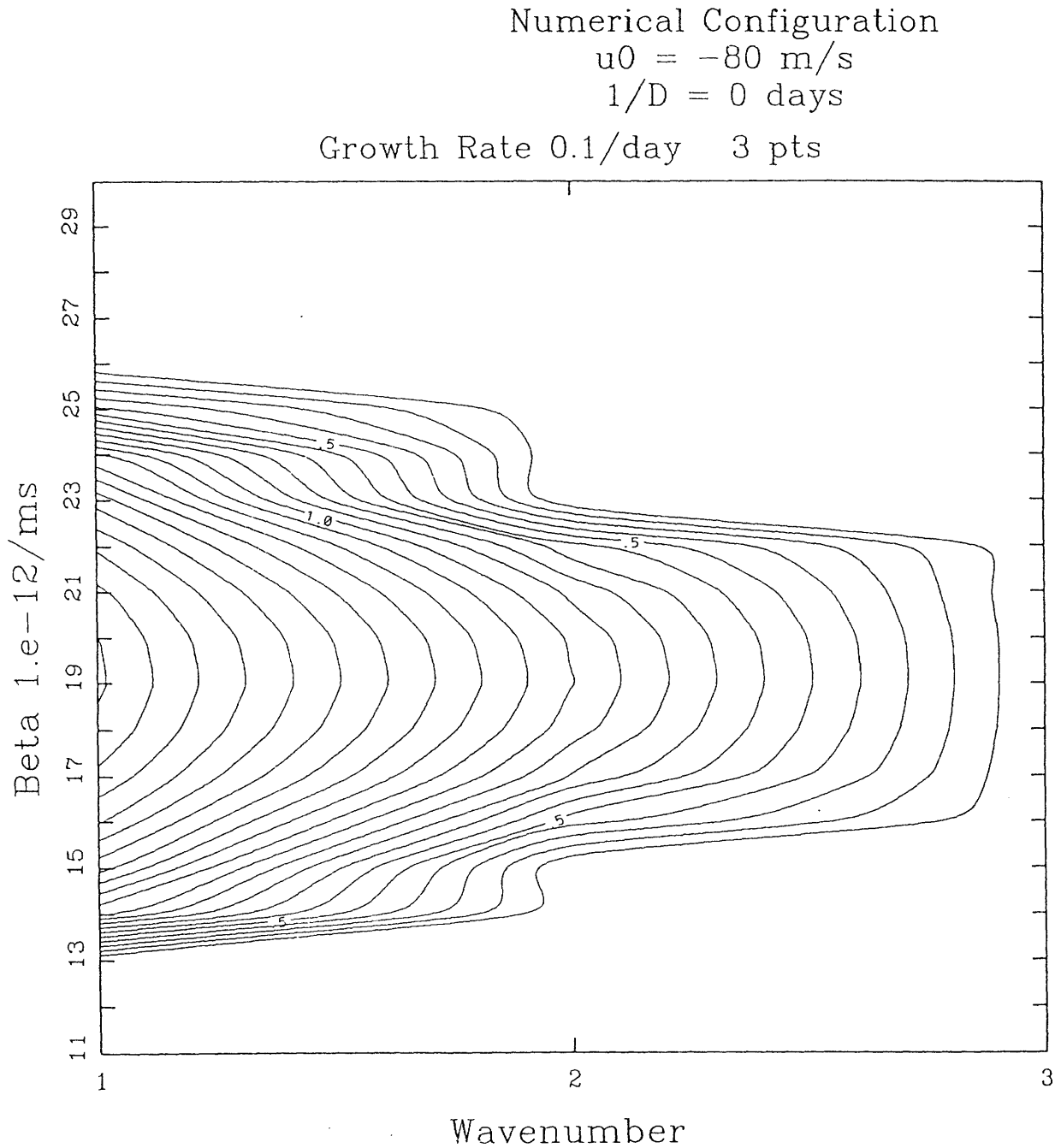Figure A-9: The growth rates of waves 1-10 when β is increased from $0.2 \times 10^{-11} \frac{1}{ms}$ to $4.0 \times 10^{-11} \frac{1}{ms}$ when the zonal mean wind is increased from 30 m/s to 80 m/s, from the 3 gridpoint staggered half jet model run without dissipation.

Charney Configuration

integrated wave enstrophy$\left(\dfrac{1}{S^2}\right)$

b = 0.19D-10/(ms), D=inf u0= 70.0m/s 9   pts

Figure A-10: The partitioning of the integrated wave enstrophy among waves 1-6, from the 9 gridpoint quasi-linear half jet model run without dissipation.

Charney Configuration

integrated wave enstrophy$\left(\frac{1}{s^2}\right)$

b = 0.19D−10/(ms), D=inf u0= 70.0m/s 5 pts

Figure A-11: The partitioning of the integrated wave enstrophy among waves 1-6, from the 5 gridpoint quasi-linear half jet model run without dissipation.

Charney Configuration

integrated wave enstrophy $\left(\frac{1}{s^2}\right)$

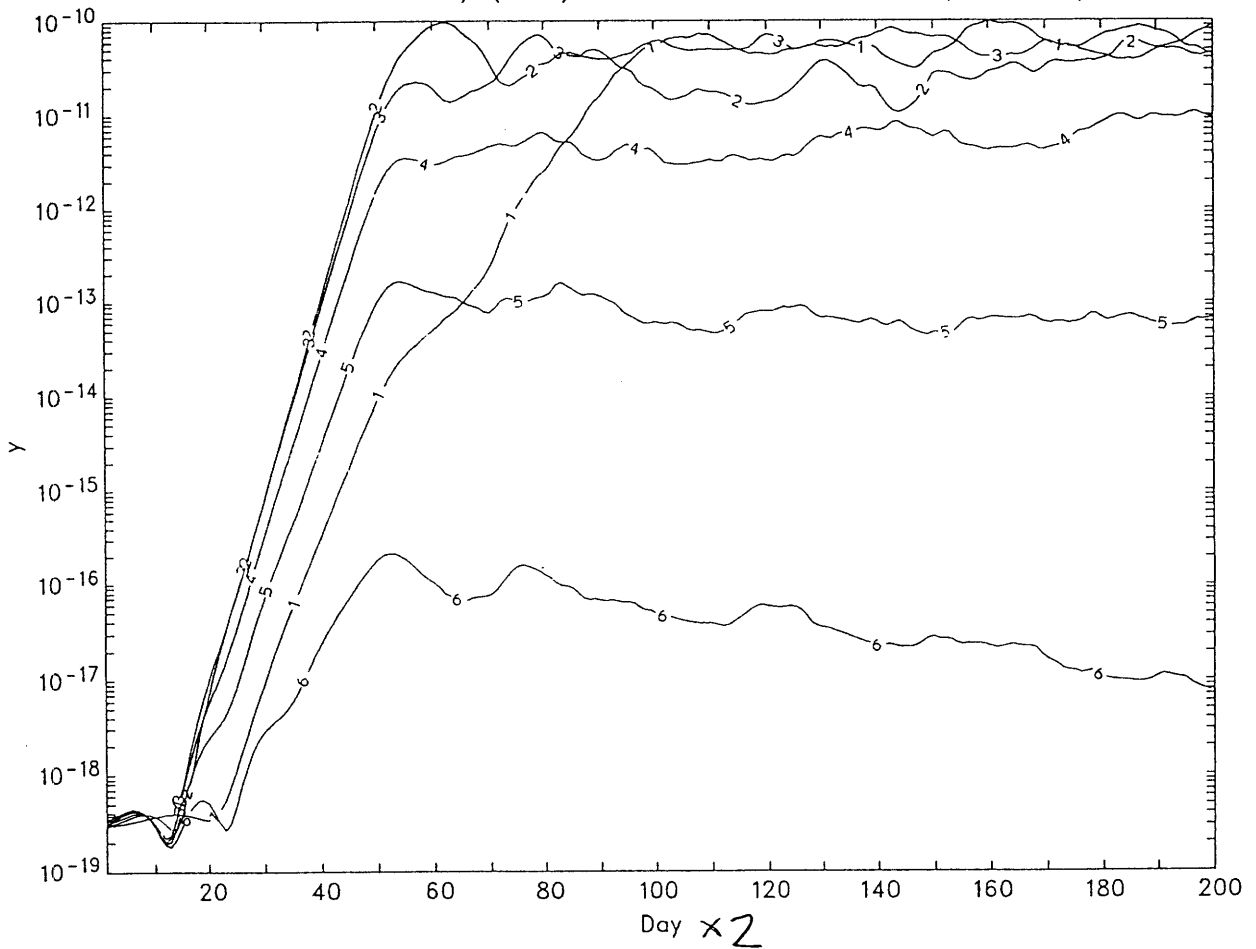b = 0.19D-10/(ms), D=inf u0= 70.0m/s 3   pts

Figure A-12: The partitioning of the integrated wave enstrophy among waves 1-6, from the 3 gridpoint quasi-linear half jet model run without dissipation.
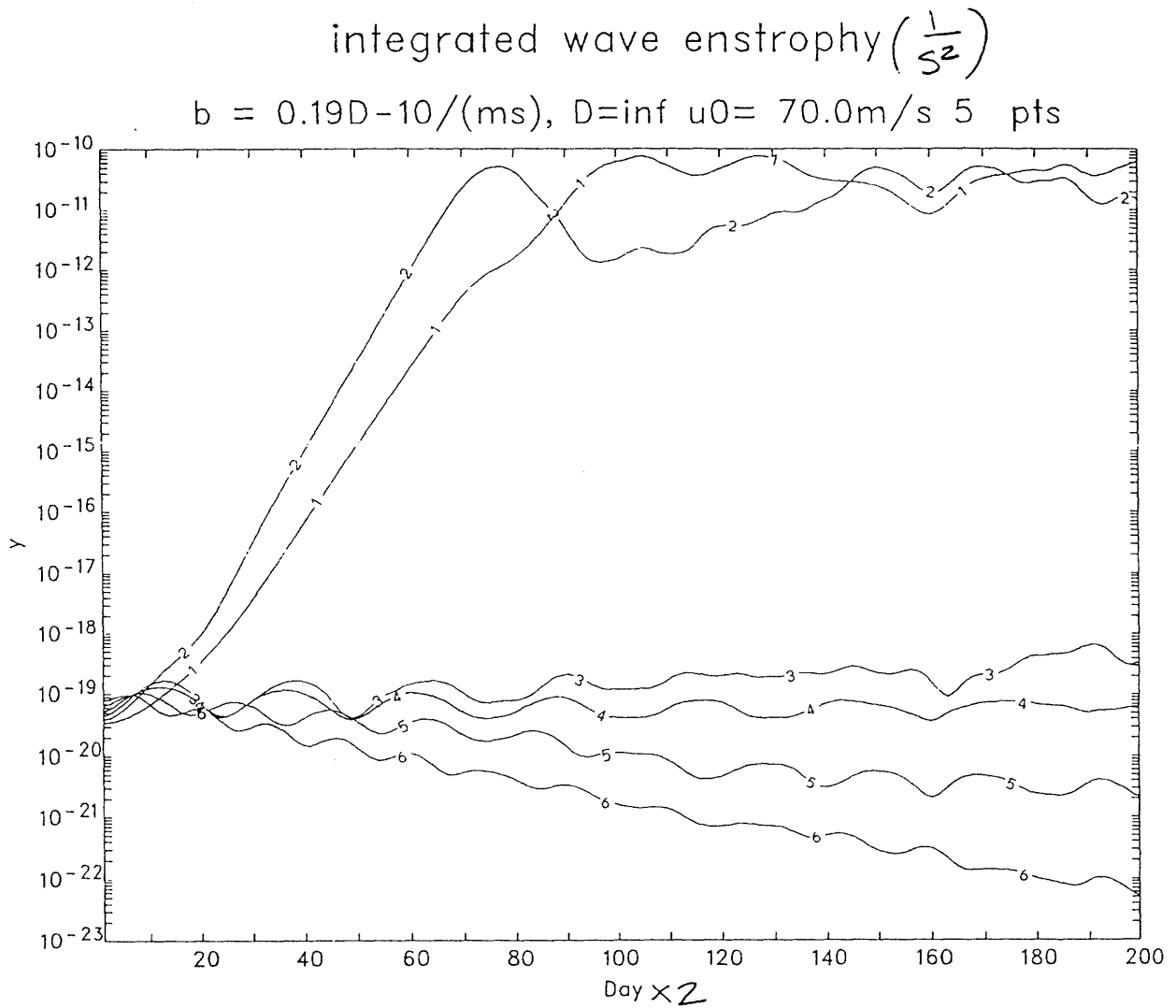
Charney Configuration

integrated wave enstrophy $\left(\dfrac{1}{S^2}\right)$

b = 0.19D-10/(ms), D= 60 u0= 70.0m/s 9 · pts

Figure A-13: The partitioning of the integrated wave enstrophy among waves 1-6, from the 9 gridpoint quasi-linear half jet model run with a dissipation timescale of 60 days.

Charney Configuration

integrated wave enstrophy $\left(\frac{1}{s^2}\right)$

b = 0.19D−10/(ms), D= 20 u0= 70.0m/s 9 pts
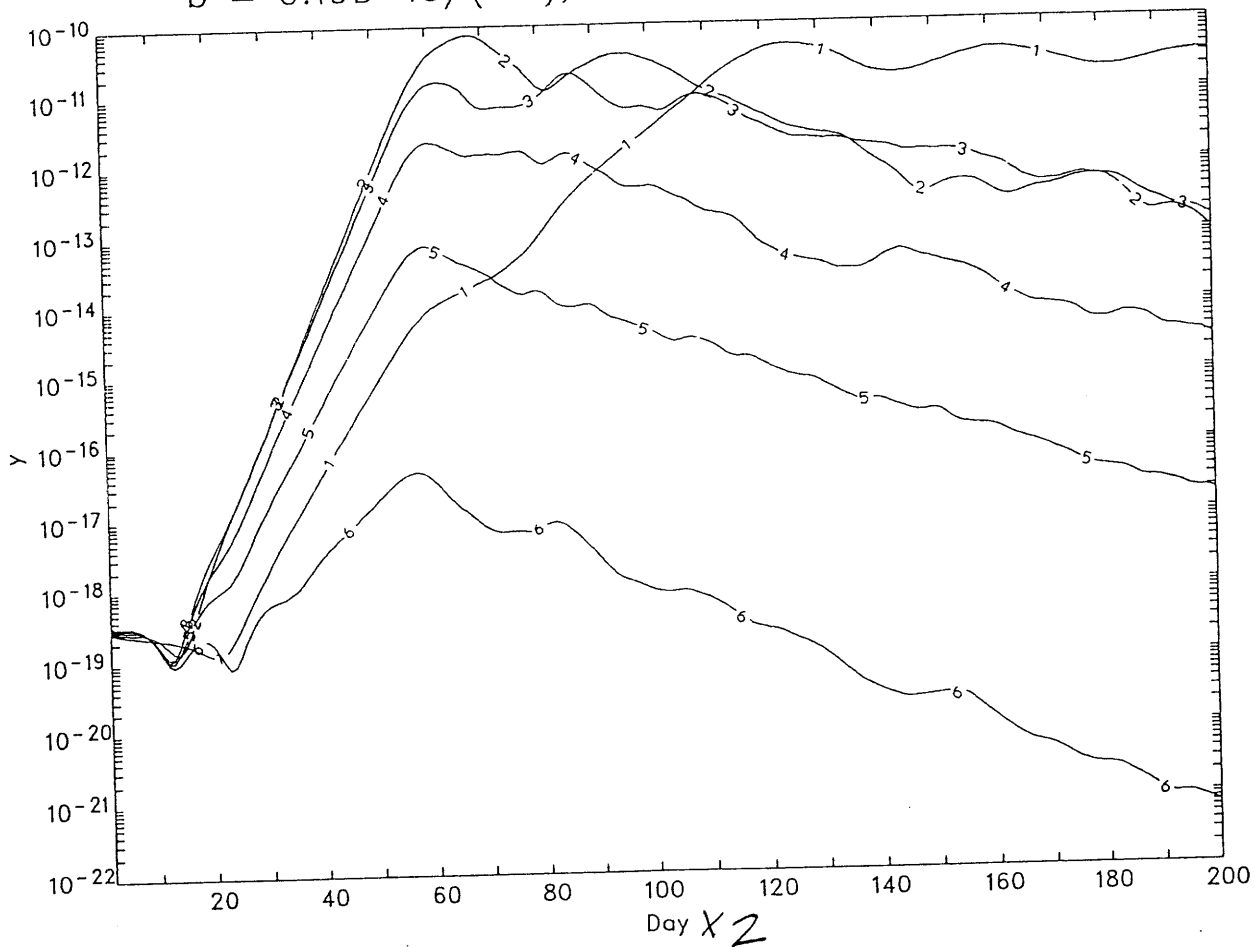
Figure A-14: The partitioning of the integrated wave enstrophy among waves 1-6, from the 9 gridpoint quasi-linear half jet model run with a dissipation timescale of 20 days.

Charney Configuration

integrated wave enstrophy $\left(\frac{1}{s^2}\right)$
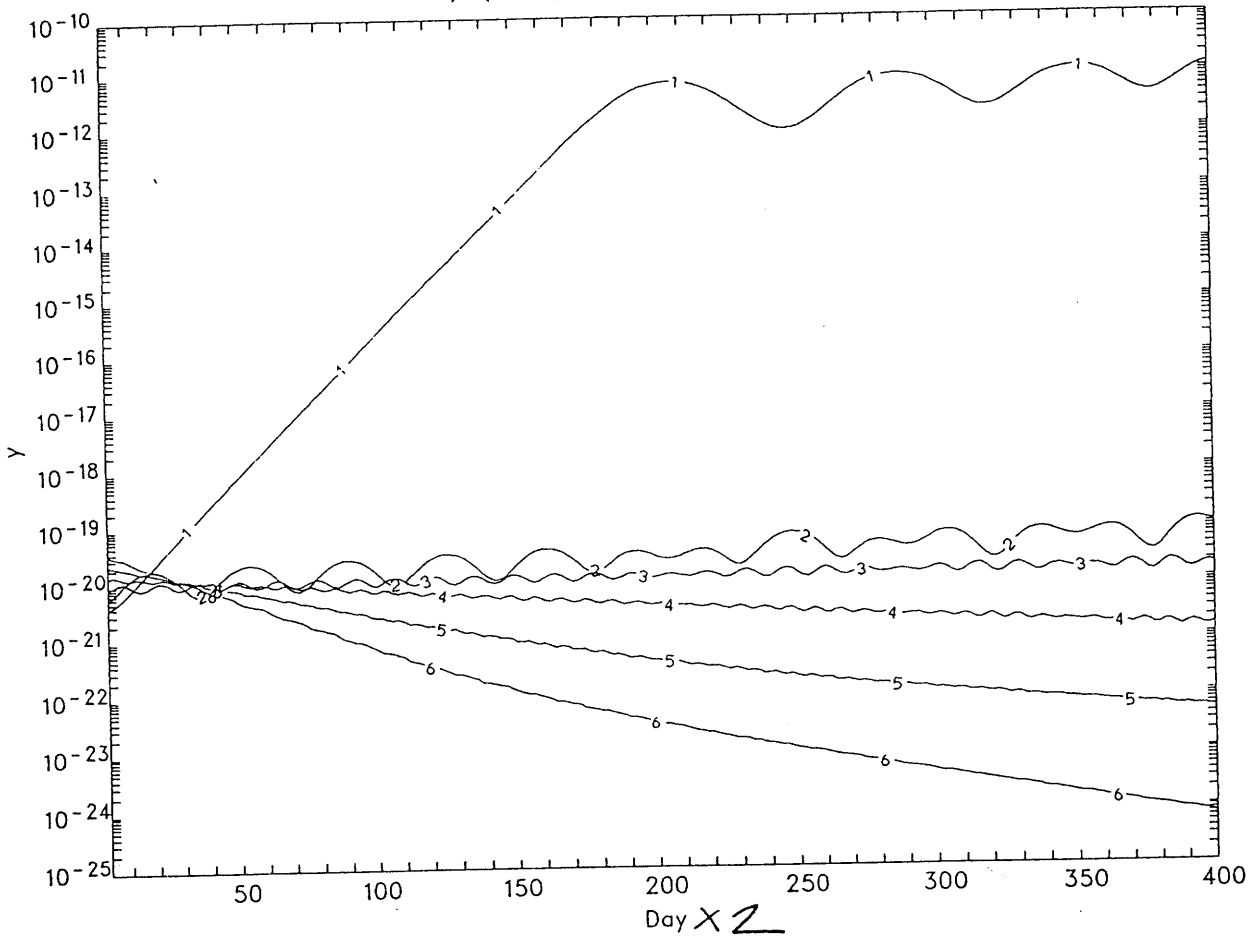
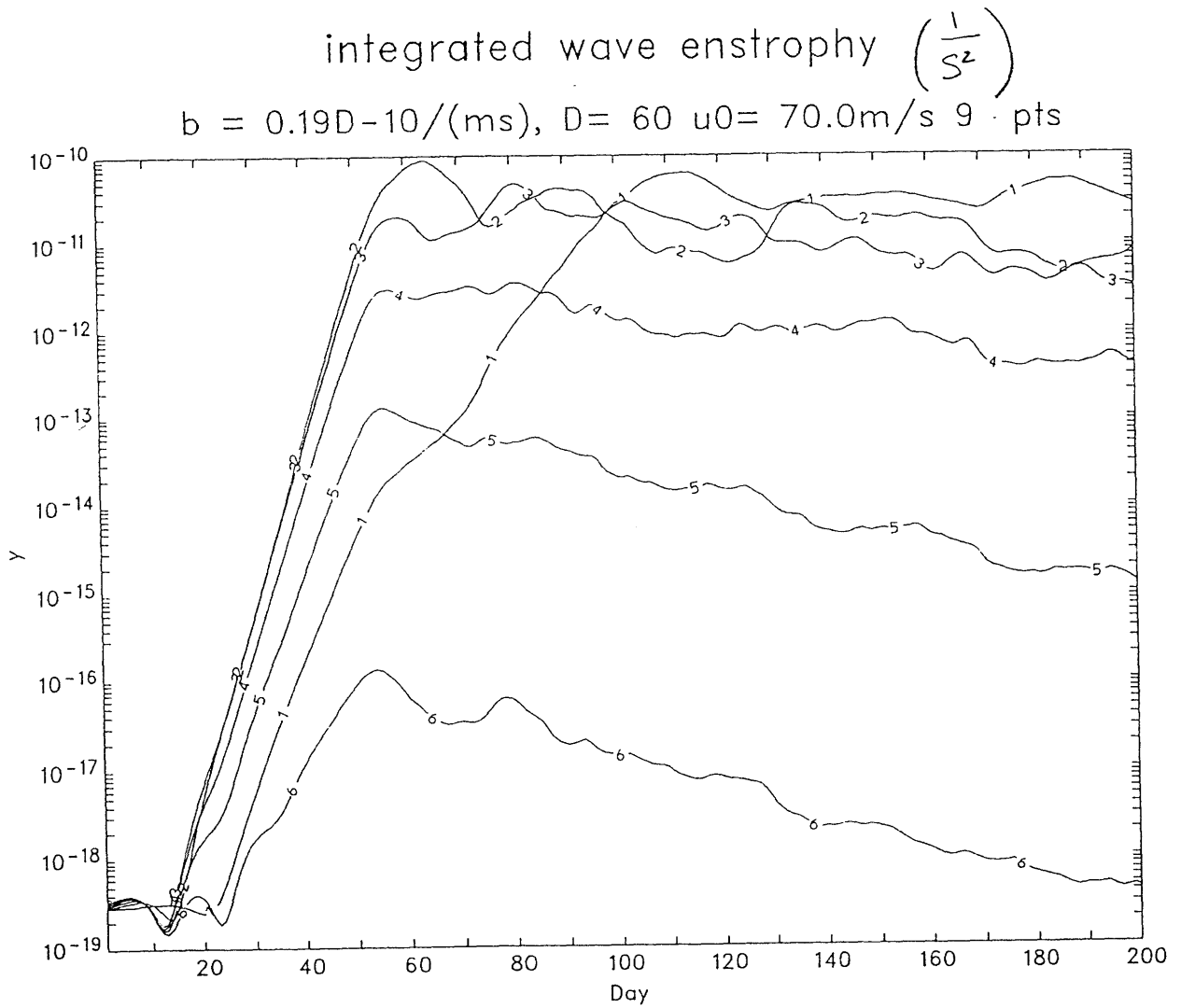b = 0.19D-10/(ms), D= 20 u0= 70.0m/s 5 pts
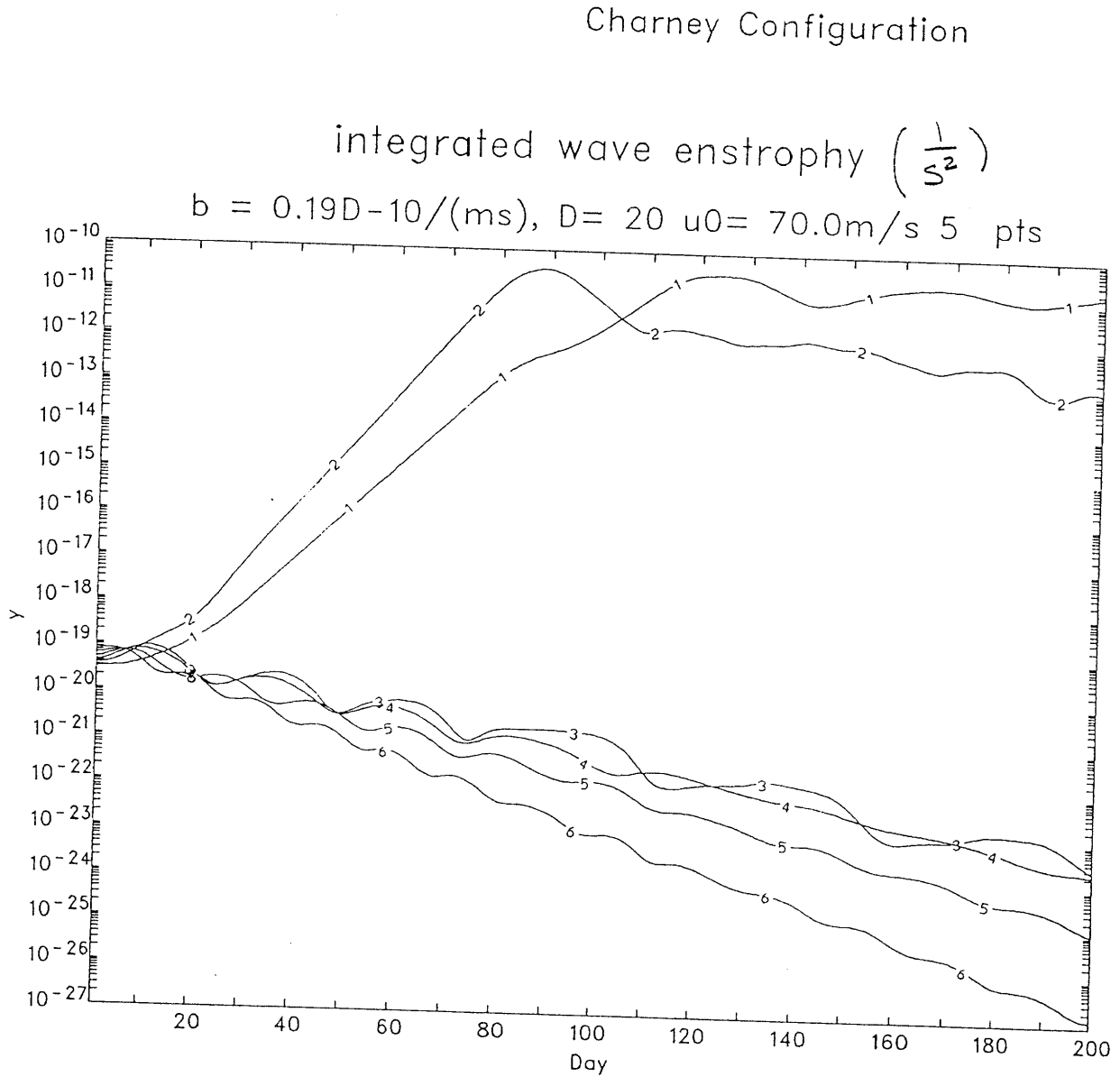
Figure A-15: The partitioning of the integrated wave enstrophy among waves 1-6, from the 5 gridpoint quasi-linear half jet model run with a dissipation timescale of 20 days.

Charney Configuration

dqdy at the jet $\left(\times 10^{-11} \frac{1}{ms} \right)$

b = 0.19D-10/(ms), D=inf u0= 70.0m/s 9 pts

Figure A-16: Meridional gradient of the potential vorticity at the jet from the 9 gridpoint quasi-linear half jet model run without dissipation and a maximum zonal mean wind equal to 70 m/s.

Charney Configuration

dqdy at the jet $\left(\times 10^{-11}\frac{1}{ms}\right)$

b = 0.19D-10/(ms), D=inf u0= 70.0m/s 5   pts

Figure A-17: Meridional gradient of the potential vorticity at the jet from the 5 gridpoint quasi-linear half jet model run without dissipation and a maximum zonal mean wind equal to 70 m/s.

Charney Configuration

dqdy at the jet $\left(\times 10^{-11} \frac{1}{ms} \right)$

b = 0.19D-10/(ms), D=inf u0= 70.0m/s 3   pts
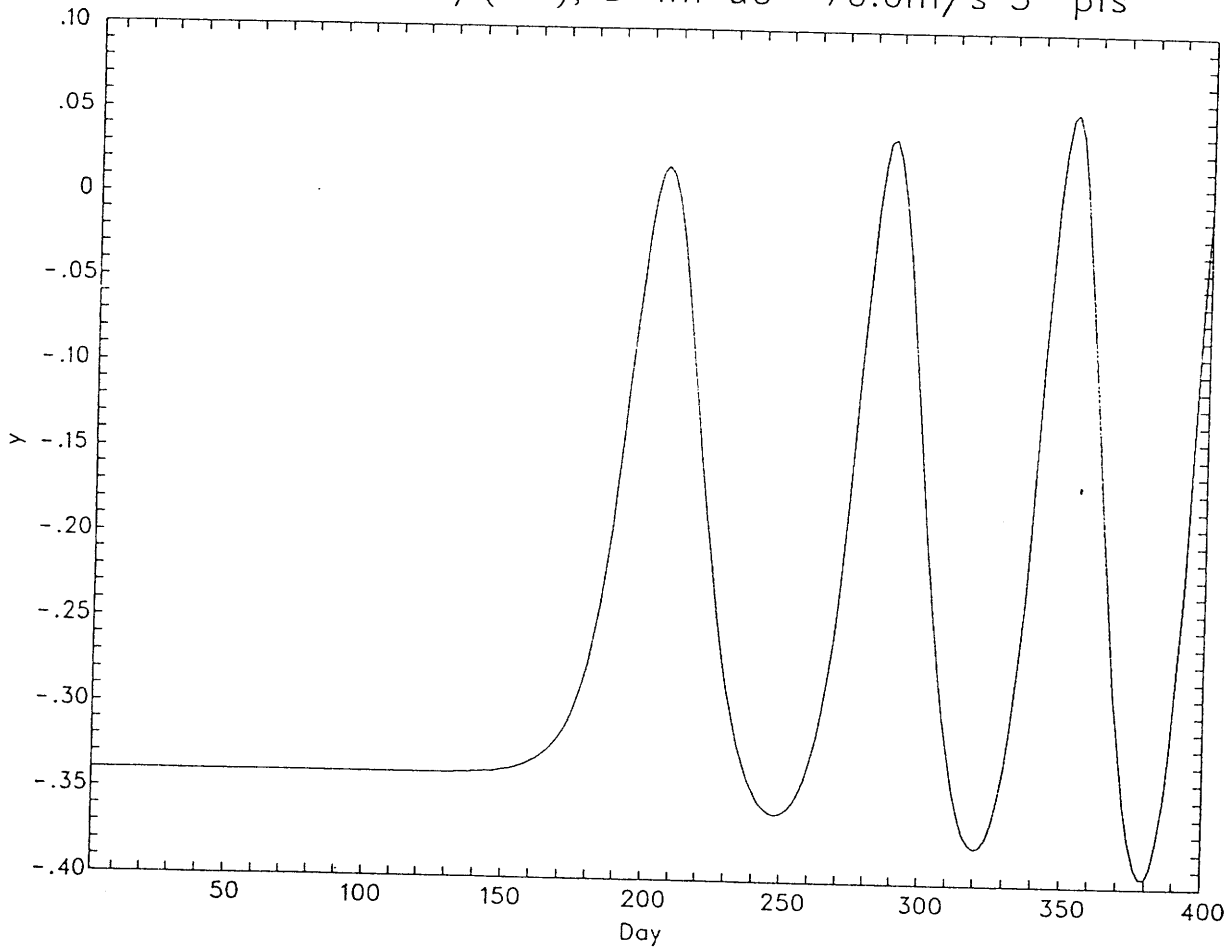
Figure A-18: Meridional gradient of the potential vorticity at the jet from the 3 gridpoint quasi-linear half jet model run without dissipation and a maximum zonal mean wind equal to 70 m/s.

Charney Configuration

$$\text{dqdy at the jet} \left(\times 10^{-11} \frac{1}{ms} \right)$$

$$b = 0.19D-10/(ms), \quad D= 20 \quad u0= 30.0m/s \quad 9 \quad pts$$
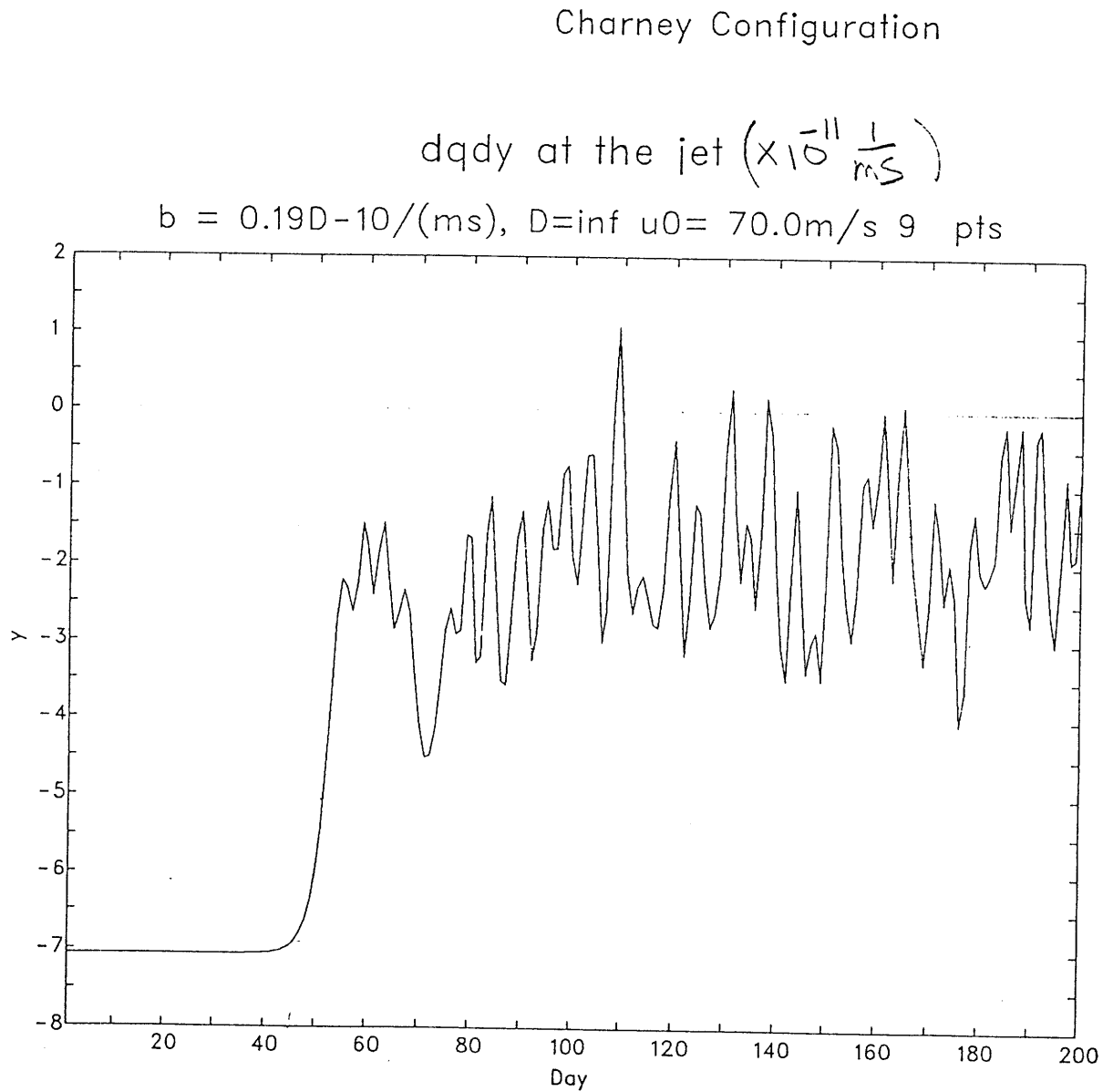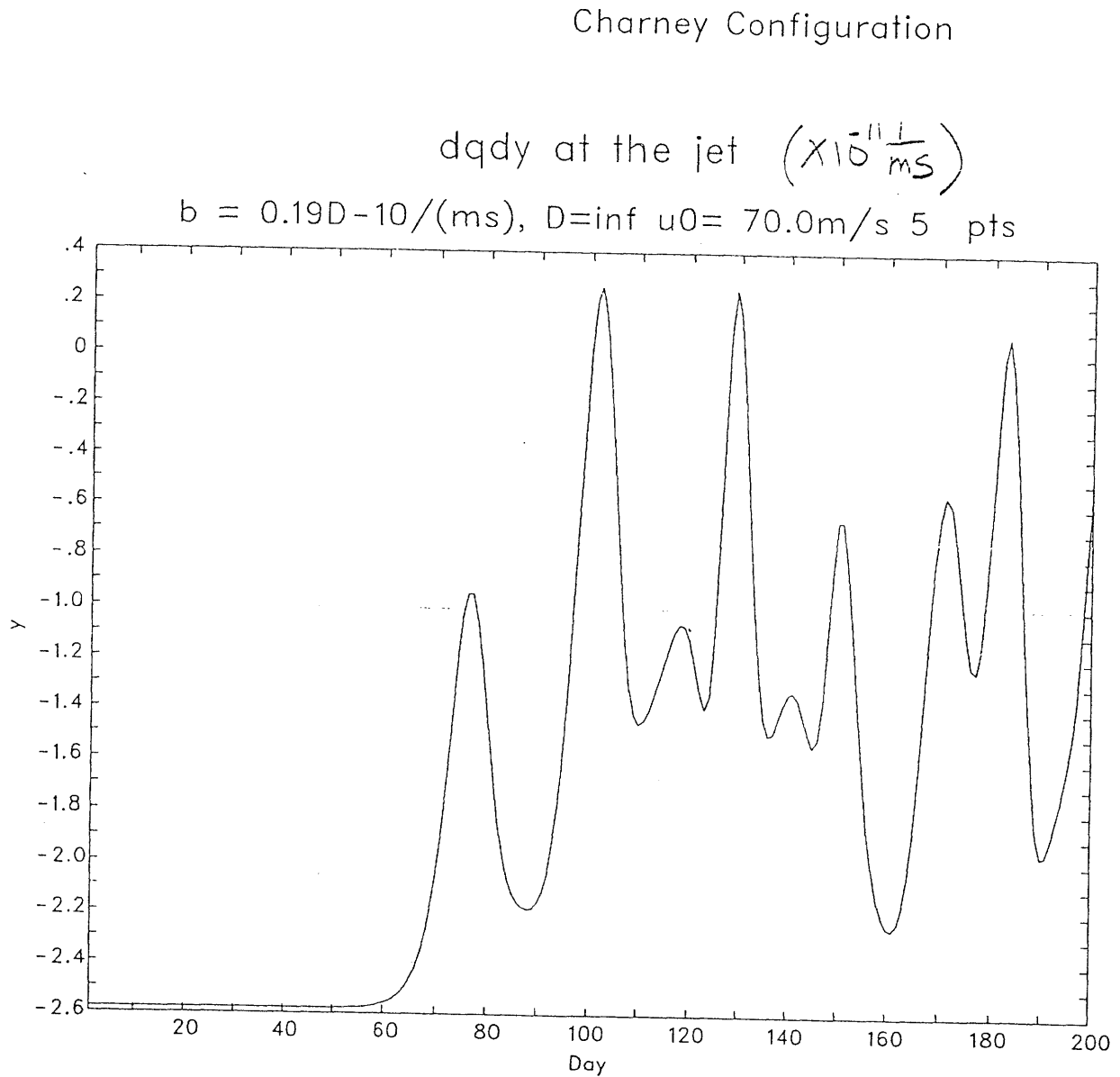

Figure A-19: Meridional gradient of the potential vorticity at the jet from the 9 gridpoint quasi-linear half jet model run with a dissipation timescale of 20 days and a maximum zonal mean wind equal to 30 m/s.

Charney Configuration

dqdy at the jet 19 pts, D= 20

Figure A-20: The jump in the potential vorticity gradient at the jet as a function of beta and the maximum zonal wind for a 19 gridpoint quasi-linear half jet model run.

Charney Configuration

$$\overline{v'q'}$$

pv transport $\left(\times 10^{-7} \frac{m}{s^2} \right)$

b = 0.19D-10/(ms), D= 20 u0= 70.0m/s 9 pts

$2 \Rightarrow y = L$

$1 \Rightarrow y = L - \Delta y$

Figure A-21: The zonally averaged transport of perturbation potential vorticity at the jet from the 9 grid-point quasi-linear half jet model run with a dissipation timescale of 20 days and a maximum zonal mean wind equal to 70 m/s.

Charney Configuration

$$\overline{v'q'}$$

pv transport $\times 10^{-7}$

b = 0.19D-10/(ms), D= 60 u0= 70.0m/s   9 pts
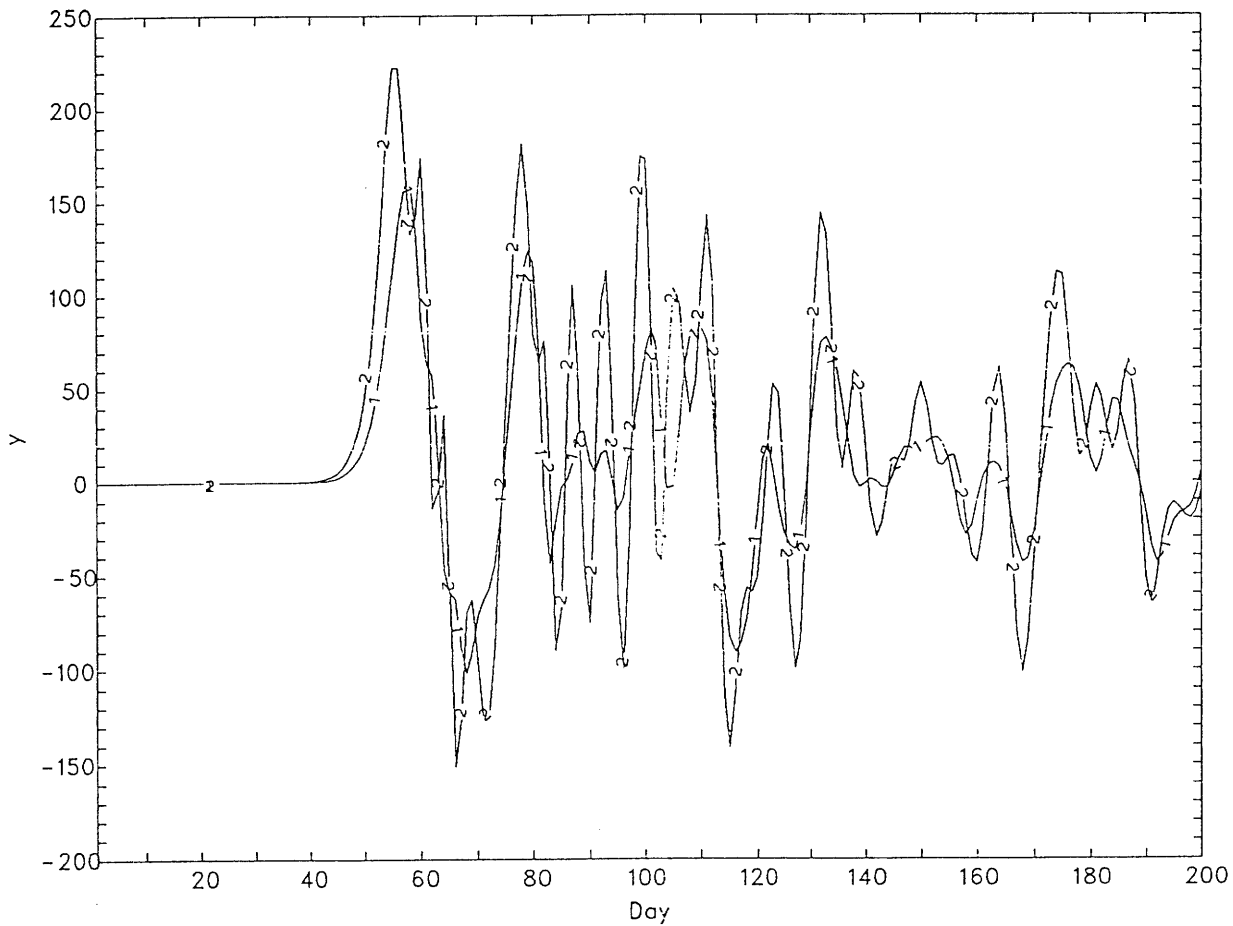
$$2 \Rightarrow y = L$$
$$1 \Rightarrow y = L - \Delta y$$

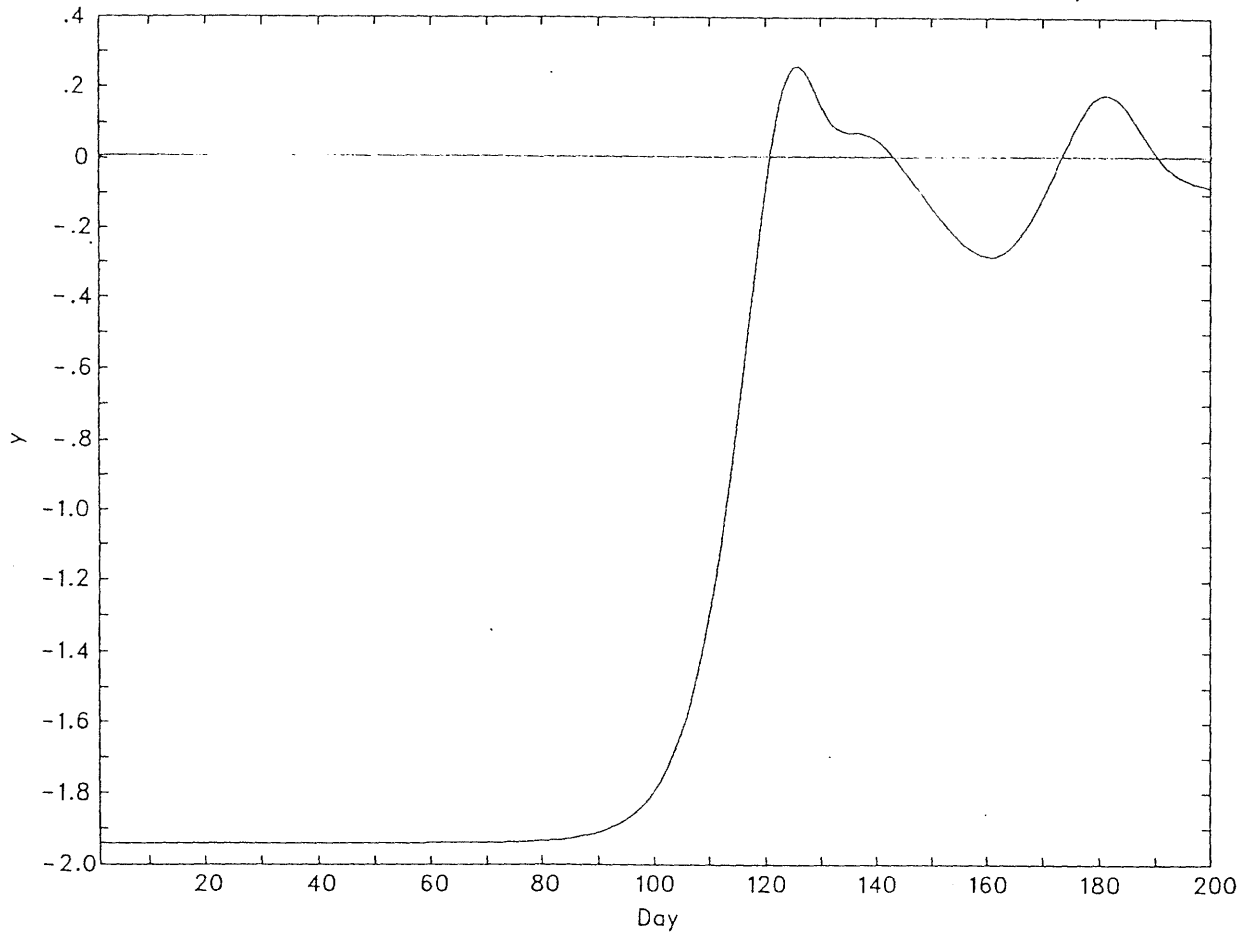Figure A-22: The zonally averaged transport of perturbation potential vorticity at the jet from the 9 grid-point quasi-linear half jet model run with a dissipation timescale of 60 days and a maximum zonal mean wind equal to 70 m/s.
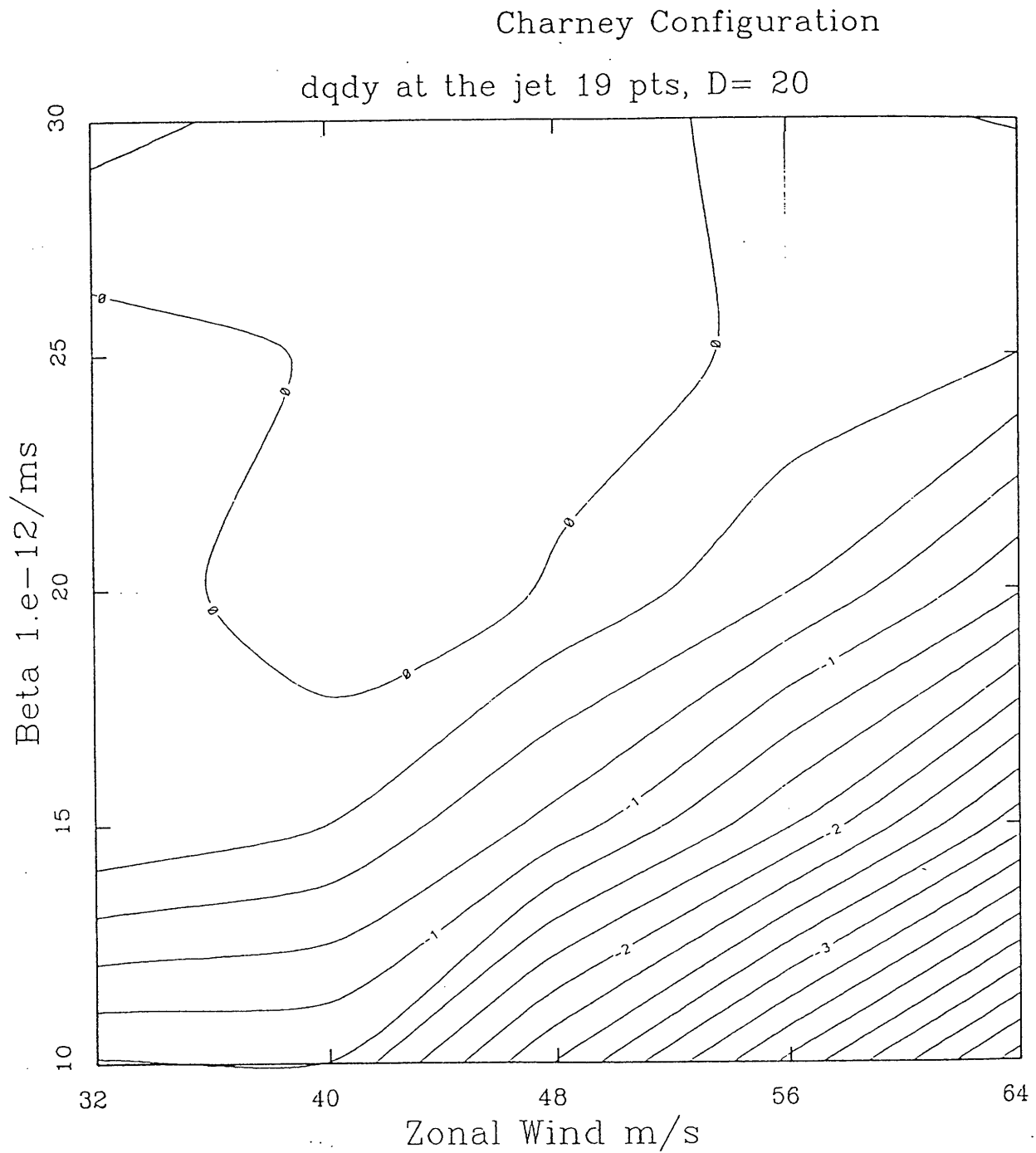
Charney Configuration

$$\overline{v'q'}$$

pv transport $\left(\times 10^{-7} \frac{m}{s^2}\right)$

b = 0.19D-10/(ms), D= 20 u0= 70.0m/s   5 pts
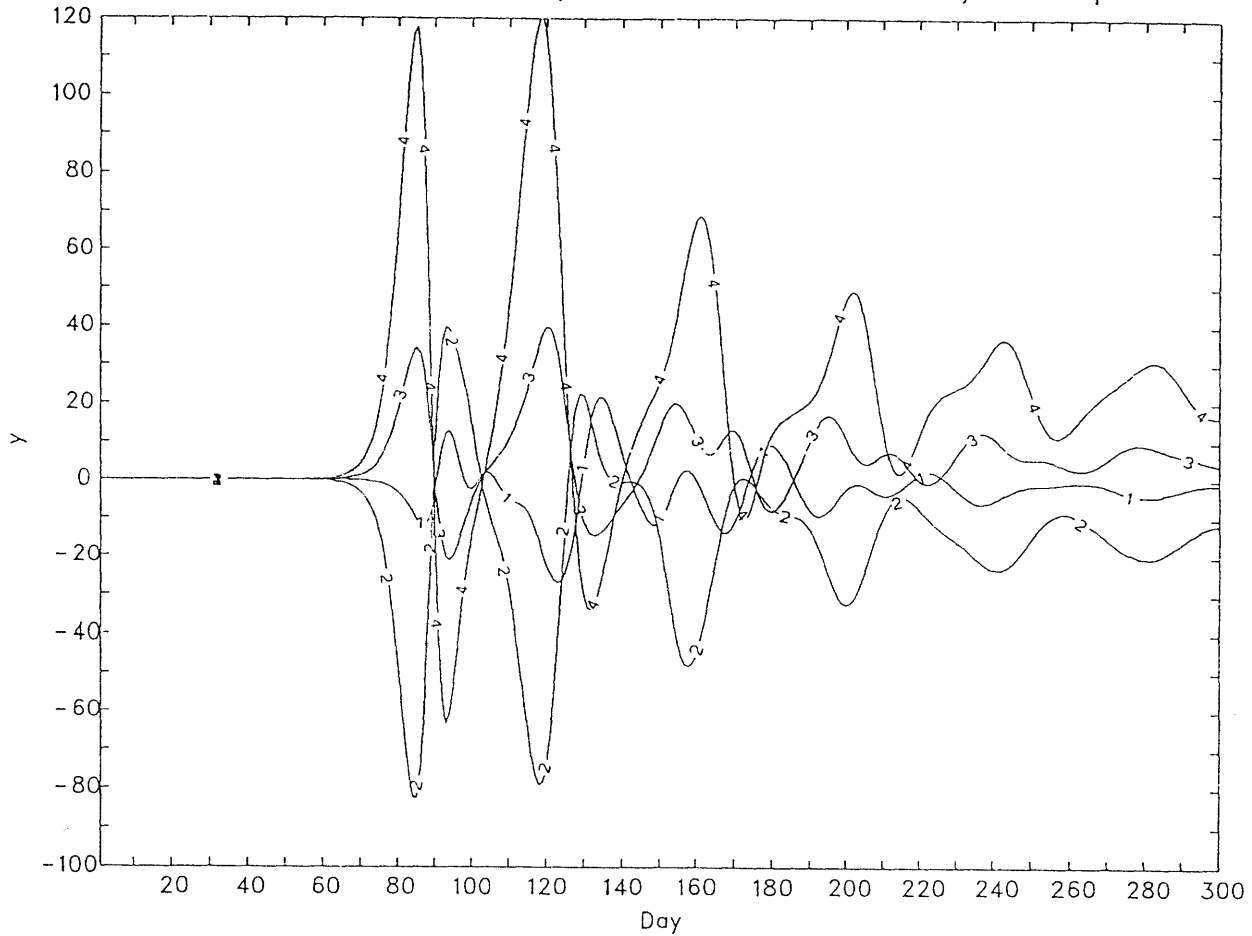
$1 \Rightarrow y = L - 3\Delta y$

$2 \Rightarrow y = L - 2\Delta y$

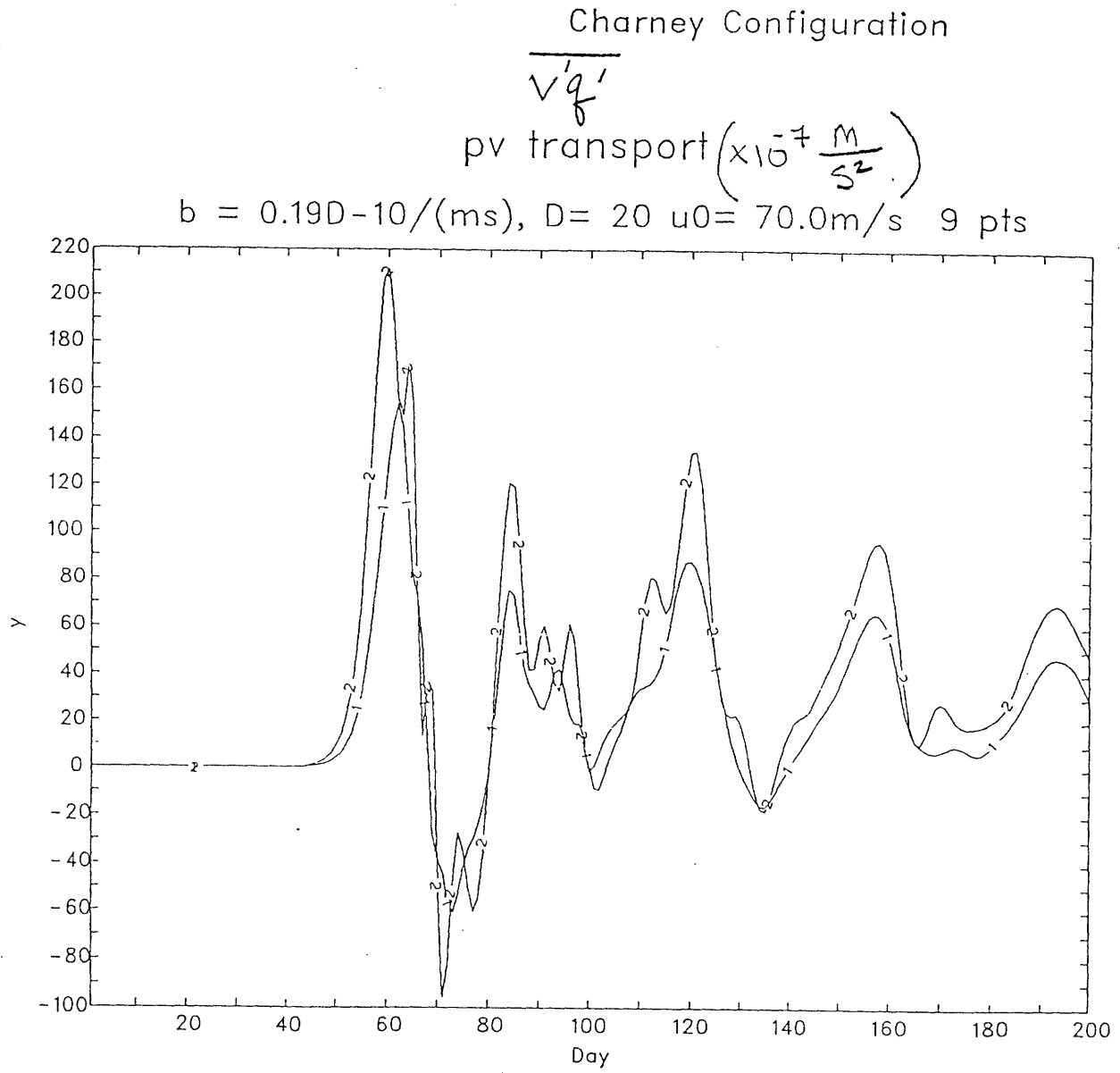$3 \Rightarrow y = L - \Delta y$

$4 \Rightarrow y = L$

Figure A-23: The zonally averaged transport of perturbation potential vorticity at the jet from the 5 grid-point quasi-linear half jet model run with a dissipation timescale of 20 days and a maximum zonal mean wind equal to 70 m/s.

Charney Configuration

$$\overline{V'q'}$$

pv transport $\left(\times 1.\bar{e}7 \ \frac{m}{s^2}\right)$

b = 0.19D-10/(ms), D= 20 u0= 70.0m/s   3 pts

$$2 \Rightarrow y = L$$
$$1 \Rightarrow y = L - \Delta y$$

Figure A-24: The zonally averaged transport of perturbation potential vorticity at the jet from the 3 grid-point quasi-linear half jet model run with a dissipation timescale of 20 days and a maximum zonal mean wind equal to 70 m/s.
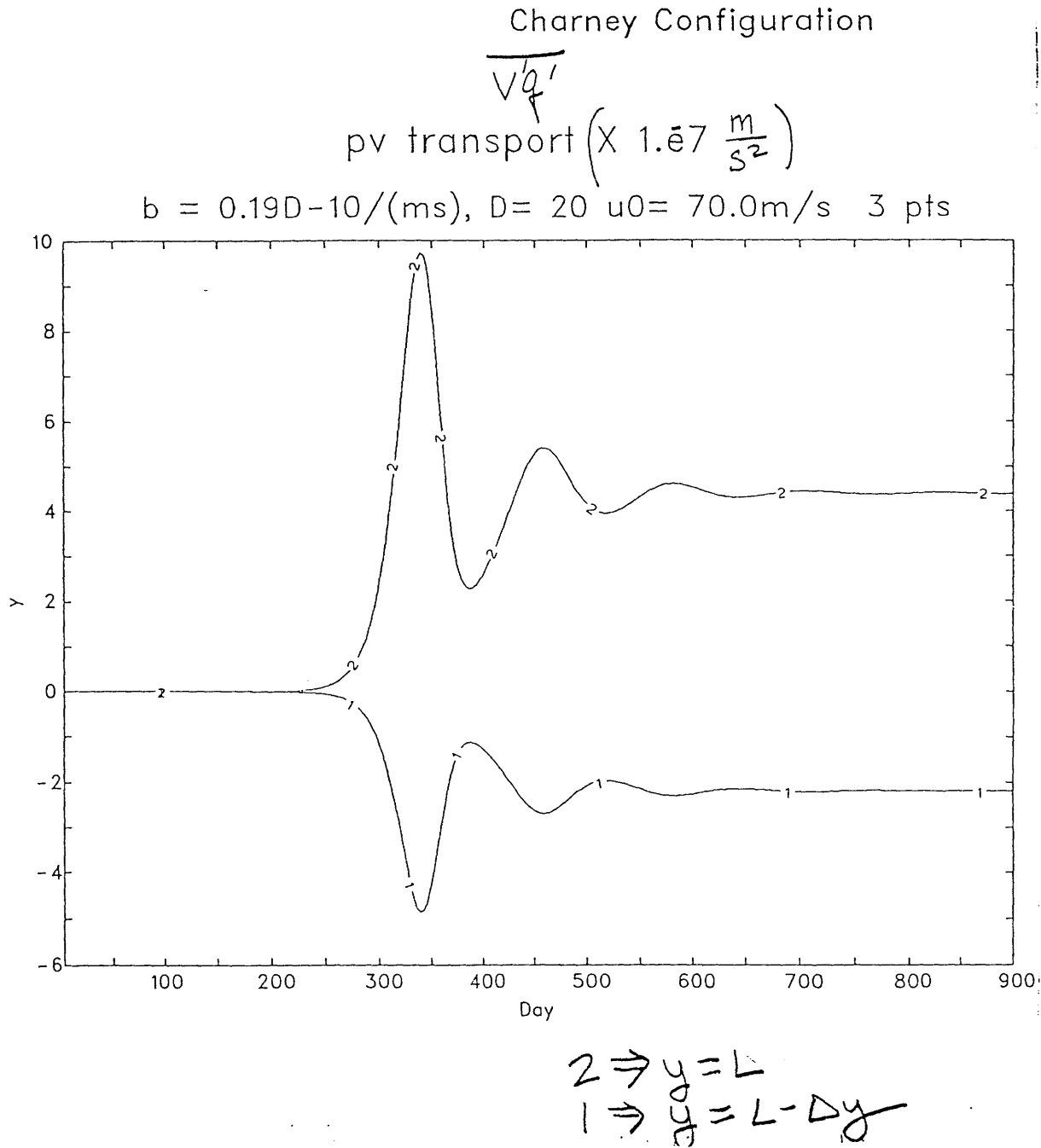
References

Arakawa,A., and S. Moorthi, 1988: Baroclinic instability in vertically discrete systems. *J. Atmos. Sci.*, **45**,1688-1707.

Bannon, P.R., and T.L. Salem Jr., 1995: Aspects of the baroclinic boundary layer. *J. Atmos. Sci.*, **52**, 574-596.

Bretherton,F.P.,1966: Critical layer instability in baroclinic flows. *Quart. J. Roy. Meteor. Soc.*,92,325-334.

Cehelsky, P., and K.K. Tung, 1991: Nonlinear baroclinic adjustment. *J. Atmos. Sci.*,48, 159-172.

Charney, J.G., and M.E. Stern, 1962: On the stability of internal baroclinic jets in a rotating atmosphere. *J. Atmos. Sci.*,19, 159-172.

Edmon, H.J., B.J. Hoskins, and M.E. McIntyre, 1980: Eliassen-Palm cross-sections for the troposphere. *J. Atmos. Sci.*,37, 2600-2616.

Farrell, B., 1985: Transient growth of damped baroclinic waves. *J. Atmos. Sci.*,42, 2718-2727.

Fullmer, J.W.A. , 1982b: Calculations of the quasi-geostrophic potential vorticity gradient from climatological data. *J. Atmos. Sci.*, **39**,1874-1877.

Gall, R., 1976: Structural changes of growing baroclinic waves. *J. Atmos. Sci.*,33, 374-390.

Gleckler, P. J., D. Randall, G. Boer, R. Coleman, M. Dix, V. Galin, M. Helfand, J. Kiehl, A. Kitoh, W. Lau, X.-Y. Liang, V. Lykossov, B. McAvaney, K. Miyakoda, S. Planton, and W. Stern, 1995: Cloud-radiative effects on implied oceanic energy transports as simulatd by atmospheric general circulation models. *Geophys. Res. Lett.* ,22, 791-794.

Gutowski, W. J., 1985a: A simple model for the interaction between vertical eddy heat fluxes and static stability. *J. Atmos. Sci.*, **42**, 346-358.

Gutowski, W. J., 1985b: Baroclinic adjustment and midlatitude temperature profiles. *J. Atmos. Sci.*, **42**, 1735-1745.

Gutowski, W. J.,L.E. Branscome,and D.A. Stewart, 1989: Mean flow adjustment during life cycles of baroclinic waves. *J. Atmos. Sci.*,46, 1724-1737.

Held, I. M., 1978a: The vertical scale of an unstable wave and its importance for eddy heat flux parameterizations. *J. Atmos. Sci.*,35, 572-576.

Held, I. M., 1978b: The tropospheric lapse rate and climatic sensitivity: Experiments with a two-level atmospheric model. *J. Atmos. Sci.*,35, 2083-2098.

Held, I.M., and B.J. Hoskins, 1985: Large-scale eddies and the general circulation of the troposphere. Adv. Geophys., **28A**, 3-31.

Held, I. M., and E. O'Brien, 1992: Quasigeostrophic turbulence in a three-layer model: effects of vertical structure in the mean shear. *J. Atmos. Sci.*. **49**, 1861-1870.

Held, I. M., and M.J. Suarez, 1978: A two-level primitive equation atmospheric model designed for climatic sensitivity experiments. *J. Atmos. Sci.*, **35**. 206-229.

Hoskins, B.J., 1983: 'Modelling of the transient eddies and their feedback on the mean flow'. In *Large-scale dynamical processes in the atmosphere.* Eds. B.J. Hoskins and R.P. Pierce. Academic Press. New York

Hoskins, B.J., M.E. McIntyre, and A.W. Robertson, 1985: On the use and significance of isentropic potential vorticity. *Q.J.R. Meteorol. Soc.*,111, 877-946.

Hua, B.L., and D.B. Haidvogel, 1986: Numerical simulations of the vertical structure of quasi-geostrophic turbulence. *J. Atmos. Sci.*, **49**. 572-576.

Ioannou, P., and R.S. Lindzen, 1986: Baroclinic instability in the presence of barotropic jets.*J. Atmos. Sci.*, **43**, 2999-3014.

Kalnay De Rivas, E., 1972: On the use of nonuniform grids in finite-difference equations. *J. Comput. Phys.*,10,202-210.

Killworth, P.D., and M.E. McIntyre, 1985: Do Rossby-wave critical layers absorb, reflect or over-reflect? *J. Fluid. Mech.*,161, 449-492.

Lin, S., and R.T. Pierrehumbert, 1988: Does Ekman friction suppress baroclinic instability? *J. Atmos. Sci.*, 45, 2920-2933.

Lindzen, R.S., 1993: Baroclinic neutrality and the tropopause. *J. Atmos. Sci.*, **50**, 1148-1151.

Lindzen, R.S., and B. F. Farrell, 1980: Role of the polar regions in global climate and a new parameterization of global heat transport. *Mon. Wea. Rev.*, **108**, 2064-2079.

Lindzen, R.S., A.Y. Hou, and B.F. Farrell, 1982: Role of convective model choice in calculating the climate impact of doubling CO_2. *J. Atmos. Sci.*, **39**, 1189-1205.

Lindzen, R.S., A.J. Rosenthal, and B. F. Farrell, 1983: Charney's problem for baroclinic instability applied to barotropic instability. *J. Atmos. Sci.*, **40**, 1029-1034.

Manabe, S. and Moller, 1961: On the radiative equilibrium and heat balance of the atmosphere. *Mon. Wea. Rev.*,**89**, 503-532.

Manabe, S. and R.T. Wetherald, 1975: The effect of doubling of CO_2 concentrations on the climate of a general circulation model. regimes. *J. Atmos. Sci.*,**32**, 3-15.

McIntyre, M.E., and W.A. Norton, 1990: Dissipative wave-mean flow interactions and the transport of vorticity or potential vorticity. regimes.*J. Fluid Mech.*,**212**, 403-435.

Morgan, M.C., 1994: An observationally and dynamically determined basic state for the study of synoptic scale waves. MIT thesis, 123 pp.

Nielsen, J. E., and M.R. Schoeberl, M.R., 1984: A numerical simulation of barotropic instability. Part 2: Wave-wave interaction. *J. Atmos. Sci.*,**41**, 2869-2881.

Pavan, V., 1996: Sensitivity of a multi-layer quasi-geostrophic β-plane channel to the vertical structure of the equilibrium meridional temperature gradient. regimes.*Q.J.R. Meteorol. Soc.*,**122**, 55-72.

Pedlosky, J., 1996: *Ocean circulation theory.* Springer-Verlag, 453 pp.

Peixoto, J.P., and A.H. Oort, 1992:*Physics of Climate.* American Institute of Physics, 520 pp.

Phillips, N.A., 1954: Energy transformation and meridional circulations associated with simple baroclinic waves in a two-level quasi-geostrophic model. *Tellus*, **6**, 273-286.

Randel, W.J., and I.M. Held, 1991: Phase speed spectra of transient eddy fluxes and critical layer absorption. *J. Atmos. Sci.*,**48**, 688-697.

Rhines, P.B., and W.R. Young, 1982a: A theory of the wind-driven circulation. I. Mid-ocean gyres. *J. Marine Res.*, **40** (Supplement), 559-596.

Rhines, P.B., and W.R. Young, 1982b: Homogenization of potential vorticity in planetary gyres. *J. Fluid Mech.*, **122**, 347-367.

Robinson, W.A., 1988: On the structure of potential vorticity in baroclinic instability. *Tellus,***41A**, 275-284.

Schoeberl, M.R., and R.S. Lindzen, 1984: A numerical simulation of barotropic instability. Part 1: Wave-mean flow interaction. *J. Atmos. Sci.,***41**, 1368-1379.

Schoeberl, M.R., and J.E. Nielsen, 1986: A numerical simulation of barotropic instability. Part 3: Wave-wave interaction in the presence of dissipation. *J. Atmos. Sci.,***43**, 1045-1050.

Shea, D. J., K. E. Trenberth and R. W. Reynolds. 1990: A global monthly sea surface temperature climatology. NCAR Technical Note NCAR/TN-345+STR, 167 pp.

Stewartson, K., 1978: The evolution of a critical layer of a Rossby wave. *Geophys. Astrophys. Fluid Dyn.,* 9, 185-200.

Stone, P.H., 1972: A simplified radiative-dynamical model for the static stability of rotating atmospheres. *J. Atmos. Sci.,* 29, 405-418.

Stone, P.H., 1978: Baroclinic adjustment. *J. Atmos. Sci.,***35**, 561-571.

Stone, P.H., and L. Branscome, 1991: Diabatically forced nearly inviscid eddy regimes.*J. Atmos. Sci.,***36**, 415-423.

Stone, P.H., and B. Nemet, 1996: Baroclinic Adjustment: A comparison between theory, observations and models. *J. Atmos. Sci.,***53**, 1663-1674.

Stone, P.H., and J.S. Risbey, 1990: On the limitations of general circulation climate models. *Geophys. Res. Lett.,* **17**, 2173-2176.

Sun, D., and R.S. Lindzen, 1994: A PV view of the zonal mean distribution of temperature and wind in the extratropical troposphere. *J. Atmos. Sci.,***51**, 757-772.

Swanson, K.L., and R.T. Pierrehumbert, 1997: Lower-tropospheric heat transport in the Pacific storm track. *J. Atmos. Sci.,***54**, 1533-1543.

Trenberth, K.E., 1992: Global analyses from ECMWF. NCAR Technical Note. NCAR/TN-373+STR, 191 pp.

Valdes, P. and B.J. Hoskins, 1988: Baroclinic instability of the zonally averaged flow with boundary layer damping. *J. Atmos. Sci.,***45**, 1584-1593.

Warn, T., and H. Warn, 1978: The evolution of a nonlinear critical level. *Stud. Appl. Maths,* **59**, 37-71.

Young, W.R., and P.B. Rhines, 1982: A theory of the wind-driven circulation. II. Gyres with western boundary currents. *J. Marine Res.*, **40**, 849-872.

Zhou, S., and P. H. Stone, 1992a: The role of large-scale eddies in the climate equilibrium, Part 1: Fixed static stability. *J. Climate.*,**6**, 985-1001.

Zhou, S., and P. H. Stone, 1992b: The role of large-scale eddies in the climate equilibrium, Part 2: Variable static stability. *J. Climate.*,**6**, 1871-1881.